Université de Strasbourg
Ecole doctorale Sciences de la Terre et de l'Univers

et

Charles University in Prague
Faculty of Science
Institute of Petrology and Structural Geology

THÉSE

Pour obtenir le grade de

DOCTEUR EN SCIENCES

Spécialité Sciences de la Terre et de l'Univers de l'Université de Strasbourg

Par

Vladimír Kusbach

Couplage et découplage entre manteau et croûte inférieure pendant l'orogenèse continentale (Strain coupling versus decoupling of mantle and crust during orogenesis).

Soutenue publiquement à Strasbourg le 23 septembre 2011
devant le jury composé de:

Prof. Olivier Vanderhaeghe	Université Henri Poincaré, Nancy	Rapporteur
Dr. Andréa Tommasi	Université Montpellier II, Montpellier	Rapporteur
Prof. Hubert Whitechurch	Université de Strasbourg, Strasbourg	Rapporteur
Prof. Didier Marquer	Université de Franche Comté, Besançon	Examinateur
Dr. Ondřej Lexa	Charles University, Prague	Examinateur
Prof. Karel Schulmann	Université de Strasbourg, Strasbourg	Directeur de thése
Dr. Stanislav Ulrich	Charles University, Prague	Co-directeur de thése

Acknowledgements

At this place I would like to thank all the people that helped me during my Ph.D. and supported me through these years to it's end represented by this thesis. Thank YOU very much.

Firstly, I would like to thank both my supervisors Karel Schulmann and Stano Ulrich for all priceless ideas, revisions, comments and of course deadlines. Many thanks belong to many people helping me with different parts of this thesis, namely Vojtěch Janoušek, Pavlína Hasalová, Pavla Štípská, František Hrouda, Marta Chlupáčová, Zuzana Kratinová, Matěj Machek and many others unmentioned but not forgotten.

My special thanks belong to the French government that was financing my stays in Strasbourg within the framework of the Co-tutelle program. This work was also supported by Czech National Grant Agency (GAČR) grant no. 205/09/0539, and the Research Intent of the Geophysical Institute, Academy of Sciences of the Czech Republic no. AV0Z30120515.

Last, but not least, I would like to thank my family, non-geological friends and ULTIMATE FRISBEE to keep me in good shape both psychical and physical.

Contents

Introduction

The crust mantle interaction during orogenesis is a major issue in understanding deep seated thermomechanical processes in large orogens and behavior of subcontinental mantle during continental collision in particular. European Variscan belt offers an exceptional opportunity to study tectonic interactions between mantle and orogenic lower crust thanks to the presence of bodies of garnet- and spinel-bearing peridotites of variable size included in largest Ky–Kfs granulite massifs within the orogenic belt (Behr, 1961 – Saxony granulite massif; Gayk and Kleinschrodt, 2000 – Vosges Massif; Medaris et al., 1995 – Bohemian Massif). The variety of structural relationships between peridotites, surrounding granulites and migmatites within the high grade core of Variscan orogens suggests, that the thermal and mechanical behavior of orogenic lower crust and underlying mantle was complex and reflect polyphase tectonic history.

In addition, seismological studies of subcrustal mantle lithosphere fabrics show contrasting orientation and strength of seismic anisotropy from shear-wave splitting and directional terms of relative P residuals and model a different fabric of the mantle lithosphere for principal terranes forming European Variscan belt (Babuška and Plomerová, 2006; Babuška et al., 2007, 2008).These data suggest heterogeneous mantle composition underneath continental crust related to Devono-Carboniferous subduction and collisional history as shown recently by Babuška et al. (2010). According to these authors the mantle lithosphere forms an integral part of individual terranes forming the Bohemian Massif implying that the mantle parts of the lithospheric blocks were rigid during main collisional event.

Bohemian Massif is characterized by presence of several hundreds of peridotite bodies of various size, chemical composition and degree of serpentinisation (Medaris et al., 2005). These peridotite massifs correspond to subcrustal mantle, which experienced various thermal and pressure history during Variscan orogeny. Several peridotite blocks (spinel-bearing harzburgites) originated during pre-collisional rifting that is recorded in P-T conditions and geochemistry characteristic for asthenospheric mantle (Medaris et al., 2005). In contrast, other blocks of garnet-bearing lherzolites reveal extreme

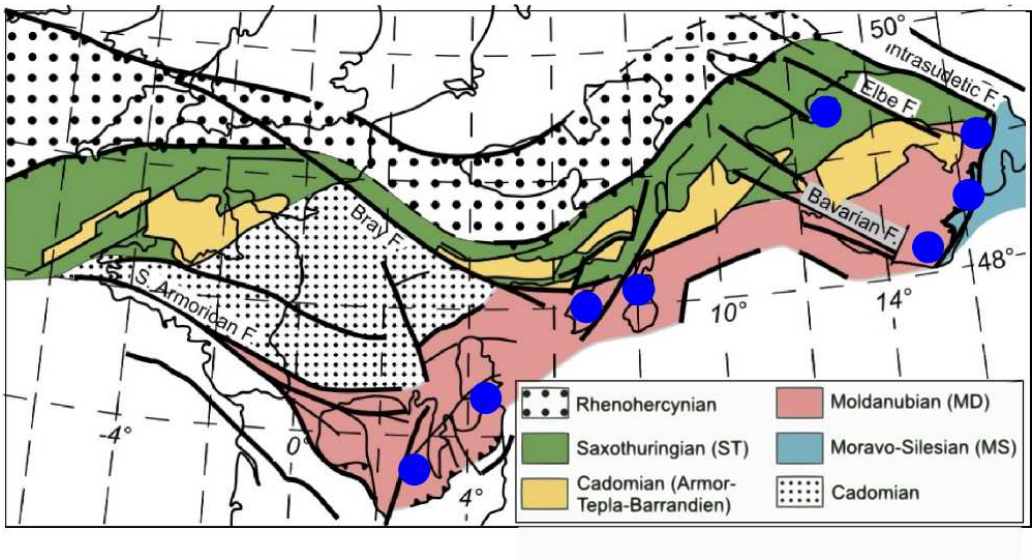

Figure 1. Map of Variscan Belt in Europe (modified after Franke, 2000). Variscides are composed of several paleogeographic domains (Rhenohercynian, Saxothuringian, Armor-Tepla-Barrandien, Moldanubian, Moravo-Silesian, Cadomian). Occurence of granulites in the european Variscan Belt is marked by blue dots.

pressure and temperature conditions of 1400 °C and 4–5 GPa and belong to the supra-subduction mantle wedge, which is sampled and exhumed by processes invoked by underlaying subduction zone (Becker, 1996, 1997; Nakamura et al., 2004; Ackermann et al., 2009; Machek et al., 2009).

Despite a considerable effort in understanding petrogenesis and metamorphic conditions of these rocks in the past (Medaris et al., 1995, 1998; 2006; Ackerman et al., 2009), sometimes coupled with petrofabric studies (Kamei et al., 2010), there is a complete lack in detailed and complex approach combining geochemistry, structural, petrology and petrofabrics. Recently, anisotropy of magnetic susceptibility method was used in order to understand relationships between internal fabric of peridotite enclaves and granulitic host rock (Hrouda et al., 2009). These works show, that the mantle fabrics are locally geometrically coupled with surrounding orogenic lower crust (Machek et al., 2009), suggesting common rheological and tectonic evolution of lithospheric mantle and lower crust, while others suggest a complete decoupling based on incoherent fabrics in the two lithologies (Hrouda et al., 2009).

The study of peridotite fragments can be approached by two ways: 1) a regional fabric analysis of the main peridotite bodies involving electron back–scattered diffraction study of olivine and pyroxene preferred orientations and anisotropy of magnetic susceptibility aiming to catalog possible fabric patterns in subcontinental mantle. 2) Detailed multidisciplinary study of selected peridotite bodies and their host rocks using geochemical, petrological, structural and geochronological methods. The second approach allows to understand processes related to the origin of mantle rocks and associated crust,

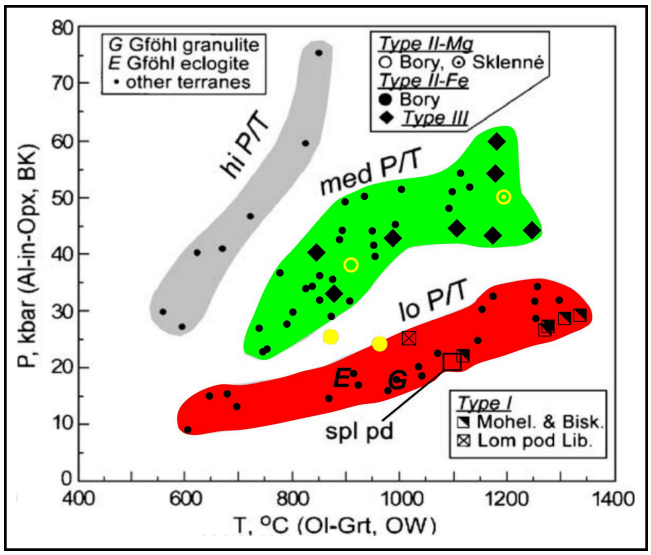

Figure 2. Various pressure – temperature conditions for Czech garnet peridotites according Medaris et al. (2005). Colour coding based on division into different types according to P/T gradient (type I – *red*, type II – *yellow*, type III – *green*).

their P–T–t evolution, and mechanical interactions both in mantle, lower crustal and shallow crustal depths. In this work we selected the second strategy, even if several other mantle bodies have been investigated as well. We have selected a serpentinized spinel and garnet harzburgite body (Mohelno peridotite) and surrounding Náměšť granulite massif, which were studied together in order to provide a detailed tectonic and petrogenetic model for future studies in other key peridotite bodies.

This thesis consists of three principal chapters which apply different techniques and respond to different questions related to peridotite origin and their behavior in crust. The first chapter deals with geochemistry and petrogenesis of peridotite together with a model of origin of host rock before orogenesis. The second chapter deals with combined structural and petrofabric study of Mohelno peridotite and attempt to explain mechanical behavior of peridotite thrust sheet in the frame of polyphase tectonic history of continental root. The third chapter is devoted to analysis of development of serpentinisation and AMS fabric in shallow crustal levels during final exhumation stages. Finally, the last part are general conclusions of so far achieved results combined with some new petrological data and a perspective of large scale geotectonic model of the eastern branch of the Bohemian Massif orogenic lower crust.

The first chapter is focused on the geochemical, petrogenetic and geochronological investigations of one of the most prominent lower crustal complex in the core of Variscan orogen – the Náměšť Granulite Massif located at the eastern margin of the Bohemian Massif. This chapter is specifically dealing with a new set of whole-rock geochemical data, petrophysical properties of the rocks and

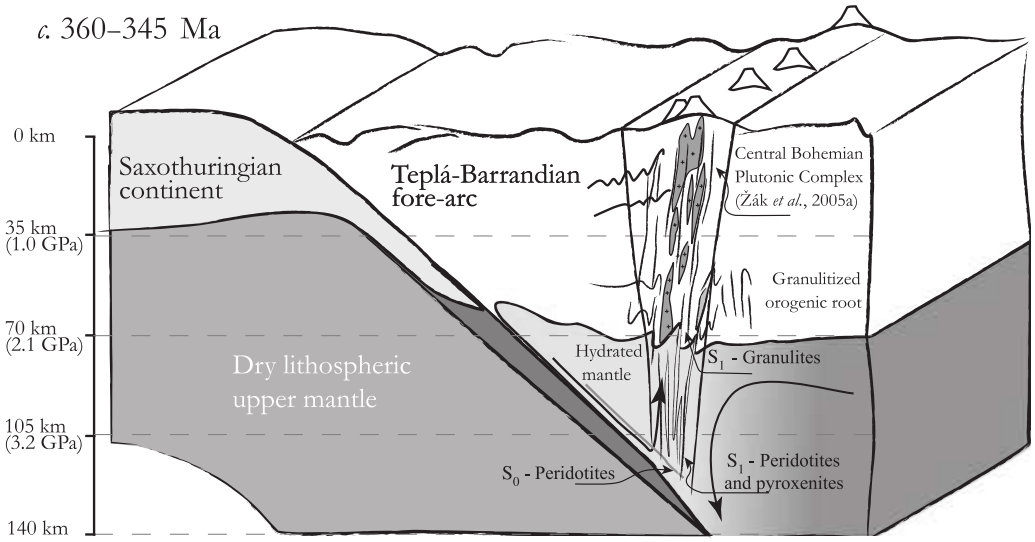

Figure 3. Three-dimensional model of a transpressional arc system for the Bohemian Massif. The tectonic and magmatic processes are linked, facilitating the upward movement of melt (Machek et al. 2009).

sensitive high-resolution ion–microprobe (SHRIMP) U-Pb zircon *in situ* dating of mineral fabrics in granulites in particular. The whole-rock geochemical analyses are obtained for all three main lithologies from the Náměšť Granulite Massif (NGM), namely felsic Ky–Kfs–Grt granulite, spinel- and garnet-bearing peridotite and garnetiferous amphibolite enveloping the NGM. The main results of this study can be summarized as follows: the geochemical signature of the Náměšť granulite share the same compositional features as other granulite occurrences in the Moldanubian Zone suggesting that the same petrogenetical model of their origin can be adopted. This is a model of a HP–HT isochemical metamorphism of continental crust of granitic composition, taking place at the bottom of thickened continental crust (Janoušek et al., 2004). The difference in protolith ages for rocks of identical chemistry may indicate, that the similar formation process of precursors of future granulites occurred in mid-Ordovician and Devonian times. The main difference is in protolith ages, that are Lower Devonian in the NMG compared to mid-Ordovician in other main granulite massifs. In addition the 353 Ma age of metamorphism is in average 13 My years older compared to more westerly equivalents. The metabasites reveal the composition of E-MORB or Within Plate Tholeiite which is in accord with similar occurences of Late Cambrian to Early Ordovician age. Because the chemistry of these rocks and their structural position are more or less similar (Höck et al., 1997) it is very likely that the studied rocks are also of Lower Palaeozoic, most probably of Late Cambrian to Early Ordovician age. The peridotites reveal composition of harzburgite of asthenospheric origin possibly refertilized in slow spreading ridge setting. Even if the existing Nd-Sm age can be considered as a cooling age, it is most likely related

to the upwelling during rifting history (Beard et al., 1992; Becker, 1997) and therefore the process of formation of studied peridotite is probably Late Devonian. This work shows that the three lithologies cannot originate in a single geodynamic environment. The granulites represent a Devonian and mid-Ordovician continental crust, while the metabasites reflects Cambro-Ordovician rifting, which precludes their common origin. Based on these characteristics and contrasting P–T data, we adopt here a model of lower crustal relamination of continental crustal allochthon below autochthonous mafic lower crust of Moldanubian continent (Lexa et al., 2011). The earlier metamorphic ages of lower crustal allochthon compared to westerly massifs are interpreted in terms of diachronous emplacement and different time scale of thermal maturation of western and eastern portions of relaminated crust, respectively. The various mantle geochemistry reflects the heterogeneous composition of subcontinental mantle, which was sampled during the process of relamination of the crust. This mechanisms can explain significant variations and P–T conditions of mantle material occuring today in individual granulite massifs in the Bohemian Massif.

The second chapter deals with peridotite sheet deformed by intra-mantle shear zone and refolded in lower to middle crustal conditions. We discuss the strength models of the continental lithosphere composed by: i) strong lithospheric mantle and weak lower crust for average and hot geotherms, ii) weak mantle based on experiments and seismic studies suggesting that the strength contrast between mantle and crust can vary in order of several magnitudes. These models result from experimental and partly also geophysical studies but field based mechanistic models are lacking so far. The internal zone of the European Variscan orogen (Bohemian Massif, Czech Republic) contains large complexes of Ky–Kfs granulites with incorporated spinel and garnet peridotites that can respond to question of mantle-lower crust strength contrast from the field perspective.

Studied garnet-spinel (Mohelno) serpentinized harzburgite occur in felsic Náměšť Granulite Massif and corresponds to large slice of depleted oceanic asthenosphere with peak PT conditions of about 2.2 GPa and 1150 °C (Medaris et al. 2005). The peridotite body forms large fold with steep hinge and vertical axial plane. Garnet belong to mineral assemblage within rarely preserved coarse-grained microstructure along the inner margin of the large fold. The original coarse-grained microstructure is dynamically recrystallized forming ultra fine-grained spinel-bearing mylonitic matrix (D = 10–20 microns). Surrounding felsic granulite shows mylonitic fabric S2 (rarely with preserved coarse-grained granulite fabric S1) revealing peak conditions of 18 kbar and 800 °C and heterogeneous D3 retrogression at about 0.7–1 GPa and 650 °C. The mylonitic granulite facies foliation S2, which is completely parallel

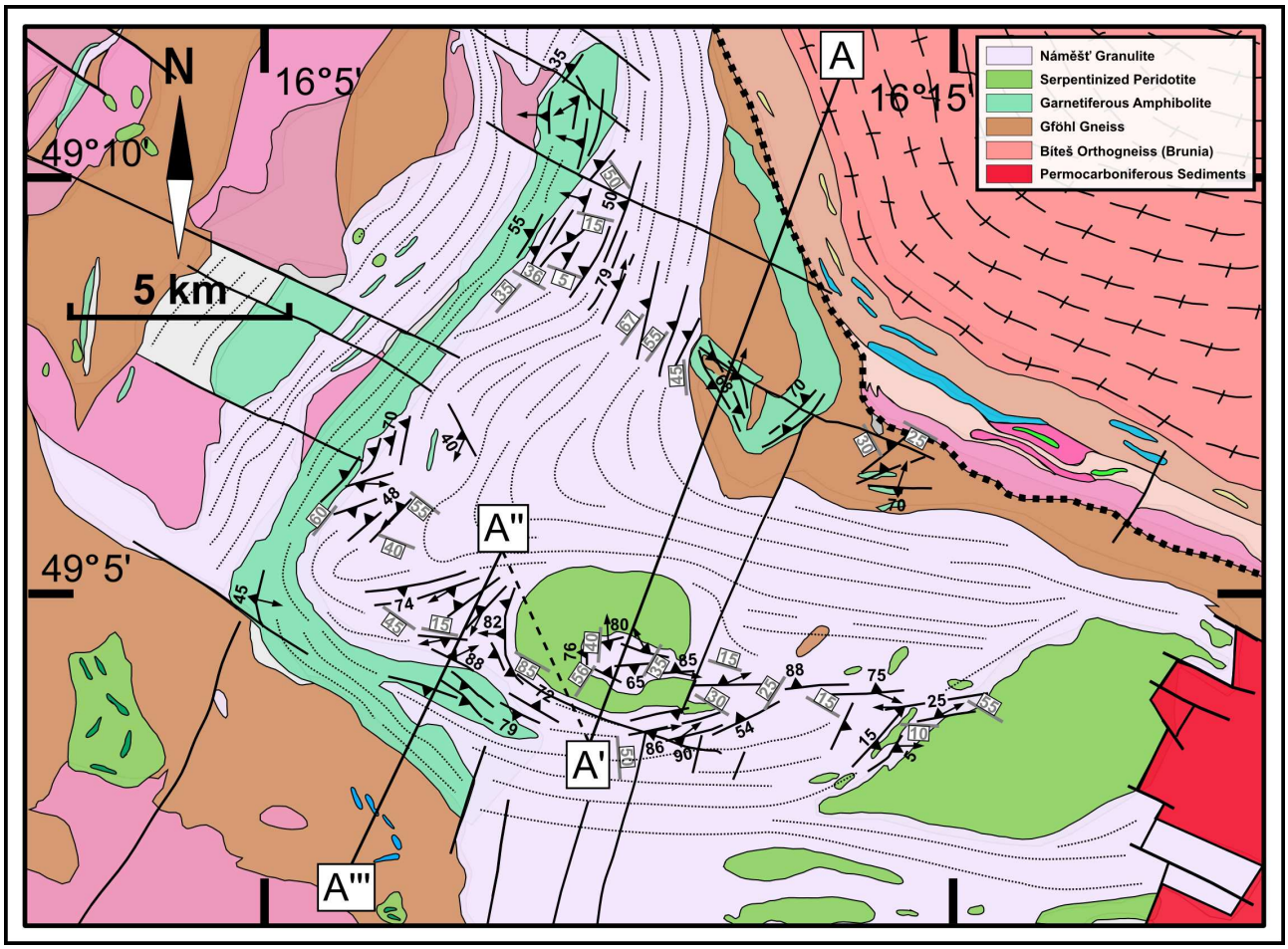

Figure 3. Geological and structural map of Náměšť Granulite Massif, Bohemian Massif, Czech Republic (according to the geological map 1:50000 sheet of the Czech Geological Survey).

with the shape of the peridotite folded sheet, is later affected by small scale folding, shearing and melting during D3 retrogression. The EBSD measurements show presence of two different dry slip patterns. The inner margin of the fold reveals presence of axial [010] LPO pattern, while the linear [100](0kl) LPO olivine pattern is dominant in the rest of the fold. Intersection of the olivine LPO foliation plains from northern limb and axial part of the megafold well defines β-axis of the fold which is in good agreement with cluster maximum of the olivine LPO lineation directions from the same area. In the southern limb of the megafold the olivine LPO foliation plains are subvertical and LPO lineation directions are randomly oriented within the foliation. Both slip systems are concordant with S2 fabric in the surrounding granulites.

Peridotite body evolution starts in the intra-mantle shear zone leading to almost homogenous reduction of the grain size into mylonitic fine-grained matrix. This deformation emplaces mylonitized peridotite into the bottom of the thickened orogenic root and also triggers HT–HP mylonitization

in surrounding granulites as well. Afterwards, the mylonitic fabric both in peridotite and granulite is actively reworked during intensive folding in front of the Brunia indenter at lower crustal conditions. Continuous advance of the indenter leads to extrusion of the granulite-peridotite complex to mid-crustal conditions and subsequent retrogression. Our dataset shows good mechanical coupling between peridotite sheet and host felsic granulite, pointing to relatively low rheological contrast between upper-mantle and lower-crustal rocks in lower crust conditions.

The third chapter deals with the magnetic fabric in a highly serpentinized ultramafic body from orogenic root. An attempt is made to understand magnetic fabric from this highly serpentinized peridotite, its link to the olivine and pyroxene microstructure and tectonic evolution of the whole area. Temperature limit of serpentinization with respect to the development of the mylonitic microstructure in the Mohelno peridotite indicate, that serpentinization occurs as static post-folding process. Serpentinization of the studied peridotite is mostly expressed by presence of the lizardite and iron oxides. Density measurement recalculations projected against bulk magnetic susceptibility reveals that widespread serpentinization alters 50 % to 100 % of the rock volume. Study of low temperature and high temperature variation of susceptibility divides the peridotite samples into three main groups. Group I shows susceptibilities lower than 10^{-3} [SI] that corresponds to paramagnetic minerals only, while Group II and Group III show magnetic susceptibilities 10^{-3}–10^{-2} [SI] and higher than 10^{-2} [SI], which require presence of ferromagnetic minerals. Analysis of thermomagnetic curves revealed that a magnetite in Groups II and III is accompanied with both high and low temperature variety of maghemite and in some specimens also by a mineral from magnetite – chromite or magnetite – spinel series. The AMS patterns from the massif can be divided in three main types according to shape of magnetic ellipsoid, degree of anisotropy and orientation of susceptibility directions. The Type I fabric is characterized by clustered K_1 directions, girdle distribution of K_2 and K_3 directions, prolate shape of AMS ellipsoid and low degree of magnetic anisotropy. The most common Type II fabric pattern is marked by clustered K_1, K_2, K_3 directions, plane strain to oblate fabrics and generally high degree of susceptibility. The Type III of fabric reveals clustered K_3 directions, girdle distribution of K_1 and K_2 directions, mainly oblate shapes of AMS and intermediate to high degree of magnetic anisotropy. The least serpentinized samples corroborates with least magnetic samples of the Group I, which also coincide with rarely preserved coarse-grained or core and mantle microstructure with large orthopyroxene porphyroclasts. This group of samples reveals presence of the Type I AMS pattern. The samples of Groups II and III show generally mylonitic fine-grained microstructure marked by strong

serpentinization. Both groups of samples reveal presence of mainly Type II and the Type III patterns. Spatial distribution of K_m and P parameters implies advancing serpentinization from the margins to the center of the body marked by presence of Group I samples in the core of the body. Orientation of magnetic foliations and lineations changes from the Group I to the Group III. Magnetic foliation follows the fold shape of the peridotite in the Group I and II, while in the Group III there are foliations forming NW-SE trending great girdle, as well as one strong subgroup of foliations dipping to the West at moderate angles. Magnetic lineation is gently plunging in the foliation without preferred orientation in the Group I, while in the Group II and III it is either gently plunging to the South or it concentrates around the peridotite fold axis moderately plunging to the West. The intensity of fabric alignment increases from the Group II towards Group III in conjunction with increasing bulk susceptibility. We suggest that the Group I samples reflect either pre-folding olivine fabric or fabric defined by large orthopyroxene porphyroclasts rotated to the easy-glide orientation within the syn-folding mylonitic matrix. Advanced serpentinization and ferromagnetic fabric measured in the Group II and III can be explained as a result of two competing factors: 1) the penetration of H_2O-rich fluids along the grain boundaries in the fine-grained microstructure and crystallization of magnetite following grain boundary network mimetize the shape of olivine and pyroxene within mylonitic microstructure. 2) the deformation superimposed on almost random serpentine and magnetite matrix,-bearing well oriented olivine and pyroxene. In our model, the weak strain is able to reorient small magnetite crystals, but does not modify strong inherited fabric of olivine and pyroxene. We propose a tectonic scenario coherent with regional structural pattern supporting the latter model.

In general conclusions we correlate so far acquired results from orogenic margin granulite massifs with that of present study, as well as with granulite and peridotite bodies preserved in the interior of the crustal root. This study will be used to integrate petrological evolution of peridotite and surrounding rocks and to develop a new model of crust and mantle interactions in thickened continental crust. We show, that the incorporation of peridotite fragments and their early exhumation together with hot orogenic lower crust occurred during independent tectonic cycle from channel flow deformation controlling the eastern margin of the orogen. We suggest, that the mantle underneath thickened orogenic crust is deformable, probably affected by heterogeneous shear zones and adjust its fabric to deformation of orogenic root systems above. It is very likely that such shear zones are not detectable by geophysical methods.

References

- Ackerman, L., Jelínek, E., Medaris Jr., G., Ježek, J., Siebel, W., Strnad, L., (2009). Geochemistry of Fe-rich peridotites and associated pyroxenites from Horní Bory, Bohemian Massif: Insights into subduction-related melt-rock reactions. Chem. Geol. 259, 152–167.

- Babuška, V., Plomerová, J., (2006). European mantle lithosphere assembled from rigid microplates with inherited seismic anisotropy. Phys. Earth Planet. In. 158, 264–280.

- Babuška, V., Plomerová, J., Fischer, T., (2007). Intraplate seismicity in the western Bohemian Massif (central Europe): A possible correlation with a paleoplate junction. J. Geodyn. 44, 149–159.

- Babuška, V., Plomerová, J., Vecsey, L., (2008). Mantle fabric of western Bohemian Massif (central Europe) constrained by 3D seismic P and S anisotropy. Tectonophysics 462, 149–163.

- Babuška, V., Fiala, J., Plomerová, J., (2010). Bottom to top lithosphere structure and evolution of western Eger Rift (Central Europe). Int. J. Earth Sci. 99, 891–907.

- Becker, H., (1996). Geochemistry of garnet peridotite massifs from lower Austria and the composition of deep lithosphere beneath a Palaeozoic convergent plate margin. Chem. Geol. 134, 49–65.

- Becker, H., (1997). Petrological constraints on the cooling history of high-temperature garnet peridotite massifs in lower Austria. Contrib. Mineral. Petrol. 128, 272–286.

- Behr, H., (1961). Beitrage zur petrographischen und tektonischen Analyse des sachsischen Granulitgebirges. Frebierger Forschungshefte C 119, 5–118.

- Franke, W., (2000). The mid-European segment of the Variscides: tectonostratigraphic units, terrane boundaries and plate tectonic evolution, In: Franke, W., Haak, V., Oncken, O., D., T. (Eds.), Orogenic processes: quantification and modelling in the Variscan Belt. Geol. Soc., Lond., Spec. Publ. 179, 35–61.

- Gayk, T., Kleinschrodt, R., (2000). Hot contacts of garnet peridotites in middle/upper crustal levels: new constraints on the nature of the late Variscan high–T/low–P event in the Moldanubian (Central Vosges/NE France). J. Metamorph. Geol. 18, 293–305.

- Hrouda, F., Faryad, S. W., Jeřábek, P., Chlupáčová, M., Vitouš, P., (2009). Primary magnetic fabric in an ultramafic body (Moldanubian Zone, European Variscides) survives exhumation-related granulite-amphibolite facies metamorphism. Lithos 111, 95.

- Höck, V., Montag, O., Leichmann, J., (1997). Ophiolite remnants at the eastern margin of the Bohemian Massif and their-bearing on the tectonic evolution. Mineral. Petrol. 60, 267–287.

- Janoušek, V., Finger, F., Roberts, M., Frýda, J., Pin, C., Dolejš, D., (2004). Deciphering the petrogenesis of deeply buried granites: whole-rock geochemical constraints on the origin of largely undepleted felsic granulites from the Moldanubian Zone of the Bohemian Massif. Earth Env. Sci. T. R. So. Edinb. 95, 141–159.

- Kamei, A., Obata, M., Michibayashi, K., Hirajima, T., Svojtka, M., (2010). Two contrasting fabric patterns of olivine observed in garnet and spinel peridotite from a mantle-derived ultramafic mass enclosed in felsic granulite, the Moldanubian Zone, Czech Republic. J. Petrol. 51, 101–123.

- Lexa, O., Schulmann, K., Janoušek, V., Štípská, P., Guy, A., Racek, M., (2011). Heat sources and trigger mechanisms of exhumation of HP granulites in Variscan orogenic root. J. Metamorph. Geol. 29, 79–102.

- Machek, M., Ulrich, S., Janoušek, V., (2009). Strain coupling between upper mantle and lower crust: natural example from the Běstvina granulite body, Bohemian Massif. J. Metamorph. Geol. 27, 721–737.

- Medaris, L., Beard, B., Johnson, C., Valley, J., Spicuzza, M., Jelínek, E., Mísař, Z., (1995). Garnet pyroxenite and eclogite in the Bohemian Massif: geochemical evidence for Variscan recycling of subducted lithosphere. Geol. Rundsch. 84, 489–505.

- Medaris, L. G., Ghent, E. D., Wang, H. F., Fournelle, J. H., Jelínek, E., (2006). The Spačice eclogite: constraints on the P–T–t history of the Gföhl granulite terrane, Moldanubian Zone, Bohemian Massif. Mineral. Petrol. 86, 203.

- Nakamura, D., Svojtka, M., Naemura, K., Hirajima, T., (2004). Very high-pressure (>4GPa) eclogite associated with the Moldanubian Zone garnet peridotite (Nové Dvory, Czech Republic). J. Metamorph. Geol. 22, 593–603.

Geochemical and geochronological arguments for heterogeneous structure and complex geodynamic scenarios for origin of Variscan continental crust : Náměšť Granulite Massif (Bohemian Massif, Czech Republic)

Vladimír KUSBACH[*1,2], Vojtěch JANOUŠEK[1,3], Pavlína HASALOVÁ[4], C. Mark FANNING[5], Karel SCHULMANN[2], Stanislav ULRICH[1,6]

Affiliations

[1)] *Institute of* Petrology *and Structural Geology, Charles University, Albertov 6, 128 43 Prague 2, Czech Republic*

[2)] *Institut de Physique du Globe de Strasbourg, IPGS – UMR 7516, CNRS et Universite de Strasbourg (EOST), 1 Rue Blessig, 67084 Strasbourg, France*

[3)] *Czech Geological Survey, Klárov 3, 118 21 Prague 1, Czech Republic*

[4)] *School of Geosciences, Monash University, Clayton, 3800, Victoria, Australia*

[5)] *Research School of Earth Sciences, Australian National University, Jaeger III, Building 61, Mills Road, Canberra, Australia*

[6)] *Institute of Geophysics v.v.i., Academy of Sciences of the Czech Republic, Boční II/1401, 141 31 Prague 4, Czech Republic*

(in preparation for the Contributions to Mineralogy and Petrology)

Abstract

Whole-rock geochemical analyses were obtained for all three main lithologies from the Náměšť Granulite Massif (NGM), namely felsic Ky-Kfs-Grt granulite, spinel- and garnet-bearing peridotite and garnetiferous amphibolite enveloping the NGM. The geochemical signature of the Náměšť granulite displays the same compositional characteristics as other granulite occurrences in the Moldanubian Zone. Protolith composition of E-MORB or Within Plate Tholeiite well explains the geochemical patterns from amphibolite of NGM metabasite envelope and is in accordance with similar occurences of Late Cambrian to Early Ordovician age at the eastern margin of the Bohemian Massif. The spinel and garnet peridotite from the Mohelno peridotite body reveal composition of harzburgite of asthenospheric origin possibly refertilized in slow spreading ridge setting. The precise data from sensitive high-resolution ion-microprobe (SHRIMP) U-Pb zircon *in situ* dating of the granulite and amphibolite yielded Early Devonian protolith ages for the Náměšť granulite and common peak metamorphic age ~353 Ma. Both these ages are different from those common for other granulites from Moldanubian Zone. This work shows that the three lithologies cannot originate in a single geodynamic environment. The granulites represent a Devonian and mid-Ordovician continental crust, while the metabasites reflects Cambro-Ordovician rifting which precludes their common origin. Based on these characteristics and contrasting P–T data we adopt here a model of lower crustal relamination of continental crustal allochthon below autochthonous mafic lower crust of Moldanubian continent. The older metamorphic ages (~353 Ma) of lower crustal allochthon compared to westerly massifs (~340 Ma) are interpreted in terms of diachronous emplacement and different time scale of thermal maturation of western and eastern portions of relaminated crust, respectively.

Keywords

whole-rock geochemistry • U-Pb SHRIMP dating • zircons • granulite • peridotite • amphibolite • Bohemian Massif

Introduction

Felsic, kyanite–K-feldspar–garnet granulites bearing volumetrically minor, but petrogenetically important, peridotite fragments called "orogenic peridotites" (garnet or spinel peridotite, pyroxenite and associated eclogite), represent a typical rock assemblage for the high grade core of the European Variscan Belt (Pin and Vielzeuf, 1983; Carswell and O'Brien, 1993; Franke, 1993; Medaris et al., 1995;

Gayk and Kleinschrodt, 2000; Cooke and O'Brien, 2001; O'Brien and Rötzler, 2003). These granulite–peridotite complexes occur at many places of the Variscan Bohemian Massif, especially in the Moldanubian and Saxothuringian zones (O'Brien and Rötzler, 2003). In the Moldanubian Zone, the granulite massifs are concentrated in the high-grade Gföhl Unit, which represents the most intensely metamorphosed part of this internal orogenic zone (Franke, 2000). The granulite massifs are commonly accompanied by a belt of garnetiferous amphibolites-bearing relics of retrogressed eclogites and banded amphibolites called collectively the "Begleit Serie – accompanying series" (Šichtařová, 1981; Finger and Steyrer, 1995; Fritz, 1995).

Recently, a new interpretation of this rock sequence was proposed based on lithological structure, geochemistry and geochronology of these rocks (Lexa et al., 2011). The common structure of this rock sequence is based on structurally highest felsic granulites and peridotites separated from middle crustal units represented by MP–MT rocks of the Varied and Monotonous formations by the "Begleit Serie" (Racek et al., 2006; 2008). This structure was classicaly interpreted as a result of large scale nappe tectonics affecting the core of the Bohemian Massif (Matte et al., 1990; Franke, 2000). However, the modern petrological, geochemical and structural studies have shown that the granulites represent originally deepest part of the double thickened crust, while the metabasic layer represents original lower crust of the Moldanubian continent located bellow middle crustal mostly metasedimentary units of late Proterozoic to Lower Paleozoic age (Schulmann et al., 2005). According to this model the granulite–peridotite complexes represent a lower crustal allochthon emplaced underneath autochthonous Moldanubian crust by mechanism called tectonic relamination (Lexa et al., 2011). The expression relamination (Hacker et al., 2007) is usually used for process of the addition of low density crust underneath the dense root. These authors also proposed, that the recent structure of the internal part of orogen is a result of Carboniferous laterally forced gravity overturns responsible for tectonic inversion of lithologies.

Understanding of the tectonic and metamorphic history of these lower crustal complexes is crucial for correct interpretation of the Variscan collisional history. During the last two decades a large effort was carried out to determine the prograde and retrograde metamorphic paths (P–T–t) of granulites in order to understand burial and exhumation processes within deep crustal root (see O'Brien and Rötzler, 2003; Kotková, 2007 for reviews). In addition, several petrological studies focussed on metamorphic evolution of garnet and spinel peridotites (Medaris, 1990; 2005) were performed attempting to understand relation between lithospheric mantle and orogenic lower crust. The petrology of amphibolites

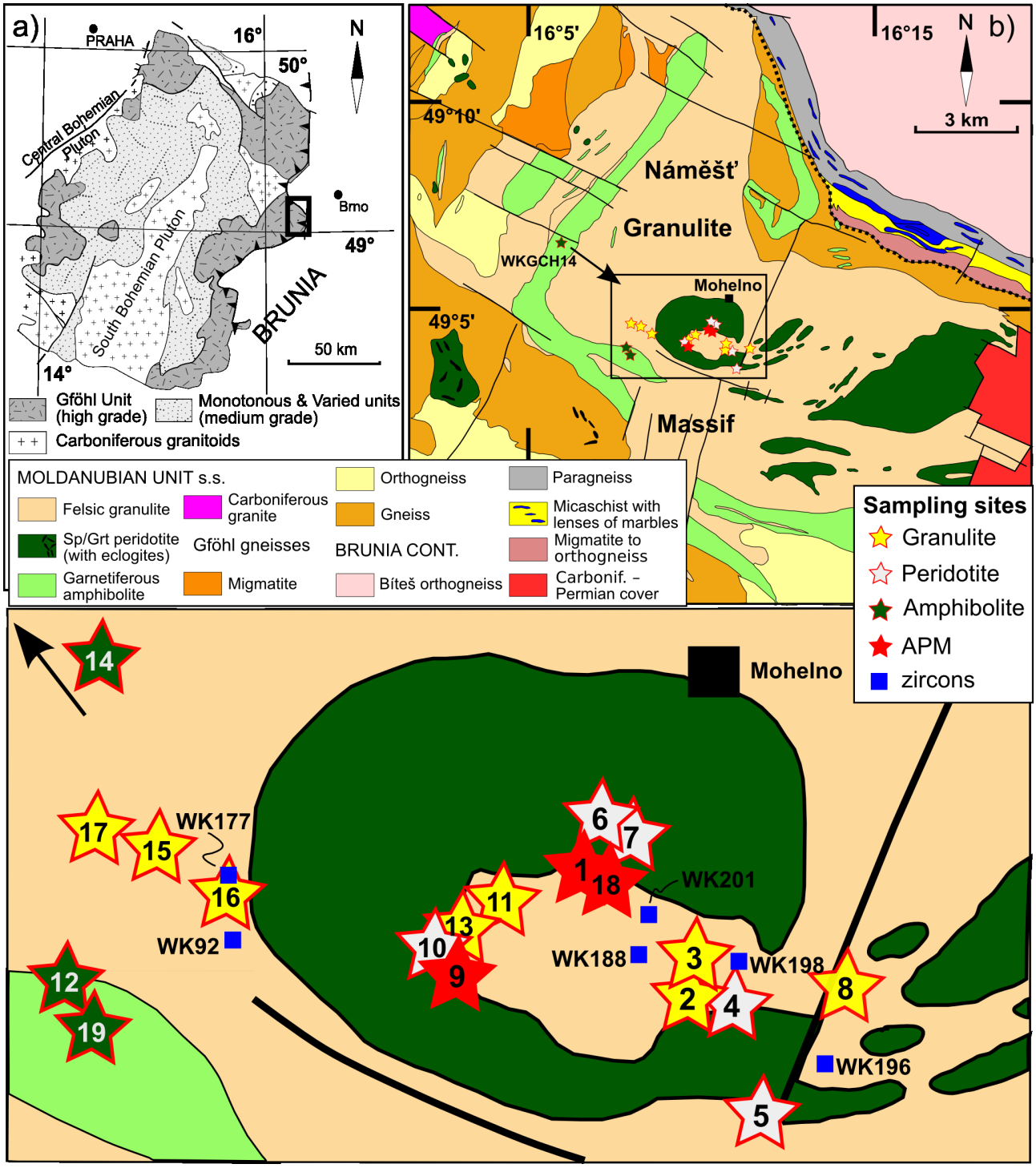

Figure 1. (a) Simplified map of the eastern margin of the Bohemian Massif with high-grade Gföhl and medium-grade Monotonous and Varied units (after European Transeuropean Suture Zone project, *http://www.geofys.uu.se/eprobe/Projects/tesz/TESZ.htm*). (b) Geological map of the Náměšť Granulite Massif with embedded Mohelno peridotite (according 1:50000 map sheet, Czech Geological Survey). (c) localization of the geochemical and zircon SHRIMP dating samples in close vicinity of the Mohelno peridotite.

was rather undervalued appart of few studies of retrogressed eclogites and mafic granulites (Štípská and Powell, 2005a; Racek et al., 2008). Lexa et al. (2011) proposed that the geochemical nature and pre-metamorphic history of the protoliths of the three key lithologies is equally important for understanding of significance of lithotectonic stratification of Variscan orogen. It was shown that whole-rock geochemical composition provides a useful information regarding protoliths of felsic and intermediate granulites from a range of granulite massifs (Janoušek et al., 2004); peridotites (Medaris et al., 2005, 2009; Ackerman et al., 2009) and more rarely from accompanying metabasite layer and other amphibolite bodies (Janoušek et al. 2008; Soejono et al. 2010). Unfortunately original field relations, primary mineral assemblages and fabrics are modified or completely erased by intense tectonometamorphic reworking.

The aim of this work is to characterize the geochemistry of protoliths of various rocks forming the Náměšť Granulite Massif including felsic Ky–Kfs–Grt granulite, embedded spinel/garnet peridotite bodies and surrounding garnet-bearing amphibolite envelope. Results of precise SHRIMP U-Pb zircon dating of both granulite and amphibolite are combined with the whole-rock geochemical data to constrain the absolute and relative timing of rock origin and their metamorphic history. Finally, an attempt is made to propose a geodynamic model of original (pre-exhumation) lithotectonic structure of the lower crust in the studied area and correlate it with other areas of the Bohemian Massif and Variscan Europe. It will be shown that the protolith and metamorphic history of peridotite, granulite and amphibolite confirms the recently proposed model of tectonic relamination based on geochemisty and geochronology data coming from the western part of the orogen. The extension of lower crustal allochthon to the East and geochronological particularities modify existing hypotheses for the geotectonic model of eastern margin of the Variscan front.

Geological setting and studied lithologies

The studied Náměšť Granulite Massif (NGM) is one of the most important lower crustal complexes of the Bohemian Massif. The study area is situated in the Moldanubian Zone forming the core of Variscan orogen at the eastern margin of the Bohemian Massif (Fig. 1a). Here, the easternmost part of the Moldanubian Zone was thrust over nappes of the Moravian Zone derived from the Brunia microcontinent in the North and East (Schulmann et al., 1991; Urban, 1992; Dallmeyer et al., 1995;

Franke, 2000). The Moldanubian Zone is interpreted as an orogenic root of the Bohemian Massif developed during the Variscan collision in the Devonian to Carboniferous times (Schulmann et al., 2005). This zone is subdivided into three main units (Fig. 1a): the medium-grade Varied and Monotonous units and the high-grade Gföhl Unit (Tollman, 1982). Both the amphibolite–facies Monotonous and Varied units are dominatly formed by sillimanite- and garnet-bearing paragneisses, orthogneisses and amphibolites accompanied in Varied Unit by marbles, quartzites and metavolcanic sequences. Both metasedimentary series show Lower Paleozoic age of sedimentation (Košler et al., 2011), while interbedded orthogneisses provide generally Late Proterozoic ages (Kröner et al., 1988; Friedel et al., 2004; Schulmann et al., 2005). In contrast, the high-grade Gföhl Unit consists of anatectic orthogneiss, amphibolite of the accompanying series, migmatite, granulite, eclogite and peridotite.

The Gföhl Unit granulite protolith is assumed to be rhyolitic or granitic (Matějovská, 1975; Fiala et al., 1987), having experienced a different degree of Carboniferous partial melting and melt loss according to different authors. The origin of felsic granulites is interpreted as result from either almost isochemical metamorphism of high-level granites subducted to large depthts of 70–100 km (Janoušek et al., 2004; Lexa et al., 2011) or by crystallization of ultra-high pressure granitic magmas at the base of thickend crust (Jakeš, 1997; Kotková and Harley, 1999). The age of the granulite protolith has been constrained by SHRIMP dating to Early Palaeozoic (488 ± 6 Ma: Friedl et al., 2003; 469.3 ± 3.8 Ma: Kröner et al., 2000a) or ~400 Ma (Schulmann et al., 2005), whereas the age of the Variscan metamorphism was estimated to ~340 Ma (conventional U-Pb ages for zircon and monazite, SHRIMP ages on zircon rims, U-Pb on monazite: van Breemen et al., 1982; Aftalion, 1989; Kröner et al., 2000a; Friedl et al., 2003 and references therein). Some peridotite bodies are interpreted either as a lithospheric mantle (garnet peridotites with eclogites) due to their geochemistry and very high pressure conditions (Nakamura et al., 2004; Medaris et al., 2005) while others reflect asthenospheric origin (spinel- to garnet-bearing harzburgites) based on different geochemical signatures and lower P–T conditions (Medaris et al., 1990). Existing, Nd-Sm ages show variations between Devonian to Carboniferous cooling ages (Beard et al., 1992; Medaris et al., 1995; Becker, 1997). The "accompanying series" amphibolites show generally MORB type geochemistry (Šichtařová, 1987; Finger and Steyrer, 1995) and are sometimes interpreted as a relic of a Silurian ocean separating Moldanubian continental domain from the Brunia continent (Finger and Steyrer, 1995; Finger and Von Quadt., 1995; Höck et al., 1997).

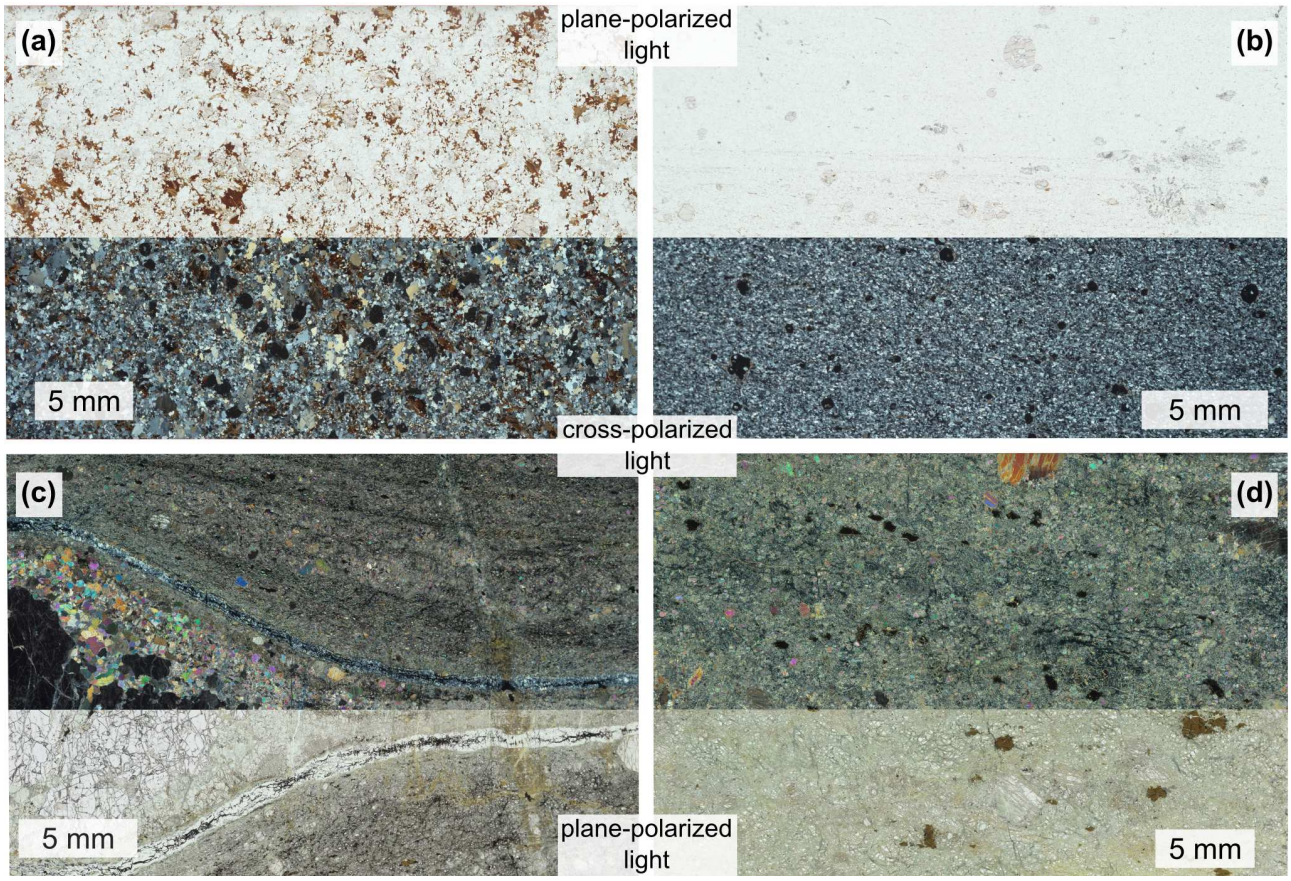

Figure 2. Textures of granulites and peridotites from the Náměšť Granulite Massif hosting the Mohelno peridotite body. (a) biotite–sillimanite granulite, sample WKGCH3, (b) Ky–ternary Fsp granulite, sample WKGCH16, (c) garnet peridotite, sample WKGCH5, (d) spinel peridotite, sample WKGCH6. Images are scans of thin sections in plane- and cross-polarized light.

Náměšť granulites and nearby granulite bodies

The Náměšť granulites are felsic garnet-kyanite-alkali feldspar rocks with dominant mylonitic fine-grained microstructure (T = 700 °C and P = 0.9–0.6 GPa at 350–330 Ma), surrounding relics of coarse-grained microstructure (T = 750 °C and P = 1.1–1.4 GPa at 370–350 Ma) of early granulite-facies stage (Urban, 1992). Nearby granulite massifs provided peak P–T conditions of 800 °C at pressure of 1.8 GPa (Štípská and Powell, 2005b; Štípská et al., 2008). Detailed petrological work has been carried out on the Lower Austrian granulites south of the NGM and showed peak P–T conditions estimated at $\geq$ 1.5 GPa and ~850 ^{o}C, while fine-grained microstructure revealed T = 760 °C and P = 1.1 GPa along the retrograde P–T path (Racek et al., 2006). North of the NGM, Strážek granulites yielded peak P–T conditions at ~1.8 GPa and ~850 °C, while decompression associated with mylonitization occurred at ~1.3 GPa and ~790 °C (Tajčmanová et al., 2006). On the other hand, Carswell and O'Brien (1993) and Cooke and O'Brien (2001) calculated peak P–T conditions to ~1000 °C at 1.6–1.8 GPa for

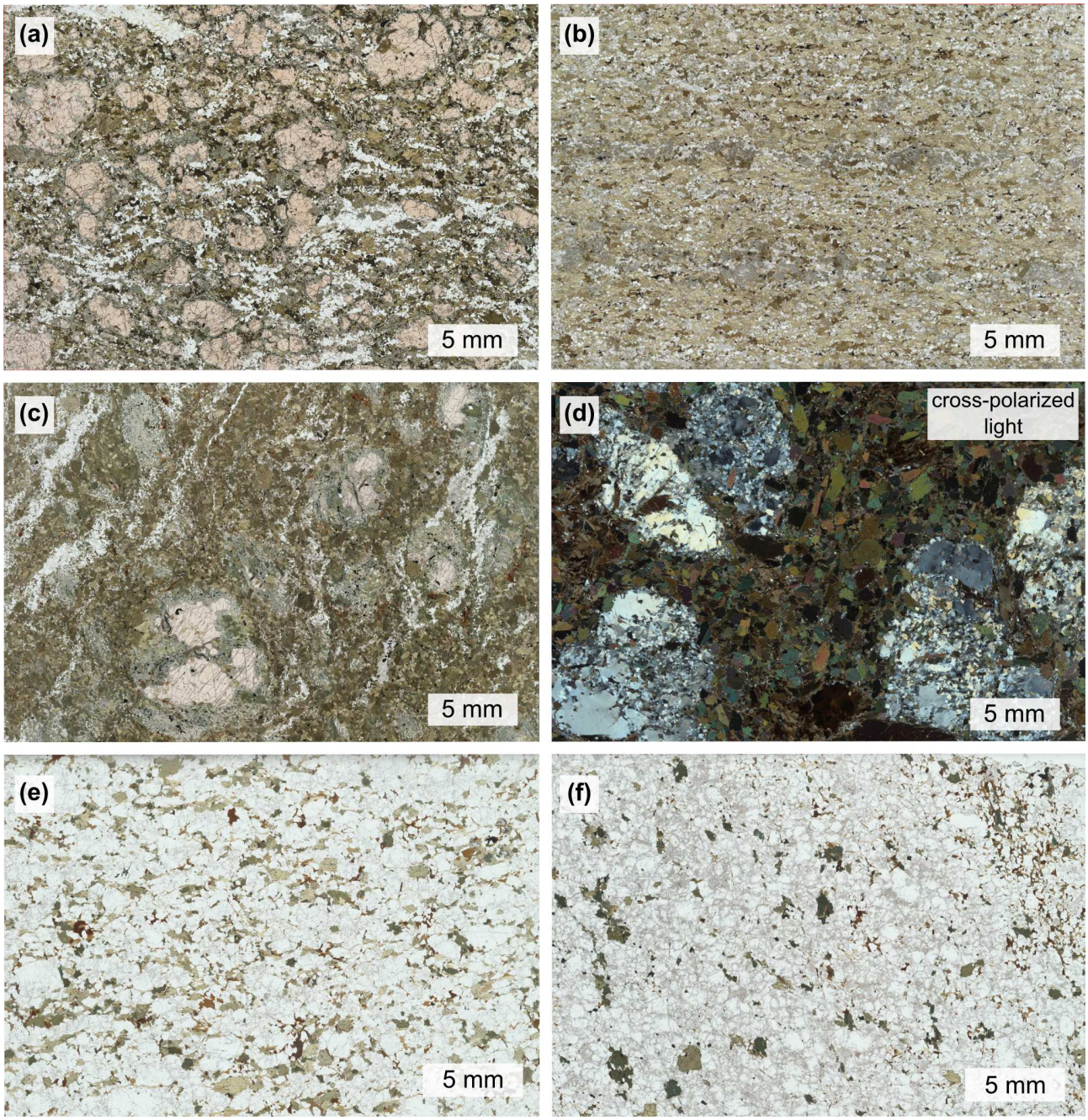

Figure 3 Textures of amphibolites and suspect igneous rocks from the Náměšť Granulite Massif (a,b,c – amphibolite, d,e,f – suspect igneous rock). (a) garnetiferous amphibolite, sample WKGCH19, (b) mylonitized garnet–bearing amphibolite, sample WKGCH14, (c) garnetiferous amphibolite, sample WKGCH12, (d) amphibole–biotite igneous rock, sample WKGCH1, (e) light amphibole–bearing igneous rock, sample WKGCH18, (f) light igneous rock with amphibole, sample WKGCH9. Images are scans of thin sections in plane- or cross-polarized light.

felsic–intermediate granulites in Lower Austria.

Recent petro-structural study (Chapter 2) reveals that the tectonic history of granulites can be described by a succession of three main metamorphic fabrics: granulitic coarse-grained S1 fabric is

characterized by a granulite–facies mineral assemblage such as garnet, kyanite, ternary feldspar and rutile and is preserved only in low-strain domain within the internal part of the Mohelno peridote fold. Ultramylonitic granulite S2 fabric shows also granulite–facies mineral assemblage with ternary feldspar preserved only as garnet inclusions. The S2 fabric was associated with emplacement of the peridotite sheet into the orogenic root and initiation of the granulite complex exhumation (Chapter 2). The S3 fabric is described as amphibolite–facies retrogressive fabric associated with partial melting forming foliation–parallel leucosomes. Granulites with S3 fabric are strongly retrogressed as shown by a syn-D3 growth of sillimanite and biotite and accumulation of elongated lenses of granitic melt.

Mohelno peridotite

The Mohelno serpentinized peridotite belongs to numerous bodies of spinel to garnet peridotite enclosed within retrogressed granulites of the NGM. Their size range up to several kilometres (Urban, 1992) and most of them have the shape of lenses, while the Mohelno serpentinized peridotite reveals a shape of isoclinal fold (Fig. 1b). There are several studies dealing with peridotite deformational history, microstructures and serpentinization related processes (Medaris et al., 2005; Kamei et al., 2010; Chapter 2; Chapter 3). Peridotites provide a geochemical signature characteristic of an asthenospheric origin (Medaris et al., 1990). Spinel peridotites from Mohelno can be stable up to pressures of 2.1–2.2 GPa within the low P–T field (based on their spinel compositions; O'Neill, 1981), but their equilibration temperature at ~1100 °C (derived from two–pyroxene geothermometry; Taylor, 1998) is significantly less compared to garnet peridotite (~1300 °C, ~2.7 GPa; Medaris et al., 2005).

Amphibolite from the Náměšť Granulite Massif

The NGM is surrounded by broad envelope of garnetiferous, migmatitic amphibolite (Fig. 1b). These rocks experienced high-grade metamorphism at granulite–facies conditions with primary mineral assemblage clinopyroxene, plagioclase and garnet ± orthopyroxene and rutile (Šichtařová, 1981; Němec, 1996). During retrogression under amphibolite–facies conditions, granulite–facies mineral assemblage was replaced by an association of amphibole, plagioclase, biotite ± garnet, ilmenite, quartz. The geochemistry of these rocks correspond to that of tholeiitic basalts (Šichtařová, 1981), or more precisely MORB basalts according to the REE-distribution (Matějovská, 1987; René, 2008, 2009)

Whole-rock geochemistry

Analytical techniques

The presented dataset consists of 19 new whole-rock analyses of the main lithologies of the Náměšť Granulite Massif (with minimal weight of source material > 15kg). Five peridotite samples as fresh as possible were collected within the Mohelno peridotite body (garnetiferous – WKGCH4, WKGCH5; spinel-bearing – WKGCH6, WKGCH7 and WKGCH10), eight samples of fresh granulites (WKGCH2, WKGCH3, WKGCH8, WKGCH11, WKGCH13, WKGCH15, WKGCH16 and WKGCH17) in surrounding Náměšť granulite (Fig. 1b, 1c and 2). Three samples of garnetiferous amphibolite (WKGCH12, WKGCH14 and WKGCH19) were obtained from the amphibolitic belt enveloping whole granulite–peridotite complex and three other samples of amphibole–plagioclase biotitic rock from the vicinity of granulite–peridotite contact (WKGCH1, WKGCH9 and WKGCH18) (Fig. 1b, 1c and 3).

After the conventional crushing and homogenization, the powders produced under aceton in agate mill have been analyzed in Acme Analytical Laboratories Ltd., Vancouver. The major and minor elements were determined by ICP-OES and most trace elements (Ba, Cs, Ga, Hf, Nb, Rb, Sr, Ta, Th, U, V, Zr, Y, and REE) by ICP-MS. The dissolution of the rock powders in both cases followed fusion with a $LiBO_2/Li_2B_4O_7$ flux. The analyses of remaining trace elements, and transition metals in particular (Cu, Pb, Zn, Cr and Ni), were carried out by ICP-MS following leaching with a $HCl–HNO_3–H_2O$ mixture at 95 ^{o}C for 1 hour.

Recalculation and visualisation of geochemical data were facilitated using the R software package *GCDkit* (Janoušek et al., 2006). The newly obtained geochemical data from all lithologies are summarized in Tab. 1 – major-elements, Tab. 2 – trace-elements and Tab. 3 – REE + Y analyses.

Granulite

The newly obtained granulite data were compared with large Moldanubian granulite geochemical database from Janoušek et al. (2004).

Major elements

All eight newly analysed granulite samples show K/Rb ratios 200–500, which fall into interval of typical continental crust (Rudnick et al., 1985), therefore they are not markedly depleted in Rb (Fig. 4). Near–linear trend for Rb vs. K/10000 implies no significant depletion in alkalis, which can be thus used for classification and petrogenetic considerations. In the diagram two groups of samples can be

Tab. 1 Major-element analyses from the Náměšť Granulite Massif (wt. %)

	WKGCH12	WKGCH19	WKGCH14	WKGCH6	WKGCH4	WKGCH7	WKGCH5	WKGCH10	WKGCH1	WKGCH9
Rock	amphibolite	amphibolite	amphibolite	peridotite	peridotite	peridotite	peridotite	peridotite	APM	APM
SiO_2	41.60	43.20	46.13	39.73	40.21	40.70	40.89	41.35	45.05	58.15
TiO_2	1.62	1.56	1.74	0.06	0.12	0.07	0.08	0.12	1.96	0.32
Al_2O_3	18.53	19.01	15.66	2.32	3.20	2.71	2.70	3.36	14.03	22.54
$Fe_2O_3{}^T$	12.66	15.17	11.29	8.01	8.15	8.05	8.08	8.26	11.02	2.44
MnO	0.17	0.24	0.18	0.11	0.11	0.11	0.11	0.12	0.11	0.02
MgO	8.92	6.16	7.87	35.86	34.16	35.14	36.06	34.61	11.89	1.58
CaO	10.85	11.14	11.14	2.05	2.36	2.33	2.09	2.64	9.55	4.99
Na_2O	1.77	2.30	3.04	0.12	0.20	0.15	0.18	0.23	2.70	6.64
K_2O	1.20	0.16	0.52	b.d.l. <0.01	b.d.l. <0.01	b.d.l. <0.01	b.d.l. <0.01	b.d.l. <0.01	2.01	1.59
P_2O_5	0.39	0.12	0.22	b.d.l. <0.01	b.d.l. <0.01	b.d.l. <0.01	0.01	b.d.l. <0.01	0.29	0.17
LOI	1.8	0.6	1.9	10.5	10.3	9.5	8.5	8.1	0.9	1.3
Σ	99.51	99.66	99.69	98.76	98.81	98.76	98.70	98.79	99.51	99.74
K_2O/Na_2O	0.68	0.07	0.17						0.74	0.24
A/CNK	0.77	0.79	0.61						0.59	1.04
$mg\#$	58.3	44.6	58.0	89.9	89.3	89.6	89.8	89.3	68.1	56.2

	WKGCH18	WKGCH17	WKGCH3	WKGCH13	WKGCH15	WKGCH2	WKGCH8	WKGCH16	WKGCH11
Rock	APM	granulite	granulite	granulite	granulite	granulite	granulite	granulite	granulite
SiO_2	59.46	65.24	67.06	73.42	74.12	74.38	74.69	75.02	77.41
TiO_2	0.49	0.58	0.74	0.20	0.26	0.13	0.25	0.14	0.04
Al_2O_3	18.74	17.09	15.27	14.00	13.82	13.82	13.72	13.11	12.73
$Fe_2O_3{}^T$	4.61	4.93	5.06	1.89	2.09	1.82	2.64	1.88	1.00
MnO	0.05	0.05	0.07	0.03	0.03	0.03	0.03	0.03	0.02
MgO	3.02	1.34	1.80	0.38	0.46	0.23	0.75	0.33	0.08
CaO	5.79	4.27	2.73	1.03	1.06	1.44	1.02	0.88	0.58
Na_2O	5.18	3.47	3.33	3.04	2.67	3.92	4.56	2.99	4.57
K_2O	1.36	2.34	2.86	4.98	5.02	3.22	1.93	4.77	2.95
P_2O_5	0.24	0.12	0.19	0.12	0.13	0.03	0.05	0.06	0.02
LOI	0.70	0.30	0.60	0.80	0.20	0.80	0.20	0.70	0.50
Σ	99.64	99.73	99.71	99.89	99.86	99.82	99.84	99.91	99.90
K_2O/Na_2O	0.26	0.67	0.86	1.64	1.88	0.82	0.42	1.60	0.65
A/CNK	0.91	1.07	1.13	1.14	1.18	1.1	1.2	1.12	1.08
$mg\#$	56.5	35.0	41.3	28.5	30.4	20.0	36.0	25.8	13.7

Tab. 2 Trace-element analyses from the Náměšť Granulite Massif (ppm)

	12	**19**	**14**	**6**	**4**	**7**	**5**	**10**	**1**	**9**
Rock	amphibolite	amphibolite	amphibolite	peridotite	peridotite	peridotite	peridotite	peridotite	APM	APM
Rb	34.7	1.2	9.7	0.2	0.2	0.2	0.3	<0.1	46.2	54.3
Cs	4.0	0.2	0.9	<0.1	<0.1	<0.1	<0.1	<0.1	0.8	1.1
Ba	735	62	48	2	2	<1	2	2	850	520
Sr	708.5	399.0	346.6	3.7	9.5	5.9	8.2	9.1	539.8	1087.0
Th	0.2	<0.2	0.7	<0.2	<0.2	<0.2	<0.2	<0.2	<0.2	<0.2
U	0.5	<0.1	0.3	<0.1	<0.1	<0.1	<0.1	<0.1	0.4	0.4
Zr	60.2	29.2	124.1	1.1	6.6	1.4	3.5	8.1	149.7	64.3
Hf	2.3	1.0	3.1	0.2	0.3	<0.1	<0.1	0.2	4.6	2.3
Nb	6.6	2.1	8.6	<0.1	<0.1	<0.1	<0.1	<0.1	9.5	2.3
Ta	0.4	0.1	0.5	<0.1	<0.1	<0.1	<0.1	<0.1	0.6	0.2
Pb	3.8	0.5	0.3	<0.1	0.1	0.1	0.1	<0.1	1.5	1.9
Ga	19.9	20.2	18.3	2.5	4.1	2.8	3.1	3.1	21.6	27.2
Sn	2	<1	1	<1	<1	<1	<1	<1	10	4
Cr*	212.1	<13.7	123.2	2415.4	2340.1	2278.6	2449.6	2388.0	95.8	<13.7
Ni	74	<20	59	2016	1866	1994	1997	1886	86	<20
Co	46.6	37.5	44.9	99.7	100.6	97.1	99.0	94.7	46.8	8.1
V	367	386	279	58	74	64	61	69	361	47
Sc	44	48	39	11	13	13	12	13	42	7
Cu	71.2	25.5	59.4	16.1	17.5	19.0	17.6	22.4	31.9	14.5
Zn	26	20	15	14	16	13	11	15	44	30
K/Rb	287.1	1106.8	445.0	–	–	–	–	–	361.2	243.1

	18	**17**	**3**	**13**	**15**	**2**	**8**	**16**	**11**
Rock	APM	granulite	granulite	granulite	granulite	granulite	granulite	granulite	granulite
Rb	37.9	57.2	81.3	170.3	175.4	77.3	32.7	174.9	89.4
Cs	0.5	0.4	0.9	0.4	0.4	0.2	<0.1	0.2	<0.1
Ba	432	895	894	460	501	1090	459	266	192
Sr	921.7	212.7	261.5	64.9	84.3	101.8	93.1	35.4	19.0
Th	0.8	7.6	1.5	13.7	4.2	<0.2	12.5	5.6	3.8
U	0.3	1.2	0.6	0.9	0.8	0.3	1.5	0.5	0.4
Zr	58.9	239.7	269.6	117	114.7	104.9	142.3	90.3	57
Hf	2.1	7.0	7.6	4.3	3.5	3.7	5.0	3.4	2.9
Nb	3.2	13.6	11.7	6.4	9.5	2.3	7.2	6.1	2.2
Ta	0.2	0.7	0.8	0.2	0.7	0.1	0.5	0.4	<0.1
Pb	0.9	0.5	0.8	1.1	1.5	0.4	0.6	0.5	0.4
Ga	24.4	20.1	17.9	16.7	15.6	18.3	18.2	16.3	19
Sn	5	<1	2	2	5	2	2	2	1
Cr*	47.9	34.2	41.1	<13.7	<13.7	<13.7	27.4	<13.7	<13.7
Ni	<20	<20	23	<20	<20	<20	<20	<20	<20
Co	12.8	6.8	10.7	2.3	3.7	1.5	3.1	1.7	0.4
V	121	56	77	14	15	15	22	10	<8
Sc	20	16	13	5	5	8	8	5	6
Cu	26.2	8.1	9.3	2.2	1.9	1.3	4.4	1.1	0.2
Zn	35	40	54	22	17	19	17	10	9
K/Rb	297.9	339.6	292.0	242.8	237.6	345.8	490.0	226.4	273.9

* Names of samples are shortened. (e.g. 5 stands for sample WKGCH5).

* Chromium calculated from Cr_2O_3.

Tab. 3 REE + Y analyses from the Náměšť Granulite Massif (ppm)

	12	**19**	**14**	**6**	**4**	**7**	**5**	**10**	**1**	**9**
Rock	amphibolite	amphibolite	amphibolite	peridotite	peridotite	peridotite	peridotite	peridotite	APM	APM
La	15.9	3.8	8.6	b.d.l. <0.1	b.d.l. <0.1	b.d.l. <0.1	b.d.l. <0.1	b.d.l. <0.1	18.8	7.4
Ce	45.3	14.0	22.0	0.3	0.5	0.4	0.5	0.5	55.6	16.8
Pr	6.96	2.59	3.33	0.04	0.12	0.06	0.08	0.09	9.66	2.29
Nd	33.6	15.0	14.3	b.d.l. <0.3	0.7	0.4	0.4	0.5	45.7	10.4
Sm	7.84	4.32	4.02	0.09	0.24	0.14	0.17	0.22	11.29	2.86
Eu	2.02	1.39	1.39	0.04	0.08	0.06	0.06	0.08	2.17	0.73
Gd	6.97	4.75	4.39	0.18	0.39	0.22	0.23	0.34	9.24	3.05
Tb	1.05	0.87	0.80	0.04	0.08	0.05	0.05	0.07	1.42	0.59
Dy	5.73	5.20	4.65	0.26	0.56	0.38	0.35	0.50	7.09	3.43
Ho	1.05	1.09	0.91	0.06	0.11	0.09	0.09	0.11	1.25	0.65
Er	2.94	3.12	2.82	0.20	0.28	0.24	0.25	0.38	3.57	1.86
Tm	0.34	0.38	0.33	0.03	0.05	0.03	0.04	0.05	0.49	0.23
Yb	2.48	2.92	2.39	0.18	0.27	0.27	0.28	0.36	2.79	1.63
Lu	0.35	0.41	0.35	0.03	0.06	0.04	0.05	0.06	0.40	0.23
Eu/Eu*	0.84	0.94	1.01	0.96	0.80	1.05	0.93	0.89	0.65	0.76
La_N/Yb_N	4.3	0.9	2.4	–	–	–	–	–	4.5	3.1
La_N/Sm_N	1.3	0.6	1.3	–	–	–	–	–	1.0	1.6
ΣREE	132.5	59.8	70.3	1.5	3.4	2.4	2.6	3.3	169.5	52.2

	18	**17**	**3**	**13**	**15**	**2**	**8**	**16**	**11**
Rock	APM	granulite	granulite	granulite	granulite	granulite	granulite	granulite	granulite
La	13.1	33.5	25.9	23.0	20.5	17.2	28.0	19.2	13.2
Ce	33.9	66.7	52.5	50.6	43.3	31.0	60.2	40.2	28.1
Pr	5.08	8.70	6.83	6.02	5.31	3.59	7.37	4.79	3.46
Nd	23.8	32.2	25.4	22.4	18.9	13.4	26.6	16.9	13.4
Sm	6.21	5.76	5.96	5.13	4.66	3.45	5.32	4.40	3.39
Eu	0.92	1.33	1.13	0.51	0.56	0.52	0.51	0.29	0.09
Gd	6.38	4.95	6.18	5.51	5.30	4.22	4.37	5.22	3.81
Tb	1.13	0.71	1.14	1.15	1.20	0.87	0.74	1.19	0.74
Dy	6.64	3.72	6.74	7.23	7.44	5.77	4.16	7.92	4.89
Ho	1.23	0.70	1.28	1.50	1.62	1.24	0.79	1.69	0.99
Er	3.73	1.70	4.05	4.63	4.80	3.70	2.45	5.54	3.24
Tm	0.46	0.23	0.48	0.61	0.63	0.53	0.34	0.72	0.45
Yb	3.17	1.90	3.61	4.29	4.69	4.09	2.49	4.92	3.52
Lu	0.45	0.31	0.54	0.59	0.63	0.63	0.39	0.71	0.53
Eu/Eu*	0.45	0.76	0.57	0.29	0.35	0.42	0.32	0.19	0.08
La_N/Yb_N	2.8	11.9	4.8	3.6	2.9	2.8	7.6	2.6	2.5
La_N/Sm_N	1.3	3.7	2.7	2.8	2.8	3.1	3.3	2.7	2.4
ΣREE	106.2	162.4	141.7	133.2	119.5	90.2	143.7	113.7	79.8

* Names of samples are shortened. (e.g. 5 stands for sample WKGCH5).

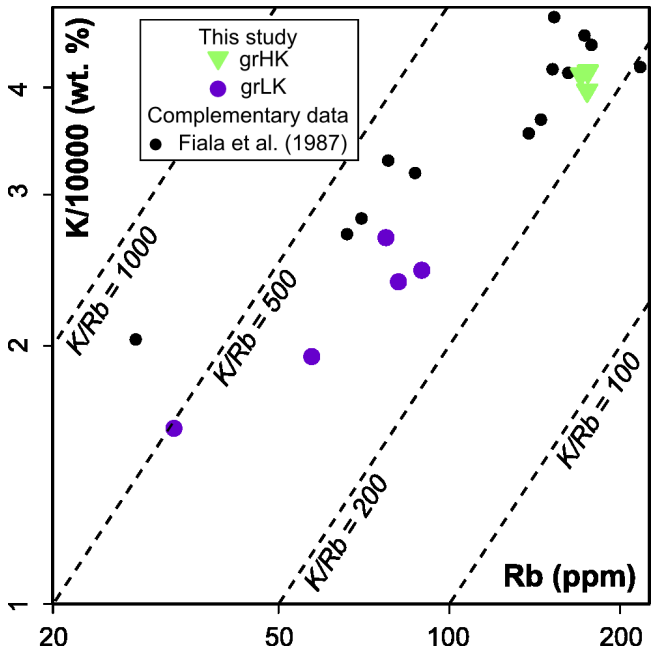

Figure 4. Rb vs. K/10000 (ppm) diagram for granulite samples from the Náměšť Granulite Massif. Based on potassium volume, samples are divided into two groups: grLK – samples with low potassium values and grHK – samples with high potassium content. *Black circles* – additional analyses of the Náměšť granulites (Fiala et al., 1987).

distinguished: (1) granulites with higher contents of both K and Rb (grHK) and (2) those with lower, but still proportional contents of K and Rb (grLK). In multicationic diagram P–Q (Debon and Le Fort, 1983) is apparent felsic (granitic) composition of previously described grHK and granodioritic composition of samples from grLK group (Fig. 5a). All the samples are slightly peraluminous in the B–A diagram of Debon and Le Fort (1983) modified by (Villaseca et al., 1998) (Fig. 5b). For classification of metamorphosed igneous rocks the immobile elements (e.g. high field strength elements – HFSE) should be preferentially used. In such classification diagram with Nb/Y vs. Zr/Ti incompatible element ratios (proposed by Winchester and Floyd, 1977, modified by Pearce, 1996), new granulite samples fall in the rhyolite/dacite field (Fig. 5c) with two crossing the boundary of the andesite field. The light peraluminosity of granulite samples is also illustrated in the ternary plot Na_2O–Al_2O_3–K_2O (mol. %) (Fig. 5d).

The major-elements composition of the felsic granulite is very silicic (SiO_2 > 73 wt. % for 6 of 8 samples, last two have SiO_2 >65 wt. %) and slightly peraluminous (A/CNK = 1.06–1.19). Three samples are K-rich (K_2O/Na_2O > 1.59), other samples have K_2O/Na_2O of 0.42–0.85 and rather variable mg# values (14–41). The Harker variation diagrams (Fig. 6) show distinctive negative correlation of SiO_2 with TiO_2, Al_2O_3, FeOt, MgO, CaO and mg# (not plotted).

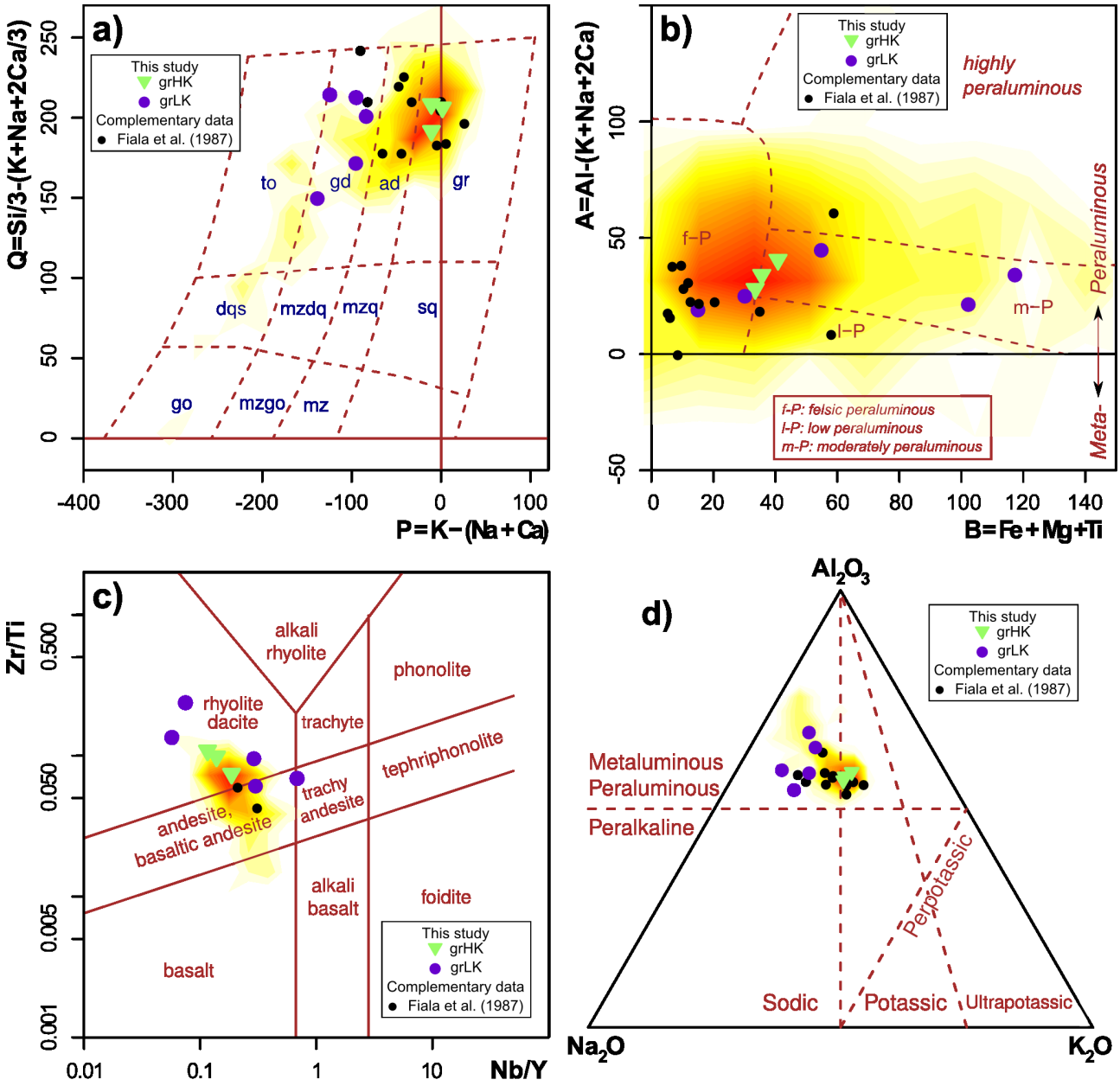

Figure 5. Various classification diagrams for the Náměšť Granulite Massif granulite. The frequency plots of Moldanubian granulites database from Janoušek et al. (2004) are used as background for comparison, the frequency is represented by colour gradient from *red* (maximum) to *yellow* (minimum). (a) Multicationic diagram P–Q (Debon and Le Fort, 1983), P describes the ratio of K-feldspar to plagioclase and Q represents the quartz content. *(ad: adamellite; dq: quartz diorite, quartz gabbro, quartz anorthosite; gd: granodiorite; go: gabbro, diorite, anorthosite; gr: granite; mz: monzonite; mzdq: quartz monzodiorite; mzgo: monzogabbro, monzodiorite; mzq: quartz monzonite; s: syenite; sq: quartz syenite; to: tonalite, trondhjemite).* (b) The B–A diagram (Debon and Le Fort, 1983) with classification fields for different types of peraluminous rocks (Villaseca et al., 1998) *(f–P: felsic peraluminous, l–P: low peraluminous, m–P: moderately peraluminous, h–P: highly peraluminous).* (c) Classification diagram Nb/Y vs. Zr/Ti (proposed by Winchester and Floyd, 1977, modified by Pearce, 1996). (d) Ternary plot Na_2O–Al_2O_3–K_2O (mol. %) with various compositional fields (Shand, 1943; Foley et al., 1987). Sample colour coding similar to Fig. 4.

Trace elements

The SiO_2–Rb plot display conspicuously inflected trend (Fig. 6). Other Harker plots show negative

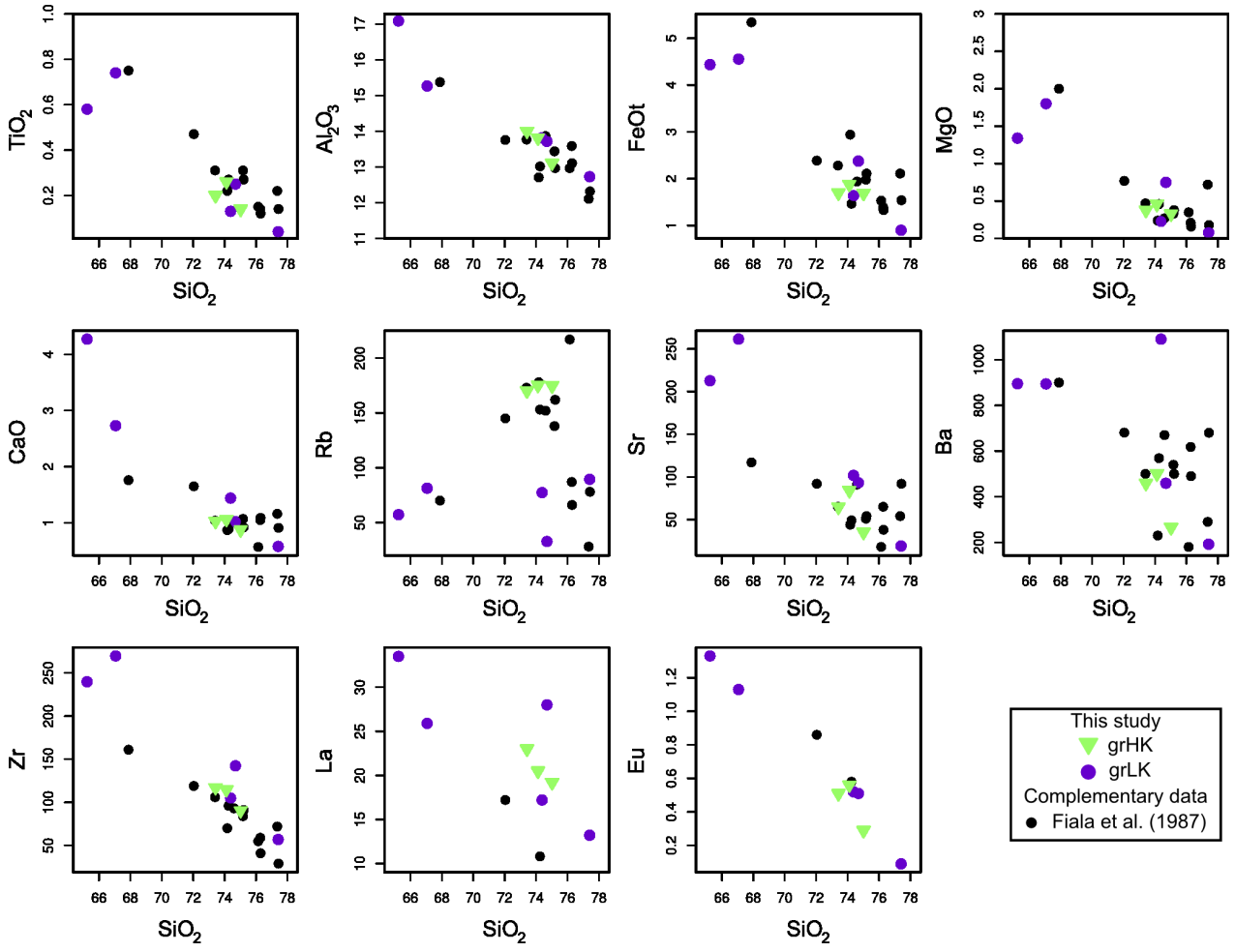

Figure 6. Binary plots of SiO_2 against major-element oxides (wt. %) and selected trace elements (ppm) for felsic granulites from the Náměšť Granulite Massif.

covariance of Sr, Ba, Zr, La and Eu with increasing SiO_2, where especially strontium and barium span over a wide range.

Trace-element contents in the felsic granulite were normalized by the average upper continental crust (Taylor and McLennan, 1995) and plotted in the spider diagram (Fig. 7a). Samples show tendency of slight LREE depletion and HREE enrichment with respect to the upper crustal values. Spiderplots are very similar to those from the Moldanubian Zone granulite database (Janoušek et al., 2004), with distinguishable throughs in Cs, U, Nb, Ta, Sr, P, Zr and Ti. Interestingly rubidium and K are above the unity line for granulites from grHK group, whereas samples from grLK are showing depletion. Chondrite-normalized (Boynton, 1984) REE patterns (Fig. 7b) feature moderate to weak enrichment in LREE (La_N/Yb_N = 2.5–11.9, La_N/Sm_N = 1.3–3.7) and negative Eu anomalies with magnitude positively correlating with increasing silica (Eu/Eu* = 0.08–0.76, Eu* = $\sqrt{Sm_N \times Gd_N}$).

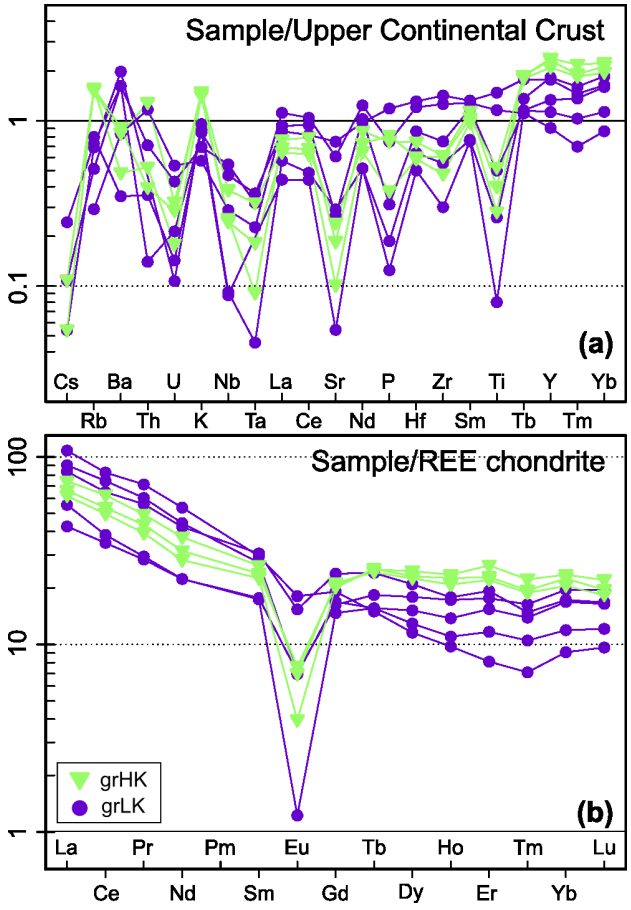

Figure 7. (a) Upper continental crust (Taylor and McLennan, 1995) normalized spider plot for the felsic granulites from the Náměšť Granulite Massif. (b) Chondrite (Boynton, 1984) normalized REE patterns in the felsic granulites from the NGM.

Such patterns are identical to those of other Moldanubian granulites, resembling highly fractionated granites (Janoušek et al., 2004).

Amphibolites and amphibole–plagioclase-bearing melts (APM)

The amphibolite dataset was supplemented by data on NGM amphibolite by Matějovská (1967), Šichtařová (1981) and René (2008, 2009).

Major elements

Amphibolites, metamorphosed basic volcanic rocks, should be also classified based on immobile elements (e.g. high field strength elements – HFSE), keeping clear from the problems with mobility of elements with low ionic potential. The subalkaline basaltic affinity of amphibolites is clearly visible from diagram Nb/Y–Zr/Ti (Fig. 8a) proposed by Winchester and Floyd (1977) and modified by Pearce (1996), whereas amphibole–plagioclase melts (APM) tends to basaltic andesite. The multicationic diagram of Jensen (1976) using less mobile elements in ternary plot Al–(Fe^T + Ti)–Mg (Fig. 8b)

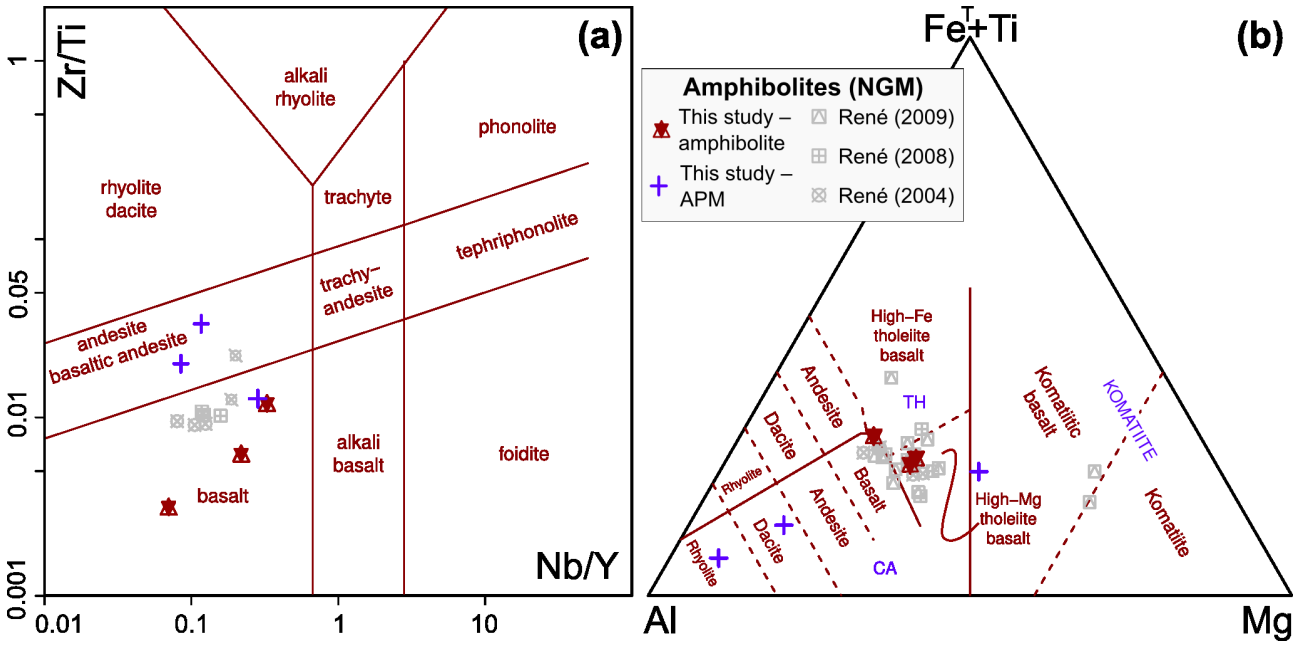

Figure 8. Various classification diagrams for the amphibolite enveloping the Náměšť Granulite Massif and amphibolite-plagioclase melts (APM). (a) Classification diagram Nb/Y vs. Zr/Ti of Pearce (1996). (b) Cationic plot Al–(Fe^T + Ti)–Mg after Jensen (1976). Published analyses from the amphibolite unit wrapping the NGM are shown for comparison (René, 2008; René, 2009).

confirmed high-Mg tholeiite basalt compositions for the amphibolites. Samples of APM span across the diagram from the komatiitic basalt field to rhyolite.

The three newly analysed amphibolites are rather primitive with low SiO_2 (41.6–46.1 wt. %), high MgO (6.1–8.9 wt. %) and fairly high mg# (44.7–58.3). On the other hand, one APM sample WKGCH1 shows extremely high MgO (11.9 wt. %) and mg# (68.1) with SiO_2 similar to those of amphibolites. Other two APM samples display mg# similar to the amphibolites, but are more silica rich (58.1–59.5 wt. %) and poorer in MgO (1.6–3 wt. %). The Fenner variation diagrams (Fig. 9) show clustering of data from amphibolites for MgO with SiO_2, TiO_2, Al_2O_3, FeOt, CaO, Na_2O, K_2O and P_2O_5. The negative correlation of MgO with SiO_2, Al_2O_3, Na_2O and positive covariance with TiO_2, FeOt, CaO and K_2O is shown for the samples from the APM group. The distribution of P_2O_5 is rather uniform throughout all samples.

Trace elements

REE contents in the garnetiferous amphibolites and amphibole–plagioclase melts (APMs) were normalized to the chondrite abundances (Boynton, 1984) and plotted in Fig. 10a. The total REE concentrations vary between 52.2 and 169.5 ppm. All samples are slightly enriched in REE compared to previously reported analyses of amphibolites from this region (René, 2008, 2009). Trend of amphibo-

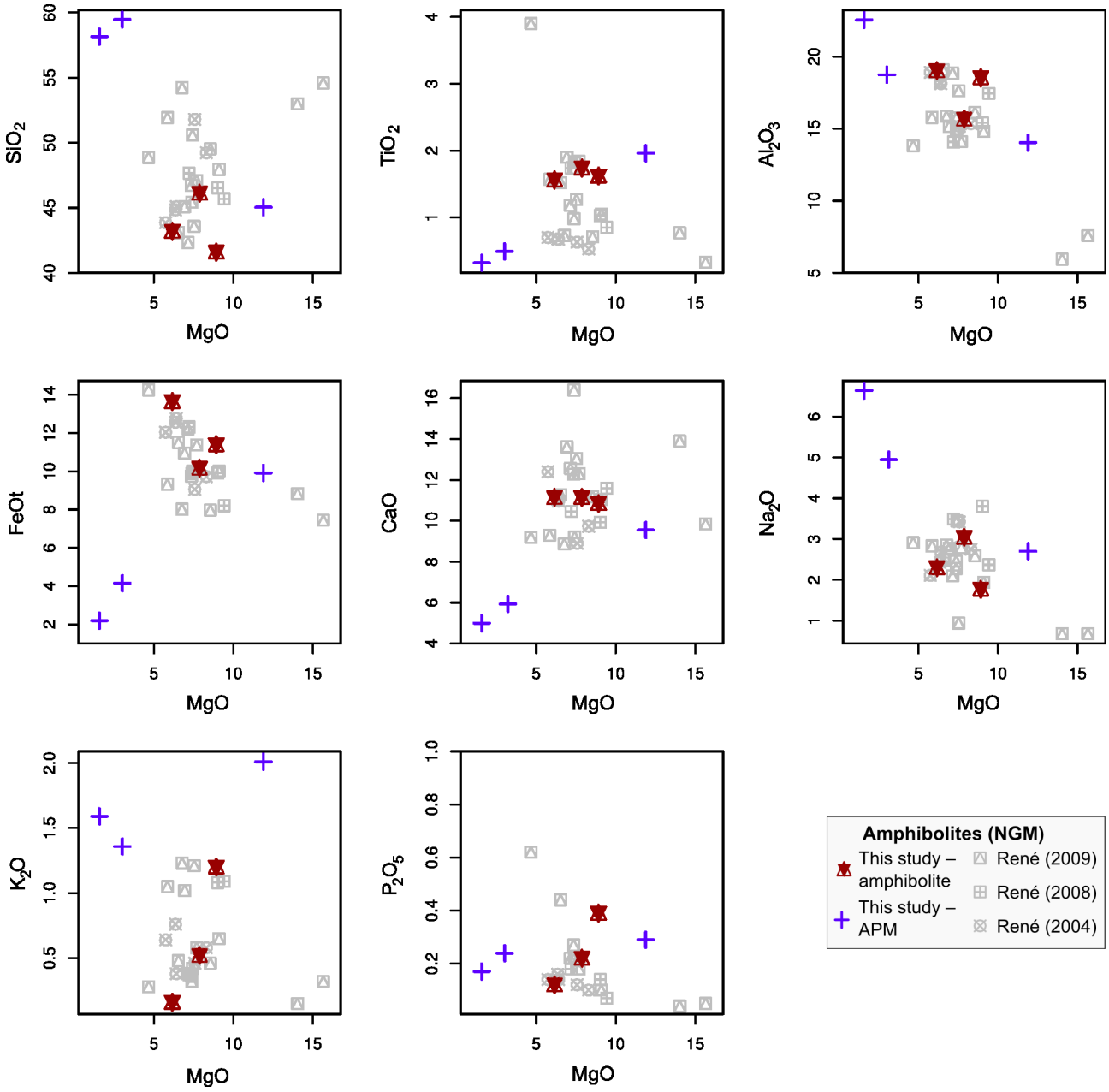

Figure 9. Binary plots of MgO against major- and minor-element oxides (wt. %) for studied metabasic rocks from the Náměšť Granulite Massif.

lite sample WKGCH19 matches very well Mid-Ocean Ridge Basalt (N-MORB) pattern, only slightly depleted in LREE ($La_N/Yb_N = 0.9$, $La_N/Sm_N = 0.6$). Other samples resemble the E-type Mid-Ocean Ridge Basalt (E-MORB) or Ocean Island Basalt (OIB) pattern with different degree of enrichment in LREE and MREE over the HREE, but samples patterns are all relatively flat ($La_N/Yb_N = 2.4$–4.5, $La_N/Sm_N = 1$–3.7). Worth noting is that the REE patterns of the amphibolites are placed in between those from the APM group, which additionally show also a distinctive negative Eu anomalies (Eu/Eu*

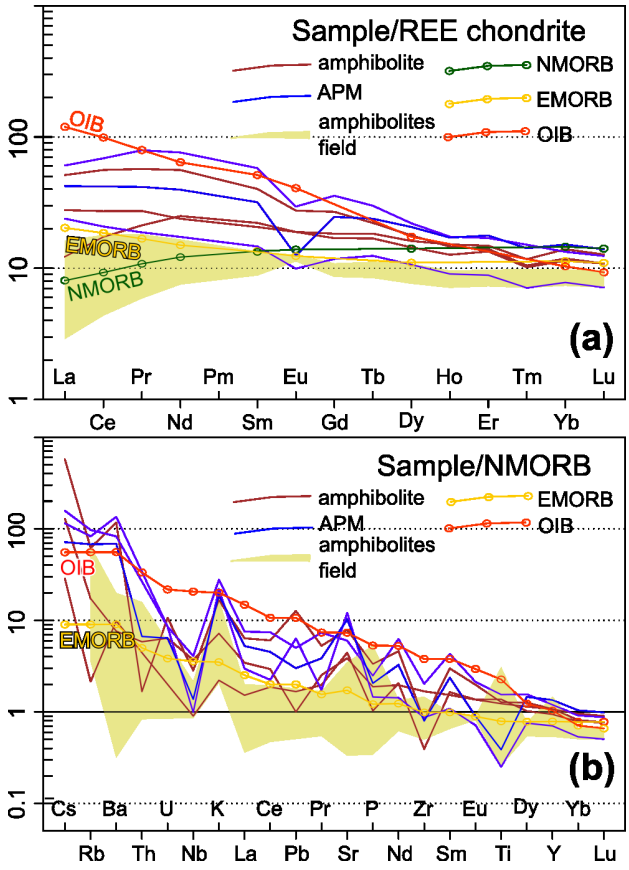

Figure 10. (a) Chondrite- (Boynton, 1984) normalized REE–patterns in the amphibolite and melt samples (APM) from the Náměšť Granulite Massif. Several reservoirs were added to the diagram: N-MORB – N-type Mid-Ocean Ridge Basalt, E-MORB – E-type Mid-Ocean Ridge Basalt, OIB – Oceanic Island Basalt (all from Sun and McDonough, 1989). 'Amphibolite field' represents all amphibolite samples from René (2008); René (2009). (b) N-MORB (Sun and McDonough, 1989) normalized spider plot for the studied samples with added E-MORB and OIB reservoirs.

= 0.45–0.76). The N-MORB–normalized (Sun and McDonough, 1989) spider plot (Fig. 10b) shows various enrichment in the LILE for all samples, both for amphibolites and the APM group. Spiderplots for all samples are more or less limited by pattern of Ocean Island Basalt (OIB) on the top and E-MORB on the bottom for range of less mobile REE and HFSE (except of depletion in Nb, Zr and Ti). Generally, the hydrous fluid mobile elements (Cs, Rb, Ba, U, K, Pb, Sr) are several times enriched, but variations are most likely due to the high-grade metamorphism.

Peridotites

To obtain information about the degree of serpentinization (progress of serpentinization) of the peridotite we used the indirect correlation of degree of serpentinization with the bulk magnetic susceptibility (Oufi et al., 2002; Bach et al., 2006). As shown in Chapter 3, this method in general describes well the degree of the Mohelno peridotite serpentinization. Obtained bulk magnetic susceptibility data

Tab. 4. Bulk susceptibility of the serpentinized peridotite [1000×SI]

Sample	K_m	sample	K_m	sample	K_m	sample	K_m	sample	K_m
WK6-1	2.269	WK7-1	4.250	WK5-1	14.940	WK10-1	31.910	WK4-1	37.530
WK6-2	1.141	WK7-2	3.455	WK5-2	19.550	WK10-2	34.270	WK4-2	32.370
WK6-3	1.538	WK7-3	2.936	WK5-3	14.350	WK10-3	25.360	WK4-3	42.980
WK6-4	2.026	WK7-4	3.870	WK5-4	11.480	WK10-4	24.170	WK4-4	36.230
WK6-5	2.209	WK7-5	3.724	WK5-5	18.780	WK10-5	29.540	WK4-5	23.390
WK6-6	1.36	WK7-6	3.872	WK5-6	20.790	WK10-6	34.200	WK4-6	30.570
WK6-7	1.981	WK7-7	3.951	WK5-7	19.090	WK10-7	27.150	WK4-7	32.760
WK6-8	1.137	WK7-8	2.619	WK5-8	12.400	WK10-8	37.900	WK4-8	30.180
WK6-9	7.089	WK7-9	2.835	WK5-9	13.370	WK10-9	34.860	WK4-9	43.450
WK6-10	1.048	WK7-10	3.243	WK5-10	11.450	WK10-10	20.050	WK4-10	40.820
		WK7-11	2.874	WK5-11	10.520	WK10-11	25.370		
		WK7-12	2.747						
WK6	2.180	**WK7**	3.365	**WK5**	15.156	**WK10**	29.525	**WK4**	35.028
st. dev.	1.786	st. dev.	0.559	st. dev.	3.740	st. dev.	5.544	st. dev.	6.381
colour	*yellow*		*orange*		*red*		*brown*		*black*

*Field : 300 A/m Holder : 871.2E-09

for five peridotite samples are summarized in the Tab. 4. The bulk magnetic susceptibility extend from 2×10^{-3} to 3.5×10^{-2} [SI] representing from medium (WKGCH6 and WKGCH7) to the highest values (WKGCH5, WKGCH10 and WKGCH4) measured in the Mohelno peridotite body (Chapter 3).

The new whole-rock data for peridotite were combined with data of Fritz (1995) and Medaris et al. (2005). The newly obtained data are subdivided based on both presence/absence of garnet and the bulk magnetic susceptibility.

Major elements

The five newly obtained whole-rock analyses (two garnet peridotite samples – WKGCH4 and WKGCH5 and three spinel peridotite samples – WKGCH6, WKGCH7 and WKGCH10) confirm the ultramafic character (SiO_2 = 39.7–41.4 wt. %) and narrow high range for MgO (34.6–36.1) and mg# (89.3–89.9). The MgO/SiO_2 vs. Al_2O_3/SiO_2 plot (Fig. 11) with a 'terrestial array' describes the successive magmatic depletion of a primitive mantle (Jagoutz et al., 1979) where highly depleted compositions are characterized by extremely low Al_2O_3/SiO_2 values (Jagoutz et al., 1979; Paulick et al., 2006) Both new peridotite whole-rock analyses and complementary data from literature follow a trend parallel to 'terrestrial array' that is systematically set off to lower MgO/SiO_2 values. Samples also show covariance between the bulk magnetic susceptibility and Al_2O_3/SiO_2 (positive) and MgO/SiO_2 (negative).

Trace elements

The REE contents in the newly analysed Mohelno peridotite are not very variable (ΣREE = 1.5–3.4 ppm). The spiderplots normalized to primitive mantle (McDonough and Sun, 1995) (Fig. 12a) show inclined patterns with progressive depletion from HREE (0.8–0.4 × primitive mantle) towards LREE (0.3–0.1 × primitive mantle). The only exceptions are Pb and Zr with values above those for primitive mantle and scattered pattern from strong to mild depletion, respectively. The whole new dataset exhibits a peculiar correlation between trace-element abundances and the bulk magnetic susceptibility value (without irregular values of Pb and Zr). Four of the five new samples show a slight negative Eu anomalies (Eu/Eu* = 0.80–0.96, value for sample without Eu anomaly 1.05). Similarly, the chondrite–normalized REE spiderplot (Fig. 12b) (Boynton, 1984), shows distinctively parallel trends set off towards higher values for samples with higher bulk susceptibility (more intense serpentinization). The less susceptibile sample WKGCH6 shows inclined pattern from LREE from 0.4 × chondrite contents to 0.9 × chondrite values for HREE. The most susceptibile sample WKGCH4 is shifted to slight enrichment values for HREE and MREE, while for LREE the values are around unity line with exception

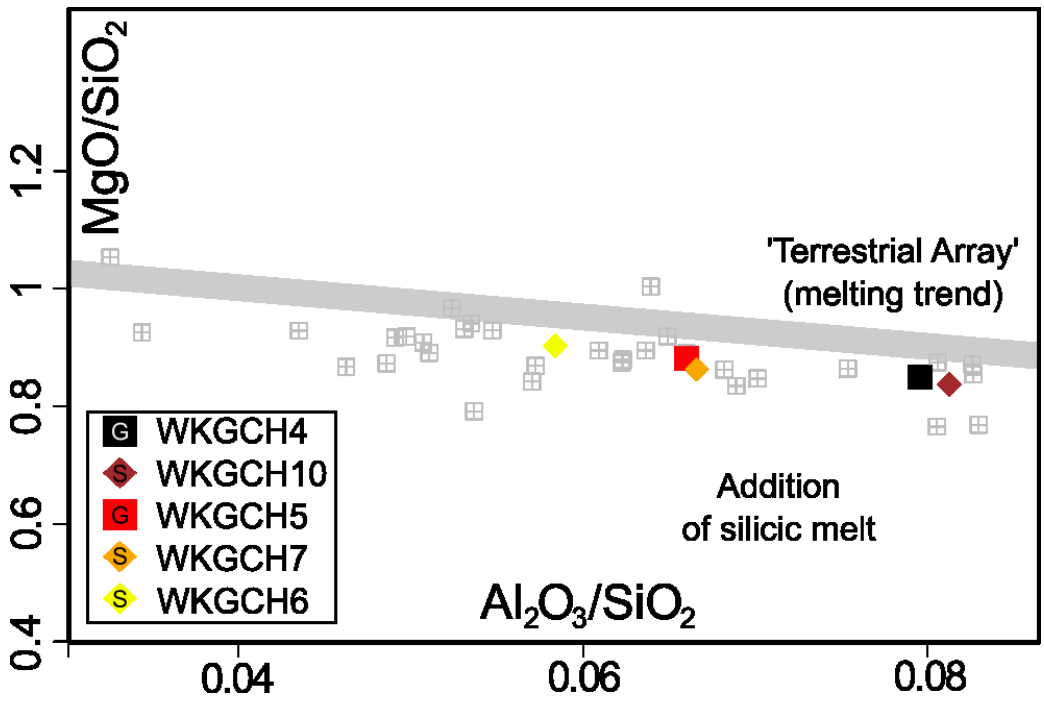

Figure 11. Binary diagram MgO/SiO_2 vs. Al_2O_3/SiO_2 for the Náměšť peridotite. New data colour coded according the magnetic susceptibility (*yellow* – lowest, *black* – highest, for precise values see Tab. 4) are, together with complementary data (*grey squares*) previously published for the Mohelno peridotite (Fritz, 1995; Medaris et al., 2005), parallel to the 'terestrial array' (Jagoutz et al., 1979).

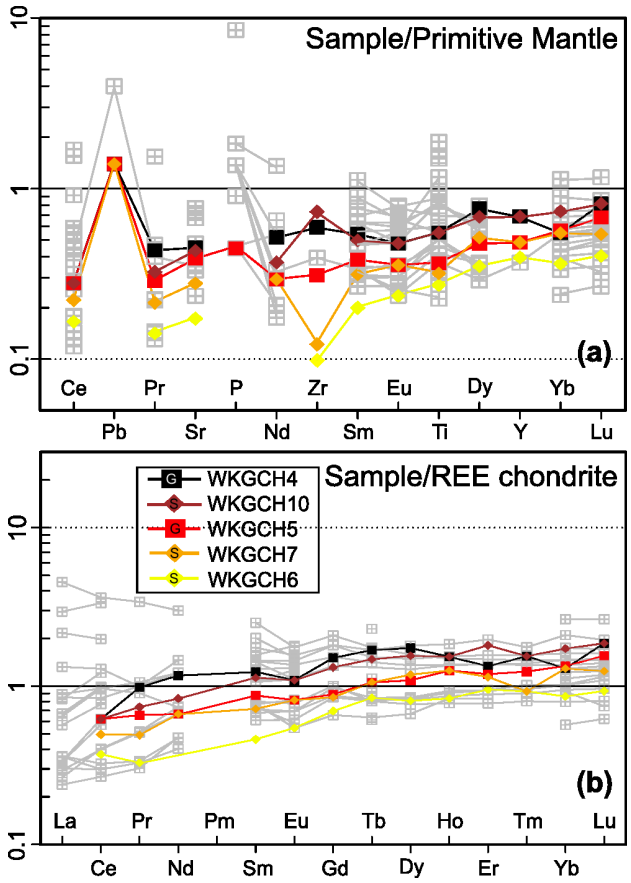

Figure 12. Trace-element abundances in the Mohelno peridotite. (a) Primitive mantle-normalized (McDonough and Sun, 1995) spider plot, (b) Chondrite-normalized (Boynton, 1984) REE patterns.The samples are colour coded according to the magnetic susceptibility (see Fig. 11).

of Ce at level of 0.6 × chondrite abundances.

Sensitive high-resolution ion-microprobe (SHRIMP) U-Pb zircon *in situ* dating

Analytical techniques

For understanding the timing of the processes in the orogenic root, in situ zircon samples from different positions in granulite and amphibolite microstructures were acquired.

For precise dating zircons from previously described granulite metamorpho-structural fabrics S1, S2 and S3 (Chapter 2) were selected along with rare zircons from amphibolite envelope of the NGM sharing S3 fabric with granulites (WK92C and WK198, Fig. 1c). Granulitic coarse-grained S1 fabric sample (WK188A,B) was sampled from granulite from the internal part of the peridotite fold (Fig. 1c). Ultramylonitic granulite S2 fabric samples (WK196AB and WK177L2) were taken from well preserved

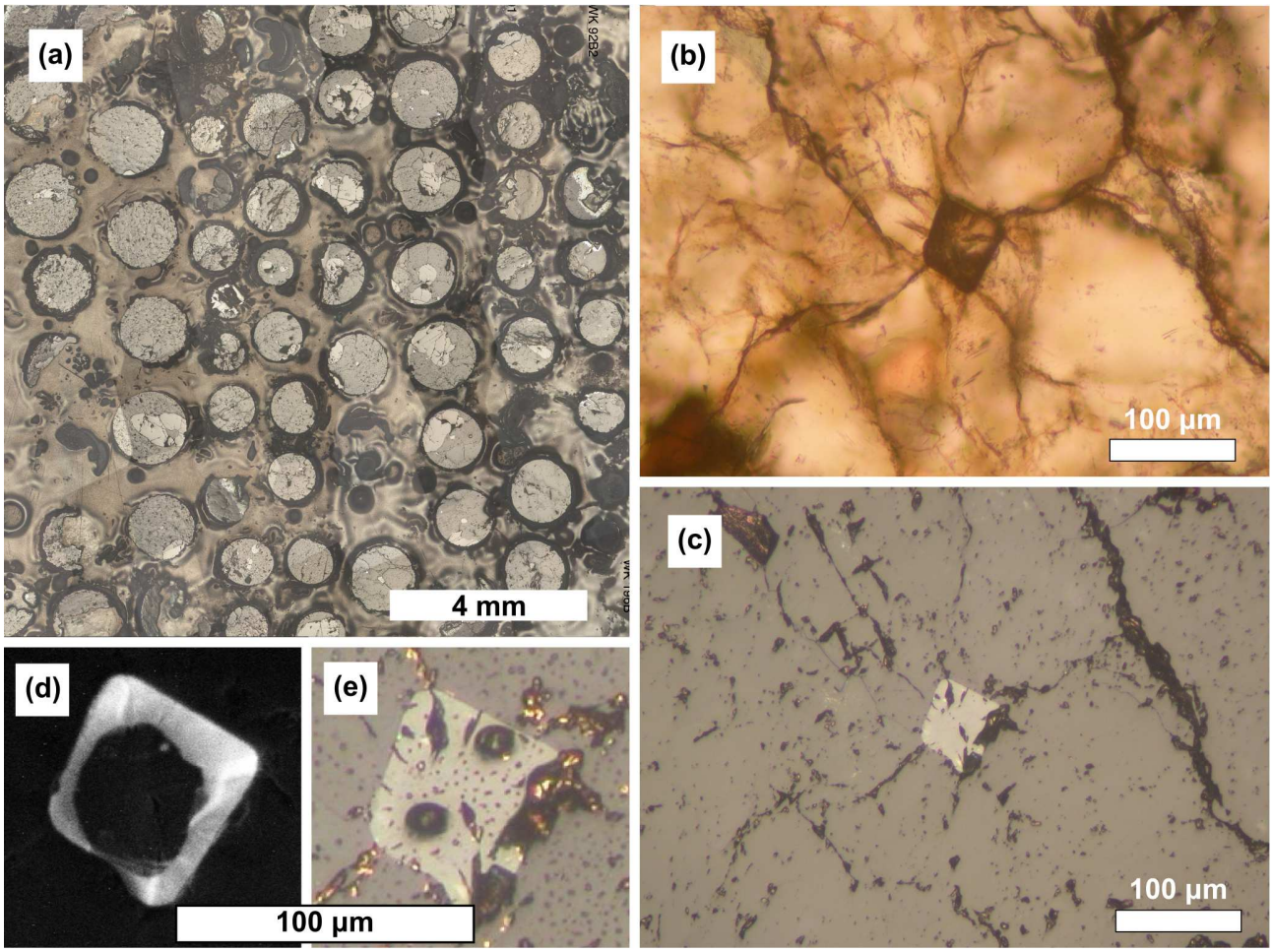

Figure 13. (a) Overview of mounted micro-drilled cores. (b) Transmitted light microphotography of zircon from sample WKGCH201. (c) Reflected light image of zircon from sample WKGCH201. (d) Cathodoluminescence (CL) image showing inner structure of zircon from sample WKGCH201. (e) Same zircon with two measuring spots, each in different single age component.

rocks in the external part of the peridotite fold hinge (Fig. 1c). The S3 fabric sample (WK201) was acquired from the retrograded foliation in the limbs of peridotite fold (Fig. 1c).

First, zircons were identified in thick (100 µm) polished thin sections using BSE imaging on scanning electron microscope CamScan4 at Charles University, Prague, Czech Republic (accelerating voltage 30 kV). Targeted zircons were then micro-drilled from the thin-sections under optical microscope (Fig. 13a) and mounted together with the Temora zircon standard (Black et al., 2003). Reflected and transmitted light photomicrographs were obtained for all zircons (Fig. 13b, c). Cathodoluminescence (CL) and Scanning Electron Microscope (SEM) images were prepared for all zircon grains. These CL and BSE images were used to decipher the internal structures of the sectioned grains (Fig.13d) and to ensure that the 10–30 µm SHRIMP spot was completely within a single composition domain (based on cathodoluminescence) within the sectioned grains (Fig. 13e). The U–Th–Pb analyses were made

using the SHRIMP II at the Research School of Earth Sciences, The Australian National University, Canberra, Australia, following procedures given in Williams (1998, and references therein). Each analysis consisted of 6 scans through the mass range, with a U–Pb reference grain analyzed for every three unknown analyses. The data have been reduced using the SQUID Excel Macro of Ludwig (2001). For the zircon analyses, the U/Pb ratios have been normalized relative to a value of 0.0668 for the Temora reference zircon, equivalent to an age of 417 Ma (see Black et al., 2003). Uncertainties in the U–Pb calibration were 0.61 % for a analytical sessions. Uncertainties given for individual analyses (ratios and ages) are at the one sigma level (Table 5).

Results

Cathodoluminescence (CL) and back–scattered SEM images of the zircon grains reveal presence of dark zircon cores and light and thin metamorphic rims in few grains from samples WK177L2 (granulite, S2 fabric, Fig. 14b) and WK201 (granulite, S3 fabric, Fig. 14c). No oscillatory zoning was observed in studied zircons but some grains show characteristic sector zoning patterns. The 44 high-resolution ion-microprobe (SHRIMP) U-Pb zircon ages are shown in the Table 5 along with corresponding isotopic data.

Two samples from granulite with S1 fabric (WK188A,B, Fig. 14a) show rounded zircon grains without any zoning pattern. These grains provided zircon ages from interval between 354.5 ± 4.1 Ma (1σ) to 334.3 ± 3.5 Ma (Tab. 5). The S2 fabric in granulite sample WK177L2 yields zircons with dark cores and clear rims with maximal value 470.1 ± 4.9 Ma (one age), large cluster of ages around 349 – 336 Ma and one age of 306.7 ± 3.8 Ma. The second sample of S2 fabric WK196A,B shows an interval of ages ranging from 367 Ma to 313 Ma. One sample from S3 fabrics (WK201) provides six ages within interval between 419.9 ± 4.6 Ma and 391.6 ± 3.9 Ma (having also two out-laying ages of 343.8 ± 5.5 Ma and 308.4 ± 3.5 Ma). Only three ages obtained from the "amphibolite" zircons spread from 349.2 ± 3.6 Ma to 324 ± 3.6 Ma.

Discussion

Whole-rock geochemical and geochronological constraints on protolithic rocks

The origin of the Moldanubian felsic granulites is widely discussed topic (Fiala et al., 1987; Jakeš et al., 1997; Kotková and Harley, 1999; Janoušek et al., 2004, and references therein). The original dis-

Tab. 4 Summary of SHRIMP U-Pb results for zircon grains analysed in situ in polished thin sections

Grain. spot	U (ppm)	Th (ppm)	Th/U	$^{206}Pb^*$ (ppm)	$^{204}Pb/^{206}Pb$	f_{206} %	Total $^{238}U/^{206}Pb$	±	Radiogenic $^{207}Pb/^{206}Pb$	±	$^{206}Pb/^{238}U$	±	Age (Ma) $^{206}Pb/^{238}U$	±	
WK188A (S1 fabric)															
2a.1	444	184	0.41	21.6	0.000317	0.20	17.66	0.21	0.0552	0.0009	0.0565	0.0007	354.5	4.1	
2a.2	1038	39	0.04	47.6	0.000054	0.07	18.74	0.20	0.0537	0.0005	0.0533	0.0006	334.9	3.6	
2a.3	1114	31	0.03	51.0	0.000051	0.15	18.76	0.20	0.0543	0.0005	0.0532	0.0006	334.3	3.5	
11a.1	896	22	0.02	41.4	0.000116	0.08	18.59	0.20	0.0538	0.0006	0.0538	0.0006	337.6	3.6	
9a.1	951	59	0.06	44.3	0.000028	0.14	18.44	0.20	0.0544	0.0005	0.0542	0.0006	340.0	3.6	
9a.2	679	73	0.11	32.0	0.000019	0.04	18.21	0.20	0.0537	0.0006	0.0549	0.0006	344.5	3.8	
6a.1	1046	24	0.02	48.6	0.000141	0.06	18.49	0.20	0.0537	0.0005	0.0540	0.0006	339.3	3.6	
4a.1	1186	29	0.02	56.9	0.000091	<0.01	17.89	0.19	0.0527	0.0005	0.0559	0.0006	350.9	3.7	
4a.2	1095	133	0.12	50.3	0.000048	0.03	18.70	0.20	0.0534	0.0005	0.0534	0.0006	335.7	3.6	
10a.1	930	30	0.03	44.9	-	<0.01	17.77	0.19	0.0533	0.0005	0.0563	0.0006	353.0	3.8	
WK188B (S1 fabric)															
5.1	1119	33	0.03	54.2	0.000145	0.17	17.73	0.19	0.0549	0.0005	0.0563	0.0006	353.2	3.8	
5.2	881	21	0.02	41.4	-	<0.01	18.28	0.20	0.0532	0.0006	0.0547	0.0006	343.5	3.7	
WK196AB (S2 fabric)															
8.1	864	69	0.08	42.2	0.000140	0.10	17.59	0.19	0.0544	0.0006	0.0568	0.0006	356.0	3.9	
8.2	108	228	2.11	5.1	-	0.31	18.03	0.30	0.0559	0.0018	0.0553	0.0009	346.8	5.6	
8.3	177	99	0.56	8.3	-	0.27	18.21	0.26	0.0555	0.0014	0.0548	0.0008	343.7	4.9	
10.1	1100	102	0.09	51.4	0.000023	<0.01	18.38	0.21	0.0532	0.0006	0.0544	0.0006	341.7	3.8	
10.2	127	46	0.36	5.9	0.000290	1.56	18.54	0.31	0.0657	0.0019	0.0531	0.0009	333.6	5.6	
11.1	2337	700	0.30	106.4	0.000078	0.10	18.87	0.20	0.0539	0.0004	0.0529	0.0006	332.6	3.4	
13.1	224	111	0.50	9.7	0.000238	0.44	19.74	0.30	0.0563	0.0023	0.0504	0.0008	317.1	4.8	
13.2	85	60	0.70	3.8	0.001472	1.88	19.17	0.39	0.0679	0.0026	0.0512	0.0011	321.7	6.5	
13.3	676	94	0.14	29.5	0.000151	0.23	19.71	0.24	0.0546	0.0008	0.0506	0.0006	318.4	3.8	
1.1	234	360	1.54	10.9	0.000579	2.01	18.50	0.26	0.0693	0.0014	0.0530	0.0007	332.7	4.6	
1.2	565	376	0.67	26.6	0.000130	<0.01	18.28	0.21	0.0523	0.0014	0.0548	0.0007	343.8	4.0	
1.3	196	171	0.87	8.5	0.001283	1.96	19.68	0.27	0.0684	0.0034	0.0498	0.0007	313.4	4.5	
12.1	1708	186	0.11	86.0	0.000077	<0.01	17.06	0.20	0.0534	0.0004	0.0586	0.0007	367.4	4.2	
12.2	145	36	0.25	6.9	0.000323	0.56	18.11	0.27	0.0579	0.0015	0.0549	0.0008	344.6	5.0	
WK177L2 (S2 fabric)															
3.1	1171	263	0.22	76.2	0.000074	0.13	13.20	0.14	0.0575	0.0004	0.0756	0.0008	470.1	4.9	
3.2	241	69	0.29	11.4	0.001359	2.83	18.13	0.24	0.0759	0.0013	0.0536	0.0007	336.5	4.4	
4.1	797	69	0.09	38.2	0.000377	0.75	17.93	0.20	0.0595	0.0006	0.0554	0.0006	347.4	3.8	
4.2	1591	58	0.04	67.7	0.000784	1.65	20.19	0.25	0.0657	0.0022	0.0487	0.0006	306.7	3.8	
2.1	589	61	0.10	28.3	0.000204	0.47	17.89	0.20	0.0573	0.0007	0.0556	0.0006	349.0	3.8	
2.2	176	53	0.30	8.3	0.000285	0.09	18.11	0.25	0.0541	0.0012	0.0552	0.0008	346.3	4.7	
6.1	696	95	0.14	38.8	0.000122	0.22	15.42	0.17	0.0566	0.0007	0.0647	0.0007	404.1	4.5	
WK201 (S3 fabric)															
1.1	3588	125	0.03	195.6	0.000170	0.17	15.76	0.17	0.0560	0.0004	0.0634	0.0007	396.0	4.1	core
1.2	4100	1588	0.39	222.0	0.000026	0.04	15.87	0.16	0.0549	0.0002	0.0630	0.0007	393.9	3.9	rim
4.1	95	63	0.67	4.5	0.002507	1.27	18.03	0.29	0.0636	0.0018	0.0548	0.0009	343.8	5.5	rim
4.2	597	232	0.39	34.6	0.000000	0.12	14.84	0.16	0.0562	0.0009	0.0673	0.0008	419.9	4.6	core
9.1	6317	425	0.07	339.6	0.000031	<0.01	15.98	0.16	0.0540	0.0002	0.0626	0.0006	391.6	3.9	core
9.2	190	31	0.17	10.3	0.000407	0.36	15.89	0.21	0.0574	0.0011	0.0627	0.0008	392.0	5.1	rim
5a.1	999	222	0.22	56.8	0.000141	0.31	15.11	0.31	0.0575	0.0010	0.0660	0.0014	411.9	8.3	rim
5a.2	631	24	0.04	27.7	0.002388	4.17	19.55	0.22	0.0860	0.0009	0.0490	0.0006	308.4	3.5	core
WK92C (amphibolite – S3 fabric)															
5.1	497	172	0.35	23.5	0.000171	0.57	18.20	0.21	0.0579	0.0009	0.0546	0.0006	342.8	4.0	
5.2	567	200	0.35	25.8	0.001334	2.77	18.86	0.21	0.0752	0.0008	0.0515	0.0006	324.0	3.6	
WK198 (amphibolite – S3 fabric)															
9.1	1256	76	0.06	60.3	0.000251	0.44	17.88	0.19	0.0570	0.0005	0.0557	0.0006	349.2	3.6	

Notes:
1. Uncertainties given at the one s level. 2. Error in Temora reference zircon calibration was 0.61% for the analytical session. (not included in above errors but required when comparing data from different mounts).
3. f206 % denotes the percentage of ^{206}Pb that is common Pb.
4. Correction for common Pb for the U/Pb data has been made using the measured $^{238}U/^{206}Pb$ and $^{207}Pb/^{206}Pb$ ratios following Tera and Wasserburg (1972) as outlined in Williams (1998).

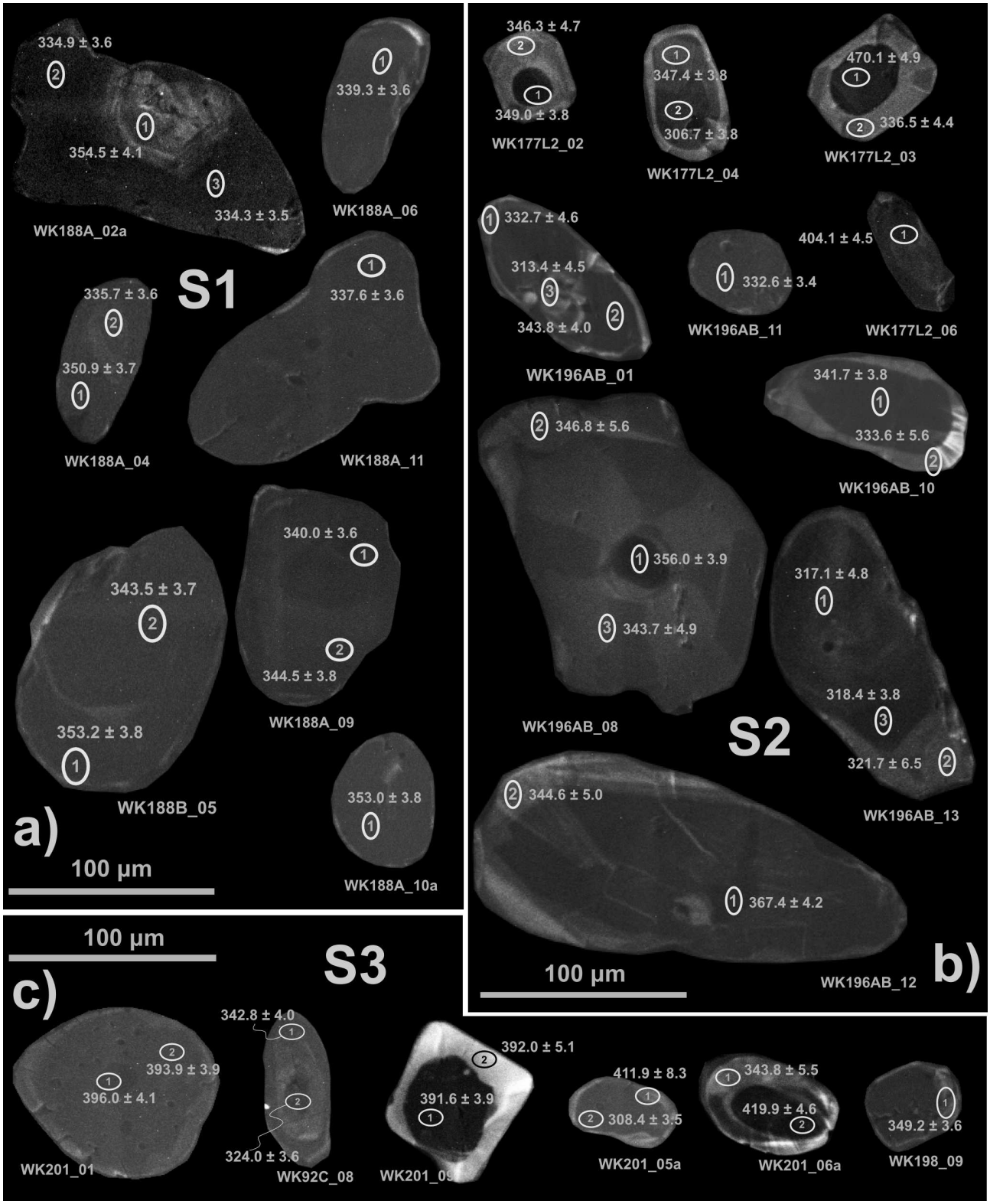

Figure 14. Cathodoluminescence (CL) images of zircon grains extracted from different structural positions showing their inner structure and measuring spots with inffered age at the one sigma level. (a) Zircon grains from granulitic coarse-grained S1 fabric sample (WK188A,B). (b) Zircon grains from ultramylonitic granulite S2 fabric samples (WK196AB and WK177L2). (c) Zircon grains from retrogressed S3 fabric samples (WK201).

cussion dealt the origin of the protolith (sedimentary vs. igneous, Suess, 1912; Matějovská, 1967; Fiala et al., 1987) the latter is nearly consensually accepted today. Two main 'igneous' models for origin of the Moldanubian felsic granulites are proposed: (a) (ultra)high-pressure melts formed and segregated during Variscan subduction (Jakeš, 1997; Kotková and Harley, 1999); (b) Early Palaezoic granites, almost isochemically metamorphosed during Variscan collision, which underwent limited partial melting (Janoušek et al., 2004; Lexa et al., 2011).

Newly obtained geochemical data from the Náměšť granulite show striking concordance of various classificational and petrogenetical characteristics with those of average Moldanubian felsic granulite massifs represented by a database of more than 200 analyses (Janoušek et al., 2004) (e.g. similar ratios of major- and trace-elements and REE abundances). Moreover, the zircon (Watson and Harrison, 1983) and monazite (Montel, 1993) saturation temperatures (Fig. 15) from the Náměšť granulites 774 ± 38 °C and 769 ± 24 °C respectively, are within the error of the average zircon saturation temperature from the database of the Moldanubian granulites (740 ± 48 °C; Janoušek et al. 2004). Based on previous studies (Kröner et al., 2000a; Friedl et al., 2003) and from new SHRIMP U-Pb zircon ages in this work it is obvious, that the Moldanubian felsic granulite contain abundant pre-metamorphic/pre-Variscan zircon relics (Fig. 16). Commonly, the older zircon cores in the Náměšť granulite are overgrown by Variscan rims, implying the crystallization of zircon rims from melt under granulite–facies conditions (Roberts and Finger, 1997; Franěk et al., 2011; Lexa et al., 2011). This excludes the possibility of zircon inheritance as a result of shielding by restitic minerals. Therefore any partial melting during the Variscan high-grade metamorphism must have been volumetrically limited (Janoušek et al., 2004). The equivalent zircon and monazite saturation temperatures (~770 °C) roughly estimate the crystallization temperatures of the protolith (Janoušek et al., 2004).

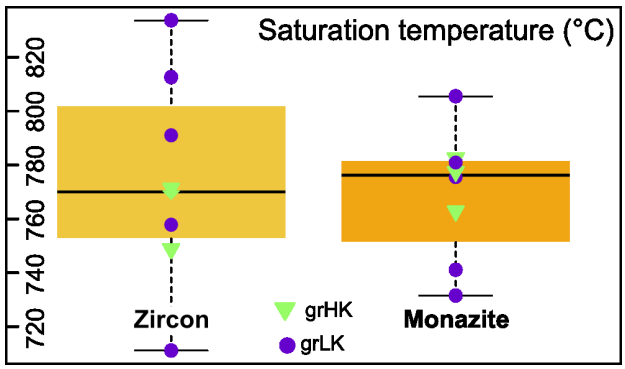

Figure 15. Zircon and monazite saturation temperatures for felsic Náměšť Granulite Massif granulites. *Left*: Watson and Harrison, 1983; *Right*: Montel, 1993. Estimations for individual samples are shown for both datasets.

The protolith age distribution from Bohemian granulites and Dunkelsteiner Wald granulites provide a dominant pre-metamorphic pattern suggesting an age of 450 Ma (Kröner et al, 2000; Friedel et al., 2004). This mean age and geochemical similarity led Janoušek et al. (2004) to propose an origin of these rocks as Saxothuringian granites, that were subducted into asthenospheric depths during Devono-Carboniferous orogeny (Janoušek and Holub, 2007). In addition, similar Ordovician and Late Proterozoic protolith U–Pb ages were obtained by Tajčmanová et al., (2010) from northerly Vír granulite body. These protolith ages are not confirmed by this study which indicates a significant age group around 400 Ma, which was also obtained for a Strážek Granulite Massif by Schulmann et al. (2005). Such a difference in protolith ages for rocks of identical chemistry may indicate that the similar formation process of precursors of future granulites occurred in mid-Ordovician and Devonian times. The peak metamorphic age of Variscan granulites of the Moldanubian Zone clusters around 340 Ma, which is not in accord with results of this study. In particular, samples from S1 fabric show a bimodal age distribution with two peaks: 353 Ma and the second 339 Ma. Similar bimodal distribution of U-Pb zircon ages was obtained by Tajčmanová et al. (2010) and was interpreted as a result of granulite–facies metamorphism around 350 Ma followed by partial melting and exhumation at 340 Ma, a hypothesis, which was already proposed by Schulmann et al. (2005) for granulites from the eastern margin of the Bohemian Massif.

Deducing the primary palaeotectonic context for an old volcanic suite exposed to high-grade metamorphic conditions and subjected to deformation processes sets an intriguing riddle. Useful information can be provided by relatively immobile trace elements (especially HFSE and REE), even for rocks with strong metamorphic overprint (Winchester and Floyd, 1977; Wood, 1980; Pearce, 1996). In the Th – Zr/117 – Nb/16 classification diagram of Wood (1980) (Fig. 17) the newly studied amphibolites plot within the field of E-MORB/Within-plate Tholeiite (WPT). This protolith estimation is in accord with conclusion from both chondrite- and N-MORB-normalized spiderplots, where amphibolites display composition confined between those of E-MORB and OIB reservoirs. Possible origin of volumetrically rare APM could be seen in limited melt extraction from partially molten amphibolite (e.g. because of the melt extraction in LREE depleted sample WKGCH19).

The Carboniferous U-Pb ages presented in this study correspond certainly to metamorphic age of these rocks. The existing isotopic ages from the metabasites of the eastern margin of the Bohemian Massif are Early Palaeozoic (~520–500 Ma from the Staré Město belt gabbros and amphibolites; Kröner et al. 2000b; Štípská et al., 2001; ~530 Ma from gabbros of Letovice ophiolite complex; Soejono et al.,

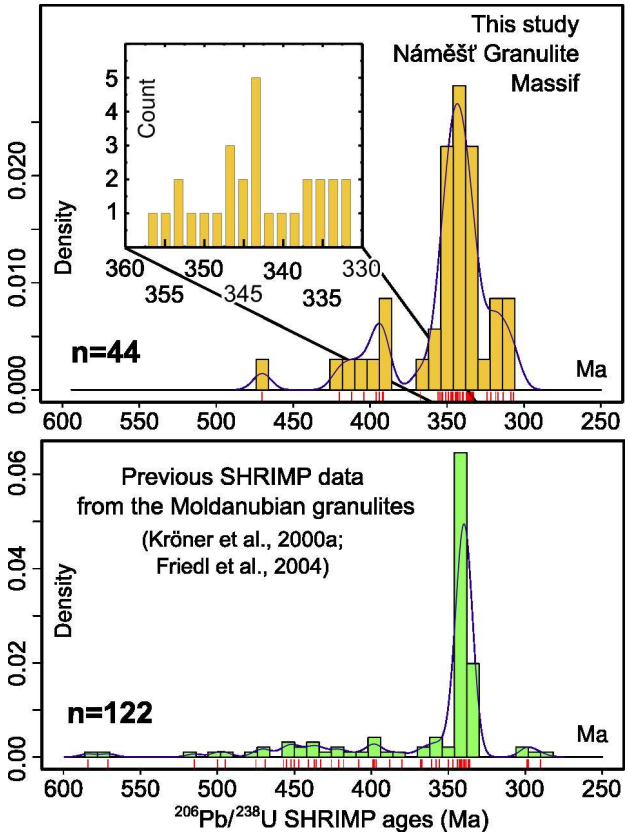

Figure 17. Histogram of frequencies for the $^{206}Pb/^{238}U$ SHRIMP zircon ages from (a) the Náměšť Granulite Massif granulites (3 ages from rare zircon in amphibolites), with inset zoomed to age span 360–330 Ma. (b) Ages from other Moldanubian granulites (Prachatice and Blanský les – Kröner et al., 2000a; Dunkelsteiner Wald – Friedl et al., 2004).

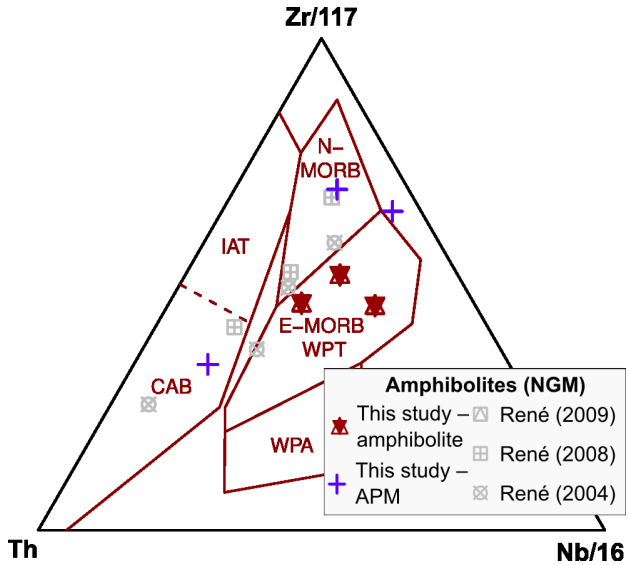

Figure 17. Geotectonic discrimination diagram Th – Zr/117 – Nb/16 of Wood (1980) for the metabasites from the Náměšť Granulite Massif. CAB – Calc-alkaline Basalts, IAT – Island-arc Tholeiites, WPA – Alkaline Within-plate Basalts, E-MORB – E-type Mid-Ocean Ridge Basalts, WPT – Within-plate Tholeiites.

2010; ~440 Ma from felsic dyke cross-cutting the Rehberg amphibolite; Finger and Von Quadt, 1995). Because the chemistry of these rocks and their structural position are more or less similar (Höck et al., 1997) it is very likely that the studied rocks are also of Lower Paleozoic, most probably of Late Cambrian to Early Ordovician age.

New peridotite whole-rock analyses from the Mohleno peridotite enhanced with bulk magnetic susceptibility data demonstrate suprising covariance between the bulk magnetic susceptibility and whole-rock geochemical features (e.g. ratio of Al_2O_3/SiO_2, position of chondrite- or primitive mantle-normalized spiderplot patterns, Fig. 12). The bulk magnetic susceptibility is used as proxy for degree of serpentinization estimations (Oufi et al., 2002; Bach et al., 2006) due to progressive crystallization of magnetite with advancing serpentinization. Modification of the REE contents by melt induced refertilization is widely reported from refractory peridotites worldwide (Bodinier and Godard, 2007 and references therein).

Therefore an attempt to reconstruct the primary peridotite modal composition before serpentinization is conducted. Newly obtained peridotite whole-rock analyses are geochemicaly modelled (Fig. 18) using a database of mineral compositions from the Mohelno peridotite (Medaris et al., 2005; Kamei et al., 2010). We choosed an individual mineral compositions randomly from the database to compile desired mineral assemblage for each modelling run. Modelled modal compositions show striking covariance with the bulk magnetic susceptibility and therefore with REE abundancies. The sample WKGCH6 characterized by minimal bulk magnetic susceptibility and ΣREE has the highest modal volume of olivine and minimal of orthopyroxene, clinopyroxene and spinel from the group of spinel peridotite samples. Decomposition of garnet by spinel – garnet equilibrium reaction: orthopyroxene + clinopyroxene + spinel → forsterite + garnet (Webb and Wood, 1986) will shift the values for garnet peridotite modal compositions towards the compositional trends defined by the spinel peridotite samples. It is likely, that the Mohelno peridotite is an example of variably refertilized harzburgite with primary mineral assemblage olivine + orthopyroxene + clinopyroxene + spinel and therefore it supports formerly proposed idea of spinel peridotite isochemical modification due to outer conditions (pressure: Chapter 2, temperature: Medaris et al. 2005; Kamei et al. 2010).

This geochemical study suggests that the Mohelno peridotite represents a harzburgite refertilized by basaltic melt (Fig. 19). Based on this geochemical signature the Mohelno peridotite was previously interpreted as a mantle fragment with asthenospheric affiliation by Medaris at al. (1990, 2005). The process of mantle refertilization is typical for slow spreading ridges environment (Dijkstra et al., 2001,

2003). Therefore, we suggest that similar tectonic setting can be also adopted for the origin of Mohelno peridotite. Critical is the age of formation of studied peridotites, which can be constrained by existing Late Devonian Sm-Nd 371 Ma ages (Beard et al., 1992; Medaris et al., 1995; Becker, 1997). Even though Sm-Nd age can be considered as a cooling age, it is most likely related to upwelling of the mantle under the rift (Medaris et al., 2006) and therefore the transport of studied peridotite into region of mantle and crust boundary took place probably in Late Devonian.

Geodynamic implications

The main question of this study is as whether the three studied rock types could have originate during a single geodynamic event i.e. as whether they represent a pre-collisional lithotectonic structure of the Moldanubian Zone. Based on our data, we can conclude, that the Mohelno peridotite corresponds to

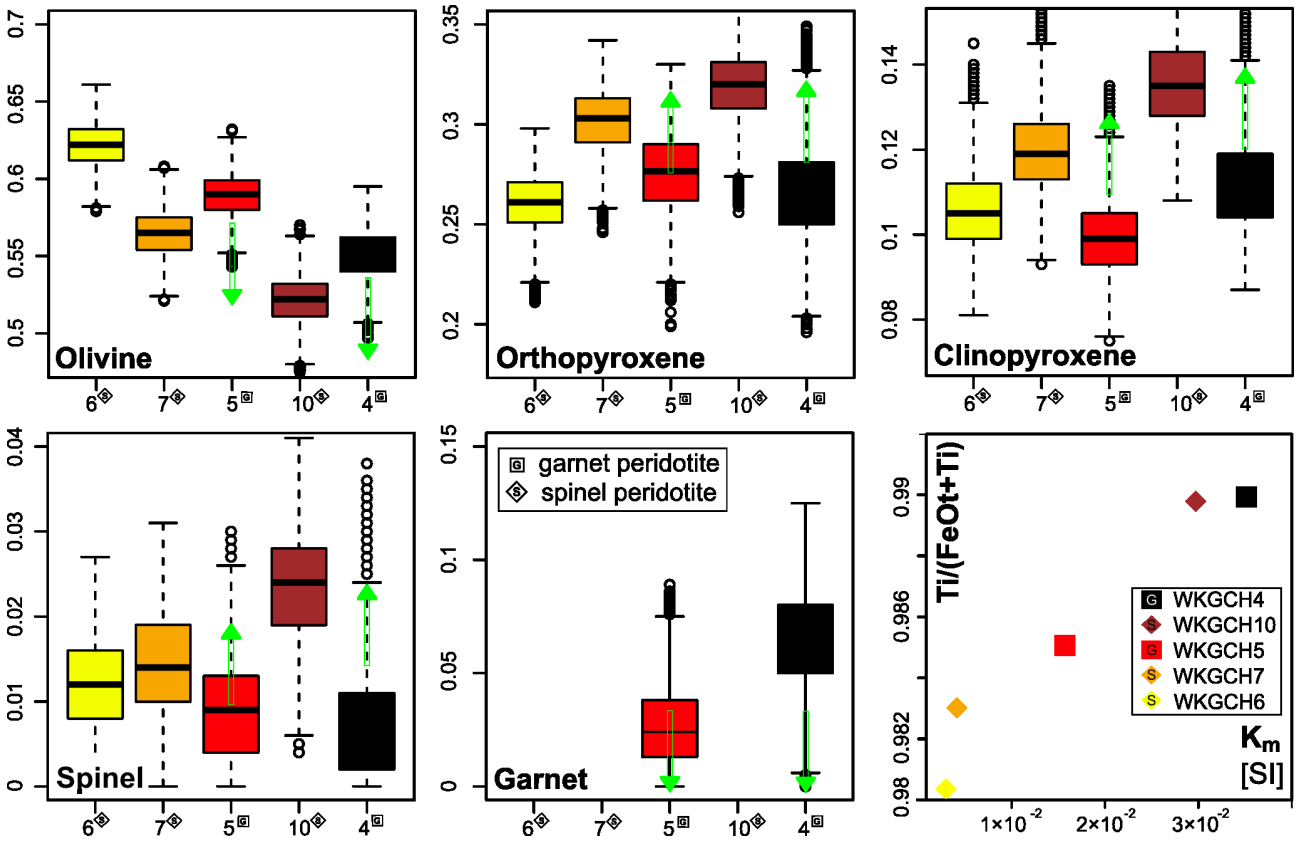

Figure 18. Modal compositions of the studied Mohelno peridotite reconstructed from published mineral analyses (Medaris et al., 2005; Kamei et al., 2010) and our whole-rock geochemical dataset. Calculated composition (from 1000 random subcompositions) is visualised with set of boxplots for each peridotite sample. For garnet peridotite samples WKGCH5 (label $5^{(G)}$) and WKGCH4 (label $4^{(G)}$) an mineral assemblage olivine + orthopyroxene + clinopyroxene + spinel + garnet is considered. For spinel peridotite samples WKGCH6 (label $6^{(S)}$), WKGCH7 (label $7^{(S)}$) and WKGCH10 (label $10^{(S)}$) same garnet-free mineral assemblage is assumed. (a)-(e) Modal % of olivine, orthopyroxene, clinopyroxene, spinel and garnet in calculated composition. (f) Binary diagram of bulk magnetic susceptibility (K_m) vs. $Ti/(FeO^T + Ti)$. Colour coding of samples according to the magnetic susceptibility (see Fig. 11).

depleted mantle with asthenospheric affiliation refertilized probably in a slow ridge environment in Late Devonian. The metabasic belt corresponds to E-MORB or to Within-plate Tholeiite, which originated most likely during Late Cambrian to Early Ordovician rifting event (based on correlation with nearby metabasite bodies in identical structural position). The dating of granulite and its geochemistry suggests high pressure reworking of precursors with Early Devonian age. These data clearly preclude genetically related origin of studied rocks and therefore a tentative geodynamic model can be proposed.

The most important are different protolith ages for felsic granulites and metabasites. The granulites represent a continental crust, while the metabasites reflects a rifting environment. Most importantly, the age of rifting is more or less in agreement with age of sedimentation of overlying sediments of Monotonous and Varied groups suggesting common passive margin/rifting history (Jastrzębski, 2009; Košler et al., 2011). Therefore, we interpret the metabasic layer as genetically related to overlying sedimentary sequences and corresponding to one geotectonic unit related to passive margin/rifting episode of Cambro-Ordovician age. In contrast, the felsic granulites protolith is significantly younger and not related to this rifting event, precluding common origin with adjacent metabasites. Therefore, it is suggested, that these rocks originated in geographically distant environment.

The last problem is related to the origin of Mohelno peridotite and its genetical link to metabasites and granulites. These rocks represent mantle rocks of asthenospheric origin that was refertilized during rifting period at Late Devonian. It is evident, that the mantle rocks did not originate together with

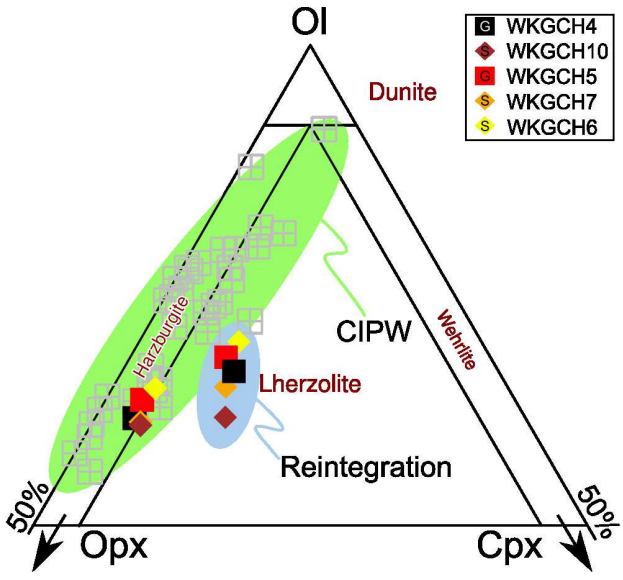

Figure 19. IUGS classification diagram for the Mohelno peridotite from the Náměšť Granulite Massif. Different results obtained from using CIPW norm or reconstructed modal composition are shown. Colour coding of samples according to the magnetic susceptibility (see Fig. 11).

felsic granulites and were incorporated together during Variscan convergence as suggested by Medaris et al. (2006). The metabasite layer reflects basaltic magmatism related to rifting period, but the Cambro-Ordovician age clearly rule out common origin during Devonian rifting indicated by Mohelno peridotite.

The petrological data acquired by author of this thesis show that the pressure and temperature range for peak conditions of Námešť granulites is the same as that of surrounding granulite massifs. Therefore, the pressure of ~1.8 GPa at temperature 800 °C can be considered as a value typical for orogenic lower crust at the eastern margin of the Bohemian Massif. Based on mineral assemblage of metabasite belt it is evident, that these rocks never achieved pressures of associated granulites. This indicates that the granulites represented the structurally deepest rock during Variscan convergence as proposed already by Lexa et al. (2011). Based on geochemical results and petrological arguments above, the tectonic relamination model seems to be the most suitable one explaining close juxtaposition of these contrasting rocks. We propose here, that the Devonian granitoids together with mostly Ordovician material (lower crustal allochthon) were thrust underneath the Moldanubian crust characterized by Cambro-Ordovician metabasic (metabasalts, metagabbros) lower crust situated underneath Late Proterozoic basement relics and Cambro-Ordovician sediments. The Devonian protolith age of the Námešť and Strážek granulites only indicate a heterogenity of crustal rocks forming the lower crustal allochthon compared to mid-Ordovician protolith ages of other Moldanubian granulites.

In addition, the systematically older metamorphic ages of granulites (~353 Ma) from the eastern margin of the Bohemian Massif compared to their westerly counterparts (~340 Ma) indicate a time scale of underthrusting. We speculate, that the granulitic massifs were relaminated to the overlying crust about 13 My earlier compared to the western part. The geochemical composition of sub-crustal mantle lithosphere was highly heterogeneous in the area of Variscan orogenic root as documented by various types of peridotite fragments enclosed in granulites and associated rocks (Medaris et. al., 2005). While the garnet lherzolites are interpreted as mantle wedge material, the spinel-garnet harzburgites reflect rifting environment (Medaris et al., 2006). Therefore we suggest, that the relaminated felsic crust sampled subcontinental mantle of various origins and remote geographic places during convergence as proposed by Machek et al. (2009) and Chapter 2. However, it is evident from above, that there is no genetical link between mantle rocks and felsic granulites and therefore the area of incorporation of mantle sheets into crust is and will remain unknown.

References

- Aftalion, M., (1989). Early Carboniferous U-Pb zircon age of garnetiferous perpotassic granulites, Blanský Les massif, Czechoslovakia. Neu. Jb. Mineral., Monatshefte 4, 145–152.
- Bach, W., Paulick, H., Garrido, C. J., Ildefonse, B., Meurer, W. P., Humphris, S. E., (2006). Unraveling the sequence of serpentinization reactions: petrography, mineral chemistry, and petrophysics of serpentinites from MAR 15°N (ODP Leg 209, Site 1274). Geophys. Res. Lett. 33, L1330.
- Beard, B. L., Medaris, L. G., Johnson, C. M., Brueckner, H. K., Mísař, Z., (1992). Petrogenesis of Variscan high-temperature group A eclogites from the Moldanubian Zone of the Bohemian Massif, Czechoslovakia. Contrib. Mineral. Petrol. 111, 468–483.
- Becker, H., (1997). Sm-Nd garnet ages and cooling history of high-temperature garnet peridotite massifs and high-pressure granulites from lower Austria. Contrib. Mineral. Petrol. 127, 224–236.
- Bodinier, J.-L., Godard, M., (2007). Orogenic, ophiolitic, and abyssal peridotites. In: Holland, H. D., Turekian, K. K. (Ed.), Treatise on Geochemistry, Pergamon.
- Boynton, W., (1984). Cosmochemistry of the rare earth elements: meteorite studies, In: Henderson, P. (Eds.), Rare Earth Element Geochemistry. Elsevier, Amsterdam, 63–114.
- van Breemen, O., Aftalion, M., Bowes, D. R., Dudek, A., Mísař, Z., Povondra, P., Vrána, S., (1982). Geochronological studies of the Bohemian Massif, Czechoslovakia, and their significance in the evolution of Central Europe. Trans. Roy. Soc. Edinb. Earth Sci. 73 (for 1982), 89–108.
- Carswell, D. A., O'Brien, P. J., (1993). Thermobarometry and geotectonic significance of high-pressure granulites: examples from the Moldanubian Zone of the Bohemian Massif in Lower Austria. J. Petrol. 34, 427–459.
- Cooke, R. A., O'Brien, P. J., (2001). Resolving the relationship between high P–T rocks and gneisses in collisional terranes: an example from the Gföhl gneiss–granulite association in the Moldanubian Zone, Austria. Lithos 58, 33–54.
- Dallmeyer, R., Franke, W., Weber, K., 1995. Pre–Permian geology of central and eastern Europe, Springer, Berlin.
- Debon, F., Le Fort, P., (1983). A chemical–mineralogical classification of common plutonic rocks and associations. Trans. Roy. Soc. Edinb. Earth Sci. 73, 135–149.
- Dijkstra, A. H., Barth, M. G., Drury, M. R., Mason, P. R. D., Vissers, R. L. M., (2003). Diffuse porous melt flow and melt–rock reaction in the mantle lithosphere at a slow-spreading ridge: A structural

petrology and LA-ICP-MS study of the Othris Peridotite Massif (Greece). Geochem. Geophys. Geosyst. 4, 8613.

- Dijkstra, A. H., Drury, M. R., Vissers, R. L. M., (2001). Structural petrology of plagioclase peridotites in the West Othris Mountains (Greece): melt impregnation in mantle lithosphere. J. Petrol. 42, 5–24.

- Fiala, J., Matějovská, O., Vaňková, V., (1987). Moldanubian granulites: source material and petrogenetic considerations. Neu. Jb. Mineral., Abh. 157, 133–165.

- Finger, F., Steyrer, H., (1995). A tectonic model for the eastern Variscides: indications from a chemical study of amphibolites in the south-eastern Bohemian Massif, Austria. Geol. Carpath. 46, 1–14.

- Finger, F., Von Quadt, A., (1995). U–Pb ages of zircons from a plagiogranite-gneiss in the south-eastern Bohemian Massif, Austria: further evidence for an important early Paleozoic rifting episode in the eastern Variscides. Schweiz. Mineral. Petrogr. Mitt. 75, 265–270.

- Franke, W., (2000). The mid-European segment of the Variscides: tectonostratigraphic units, terrane boundaries and plate tectonic evolution, In: Franke, W., Haak, V., Oncken, O., D., T. (Eds.), Orogenic processes: quantification and modelling in the Variscan Belt. Geological Society, London, Special Publications 179, 35–61.

- Franke, W., (1993). The Saxonian granulites: a metamorphic core complex?. Geol.Rundsch. 82, 505–515.

- Franěk, J., Schulmann, K., Lexa, O., Tomek, Č., Edel, J.-B., (2011). Model of syn-convergent extrusion of orogenic lower crust in the core of the Variscan belt: implications for exhumation of high-pressure rocks in large hot orogens. J. Metamorph. Geol. 29, 53–78.

- Friedl, G., Cooke, R., Finger, F., McNaughton, N., Fletcher, A., (2003). U-Pb SHRIMP dating and trace element investigations on multiple zoned zircons from a South-Bohemian granulite. J. Czech Geol. Soc. 48, 51–52.

- Friedl, G., Finger, F., Paquette, J.-L., von Quadt, A., McNaughton, N. J., Fletcher, I. R., (2004). Pre-Variscan geological events in the Austrian part of the Bohemian Massif deduced from U–Pb zircon ages. Int. J. Earth Sci. 93, 802–823.

- Fritz, H., (1995). The Raabs Series: a probable Variscan suture in the SE Bohemian Massif. Jb. Geol. B–A 138, 639–653.

- Gayk, Kleinschrodt, (2000). Hot contacts of garnet peridotites in middle/upper crustal levels: new constraints on the nature of the late Variscan high-T/low-P event in the Moldanubian (Central Vosges/NE France). J. Metamorph. Geol. 18, 293–305.

- Gruau, G., Bernard-Griffiths, J., Lécuyer, C., (1998). The origin of U-shaped rare earth patterns in ophiolite peridotites: assessing the role of secondary alteration and melt/rock reaction. Geochim. Cosmochim. Acta 62, 3545–3560.

- Hacker, B. R., Kelemen, P.B., Behn, M.D., 2007. Continental relamination drives compositional and physical-property changes in the lower crust. Eos Trans. AGU, 88, Fall Meeting Suppl., Abstract V32A-06.

- Hoskin, P., Kinny, P., Wyborn, D., Chappell, B., (2000). Identifying accessory mineral saturation during differentiation in granitoid magmas: an integrated approach. J. Petrol. 41, 1365–1396.

- Höck, V., Montag, O., Leichmann, J., (1997). Ophiolite remnants at the eastern margin of the Bohemian Massif and their bearing on the tectonic evolution. Mineral. Petrol. 60, 267–287.

- Jagoutz, E.; Palme, H.; Baddenhausen, H.; Blum, K.; Cendales, M.; Dreibus, G.; Spettel, B.; Waenke, H.; Lorenz, V., (1979). The abundances of major, minor and trace elements in the earth's mantle as derived from primitive ultramafic nodules, Lun. and Planet. Sci. Conf. Proc. 10 : 2031–2050.

- Jakeš, P., (1997). Melting in high-P region – case of Bohemian granulites. Acta Univ.Carol., Geol. 41, 113–125.

- Janoušek, V., Farrow, C., Erban, V., (2006). Interpretation of whole-rock geochemical data in igneous geochemistry: introducing Geochemical Data Toolkit (GCDkit). J.Petrol. 47, 1255–1259.

- Janoušek, V., Finger, F., Roberts, M., Frýda, J., Pin, C., Dolejš, D., (2004). Deciphering the petrogenesis of deeply buried granites: whole-rock geochemical constraints on the origin of largely undepleted felsic granulites from the Moldanubian Zone of the Bohemian Massif. Earth Env. Sci. T. R. So. Edinb. 95, 141–159.

- Janoušek, V., Holub, F. V., (2007). The causal link between HP–HT metamorphism and ultrapotassic magmatism in collisional orogens: case study from the Moldanubian Zone of the Bohemian Massif. P. Geologist. Assoc. 118, 75–86.

- Janoušek, V., Vrána, S., Erban, V., Vokurka, K., Drábek, M., (2008). Metabasic rocks in the Varied Group of the Moldanubian Zone, southern Bohemia – their petrology, geochemical character and possible petrogenesis. J.Geosci. 53, 31–64.

- Jastrzębski, M., (2009). A Variscan continental collision of the West Sudetes and the Brunovistulian terrane: a contribution from structural and metamorphic record of the Stronie Formation, the Orlica-Śnieżnik Dome, SW Poland. Int. J. Earth Sci. 98, 1901–1923.

- Jensen, L. S., (1976). A new cation plot for classifying subalkalic volcanic rocks. Ont. Div. Mines, Misc Pap. 66, 1–21.

- Kamei, A., Obata, M., Michibayashi, K., Hirajima, T., Svojtka, M., (2010). Two contrasting fabric patterns of olivine observed in garnet and spinel peridotite from a mantle-derived ultramafic mass enclosed in felsic granulite, the Moldanubian Zone, Czech Republic. J. Petrol. 51, 101–123.

- Kotková, J., (2007). High-pressure granulites of the Bohemian Massif: recent advances and open questions. J. Geosci. 52, 45–72.

- Kotková, J., Harley, S., (1999). Formation and evolution of high-pressure leucogranulites: experimental constraints and unresolved issues. Phys. Chem. Earth (A) 24, 299–304.

- Košler, J.; Konopásek, J.; Sláma, J.; Vrána, S.; Racek, M. & Svojtka, M. (2011). U-Pb zircon provenance of Moldanubian metasediments in the Bohemian Massif, CETEG 2011, Trav. Geophys. 40, 84.

- Kröner, A., Hegner, E., Jaeckel, P., (1998). Precambrian basement in the eastern part of the Bohemian massif and its possible origin and correlation. Acta Univ. Carolinae. Geol. 46, 637–649.

- Kröner, A., O'Brien, P. J., Nemchin, A. A., Pidgeon, R. T., (2000a). Zircon ages for high pressure granulites from South Bohemia, Czech Republic, and their connection to Carboniferous high temperature processes. Contrib. Mineral. Petrol. 138, 127–142.

- Kröner, A., Štípská, P., Schulmann, K., Jaeckel, P., (2000b). Chronological constraints on the pre-Variscan evolution of the northeastern margin of the Bohemian Massif, Czech Republic, In: Franke, W., Haak, W., Oncken, O., Tanner, D. (Eds.), Orogenic processes: quantification and modelling in the Variscan belt. Geol. Soc., Lond., Spec. Publ. 179, 175–198.

- Lexa, O., Schulmann, K., Janoušek, V., Štípská, P., Guy, A., Racek, M., (2011). Heat sources and trigger mechanisms of exhumation of HP granulites in Variscan orogenic root. J. Metamorph. Geol. 29, 79–102.

- Ludwig, K. (2001). SQUID 1.02, A user's manual, Berkeley Geochronology Center Special Publication 2.

- Matte, P., Maluski, H., Rajlich, P., Franke, W., (1990). Terrane boundaries in the Bohemian Massif: Result of large-scale Variscan shearing. Tectonophysics 177, 151–170.

- Matějovská, O., (1967). Petrogenesis of the Moldanubian granulites near Náměšť nad Oslavou. Krystalinikum 5, 85–104.

- Matějovská, O., (1975). The Moldanubian gneiss series of south-western Moravia and its relation to granulites.. Věstn. Ústřed. Ústav. Geol. 50, 345–351.

- Matějovská, O., (1987). Fe-rich amphibolites with tholeiitic affinity from the SE margin of the Bohemian Massif. Jb. Geol. B.–A. 130, 493–503.

- McDonough, W. F., Sun, S., (1995). The composition of the Earth. Chem. Geol. 120, 223–253.

- Medaris, L. J., Wang, H., Mísař, Z., Jelínek, E., (1990). Thermobarometry, diffusion modelling and cooling rates of crustal garnet peridotites: Two examples from the Moldanubian zone of the Bohemian Massif. Lithos 25, 189–202.

- Medaris, L., Beard, B., Johnson, C., Valley, J., Spicuzza, M., Jelínek, E., Mísař, Z., (1995). Garnet pyroxenite and eclogite in the Bohemian Massif: geochemical evidence for Variscan recycling of subducted lithosphere. Geol. Rundsch. 84, 489–505.

- Medaris, L. J., Wang, H., Jelínek, E., Mihaljevič, M., Jakeš, P., (2005). Characteristics and origins of diverse Variscan peridotites in the Gföhl Nappe, Bohemian Massif, Czech Republic. Lithos 82, 1–23.

- Medaris, L. G., Beard, B. L., Jelínek, E., (2006). Mantle-derived, UHP garnet pyroxenite and eclogite in the Moldanubian Gföhl Nappe, Bohemian Massif: a geochemical review, new P–T determinations, and tectonic interpretation. Int. Geol. Rev. 48, 765–777.

- Montel, J.-M., (1993). A model for monazite/melt equilibrium and application to the generation of granitic magmas. Chem. Geol. 110, 127–146.

- Nakamura, D., Svojtka, M., Naemura, K., Hirajima, T., (2004). Very high-pressure (>4GPa) eclogite associated with the Moldanubian Zone garnet peridotite (Nové Dvory, Czech Republic). J. Metamorph. Geol. 22, 593–603.

- Němec, D., (1996). Granulite facies metabasites in the Náměšť granulite complex, western Moravia. Věst.Čes.geol.úst. 71, 277–284.

- O'Brien, P. J., Rötzler, J., (2003). High-pressure granulites: formation, recovery of peak conditions and implications for tectonics. J. Metamorph. Geol. 21, 3–20.

- O'Neill, H. S. C., (1981). The transition between spinel lherzolite and garnet lherzolite, and its use as a geobarometer. Contrib. Mineral. Petrol. 77, 185–194.

- Oufi, O., Cannat, M., Horen, H., (2002). Magnetic properties of variably serpentinized abyssal peridotites. J. Geophys. Res. 107, 2095.

- Paulick, H., Bach, W., Godard, M., De Hoog, J., Suhr, G., Harvey, J., (2006). Geochemistry of abyssal peridotites (Mid-Atlantic Ridge, 15°20'N, ODP Leg 209): Implications for fluid/rock interaction in slow spreading environments. Chem. Geol. 234, 179–210.

- Pearce, J. A., (1996). A user's guide to basalt discrimination diagrams. In: Wyman, D. A. (Ed.), Trace element geochemistry of volcanic rocks: applications for massive sulphide exploration, Geol. Assoc. Can., Short Course Notes 12.

- Pin, C., Vielzeuf, D., (1983). Granulites and related rocks in Variscan Median Europe: a dualistic interpretation. Tectonophysics 93, 47–74.

- Racek, M., Štípská, P., Pitra, P., Schulmann, K., Lexa, O., (2006). Metamorphic record of burial and exhumation of orogenic lower and middle crust: a new tectonothermal model for the Drosendorf window (Bohemian Massif, Austria). Mineral. Petrol. 86, 221–251.

- Racek, M., Štípská, P., Powell, R., (2008). Garnet–clinopyroxene intermediate granulites in the St. Leonhard massif of the Bohemian Massif: ultrahigh-temperature metamorphism at high pressure or not?. J. Metamorph. Geol. 26, 253–271.

- René, M. (2008). Geochemistry and petrography of amphibolites from the Tulešice quarry, Geol. výzk. Mor. Slez. 72–74.

- René, M. (2009). Geochemistry and petrography of amphibolites from the Vícenice quarry near Náměšť nad Oslavou, Geol. výzk. Mor. Slez. 114–117.

- Roberts, M., Finger, F., (1997). Do U-Pb zircon ages from granulites reflect peak metamorphic conditions?. Geology 25, 319–322.

- Rudnick, R., McLennan, S., Taylor, S., (1985). Large ion lithophile elements in rocks from high-pressure granulite facies terrains. Geochim. Cosmochim. Acta 49, 1645–1655.

- Schulmann, K., Kroner, A., Hegner, E., Wendt, I., Konopásek, J., Lexa, O., Štípská, P., (2005). Chronological constraints on the pre-orogenic history, burial and exhumation of deep-seated rocks along the eastern margin of the Variscan Orogen, Bohemian Massif, Czech Republic. Am. J. Sci. 305, 407–448.

- Schulmann, K., Ledru, P., Autran, A., Melka, R., Lardeaux, J., Urban, M., Lobkowicz, M., (1991). Evolution of nappes in the eastern margin of the Bohemian Massif: a kinematic interpretation, Geol. Rundsch. 80 : 73–92.

- Soejono, I., Žáčková, E., Janoušek, V., Machek, M., Košler, J., (2010). Vestige of an Early Cambrian incipient oceanic crust incorporated in the Variscan orogen: Letovice Complex, Bohemian Massif. J. Geol. Soc. Lond. 167, 1113–1130.

- Suess, F. E., (1912). Die moravischen Fenster und ihre Beziehung zum Grundgebirge des Hohen Gesenke. Denkschrichte des Koeniglischen Akademie der Wissenscahft, Mathematik, Naturwissenschaft 83, 541–631.

- Sun, S., McDonough, W., (1989). Chemical and isotopic systematics of oceanic basalts: implications for mantle composition and processes, In: Saunders, A. D., Norry, M. (Eds.), Magmatism in ocean basins. Geol. Soc., Lond., Spec. Publ. 42, 313–345.

- Šichtařová, I., (1981). Moldanubian amphibolites in the area SE of Náměšť nad Oslavou. Věstn. Ústřed. Ústav. Geol. 56, 203–214.

- Štípská, P., Powell, R., (2005a). Constraining the P–T path of a MORB-type eclogite using pseudosections, garnet zoning and garnet-clinopyroxene thermometry: an example from the Bohemian Massif. J. Metamorph. Geol. 23, 725–743.

- Štípská, P., Powell, R., (2005b). Does ternary feldspar constrain the metamorphic conditions of high-grade meta-igneous rocks? Evidence from orthopyroxene granulites, Bohemian Massif. J. Metamorph. Geol. 23, 627–647.

- Štípská, P., Schulmann, K., Powell, R., (2008). Contrasting metamorphic histories of lenses of high-pressure rocks and host migmatites with a flat orogenic fabric (Bohemian Massif, Czech Republic): a result of tectonic mixing within horizontal crustal flow?. J. Metamorph. Geol. 26, 623–646.

- Tajčmanová, L., Konopásek, J., Schulmann, K., (2006). Thermal evolution of the orogenic lower crust during exhumation within a thickened Moldanubian root of the Variscan belt of Central Europe. J. Metamorph. Geol. 24, 119.

- Tajčmanová, L., Soejono, I., Konopásek, J., Košler, J., Klotzli, U., (2010). Structural position of high-pressure felsic to intermediate granulites from NE Moldanubian domain (Bohemian Massif). J. Geol. Soc. Lond. 167, 329–345.

- Taylor, S. R., McLennan, S. M., (1995). The geochemical evolution of the continental crust. Rev. Geophys. 33, 241–265.

- Taylor, W. R., (1998). An experimental test of some geothermometer and geobarometer formulations for upper mantle peridotites with application to the thermobarometry of fertile lherzolite and garnet websterite. Neu. Jb. Mineral., Abh. 172, 381–408.

- Tera, F., Wasserburg, G., (1972). U-Th-Pb systematics in three Apollo 14 basalts and the problem of initial Pb in lunar rocks. Earth Planet. Sci. Lett. 14, 281–304.

- Tollmann, A., (1982). Grossräumiger variszischer Deckenbau im Moldanubikum und neue Gedanken zum Variszikum Europas. Geotekton. Forsch. 64, 1–91.
- Urban, M., (1992). Kinematics of the Variscan thrusting in the Eastern Moldanubicum (Bohemian Massif, Czechoslovakia): evidence from the Náměšť granulite massif. Tectonophysics 201, 371–391.
- Villaseca, C., Barbero, L., Herreros, V., (1998). A re-examination of the typology of peraluminous granite types in intracontinental orogenic belts. Trans. Roy. Soc. Edinb. Earth Sci. 89, 113–119.
- Watson, E. B., Harrison, T. M., (1983). Zircon saturation revisited: temperature and composition effects in a variety of crustal magma types. Earth Planet. Sci. Lett. 64, 295–304.
- Webb, S. A. C., Wood, B. J., (1986). Spinel–pyroxene–garnet relationships and their dependence on Cr/Al ratio. Contrib. Mineral. Petrol. 92, 471–480.
- Winchester, J., Floyd, P., (1977). Geochemical discrimination of different magma series and their differentiation products using immobile elements. Chem. Geol. 20, 325–343.
- Wood, D. A., (1980). The application of a ThHfTa diagram to problems of tectonomagmatic classification and to establishing the nature of crustal contamination of basaltic lavas of the British Tertiary Volcanic Province. Earth Planet. Sci. Lett. 50, 11–30.

Supplementary material

Chemical compositions of the main mineral constituents of the Mohelno peridotite body.

Tab. Appendix 1. Selected analyses from Mohelno peridotite (wt %) (Kamei et al., 2010)

Mineral	description	SiO_2	TiO_2	Al_2O_3	Cr_2O_3	FeOt	MnO	MgO	CaO	Na_2O	NiO	Sum
Ol_1	CS	41.19	0	0	0	9.87	0.12	48.31	0	0	0.47	99.96
Ol_2	FS	41.34	0	0	0	9.16	0.14	50.07	0	0	0.45	100.71
Ol_3	CG	40.51	0	0	0	9.5	0.15	48.16	0	0	0.48	98.32
Ol_4	CG(inclusion)	40.92	0	0	0	8.97	0.12	48.53	0	0	0.46	98.54
Ol_5	FG	41.12	0	0	0	8.97	0.12	49.9	0	0	0.41	100.11
Opx_1	CS pc core	53.67	0.15	5.78	0.58	6.19	0.19	30.97	1.14	0	0	98.67
Opx_2	CS pc rim	54.18	0.09	3.95	0.33	6.84	0.2	31.7	0.32	0	0	97.61
Opx_3	CS matrix neoblast	55.6	0.12	3.34	0.31	6.91	0.15	32.67	0.47	0	0	99.57
Opx_4	FS pc core	54.09	0.15	5.78	0.57	5.89	0.14	31.57	1.11	0	0	99.3
Opx_5	FS pc rim	54.04	0.17	4.65	0.4	6.3	0.15	32.7	0.65	0	0	99.06
Opx_6	FS matrix neoblast	55.21	0.11	3.28	0.29	6.61	0.2	33.64	0.46	0	0	99.8
Opx_7	CG pc core	53.64	0.13	5.26	0.47	6.3	0.13	31.77	1.13	0	0	98.83
Opx_8	CG pc rim	55.63	0.17	4.46	0.41	6.74	0.19	32.42	0.54	0	0	100.56
Opx_9	CG inc core	54.45	0.13	4.57	0.49	6.09	0.14	31.82	0.97	0	0	98.66
Opx_{10}	CG inc rim	54.25	0.13	5.94	0.65	5.3	0.12	32.24	0.7	0	0	99.33
Opx_{11}	CG matrix neoblast	55.4	0.13	3.29	0.32	6.63	0.13	32.72	0.45	0	0	99.07
Opx_{12}	CG AGG	54.25	0.11	4.98	0.28	6.81	0.15	31.91	0.49	0	0	98.98
Opx_{13}	FG pc core	54.57	0.16	4.91	0.57	5.91	0.12	32.76	0.66	0	0	99.66
Opx_{14}	FG pc rim	55.59	0.14	3.99	0.34	5.99	0.13	33.9	0.53	0	0	100.61
Opx_{15}	FG inc core	53.29	0.21	5.82	0.71	6.05	0.11	31.52	1.01	0	0	98.72
Opx_{16}	FG inc rim	53.22	0.22	6.7	0.85	5.22	0.09	32.12	0.71	0	0	99.13
Opx_{17}	FG matrix neoblast	54.79	0.16	3.08	0.27	6.42	0.14	33.56	0.55	0	0	98.97
Opx_{18}	FG AGG	54.56	0.25	4.41	0.25	6.04	0.21	32.9	0.59	0	0	99.21
Opx_{19}	FG kely inner	53.83	0.18	5.55	0.34	6.17	0.14	32.56	0.54	0	0	99.31
Opx_{20}	FG kely outer	52.54	0.14	6.96	0.5	6.77	0.15	32.62	0.42	0	0	100.1

Tab. Appendix 1. Selected analyses from Mohelno peridotite (wt %) (Kamei et al., 2010)

Mineral	description	SiO_2	TiO_2	Al_2O_3	Cr_2O_3	FeOt	MnO	MgO	CaO	Na_2O	NiO	Sum
Cpx_1	CS pc core	51.95	0.34	6.3	0.8	2.68	0.1	15.3	20.84	1.24	0	99.55
Cpx_2	CS pc rim	52.66	0.29	4.75	0.58	2.54	0.12	15.46	21.84	1.01	0	99.25
Cpx_3	CS matrix neoblast	52.02	0.33	5.42	0.63	2.77	0.12	16.14	21.36	1.16	0	99.95
Cpx_4	FS pc core	52.29	0.39	6.83	0.87	2.82	0.08	15.33	19.49	1.76	0	99.86
Cpx_5	FS pc rim	53.17	0.27	5.41	0.64	2.13	0.05	14.95	21.72	1.44	0	99.78
Cpx_6	FS matrix neoblast	52.71	0.43	5.72	0.85	2.31	0.06	15.18	21.44	1.5	0	100.2
Cpx_7	CG pc core	50.74	0.5	6.62	1.12	3.16	0.05	15.58	18.71	1.55	0	98.03
Cpx_8	CG pc rim	51.87	0.54	6.08	0.88	2.3	0.08	16.11	21.16	1.26	0	100.28
Cpx_9	CG inc core	52.56	0.52	6.66	1.06	2.4	0.1	14.01	21.47	1.7	0	100.48
Cpx10	CG inc rim	52.66	0.59	7.07	1.08	2.17	0.05	14.53	20.68	1.72	0	100.55
Cpx_{l1}	CG matrix neoblast	52.99	0.41	5.46	0.7	2.09	0	15.49	21.43	1.33	0	99.9
Cpx_{l2}	CG AGG	52.13	0.5	6.98	0.54	2.48	0.08	14.6	21.13	1.43	0	99.87
Cpx_{l3}	FG pc core	51.57	0.66	7.24	0.87	2.75	0.11	15.11	18.98	1.71	0	99
Cpx_{l4}	FG pc rim	51.73	0.56	6.42	0.69	2.83	0.09	15.1	19.34	1.72	0	98.48
Cpx_{l5}	FG inc core	50.9	0.68	7.53	1.16	2.93	0.09	14.3	18.98	1.89	0	98.46
Cpx_{16}	FG inc rim	50.79	0.79	8.43	1.19	2.6	0.08	14.42	18.51	1.97	0	98.78
Cpx_{17}	FG matrix neoblast	52.13	0.49	6.32	0.82	2.95	0.08	15.59	19.4	1.71	0	99.49
Cpx_{18}	FG AGG	52	0.61	7.11	0.43	2.73	0.15	14.89	19.66	1.78	0	99.36
Cpx_{19}	FG kely outer	51.77	0.66	8.27	0.49	2.1	0.1	13.53	20.02	2.24	0	99.18
Grt_1	CG core	42.63	0.19	22.57	1.69	7.38	0.29	20.52	5.16	0	0	100.43
$Grtx_2$	CG rim-opx	42.25	0.14	22.29	1.56	9.04	0.43	19.59	5.25	0	0	100.55
Grt_3	CG rim-kely	42.78	0.15	22.46	1.4	10.45	0.63	18.82	5.02	0	0	101.71
Grt_4	FG core	42.32	0.23	22.45	1.61	6.93	0.34	20.94	4.84	0	0	99.66
Gr_5	FG rim-opx	42.15	0.16	22.79	1.33	7.44	0.32	20.41	5	0	0	99.6
Grt_6	FG rim-kely	42	0.24	22.13	1.55	10.3	0.72	18.41	4.99	0	0	100.34
Sp_1	CS matrix	0	0.12	54.92	11.69	12.92	0.12	19.55	0	0	0.45	99.77
Sp_2	FS matrix	0	0.1	55.29	12.65	12.28	0.18	19.29	0	0	0.33	100.12
Sp_3	CG incl	0	0.01	51.67	18.43	9.76	0.22	19.57	0	0	0.29	99.95
Sp_4	CG matrix	0	0.05	56.99	9.93	11.47	0.11	19.62	0	0	0.42	98.59
Sp_5	CG AGG	0	0.04	60.61	6.23	10.25	0.16	20.91	0	0	0.45	98.65
Sp_6	FG matrix	0	0.08	54.49	12.83	10.96	0.11	19.55	0	0	0.37	98.39
Sp_7	FG AGG	0	0.13	57.48	9.6	10.85	0.1	19.69	0	0	0.39	98.24
Sp_8	FG kely	0	0.09	63.4	4.89	9.06	0.08	21.28	0	0	0.4	99.2

Tab. Appendix 2 Selected analyses from Mohelno peridotite (wt %) (Medaris et al., 2005)

Mineral	SiO_2	TiO_2	Al_2O_3	Cr_2O_3	FeO^T	MnO	MgO	CaO	Na_2O	NiO	Sum
Ol_1	40.7	0	0	0	9.94	0.12	49.6	0	0	0.41	100.77
Ol_2	40.8	0	0	0	10.1	0.14	48.5	0	0	0.38	99.92
Ol_3	41.2	0	0	0	9.73	0.13	48.9	0	0	0.42	100.38
Ol_4	40.6	0	0	0	9.85	0.26	48.8	0	0	0.45	99.96
Opx_1	54.4	0	4.32	0.48	6.62	0.14	33.7	0.6	0.02	0	100.28
Opx_2	54.1	0.13	4.56	0.38	6.88	0.14	32.9	0.65	0	0	99.74
Opx_3	54.9	0	4.04	0.54	6.18	0.11	33.1	1.02	0.13	0	100.02
Opx_4	53.8	0	5.63	0.59	6.58	0.07	33	0.59	0	0	100.26
Cpx_1	52.6	0.62	6.53	0.93	3.47	0.11	15.8	17.2	1.74	0	99.00
Cpx_2	52.9	0.52	6.88	0.71	3.53	0.11	15.6	17.5	1.71	0	99.46
Cpx_3	52.8	0	6.04	1.14	2.44	0.08	14.9	20.2	2.19	0	99.79
Cpx_4	51.8	0	6.56	0.96	2.64	0.02	15.4	20.7	1.2	0	99.28
Grt_1	41.1	0	22.1	1.68	7.51	0.28	21.9	4.77	0	0	99.34
Grt_2	41.4	0	22.5	1.27	7.69	0.28	21.8	4.68	0	0	99.62
Grt_3	42	0	22.3	1.52	7.84	0.34	21.3	4.7	0	0	100.00
Sp	0	0.07	51.7	13.7	13.6	0.04	18.3	0	0	0.29	97.70

Sample descriptions

WKGCH1

(N 49°6'12.68" E 16°11'11.71", WK86, right bank of the Jihlava river, against the meadow above the Mohelenský mill)

Sample WKGCH1 represents dark enigmatic rock from outcrop close to the contact between peridotite and surrounding granulite. Large plagioclase porphyroclasts (1-3 cm) are formed by fine plagioclase grains, sometimes preserving core and mantle microstructure. These plagioclase porphyroclasts are within the fine-grained amphibolite and biotite matrix. Porphyroclasts form weak magmatic/deformational fabric parallel to the fabric in the neighbour granulite. Also matrix minerals (amphibolite and biotite) show signs of grain size reduction via dynamic recrystallization.

WKGCH2

(N 49°5'55.5" E 16°11'38.16", WK199, right bank of the Jihlava river, 30m upstream from bridge over river on the Mohelno-Dukovany road 392)

Felsic granulite with fine-grained (<0.2 mm) mylonitic quartz – K-feldspar - plagioclase matrix, small porphyroclasts of garnet (<1 mm) without inclusions and biotite. Evenly distributed biotite flakes are associated with large quartz disc grains (length up to 2 mm) and together are forming well defined foliation. In discrimination according Kusbach et al. (2011) this microstructure corresponds to S2-S3 transition.

WKGCH3

(N 49°6'2.33" E 16°11'39.46", next to the Mohelno-Dukovany road 392, close to the car accident tombstone)

The retrogressed granulite at this locality is dark and very massive without strong oriented fabric, sometimes alternating with lighter layer rich in plagioclase. The basis of the microstructure is intermixed fine-grained mylonitic intermixed

quartzo – feldspathic matrix (<0.2 mm). often the fine-grained microstructure is annealed to microstructure with regular triple points and large lobate neoblasts of quartz and plagioclase (> 1 mm). Large garnet crystals (~ 1 mm) with irregular shapes rich in inclusion of quartz and plagioclase are distributed evenly in the rock. Large biotite crystals occur in close vicinity of garnet and small crystals are widely distributed along matrix minerals' triple point throughout whole rock.

WKGCH4

(N 49°5'57.09" E 16°11'46.98", WK25, outcrop with cabin 08, left bank of the Jihlava river, downstream 50m from the bridge on the Mohelno-Dukovany road 392)

Sample is characteristic example of the Mohelno garnet peridotite. Peridotite is highly serpentinized, with mylonitic olivine – orthopyroxene matrix (fine-grained < 100 μm) with rare presence of clinopyroxene. Small orthopyroxene porphyroclast (~ 1 mm) and large garnet porphyroclasts (> 5 mm) with spinel inclusions are aligned within mylonitic fabric. Macroscopic banded appearance of the rock is caused by distribution of serpentine minerals with different proportions of opaque minerals and submicroscopic pigment of iron oxides dispersed in serpentine minerals. Talc and chlorite are present as accessories.

WKGCH5

(N 49°5'36.54" E 16°11'58.79", WK142, in the gorge with weak stream, next to the Mohelno-Dukovany road 392)

Black massive garnet peridotite from this locality has strong ultra-mylonitic fabric with serpentinized olivine – orthopyroxene matrix. Large garnet porphyroclast (>1 cm) with olivine and pyroxene inclusions surrounded by coarse-grained microstructure are rarely preserved. Visible shaded banding is caused by different colouring of the serpentine minerals (due to pigment of iron oxides) and thin bands of recrystallized orthopyroxene porphyroclasts.

WKGCH6

(N 49°6'21.81" E 16°11'13.26", WK3, large outcrop on the left bank of the Jihlava river next to river weir for the Mohelenský mill)

Sample WKGCH6 is highly serpentinized greenish spinel peridotite. Spinel porphyroclast (>1 mm) and orthopyroxene porphyroclasts (~ 2 mm) are aligned in fine-grained mylonitic olivine – orthopyroxene matrix with rare clinopyroxene. At this locality orthopyroxene bands wide several centimeters are very common and sample was prepared to avoid them.

WKGCH7

(N 49°6'19.41" E 16°11'20.64", WK56, in the road cutting towards Mohelno, in the serpentine above Mohelenský mill)

Similar characteristics as other samples of spinel peridotite. Massive greenish serpentinized spinel peridotite with abundant large orthopyroxene porphyroclasts (~ 3mm). Spinel is homogenously distributed in the mylonitic matrix. Systems of polygonal fractures are perpendicularly cutting orthopyroxene bands and are filled with serpentine minerals.

WKGCH8

(N 49°5'56.71" E 16°12'14.43", WK7, sample from the vertical fold in the outcrop in the slope above the campsite)

Granulite from the sampling site WKGH8 is characteristic for the retrogression from the S2 to the S3 fabric. Light felsic granulite is associated with darker bands rich in biotite. Garnet porphyroclast with common crystallographically oriented rutile rods and also quartz and feldspars inclusions are surrounded with the fine grained quartzo-feldspathic groundmass. Biotite is growing around garnet on its expense and also small biotite flakes are evenly distributed along the foliation defined mostly by alignment of the elongated quartz grains.

WKGCH9

(N 49°5'54.6" E 16°10'38.57", WK126, under the small waterfall, on crossing of stream and red tourist mark)

Non-deformed massive light igneous rock composed of feldspar, quartz, amphibole, biotite and muscovite and with abundant accessory opaque minerals. Rock is without obvious magmatic or deformational fabric, with grain boundaries forming regular triple points and with grain size from 0.5 mm up to 3 mm for all major minerals.

WKGCH10

(N 49°5'58.87" E 16°10'39.46", WK127, at the bottom of the gorge, close to stream entry in the dam)

Next sample of spinel peridotite is slightly banded due to the coloured serpentine minerals. Fine-grained olivine-orthopyroxene groundmass is intensively serpentinized with abundant occurrence of the opaque minerals. Large orthopyroxene porphyroclasts with olivine inclusions and randomly oriented fractures annealed with serpentine are preserved.

WKGCH11

(N 49°6'6.61" E 16°10'51.85", WK171, outcrop next to the southern end of the Mohelno barrage, disused small quarry)

Ultimate example of the so-called "weisstein". Granulite composed almost exclusively from the quartz and feldspars, with minimum of garnet and biotite. Needles of biotit are not preferentially oriented, weak alignment can be observed for small garnet remnants. Grain boundaries are lobate both for quartz and feldspars. Felsic matrix is fine-grained with occasionally larger elongated quartz grains. Euhedral crystals of accessory opaque mineral (magnetite?) are common.

WKGCH12

(N 49°5'50.34" E 16°9'10.48", WK12, large outcrop Rabštejn above the nuclear power plant water supply station)

Sample of coarse-grained amphibolite with garnets up to several centimetres in diameter. For the geochemical sampling was chosen more homogenous part of the outcrop. Large garnet porphyroclasts with amphibole and quartz inclusions are recrystallized into amphibole-feldspar symplectite with abundant accessory opaque minerals. Both feldspars and amphibolite from the fine-grained structures around garnet are segregating into monomineralic bands parallel with garnet structures elongation.

WKGCH13

(N 49°6'0.21" E 16°10'41.08", WK106, at the bottom of the gorge, between road and dam bank)

Felsic granulite with typical layering of several millimetres thin dark bands rich in biotite with layers composed predominantly from quartz and feldspars. Garnet porphyroclasts with quartz and feldspar inclusions are evenly distributed throughout the rock. Both quartz and feldspars are forming intermixed mylonitic matrix, while only quartz forms long recrystallized disc-shaped porphyroclast aligned into foliation. Kyanite is replaced by sillimanite in the foliation defined by quartz discs and biotite.

WKGCH14

(N 49°7'21.82" E 16°7'17.13", outcrop in the road cutting on the southern side of the Dalešice barrage)

The amphibolite at this locality has (ultra)mylonitic microstructure and is associated with the eastern margin of the Náměšť Granulite Massif. All minerals (amphibole, feldspar, garnet, pyroxene and quartz, together with abundant opaque mineral are intermixed in mylonitic matrix. Occasionally small garnet porphyroclasts (> 1 mm) can be found. Appearance of the rock is massive with well defined foliation, but the separation of feldspar to monomineralic bands is rare and only on small scale (thickness of feldspar bands < 1 mm).

WKGCH15

(N 49°6'9.18" E 16°9'29.39", WK179, outcrop in the forest road cutting on the left dam left bank) Light felsic granulite sample with typical thin dark bands rich in biotite with almost migmatitic appearance as hand size specimen. Peak granulite mineral assemblage quartz + ternaty feldspar + garnet and kyanite is slightly retrogressed. Garnet porphyroclasts with large inclusion of quartz and feldspar in quartzo-feldspathic matrix are consumed by biotite. Foliation is defined by elongation of garnet porphyroclast, alignment of kyanite needles and biotite flakes growing along parallel grain boundaries.

WKGCH16

(N 49°6'3.27" E 16°9'46.49", WK177, outcrop on the left dam bank, small cliff in the middle of the slope)

Extra ultramylonitic felsic granulite with intermixed quartz and feldspars matrix with average grain size ~ 50 micrometers in diameter. Garnet porphyroclasts (~ 0.5 mm) with quartz and feldspar inclusions are slightly retrogressed into biotite rims. Foliation fabric is marked by biotite flakes evenly distributed in the matrix and also oriented non-retrogressed kyanite grains.

WKGCH17

(N 49°6'10.91" E 16°9'13.87", WK101, outcrop on the left dam bank, large cliff in the slope)

Darker variety of the felsic granulite with granulite facie mineral assemblage quartz + feldspars + garnet + kyanite + biotite. Intensive foliation fabric is caused primarily by alignment of the garnet porphyroclast, which are retrogressively consumed by biotite. Often garnet forms atollic structures with enclosed grains of quartz and plagioclase. Quartzo-feldspathic mylonitic groundmass is annealing into larger elongated crystals, from which lobate quartz grains are forming monomineralic elongated aggregates.

WKGCH18

(N 49°6'11.66" E 16°9'13.87", WK195, outcrop on the right side of the Jihlava river, opposite to the Mohelenský mill, close to the WKGCH1)

Strangely looking migmatitic rock with "magmatic" microstructure. Rock displays only weak foliated fabric mainly because of abundant biotite and amphibolite. Quartz and plagioclase have regular grains with common triple points in which biotite, amphibolite or opaque mineral crystallize.

WKGCH19

(N 49°5'41.75" E 16°9'16.16", WK11, outcrop on the right side of the dam, close to the forest road with the green tourist mark)

Coarse-grained amphibolite with large garnet porphyroclasts (> 1cm) surrounded with fine-grained rims of plagioclase and opaque minerals. Garnet is rich in inclusions of clinopyroxene, rutile and quartz. Foliated fabric is caused mainly by felsic minerals, which starts forming monomineralic bands, yet not ideally parallel with foliation plane.

Ductile deformation and rheology of sub-continental mantle in a hot collisional orogeny: example from the Bohemian Massif

Vladimír KUSBACH[*,1,2], Stanislav ULRICH[3], Karel SCHULMANN[2]

Affiliations

[1)] Institute of Petrology and Structural Geology, Charles University in Prague, Albertov 6, 12843 Praha 2, Czech Republic

[2)] Institut de Physique du Globe de Strasbourg, IPGS – UMR 7516, CNRS et Universite de Strasbourg (EOST), 1 Rue Blessig, 67084 Strasbourg, France

[3)] Geophysical Institute v.v.i., Academy of Sciences of the Czech Republic, Boční II/1401, 141 31, Praha 4, Czech Republic

[*]Corresponding author.

(published online in Journal of Geodynamics)

Abstract

Fabric patterns of strongly serpentinized peridotite have been determined using eigenvector analysis and eigenvalue classification of lattice preferred orientation of olivine and orthopyroxene. This approach has been applied to a rootless fold-shaped body of mylonitized spinel to garnet peridotite surrounded by fine-grained and partially retrogressed Ky - Kfs felsic granulite. The EBSD data show either axial [010] or [100](0kl) pattern, both characteristic for 'dry' slip systems. The former pattern occurs predominantly along the inner margin and southern limb while the latter is mainly developed in the hinge of the fold shaped body. Foliations and lineations deciphered from the LPO data suggest that the [100](0kl) pattern reflects constrictional deformation (prolate strain ellipsoid) in the hinge of peridotite fold while the axial [010] pattern reflects pure flattening (oblate strain ellipsoid) inherited from period of emplacement of the peridotite sheet in the crust. Similarity in finite strain pattern of peridotite and surrounding granulites indicates their common thermal and mechanical evolution during folding. The petrology and structural data result in a model of burial of peridotite below thickened crustal root, its exhumation and folding. The burial stage is associated with prograde metamorphism resulting in coarse-grained microstructure and development of spinel and garnet zones. The emplacement of peridotite into lower crustal granulites occurred along a shear zone associated with grain size reduction in both lithologies and rapid cooling of mylonitized peridotite to the ambient temperatures of lower crust. Further exhumation to mid-crustal levels occurred within the vertical granulite channel. Final fold shape of peridotite developed during subsequent indentation of weak vertically anisotropic crust by adjacent continental promontory. The degree of mechanical coupling between folded peridotite and granulite in mid-crustal levels is estimated using comparison of studied microstructures with experimental data.

Research Highlights

> Structural and microstructural study of granulite and embedded peridotite. > Eigenvector analysis and eigenvalue classification of lattice preferred orientation. > Coupled deformation between granulite and peridotite. > Peridotite embedded within the felsic lower crust is viscously deformable.

Keywords

Olivine lattice preferred orientation, peridotite mylonite, strain, crust-mantle coupling, Variscan orogen

Introduction

Continental lithosphere consists of different layers of contrasting rheology: brittle upper continental crust, weak and ductile lower continental crust and stronger sub-crustal mantle, with rheology evolving with temperature, pressure, depth and composition (Brace and Kohlstedt, 1980; Ranalli and Murphy, 1987). Rheological models of the lithosphere are based on experimental rheological laws describing brittle and ductile behavior of rocks. Relative strength of the different layers is evolving through time due to changes in tectonic style and thermal evolution of the lithosphere (Thompson et al., 2001). Lithosphere rheology models can be validated using depth of earthquakes hypocentres, which should be in accordance with the thermal structure of the lithosphere and assumed the thickness and depth position of lithological layers. Earthquakes hypocentres located in the upper crust and in the uppermost part of lithospheric mantle indicate that these layers can be relatively strong and brittle (Molnar and Chen, 1983; Liang et al., 2008). Nevertheless, earthquakes located in the uppermost mantle, where Byerlee's law cannot be extrapolated, are rare and their source mechanism is still debated (Monsalve et al., 2009). These observations are commonly interpreted using a "jelly sandwich" model in which a weak lower crust is sandwiched between strong elastic-brittle upper crust and an elastic-ductile upper mantle (Burov and Watts, 2006). Other seismological studies show an absence of earthquakes in the upper mantle underneath thick orogens, which is interpreted using so called "crème brûlée" model made of strong seismogenic crust and a weak and "wet" upper mantle (Jackson, 2002). Aseismic behavior of upper mantle is also supported by presence of ductile shear zones recorded in spinel peridotite massifs and xenolites (Drury et al., 1991; Tommasi et al., 2000) deformed at depth greater than 30–40 km (Dijkstra et al., 2004).

Deformation of the lithosphere and mechanical coupling of crust and mantle are not only dependent on rheology but also on the kinematic regime. For convergent plate boundaries there are two general models of mechanical behavior of the crust and the mantle based on structural observations and mantle anisotropy geophysical studies: (1) vertical deformation coupling between crust and mantle expressed by steep deformation fabrics in the crust and underlying mantle associated with transcurrent/tranpressive deformations (Vauchez et al., 1998), (2) clutch tectonic model implying transfer of

ductile deformation from the mantle to the crust along a weak lower crustal zone (Tikoff et al., 2002, 2004). The latter model is supported by a concept of weak lower crust flowing over strong and mechanically passive upper mantle preserving "frozen" fabric from the period of the mantle lithosphere formation (Babuška and Plomerová, 2006; Babuška et al., 2008). The degree of coupling between the crustal and mantle parts of the lithosphere is also a function of the balance among surface forces related to plate tectonics, the gravity force related to lateral variations in lithospheric thickness, and the buoyancy forces related to density variations (Artyushkov, 1973; Ramberg, 1981; Molnar et al., 1993; Chemenda et al., 1995; Ellis, 1996; Molnar and Lyon-Caen, 1988).

There exist only rare structural and microstructural data from peridotites allowing direct assessment of rheological behavior of sub-continental mantle (Precigout et al., 2007; Roux et al., 2008; Soustelle et al., 2009) recorded during continental rifting and crustal thinning. However, there is no information about rheological behavior of subcontinental mantle during continental collision and crustal thickening. The Bohemian Massif represents such an internal orogenic zone of double thickened Variscan crust which contains the high grade lower crustal Gföhl Unit marked by the presence of garnet and spinel peridotite bodies of different origin (Medaris et al., 1990) enclosed within large complexes of high pressure granulites (Carswell and O'Brien, 1993). Large exposures of orogenic lower crust and upper mantle allow studying mechanical interactions between these two key lithologies at elevated temperatures and pressures corresponding to actual crustal thickness and temperature of the Tibetean or Andean orogens (Guy et al., 2011; Lexa et al., 2011). However, up to the present time, there are only few studies concerning internal deformation fabric of some of large peridotite bodies in the Bohemian Massif (Machek et al., 2009; Medaris et al., 2009; Kamei et al., 2010) compared to a number of structural and microstructural studies of HP granulites and to studies of similar lower crustal complexes (e.g. Caledonian Western Gneiss Region in Norway; Brueckner, 1998; Brueckner et al., 2002). Lack of such studies in peridotites is due to high degree of serpentinisation of these rocks allowing only petrological and geochemical analyses of few well preserved mineral assemblages and because such peridotite–granulite association are relatively rare at outcrop level (Medaris et al., 1990, 2005; Schmädicke and Evans, 1997; Schmädicke et al., 2010).

This work attempts to combine structural and microfabric data from a relatively well preserved peridotite body and surrounding HP granulites with existing petrological and geochronological constraints to propose a consistent model of rheological behavior of crust and mantle in a deep orogenic root. Apart from the conceptual mechanistic model these dataset results in the semi-quantitative assessment

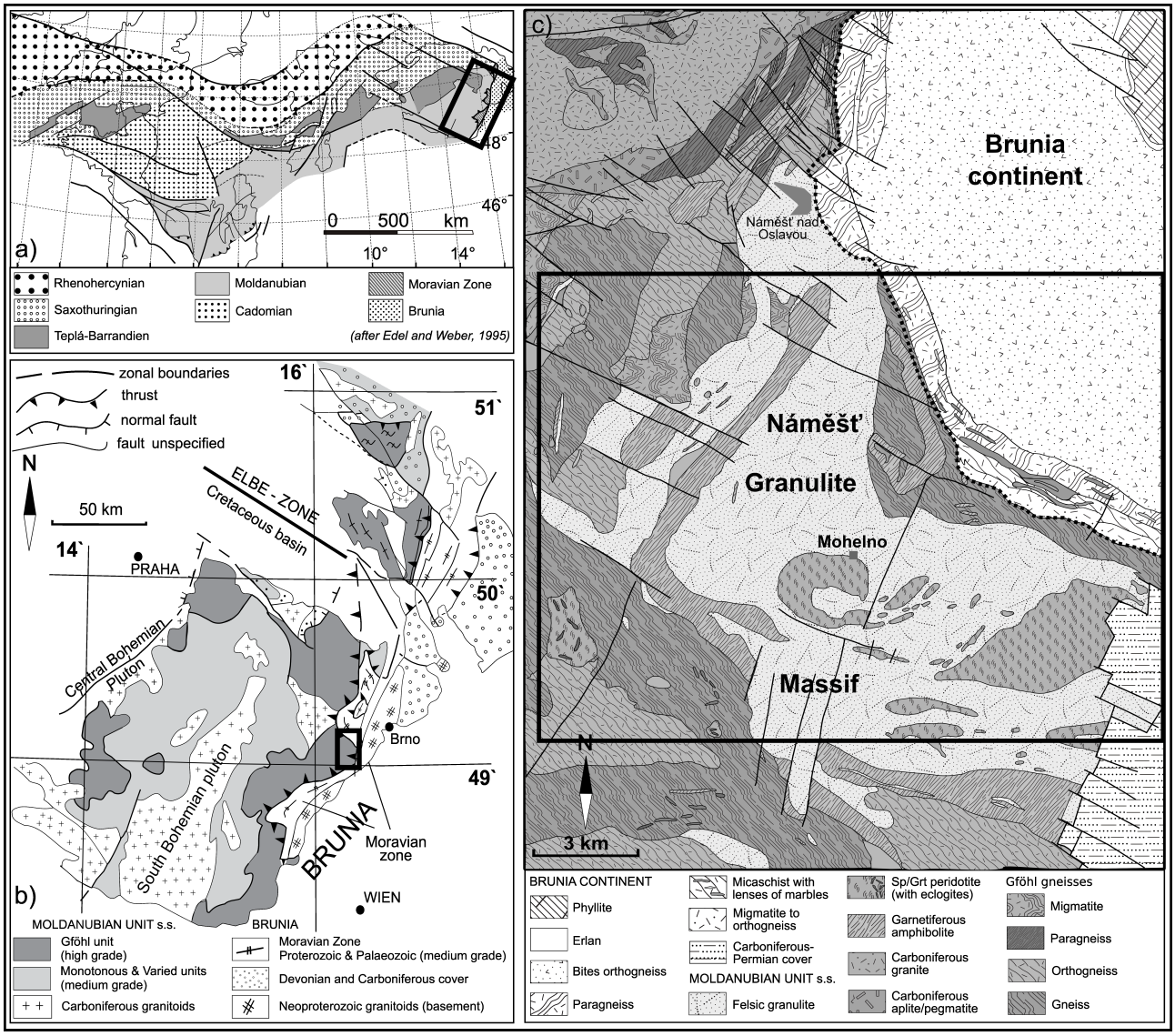

Figure 1. Geological setting: (a) position of the Bohemian Massif in the framework of the European Variscides (modified after Franke, 2000) and (b) simplified tectonic map of the eastern margin of the Bohemian Massif; (c) a simplified geological map of the study area according to the geological map 1:50,000, sheet of the Czech Geological Survey.

of the degree of rheological and mechanical coupling between crust and mantle during orogeny.

Geological setting

The present day structure of the Bohemian Massif originated by the southeastward subduction of the Saxothuringian Ordovician Ocean underneath the Teplá–Barrandian domain continental lithosphere during Upper Devonian (Franke, 2000). Closure of the Saxothuringian Ocean followed by underthrusting of the Saxothuringian lithosphere beneath the Teplá–Barrandian domain led to development of a

double-thickened orogenic root represented by the upper crustal Teplá–Barrandian domain and middle/lower crustal Moldanubian domain (Schulmann et al., 2009) (Fig. 1a). Thickening of the orogenic root domain was followed during Lower Carboniferous by the continental promontory of the Brunia continent indentation in the southwestward direction, triggering extrusion and exhumation of the orogenic lower crust into the mid-crustal depths (Schulmann et al., 2005). The studied area is located in the Gföhl Unit of Moldanubian domain representing outcrops of this orogenic lower crust at the eastern margin of the Bohemian massif (Fig. 1b).

The Gföhl Unit consists of partially molten orthogneisses, amphibolites and migmatite gneisses including bodies of granulites, eclogites and peridotites (Tollmann, 1982). Felsic granulites of granite/rhyolite affinity (Fiala et al., 1987) are composed of quartz, garnet, kyanite, alkaline feldspar, plagioclase and rutile (Carswell and O'Brien, 1993). Typical felsic granulites are interpreted as metamorphosed equivalents of Lower Palaeozoic, probably high-level granites underthrust and buried to form the deepest part of the continental root during the Variscan collision (Janoušek et al., 2004; Janoušek and Holub, 2007; Lexa et al., 2011). Petrological studies of felsic and pyroxene-bearing intermediate granulites show peak conditions of 800–1000 °C and 1.6–2 GPa (Cooke, 2000; Cooke and O'Brien, 2001; Štípská et al., 2004; Tajčmanová et al., 2006; Racek et al., 2006, 2008;) and amphibolites facies retrogression at 750–700 °C and 0.4–0.9 GPa. The process of vertical movement of high-grade granulite complexes to mid crustal levels has been recently described and attributed to a vertical extrusion of orogenic lower crust (Schulmann et al., 2005; Tajčmanová et al., 2006). The extrusion was later followed by horizontal channel flow (Schulmann et al., 2008; Štípská et al., 2008) in middle crustal level, coupled with retrogression of granulites and intensive melting (Hasalová et al., 2008a).

The studied granulite–peridotite rock association occurs within the Náměšť Granulite Massif (Matějovská, 1967) at the boundary with the continental Brunia promontory to the East and to the North (Fig. 1b and c). The granulite body is nearly completely enveloped by a belt of pyroxene and/or garnet amphibolites with a tholeiitic geochemical signature (Šichtařová, 1981). This granulite–amphibolite complex is further surrounded by garnet- and sillimanite-bearing gföhl gneisses (Matějovská, 1975). Hasalová et al. (2008a,b) showed that the different orthogneiss types can be considered as a continuous sequence ranging from banded orthogneiss to nebulitic migmatites, developed by melt infiltration in a middle-crustal channel.

The Mohelno peridotite belongs to numerous bodies of spinel to garnet peridotites enclosed within retrogressed granulite of the Náměšť Granulite Massif.

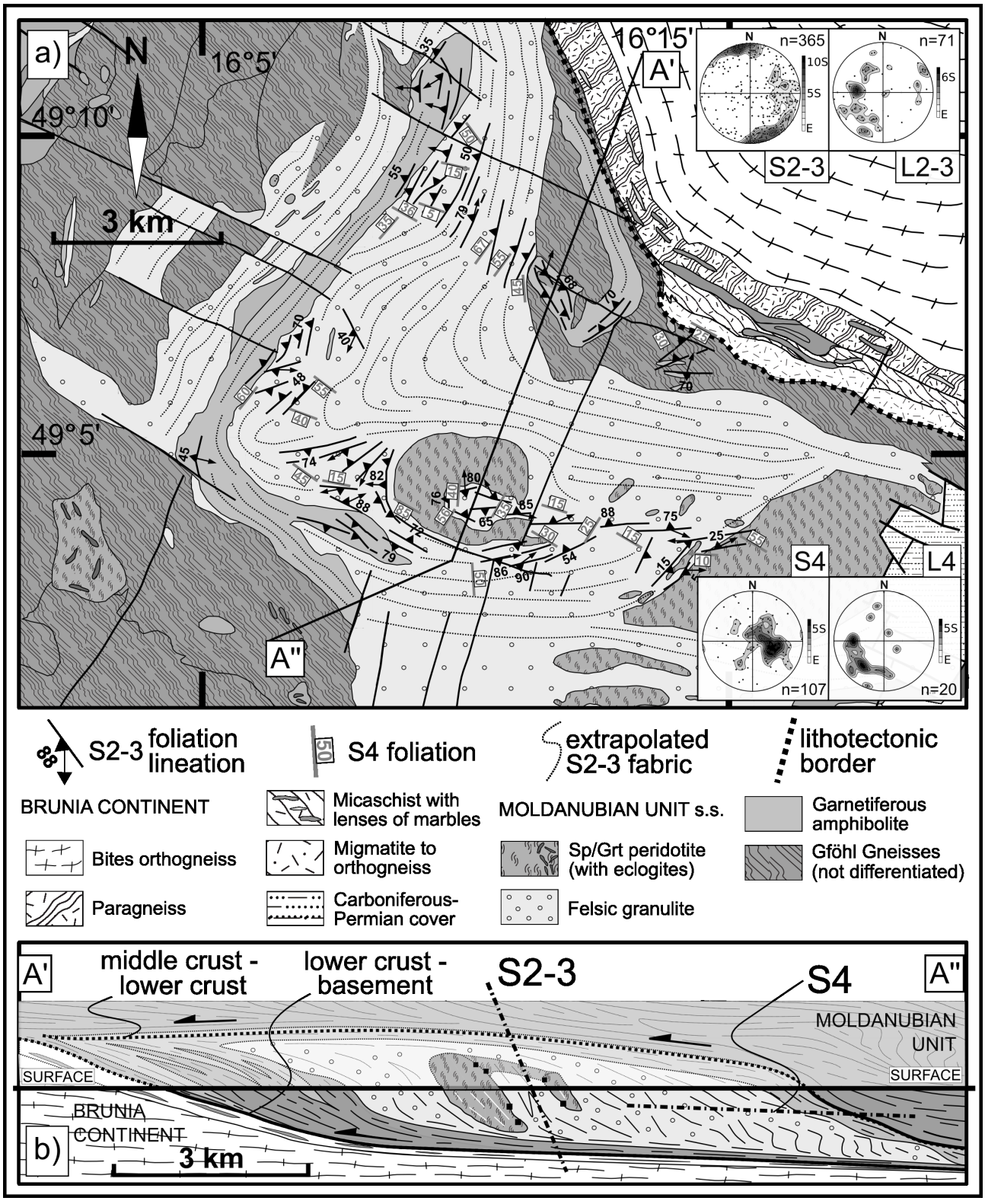

Figure 2. Structures in granulites observed in the field: (a) the structural map of the study area shows trajectories of S2–3 foliation, contoured pole figures of mylonitic finegrained foliations (S2–3) and lineations (L2–3) in granulites as well as S4 and L4 structures; (b) the idealized cross-section shows a Náměšť Granulite Massif as a low strain domain preserving steep S2 mylonitic foliations affected by S4 flat fabric due to underthrusting of the Brunia basement promontory.

These bodies form lenses ranging from meters to several kilometers in size (Urban, 1992), while the Mohelno serpentinized peridotite exhibits a form of a large fold arc with decreasing thickness from ~1000 m in the northern limb to ~300 m in the southern one (Fig. 1c). Peridotites are strongly serpentinized (50–100 %) but their original pristine microstructure is locally preserved. The original mineral assemblage of the peridotites is represented by olivine, orthopyroxene, clinopyroxene and spinel (Stage I of Medaris et al., 1990). Primary spinel is overgrown by garnet (Stage II) followed by further breakdown to clinopyroxene and spinel (Stage III) and amphibole and spinel symplectites (Stage IV) associated with fine-grained mylonitic microstructure. Peridotites display a geochemical signature characteristic for an asthenospheric origin, and because of presence of pyroxenite veins, it was proposed that the original spinel peridotite developed at temperatures close to dry pyrolite solidus (Medaris et al., 1990; Kamei et al., 2010). However, pressure estimates for this evolutionary stage have not been quantified. According to standard geothermobarometry the peak mineral assemblage of garnet peridotite occurred at 2.3–2.8 GPa and temperature ~1200 °C (Medaris et al., 1990) or at 1.8–2.5 GPa at 1100–1250 °C (Kamei et al., 2010) while mylonitic microstructure with secondary spinel reveals conditions of 0.8–1.5 GPa at 800–950 °C. The clinopyroxene-spinel and amphibole-spinel kelyphite assemblage around garnets are correlated with granulite facies and amphibolite facies retrogression of the surrounding granulites, respectively (Medaris et al., 1990, 2005; Kamei et al., 2010). The contact zone between granulite and peridotite along the inner margin of the Mohelno peridotite body is characterized by the presence of various magmatic rocks as hornblendite, biotitite and gabbrodiorite interpreted as a reaction zone between hot peridotite and host granulites (Dobretsov et al., 1984).

Structural geology of Mohelno peridotite and host rocks

The structural pattern of the Mohelno peridotite reveals homogeneous mylonitic fabric and pyroxenite layering while the surrounding granulite and amphibolite exhibit a polyphase structural evolution (Fig. 2). Special attention was paid to the distribution of garnet and coarse spinel within the Mohelno Peridotite Body (MPB). Our study shows that the coarse-grained spinel variety occupies the majority of the peridotite body, while the garnet one is rimming the inner arc of the fold hinge with exception of one sample located in the southeastern extremity of the peridotite body (Fig. 3e). In general, the peridotite mineral assemblage is rarely preserved due to extensive serpentinization.

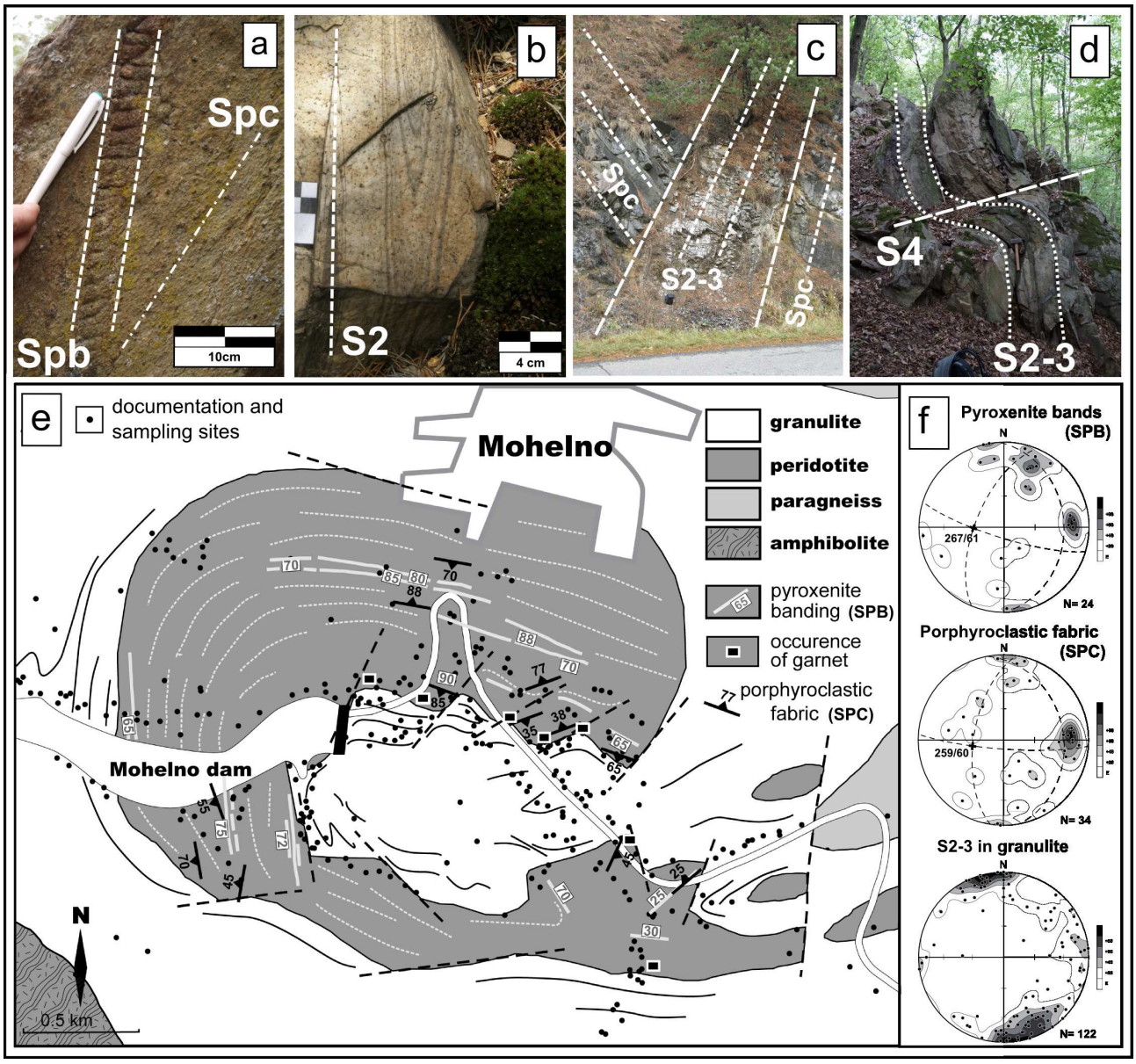

Figure 3. Main structural elements in the close vicinity of the Mohelno peridotite body observed in the field. (a) Mylonitic foliation in peridotite is defined by elongated porphyroclasts of orthopyroxenes (Spc) and rework also websterite layers (Spb) that occur parallel or oblique to the mylonitic foliation; (b) mylonitic fine-grained foliation S2 in granulites show often isoclinal folds; (c) a granulite–peridotite interface along the inner fold with felsic partial melts and granulite wedging towards the peridotite; (d) localized flat S4 shear zones in granulites rework subvertical S2–3 foliation; (e) a simplified geological map of the study area shows trajectories of the mylonitic foliation and websterite layering in peridotites, and S2–3 foliation in granulites. Occurrences of garnet (black squares) and sampling sites (black circles) are shown as well as foliations measured in the field; (f) contoured pole figures of the poles to porphyroclastic foliation, websterite layers and S2 together with S3 foliations.

Both coarse-grained spinel- and garnet-bearing peridotite are mylonitized resulting in development of fine-grained spinel-bearing matrix and orthopyroxene porphyroclasts (Fig. 3a). This mylonitic foliation is generally steeply dipping and its orientation follows the fold shape of the peridotite body with the fold hinge steeply plunging to the West (Fig. 3e). The second fabric element is represented

by milimetres to several centimetres thick bands of websterites to orthopyroxenites (Fig. 3a) that form layers either parallel or oblique with respect to principal mylonitic fabric. The pyroxenite layers are also mylonitized and affected by late fractures which progressively disappear in the surrounding serpentinized matrix.

Four deformation fabrics were recognized within the Náměšť Granulite Massif directly surrounding the Mohelno peridotite. Both S1 and S2 fabrics are characterized by a granulite facies mineral assemblage such as garnet, kyanite, perthitic feldspar and rutile. Coarse-grained granulite facies S1 fabric is preserved only in low-strain domain within the internal part of the fold hinge and is defined either by lithological layering or by a faint shape preferred orientation of mineral aggregates. Due to strong D2 transposition the geographical orientation of S1 fabric cannot be determined in the field. Reworking of the S1 fabric is correlated with evolution of (ultra)mylonitic granulite S2 fabric associated with development of isoclinal folds F2 (Fig. 3b). S2 foliation is striking N–S and E–W in the northern and in the southern parts of the Náměšt' Granulite Massif, respectively (Fig. 2a). Here, the subvertical S2 is turned together with the peridotite layer and bears a mineral lineation moderately plunging to the West (Fig. 2a). The rotation of the S2 foliation into the E–W direction is associated with the large scale F3 folding of the granulite layering and peridotite sheet resulting in formation of upright peridotite F3 folds with E–W trending axial plane and West plunging hinge. The large scale folding is accompanied with a retrogression E–W trending S2 fabrics under amphibolite facies conditions associated with partial melting forming foliation parallel leucosomes. The retrogression along fold limbs leads to development of steep composite S2–3 fabric marked by alternations of felsic granulites with migmatitic granulitic gneiss (Matějovská, 1975). The internal part of the peridotite fold hinge is affected by D3 shear zones which may be interpreted as axial cleavage of large scale F3 folds. Here, the granulites are strongly sheared and retrogressed as shown by a syn-D3 growth of sillimanite and biotite and elongated lenses of granitic melt. Farther away from the peridotite body is D3 expressed also by the development of meter scale parasitic F3 folds.

Sub-vertical S2 and S3 fabrics are reworked by sub-horizontal S4 foliation, which is a common structure of the Náměšť Granulite Massif. In the volumetrically more important western part of the Náměšť Granulite Massif, the N–S and E–W striking steep S2–3 foliations are reworked by flat shear zones and recumbent open folds with N–S and E–W trending hinges, respectively (Fig. 3d). In the eastern extremity of the massif the degree of the D4 deformation is more important leading to development of close to isoclinal E–W trending F4 folds associated with development of a pervasive S4

migmatitic foliation. Here, the S4 is marked by preferred orientation of biotite and coarse leucosome layers. The S4 bears SW plunging mineral and stretching lineation marked by alignment of sillimanite and elongation of quartz-feldspar aggregates (Fig. 2a).

Peridotite and granulite microstructures

According to experimental works, deformation microstructures and grain size depend on temperature, stress and/or strain rate and can be used to decipher prevailing deformation mechanisms (Rutter and Brodie, 1992). These data may contribute to understand mechanical behavior of mantle and crust during different stages of tectonic evolution. In peridotite, grain size was measured in less serpentinized domains using linear-intercept method. Individual microstructures of granulites were manually traced and median grain size was estimated using area-intercept method for individual phases. It is noteworthy that serpentinization alters 50–100% of the rock volume and is expressed by presence of antigorite bands coloured with a dispersed submicroscopic pigment of iron oxides. Ferromagnetic minerals, mainly magnetite and maghemite are also abundant, and chlorite and talc are present as accessories.

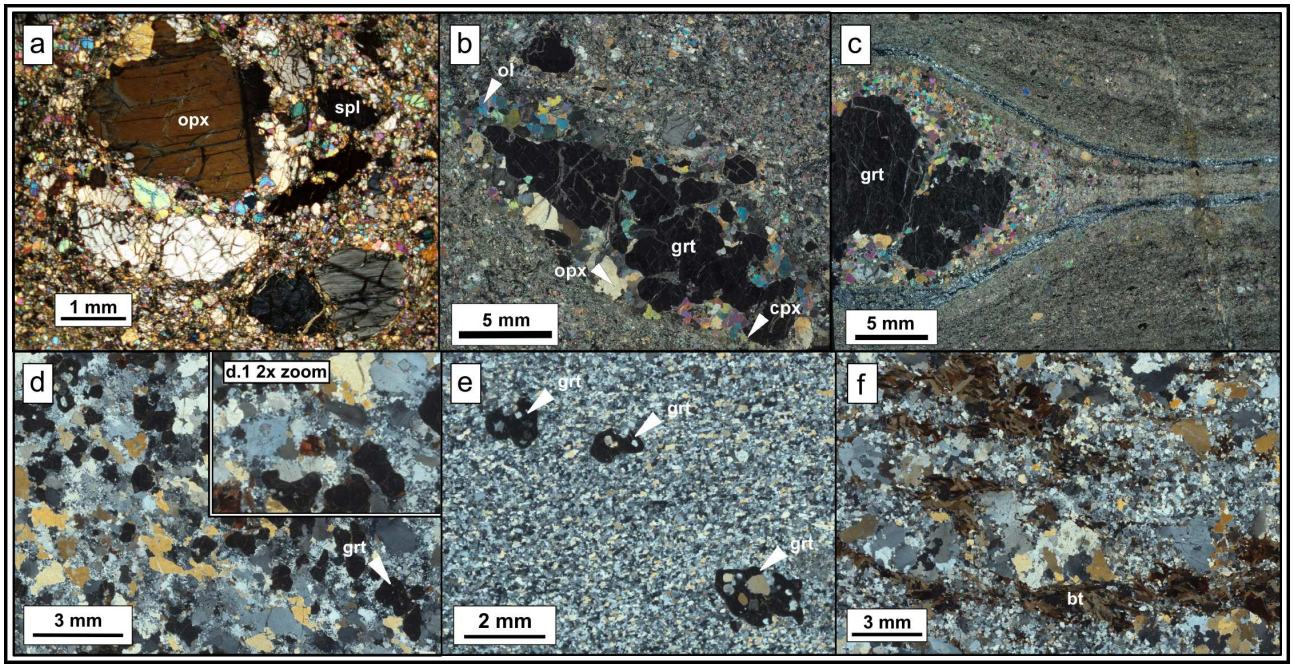

Figure 4. Microphotographs of the most important microstructures: (a) a coarse-grained opx + spl + ol porphyroclastic domain characterises the original mineral association in the majority of the peridotite body; (b) elongated garnet in coarse-grained microstructure along the inner margin of the body; (c) garnet-pyroxene porphyroclast surrounded by serpentinized mylonitic microstructure; (d) coarse S1 microstructure in granulite, with core-mantle features visible in zoomed part (d.1); (e) ultra-mylonitic S2 microstructure in granulite; (f) S3 microstructure in granulite (mineral abbreviations after Kretz, 1983).

The original coarse-grain microstructure is reported for both, spinel and garnet peridotite relics, preserved in less serpentinised domains (Medaris et al., 2005; Kamei et al., 2010). Coarse-grained spinel peridotite relics contain large orthopyroxene (1–15 mm), olivine (1–4 mm), clinopyroxene (1–2 mm) and coarse spinel (1–2 mm) (Fig. 4a). Orthopyroxene porphyroclasts locally show thin exsolution lamellae of clinopyroxene along mineral cleavage. In the coarse-grained garnet peridotite the garnet occurs in form of large and elongated (up to several centimetres in size on diameter) crystals (Fig. 4b and c) surrounded by coarse-grained matrix preserving stable grain boundaries with orthopyroxene (1–4 mm), olivine (1–3 mm) and clinopyroxene (1–2 mm) (Fig. 4b). In the whole MPB the coarse-grained original microstructure is converted into dynamically recrystallized fine-grained spinel-bearing mylonitic matrix (mean grain size ~60 µm). Many garnets found in the fine-grained spinel-bearing matrix show inner clinopyroxene-spinel and outer amphibole-spinel kelyphytic rims (Medaris et al., 2005; Kamei et al., 2010).

Millimeter to several centimeter-thick pyroxenites bands exhibit a porphyroclastic microstructure defined by orthopyroxene porphyroclasts surrounded by polygonal orthopyroxene grains. Fine-grained clinopyroxene is occasionally preserved within dynamically recrystallized orthopyroxenes with mean grain size of ~60 µm.

Rare felsic granulite S1 microstructure is characterized by coarse-grained mineral assemblage (several mm in size) of quartz + perthite + garnet + kyanite + biotite. The S1 fabric is defined by elongation of garnet grains and quartz ribbons (Fig. 4d). Perthitic feldspars (~200 µm) show core and mantle microstructure rimmed by neoblasts of plagioclase (~35 µm) and K-feldspar (~30 µm; Fig. 5). Large quartz grains (~200 µm) occur within platy ribbons and exhibit highly lobated grain boundaries pointing to grain boundary migration recrystallization mechanism (Guillope and Poirier, 1979). Felsic granulite from a close vicinity of the peridotite body show well developed mylonitic granulite S2 fabric with stable mineral association of high pressure granulites (qtz + kfs + plg + grt + ky + rt + bt). Recrystallized feldspars as well as quartz are intermixed within equal-sized fine-grained recrystallized microstructure of quartz (~59 µm), plagioclase (~50 µm) and K-feldspar (~43 µm) (Fig. 4e, Fig. 5). Garnet crystals are rich in large quartz and perthitic feldspar inclusions with lobate grain boundaries. These inclusions reveal larger grain size compared to the fine-grained matrix. Similarly, kyanite crystals form inclusions inside rims of coarser perthitic feldspars pointing out to their early growth. Retrogression of S2 by D3 deformation is generally characterized by fabric coarsening and more specifically by growth of plagioclase around unstable kyanite, formation of coarse-grained quartz

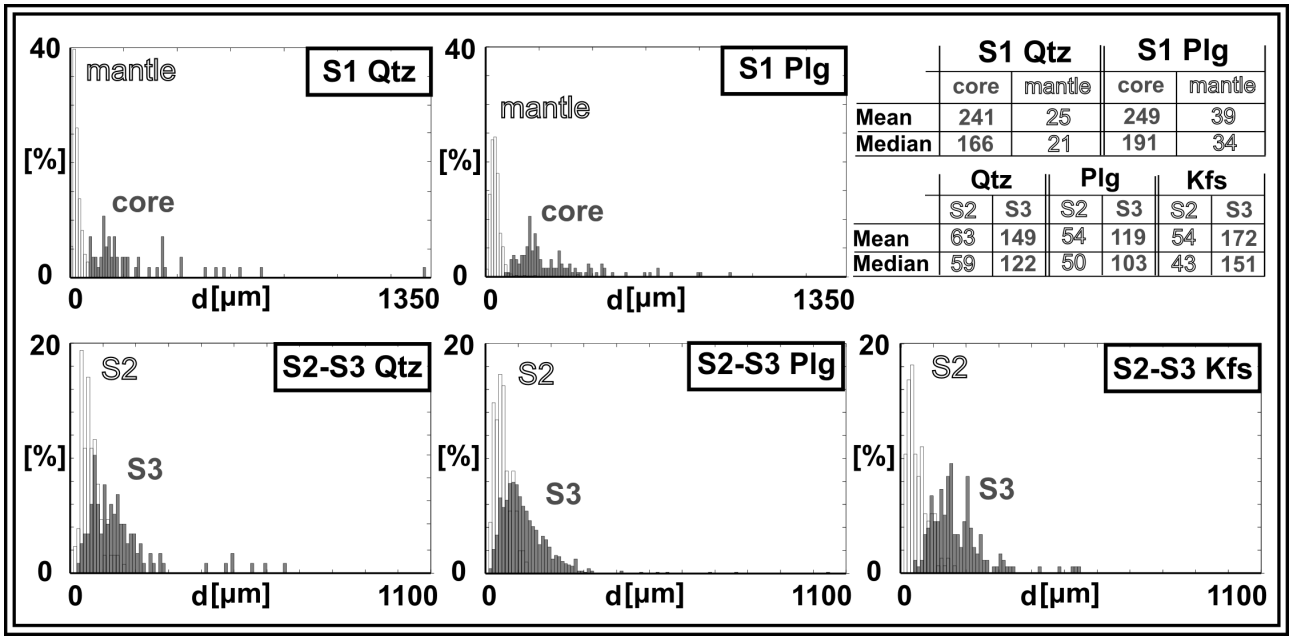

Figure 5. Histograms showing grain size distribution of quartz and plagioclase in S1 microstructure, and quartz, plagioclase and K-feldspar in S2/S3 microstructure. Tables with statistical data in the top right corner.

ribbons and leucosome layers parallel to the S2 fabric. The S4 fabric is associated with a formation of amphibolite facies mineral assemblage represented by qtz + kfs + plg + bt ± grt ± ky ± sill ± ms ± rt ± ilm. Retrogression is mostly characterized by heterogeneous grain coarsening, hydration of original mineral assemblage marked by development of biotite rich bands and leucosome layers parallel to S4 foliation (Fig. 4f), and growth of a new fine-grained garnet as reported also by Hasalová et al. (2008a). Kyanite is replaced by sillimanite forming acicular aggregates or fibrous crystals aligned with biotite schlierens replacing garnet. Locally, muscovite formed at the expense of biotite. Both feldspars form coarser-grained matrix composed of K-feldspar (~151 µm) and plagioclase (~103 µm) that enclose thick ribbons consisting of coarse quartz grains (~122 µm) with lobated grain boundaries (Figs. 4f and 5).

Lattice preferred orientation and deformation mechanisms

Lattice preferred orientation of olivine and orthopyroxene in peridotite allows determining the orientation of the main fabric preserved from static serpentinization. It also provide information on active slip systems of olivine and orthopyroxene that depend on (a) deformation regime (Tommasi et al., 1999), (b) temperature (Tommasi et al., 2000; Demouchy et al., 2009), (c) pressure (Couvy et al., 2004; Raterron et al., 2009) and probably (d) water content (Chopra and Paterson, 1984; Mackwell et

al., 1985; Jung and Karato, 2001).

Methods

Lattice preferred orientation of olivine was measured on a scanning electron microscope CamScan4 at the Institute of Petrology and Structural Geology, Charles University in Prague by electron back–scattered diffraction (EBSD) using HKL technologies CHANNEL 5 software (Schmidt and Olesen, 1989). Diffraction patterns were acquired at a working distance of 40 mm and using an accelerating voltage of 17 kV. The whole procedure (pattern acquisition, image freezing, band detection, indexing and result backup) was carried out on the studied samples manually. Additionally lattice preferred orientation of olivine and orthopyroxene were measured on a TESCAN scanning microscope at the EOST, University of Strasbourg using EDAX OIM software. LPO data were obtained in automatic mode along with chemical elements distribution to minimize mis-indexing. Measured raw data were manually processed to orientation data sets based on one point per grain. In both approaches each individual grain is represented by only one orientation measurement, and equal weighting to each orientation measurement has been given for the contouring of the pole figures.

Due to strong serpentinization, the LPO was measured in thin sections prepared in three ways: (a) normal to porphyroclastic foliation and parallel to stretching lineation both defined in the field ("matching F&L" samples in Fig. 6), (b) normal to porphyroclastic foliation defined in the field and parallel to its dip direction ("matching F" samples in Fig. 6), (c) in case of strongly serpentinized samples, normal to a randomly chosen fracture plane and parallel to its dip direction ("not matching" samples in Fig. 6). All LPOs were rotated and presented in non-polar, lower hemisphere equal area projections in the geographic coordinates (North is located in the top of the pole figure). Foliation plane and lineation measured in the field are presented in the pole figure as solid line and triangle, respectively. The different patterns of olivine LPOs are illustrated in three pole figures of the main axes [100], [010] and [001].

In order to characterize the occurrence of the given type of olivine LPO in a more objective way, a PGR diagram was carried out according to Vollmer (1990). He proposed the eigenvalue classification for orientation data in order to quantify the type of distribution (point, girdle and random). The magnitude of three eigenvalues for every presented crystallographic direction ($\lambda_1 \geq \lambda_2 \geq \lambda_3$ with the normalization $\lambda_1 + \lambda_2 + \lambda_3 = 1$) are used to define three PGR fabric indices, point maximum ($P = \lambda_1 - \lambda_2$), girdle ($G = 2(\lambda_2 - \lambda_3)$) and random ($R = 3\lambda_3$). These indices range from 0 to 1

and have the property that P + G + R = 1. Both analyses as well as projection of pole figures have been carried out by software from the shareware package (Mainprice, 1990); ftp://www.gm.univ-montp2.fr/mainprice//CareWare_Unicef_Programs/).

Additionally strength of the fabric in every sample was expressed in misorientation index (M-index, Skemer et al., 2005). The M-index is based on the distribution of uncorrelated misorientation angles. Value of the M-index corresponds to the difference between the observed distribution of uncorrelated misorientation angles and that predicted for a random fabric. It has values from 0 (for random LPO fabric) to 1 (for a single crystal fabric).

Results

Lattice preferred orientation of olivine is not uniform in the measured samples. The eigenvalue classification shows a strong component of random distribution in all samples, but also allow to identify two types of LPO patterns (Fig. 6). The first type shows girdle distribution of the [100] axes with the sub-maximum inside the girdle and broad point maximum of the [010] axes providing the strongest maximum. The [001] axes show generally weak preferred orientation, but some samples show a weak point maximum (Fig. 6). In the PGR diagram the [100] axis plots in between G and R corners, indicating girdle dominated distribution of this axis, while the [010] axis plots between P and R apexes suggesting a point type distribution (Fig. 8b). This LPO is characteristic for the AG-type (Mainprice, 2007) or axial [010] pattern according to Tommasi et al. (2000), also called [010]-fiber pattern (Bunge, 1982). It is developed preferentially along the inner margin of the fold-shaped serpentinized peridotite body. Locally, it has also been measured in a few samples from the central part of the southern limb of the peridotite fold (Fig. 8a). The second LPO type shows the strongest point maximum of [100] and girdle distribution for both the [010] and the weakest [001] axes (Fig. 6). In the PGR diagram the [100] axes plot between P and R corners while the [010] axes plot in between G and R apexes. Such a type of texture corresponds to [100](0kl) pattern (Tommasi et al., 2000) or D-type (Karato et al., 1980; Jung and Karato, 2001; Mainprice, 2007) or [100]-fiber pattern (Bunge, 1982) and is typically developed in the interior and along the outer parts of the fold shape peridotite body (Fig. 8).

In several sites the macroscopic lineation or both lineation and foliation were not known (Fig. 6, matching F and not matching samples) and therefore the eigenvalue analysis was used to identify the orientation of these fabric elements.

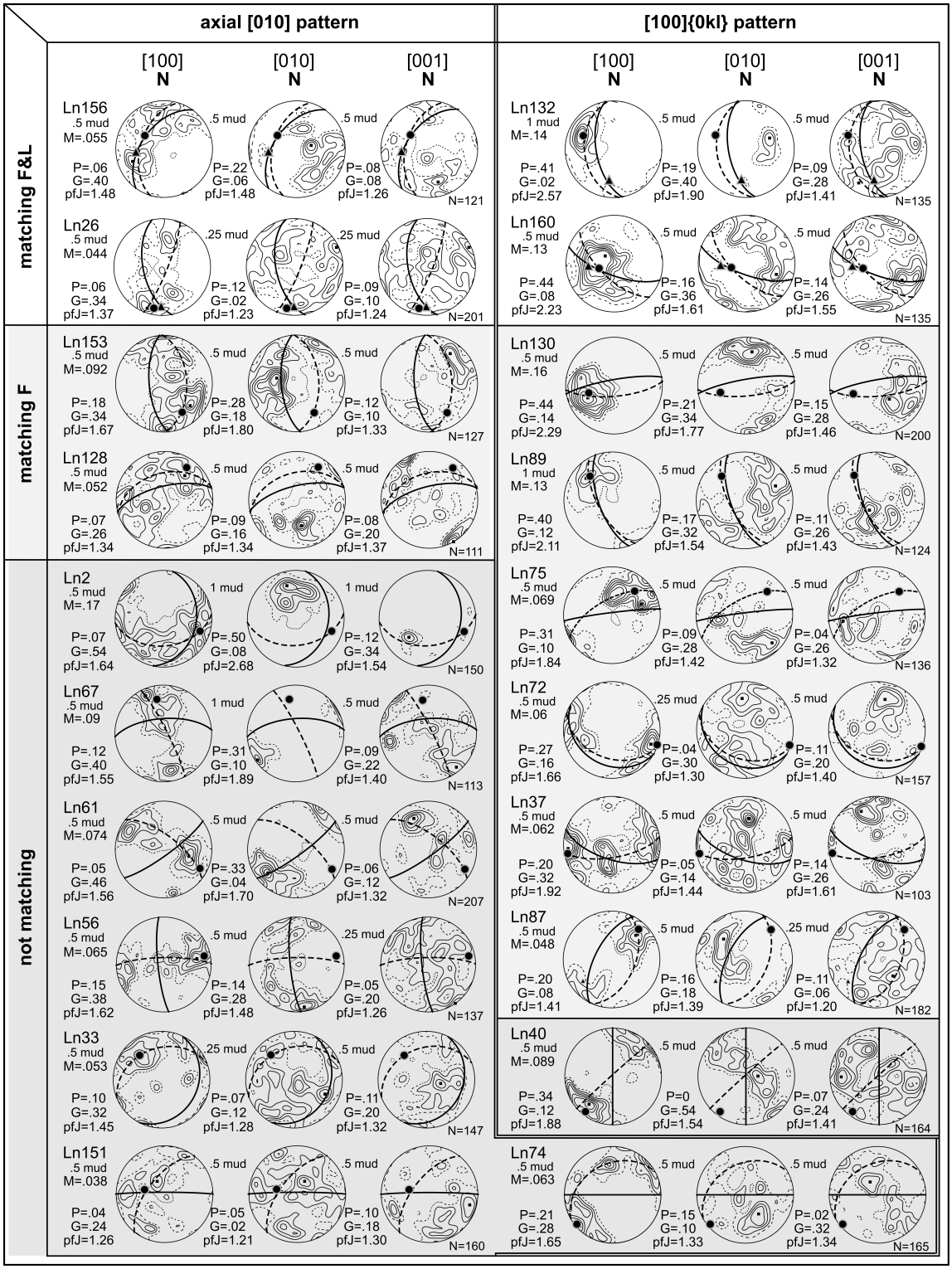

Figure 6. Measured olivine LPO is presented in contoured pole figures of [100], [010] and [001] crystal directions in geographic coordinates. The left column shows LPO with axial [010] pattern, while right column present LPO with [100](0kl) pattern. 'Matching F&L' group of LPOs correspond to samples with clearly defined foliation and stretching lineation in the field. 'Matching F' (mylonitic foliation recognised) and 'not matching' (neither foliation nor lineation recognised) group show LPOs that belong to more intensely serpentinized samples. Full line and dashed line half-circle correspond to the trace of the mylonitic foliation measured in the field and defined from the eigenvector analysis, respectively. Full triangles and full circles show positions of the stretching lineation measured in the field and calculated from the eigenvector analysis, respectively. Pole figures are in equal area projection on lower hemisphere, and contoured at 0.5 times of uniform distribution interval (.5 mud). M is a value of M-index, P and G values are calculated from the eigenvalue analysis, pfJ is a value of texture index (J-index) and N is a number of measured grains.

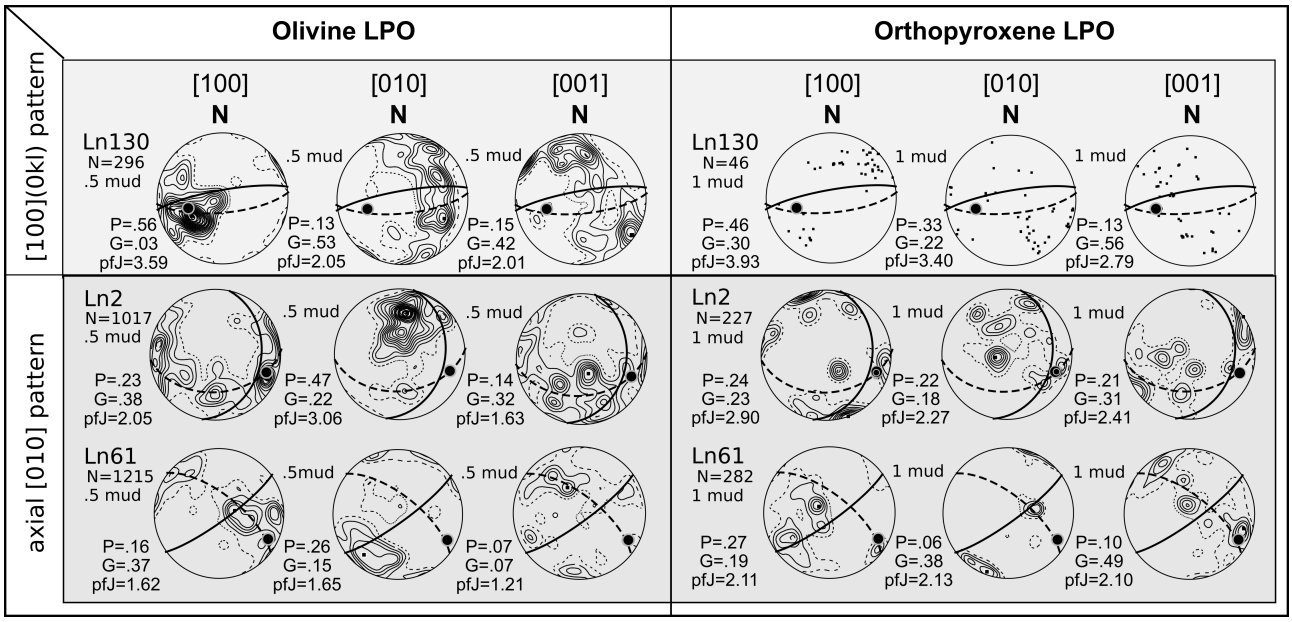

Figure 7. LPO of olivine and orthopyroxene measured on 'not matching' samples show parallelism of the olivine [100] with orthopyroxene [001] maxima positions which represent independent control of the stretching lineation determination. Pole figures are in equal area projection on lower hemisphere, and contoured at 0.5 or 1.0 times of uniform distribution interval (.5 or 1 mud). P and G values are calculated from the eigenvalue analysis, pfJ is a value of texture index (J-index) and N is a number of measured grains.

Because, the [100](010) slip system is the most active in both LPO types the maximum eigenvector orientations for the [100] and [010] axes were attributed to the stretching lineation and the pole of foliation, respectively. In order to confirm the orientation of lineation and foliation deduced from olivine LPO the lattice preferred orientation of orthopyroxene was measured in several samples. Orthopyroxene LPO shows point maximum in [100] and [010] direction, and girdle distribution of the [001] axes with the sub-maximum inside the girdle (Fig. 7) suggesting main activity of the [001](010) and minor contribution of the [001](100) slip systems. These pole figures show that the orthopyroxene LPO confirms the foliation and lineation orientations deduced from olivine LPO measurements.

M-index calculation shows small strength of the olivine LPO in majority of samples providing values less than 0.1. Several samples exhibit a higher LPO strength, however there is no correlation with the type of the LPO (Fig. 8a).

Discussion

Data presented in this work show the procedure for reconstruction of fabric features such as foliation and lineation using olivine LPO data in strongly serpentinized peridotite.

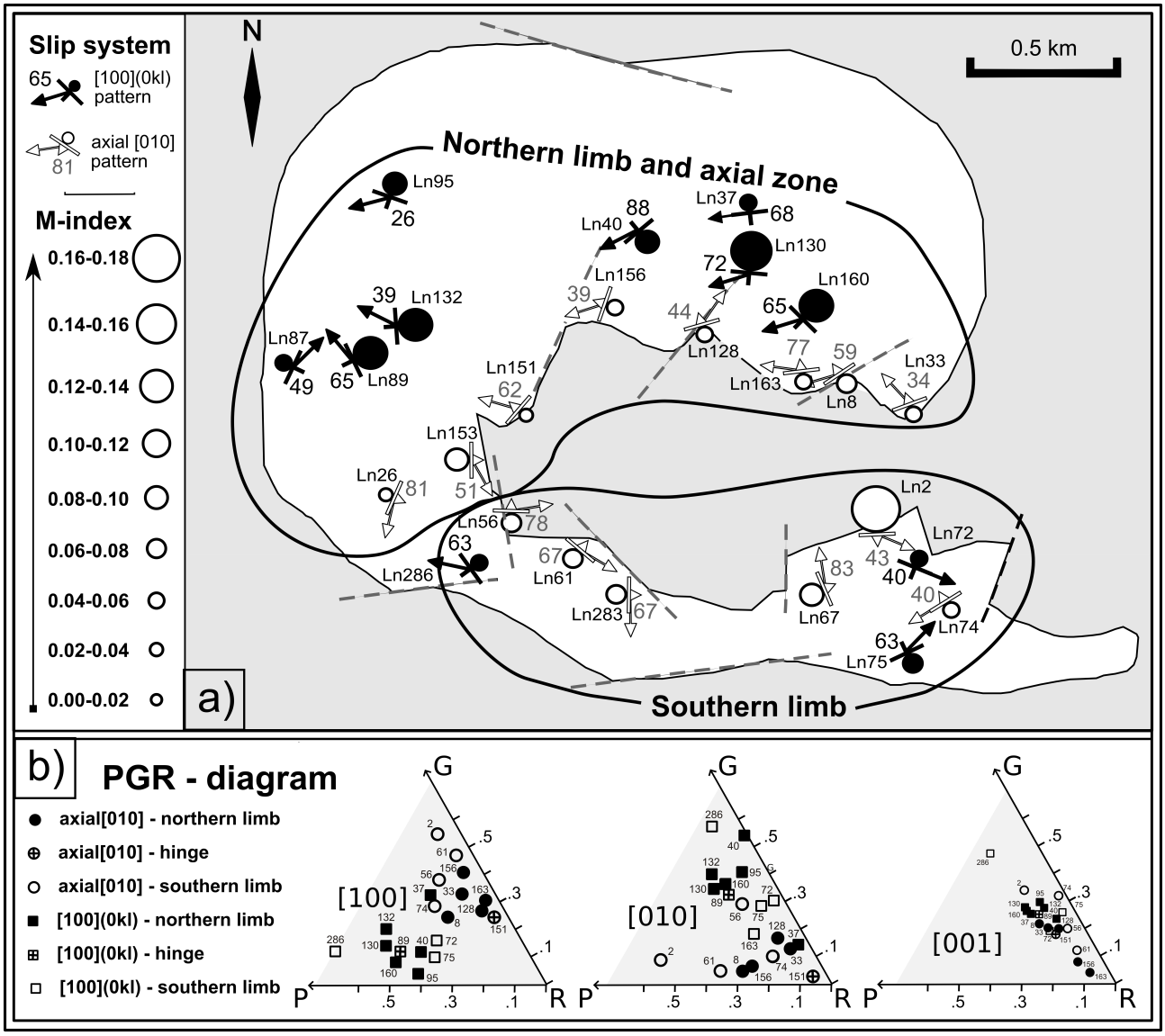

Figure 8. (a) Orientations of foliation and lineation within the Mohelno serpentinized peridotite body (MPB) according to the eigenvector analysis of olivine LPO. LPO revealed that the axial [010] pattern occur mainly along the inner margin and the southern limb of the fold, while the [100](0kl) pattern occur in the rest of the body. Values of M-index for each measured sample are presented in the map with contours of the MPB; (b) point–girdle–random (PGR) diagrams for main crystallographic directions. Each symbol in individual diagram represents one measured sample. Circles characterize olivine LPO with axial [010] pattern either from the northern limb (black circles) or southern limb (white circles). Square symbols correspond to the [100](0kl) pattern.

A preservation of the lattice preferred orientation in studied samples shows that serpentinization postdate development of the LPO, and its randomization is more likely related to dynamic recrystallization of olivine during development of porphyroclastic microstructure than to a late serpentinization related event.

EBSD measurements of remnant olivine and pyroxene together with the eigenvector analysis and the eigenvalue classification (Vollmer, 1990) helped to constrain the active slip system and provide

information about LPO symmetry. The studied samples with porphyroclastic microstructure show either [100](0kl) LPO or axial [010] LPO pattern, implying that they have been deformed under relatively high stress and 'dry' conditions (Jung and Karato, 2001; Mainprice, 2007). However, origin of the olivine LPO is still not clearly established. The olivine [100](0kl) pattern corresponds to the most common olivine slip patterns and is expected to occur at medium temperatures ca. 1000 °C (Carter and Ave'Lallemant, 1970). It is commonly reported from peridotites with a coarsegrained microstructure (e.g. Ildefonse et al., 1995; Soustelle et al., 2010) and from high shear strain experiments (Bystricky et al., 2000). In terms of deformation regime this pattern of olivine LPO was numerically modeled as a result of transtensional deformation (Tommasi et al., 1999). The axial [010] LPO pattern can either indicate contribution of the [001] glide in olivine (Demouchy et al., 2009; Tommasi et al., 2000), or it can be caused by flow component orthogonal to shear plane in transpressional regime. This pattern was numerically simulated for dynamically recrystallized polycrystalline olivine in transpressional regime (Tommasi et al., 1999). Recently, the latter pattern was measured in refractory harzburgites refertilized in mantle conditions, and explained as a result of combination of recovery and static recrystallization that may modify strain-induced axial [100] LPO pattern (Tommasi et al., 2008). The same patterns were also observed in Kerguelen xenoliths (Bascou et al., 2008), and in this case the least metasomatized peridotites (harzburgites) display a axial [010] LPO pattern while the most metasomatized (dunites) display either an orthorhombic symmetry or a [100](0kl) pattern.

Significance of the two types of olivine fabrics: a record of the thermal history of a quenched peridotite?

Our results confirm previously reported typology of olivine LPO patterns from the Mohelno Peridotite Body (Kamei et al., 2010). According to these authors, the existence of the two LPO types can be correlated to the thermal history of a hot peridotite emplaced into the colder granulites. Because of the slow cooling and continuous deformation in the interior of the peridotite body, the original [100](010) to axial [010] pattern (suggested as a high temperature fabric) in the spinel peridotite was converted to the axial [100] pattern (suggested as a lower-temperature type). It was proposed that the high-temperature [100](010) to axial [010] pattern was preserved only at the garnet-bearing margin of the peridotite body where cooling was rapid and the texture was quenched. According to this model the reduction of grain size that occurred during later deformation partly obliterated the two types of previously developed fabric patterns in both garnet and spinel peridotites. The initial rapid cooling

at high temperatures associated with deformation probably occurred after the mantle peridotite was emplaced into the granulites, which implies that the spinel- to garnet-peridotite transformation took place in the continental crust (Kamei et al., 2010).

This interpretation is mainly based on the petrological arguments and idea that garnet is not a primary mantle mineral, but crystallizes at the margin of the body due to differential cooling between the interior and the margin during emplacement of the peridotite sheet in the granulite rocks (Medaris et al., 1990; Kamei et al., 2010). According to the published chromium content of primary spinel (Y_{cr} = 0.121–0.193; Kamei et al., 2010), such an interpretation requires hypothetical crystallization of garnet between 1100–1200 °C during an isobaric cooling at pressures of ~2.3 GPa (Fig. 10a). However, such extreme P–T conditions were never reported from Bohemian Massif granulites and significantly lower temperatures of 800–900 °C were commonly calculated (Štípská et al., 2004; Tajčmanová et al., 2006; Racek et al., 2008; Franěk et al., 2011). In addition, our detailed mapping showed that garnet occurs only along the inner margin of the peridotite megafold and not all around the whole peridotite body as it required by the quenching model. Also, 'the quenching' of the high temperature LPO and microstructure in the body margin and its continuous alteration associated with decreasing temperature towards the centre of the peridotite does not fit with the regional grain size distribution of recrystallized pyroxenes reported by Kamei et al. (2010). According to model, the larger grain sizes of pyroxenes now in the body centre should theoretically occur in the quenched body margin that preserves higher temperature microstructure. On the basis of all these arguments, we do not agree with the quenching model of LPO development and in the following pages, we provide arguments favoring deformation history that explains origin and regional distribution of both olivine LPO types.

Relationship between field structure and olivine LPO

Field observations carried out in the Náměšť granulite body show well preserved S2 steep mylonitic fabric concordant with olivine and orthopyroxene foliation of the fold-shaped Mohelno Peridotite Body (Fig. 3). In order to compare internal strain patterns of the peridotite with those of surrounding granulite, the orientations of the constructed olivine foliations and lineations were projected on the map (Fig. 8a) and into the stereographic projections (Fig. 9). The structural map shows that the olivine foliations generally follow the shape of the peridotite body for both types of LPO. The axial [010] type distribution is dominant along the inner margin of the body and along the southern limb of the large fold thereby coinciding only partly with occurrence of garnet. In contrast, the [100](0kl)

pattern is developed in the northern limb and the hinge of the MPB fold.

The poles to foliation of all LPO data (Fig. 9a) are dominantly distributed along a great circle and the pole of the great circle coincides with the megafold hinge (β-axis of Sander, 1930; Fig. 3). In addition, the lineations obtained from [100](0kl) pattern occupy a similar position in the stereographic diagram (Fig. 9b). In contrast, lineations from the axial [010] are rotated along the fold hinge (Fig. 9c). This fabric pattern can be interpreted as a result of large scale folding of pre-existing olivine fabric and its rotation around a fold hinge. Our data show that the high M-index coincides with prolate fabric in the hinge and northern limb of the MPB fold compared to oblate fabric and weak M-index in the southern limb and inner part of the northern limb. This pattern can be explained by a two phase structural evolution. During the first stage the whole peridotite body acquired weak oblate deformation related to emplacement of mantle sheet into lower crustal granulites (Fig. 11b). Subsequently, the vertical N–S striking sheet becomes folded due to horizontal N–S shortening and vertical extrusion (Fig. 11c) as proposed by Franěk et al. (2011) and Lexa et al. (2011). The vertical extrusion is associated with folding of the peridotite sheet and favors constrictional deformation in fold

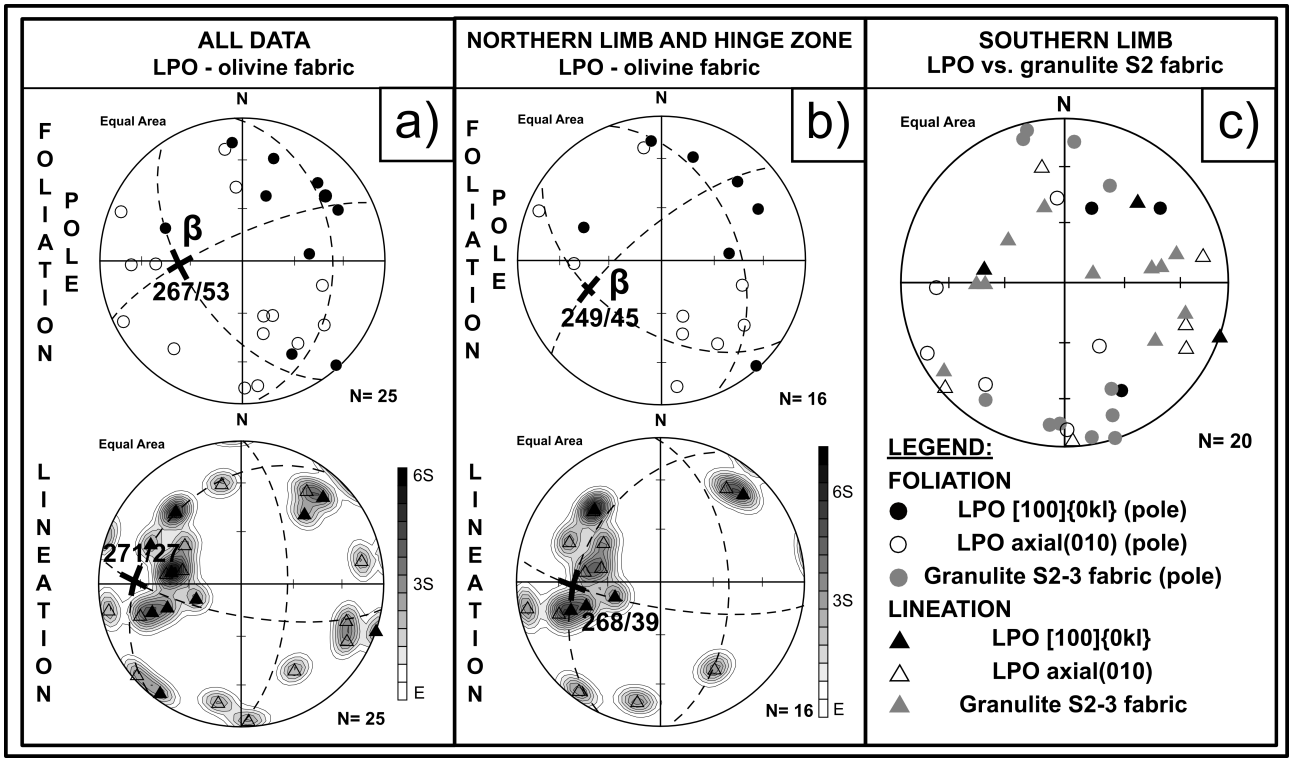

Figure 9. Lower hemisphere, equal area stereographic projections of poles to foliations and lineations calculated from (a) all olivine LPO data; (b) LPO data from the fold northern limb and the hinge zone; (c) LPO data from the fold southern limb and adjacent granulite.

hinges, while folded limbs can preserve oblate fabrics. If the vertical extrusion channel has circular or elliptical section, the constrictional flow is producing folds with vertical hinges due to lateral shortening of the vertical anisotropy (Weijermars, 1993; Kratinová et al., 2006).

Thermal and mechanical interactions between mantle and crust

Medaris et al. (2005) proposed that the Mohelno peridotite corresponds to the upper mantle depleted during Late Devonian intracontinental rifting. The spinel preserved in garnet porphyroblasts is interpreted as a relic of this stage (Medaris et al., 1990). Lithospheric thinning was followed by the development of a 70 km thick orogenic root (Schulmann et al., 2005, 2009). The crustal thickening model fits well with petrological studies of spinel and garnet peridotites which reveal that both coarse-grained microstructure equilibrated at similar temperatures 1100–1200 °C and pressures of around 2.3 GPa (Fig. 10; Medaris et al., 1990; Kamei et al., 2010). Such P–T values could be regarded as peak P–T conditions of the Mohelno peridotite, and the mineral zoning may reflects position of the spinel–garnet isograde in the mantle (O'Neill, 1981; Klemme and O'Neill, 2000; Kamei et al., 2010). In such a setting the spinel–garnet transition is located only 5–10 km under the double thickened Moho corresponding to a depth of 80 km (Fig. 11a). Rheology of the lithosphere during both thinning and

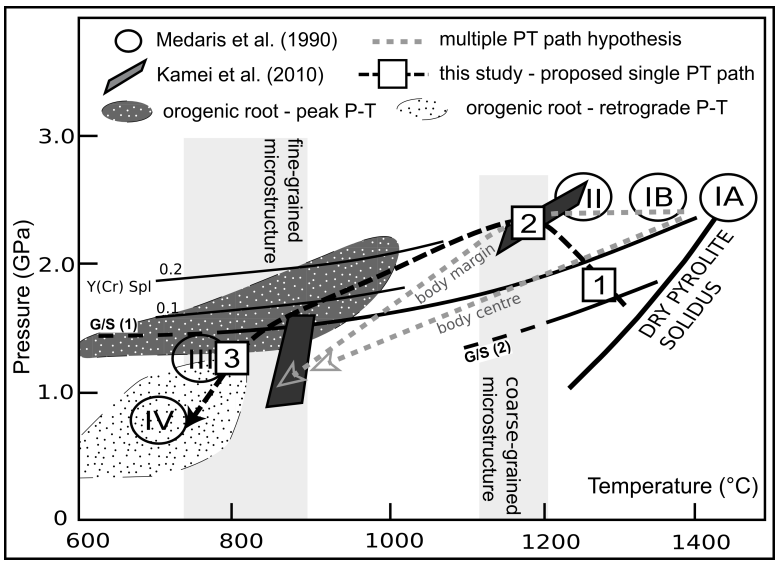

Figure 10. Pressure–temperature diagram showing results of previous petrological studies and two contrasting P–T–t paths (grey dashed lines) for differential cooling of central and marginal part of the Mohelno peridotite during ascent (Medaris et al., 1990). A novel single P–T–t path is proposed (black dashed line) that reflects initial burial of the depleted peridotite to the garnet stability field, its further emplacement into granulites and its rapid cooling. Garnet-spinel isoplets are after (1) Klemme and O'Neill (2000) and (2) Walter et al. (2002). Grt–spl isoplets shifted due to Y(Cr) in spinel after O'Neill (1981).

thickening stages was calculated according to Thompson et al. (2001) and Schulmann et al. (2002) and suggests that the warm and thin lithospheric mantle was inherited from the thinning stage. This tectonic setting is supposed to be the necessary prerequisite for further tectonic evolution (Fig. 11a).

Tectonic evolution continues by mylonitization of the peridotites and the enclosed pyroxenite layers that could be linked to the process of development of an intra-mantelic shear zone followed by imbrications of peridotite and granulite at the bottom of the orogenic root during ongoing E–W shortening (Fig. 11b). This shortening event is responsible for the formation of N–S trending crustal megafolds and gravity driven overturns transporting lower crustal and mantle fragments upwards (Schulmann et al., 2008, 2009; Lexa et al., 2011). The conditions of mantle shearing during its emplacement into the crust are recorded in clinopyroxene-spinel II kelyphite assemblage around garnets, which may be correlated to kyanite, K-feldspar and garnet assemblage in surrounding granulites (Medaris et al., 1990, 2005; Kamei et al., 2010). Progressively, both peridotite and granulite assemblages equilibrated at temperatures and pressures of 800–900 °C and 1.5–0.8 GPa (Figs. 10 and 11).

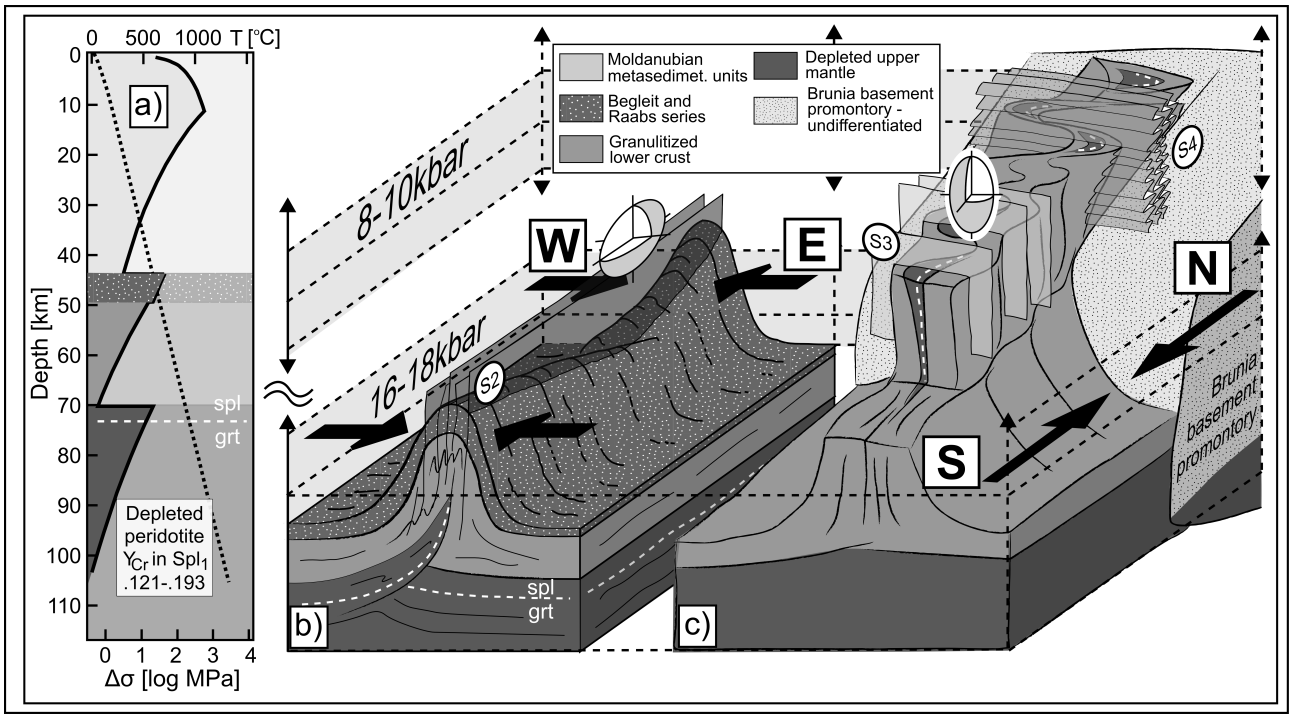

Figure 11. Tectonic evolution of the Mohelno peridotite body: (a) rheological profile through thickened orogenic crust, spinel/garnet isograde according to Klemme and O'Neill (2000) and O'Neill (1981), (b) 3D model of imbrications of lithospheric mantle and emplacement of the peridotite sheet into the folded lower crust during the stage D2. Oblate ellipsoid is shown indicating development of first crystal plastic deformation in the cooled peridotite. (c) Model of indentation of the Brunia promontory orthogonal to S2 fabrics, and development of F3 folds with steep fold hinges affecting both peridotite and granulite. Prolate ellipsoid shown for fold hinge deformation.

Field structural observations as well as EBSD study show that S2 fabric in granulites and porphyroclastic fabric in peridotites were actively folded during large scale F3 folding of the MPB associated with partial melting of granulite and D3 amphibolite facies retrogression. This event is correlated to the development of amphibole-spinel coronas around garnet estimated to 700 °C and 0.5–0.8 GPa (Fig. 10a; stage IV of Medaris et al., 1990). A similar transition from the granulite fine-grained mylonitic fabric (S2) to the coarser-grained fabric (S3) associated to the partial melting has been described in other granulites in the Bohemian Massif as a result of decompression after rapid ascent of hot granulites to the mid-crustal levels (Franěk et al., 2006; Franěk et al., 2011). The F3 folding occurred at the regional scale and is associated with indentation of the thickened orogenic root by the Brunian promontory (Fig. 11c) as proposed by Schulmann et al. (2008). According to these authors, the S4 fabric records the later subhorizontal channel flow which transported passively the peridotite and granulite fold in partially molten rocks above the Brunia basement.

Emplacement of the Mohelno peridotite body along the highstress shear zone into the granulite followed by ascent to the mid-crustal levels and active folding fits well also with bilinear cooling histories calculated from garnet composition. Medaris et al. (1990) showed that the garnet core temperatures in excess of 1100 °C required extremely rapid cooling to quench the low almandine composition in the garnet interior. This event reflects emplacement of the hot peridotite into the colder granulitic lower crust during early stages of D2 event. The existence of garnet rim zoning requires a significant decrease of the cooling rate during the isothermal decompression associated with the vertical ascent of granulite and peridotite to the mid crustal levels during late stages of D2 and D3.

Rheological constraints for mechanical behavior of peridotite and granulite

An attempt is made to assess the rheological behavior of the Mohelno peridotite body and adjacent granulites for the P–T–D history discussed above. The coarse–grained peridotite microstructure cannot be successfully assessed because of insufficient number of measurable grains of olivine and pyroxene. However, existing data from mantle xenoliths show the presence of LPO, which is commonly interpreted as a result of dislocation creep at high temperatures and slow strain rates (e.g. Ildefonse et al., 1995; Soustelle and Tommasi, 2010). Dynamic recrystallization of studied peridotite occurred very likely at elevated stress conditions leading to significant grain size reduction down to 50 μm in diameter from an original coarse-grained microstructure in the intra-mantelic shear zone. Microstructural analyses of other peridotite mylonites indicate that shear localization results from the combined effects of grain

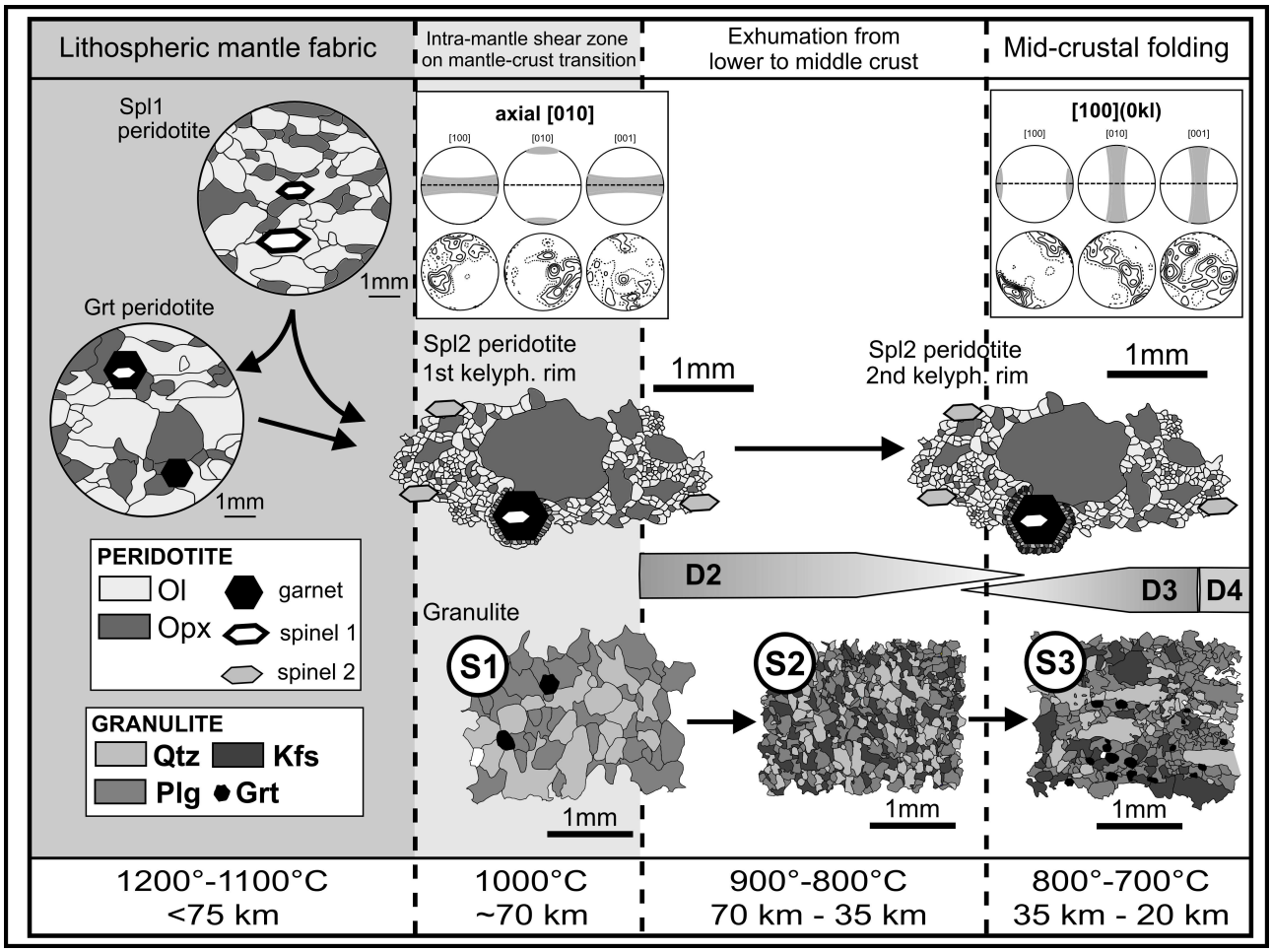

Figure 12. Diagram illustrating the evolution of the peridotite and granulite microstructures for different tectonic stages along proposed PT path. Active slip systems in olivine are proposed for different evolutionary stages of peridotite shearing and folding.

size reduction, grain boundary sliding and second phase pinning during deformation (Kennedy et al., 2002; Warren and Hirth, 2006; Toy et al., 2010). Microstructural analyses of the mylonite fabric in study as well as other peridotite bodies suggest that deformation of aggregates with a grain size of 10–100 μm occurred by dislocation-accommodated grain boundary sliding which produces an LPO. Grain boundary pinning, due to the mixing of pyroxenes and spinel among olivine grains during dislocation accommodated grain boundary sliding may result in permanent grain size reduction (Vissers et al., 1995; Jin et al., 1998; Warren and Hirth, 2006).

According to our model (Figs. 11b and 12) the axial [010] pattern originated at mantle P–T conditions during intra-mantllic shearing leading to crystal plasticity characteristic for transpressional regime (Tommasi et al., 1999). Subsequent thrust related emplacement of peridotite sheet into the crust and associated rapid quenching led very likely to important hardening of the peridotite and

freezing of intra-mantelic fabric. The D2 fine-grained microstructure of all phases in the host granulite suggests an accommodation of most of the strain during lower crustal ascent transporting passively peridotites (Fig. 12).

Our model also shows that the lineations calculated from the [100](0kl) patterns coincide with the MPB fold hinge, which suggest that this LPO pattern was acquired during deformation at mid-crustal conditions estimated at ~750 °C. This is in agreement with experimental studies (Demouchy et al., 2009) as well as natural mylonites (e.g. Warren and Hirth, 2006), which show that the lithospheric mantle can be deformed plastically at relatively low temperatures (600–800 °C). It is during the late D3 event when vertically anisotropic crust and mantle multilayer oriented at high angle to the advancing promontory (Fig. 11c) is folded thereby producing high stress concentrations in fold hinge regions (Fig. 4 in Schmalholz and Podladchikov, 1999). In this scenario, the folding of relatively strong peridotite layer may reactivate inherited fine-grained microstructure in hinge zone and produce new LPO pattern. For such a microstructure, a low stress is enough to activate further plastic deformation via dislocation-accommodated grain boundary sliding that produces LPO (Vissers et al., 1995; Jin et al., 1998; Warren and Hirth, 2006). The host granulite structures like parasitic folds and axial cleavage zones indicate that the host rocks were significantly weaker and accommodated folding of the peridotite layer.

References

- Artyushkov, E. V., (1973). Stresses in the lithosphere caused by crustal thickness inhomogeneities. J. Geophys. Res. 78, 7675–7708.

- Babuška, V., Plomerová, J., (2006). European mantle lithosphere assembled from rigid microplates with inherited seismic anisotropy. Phys. Earth Planet. In. 158, 264–280.

- Babuška, V., Plomerová, J., Vecsey, L., (2008). Mantle fabric of western Bohemian Massif (central Europe) constrained by 3D seismic P and S anisotropy. Tectonophysics 462, 149–163.

- Bachmann, F., Hielscher, R., Schaeben, H., (2010). Texture analysis with MTEX – Free and open source software toolbox. Solid State Phenom. 160, 63–68.

- Bascou, J., Delpech, G., Vauchez, A., Moine, B. N., Cottin, J. Y., Barruol, G., (2008). An integrated study of microstructural, geochemical, and seismic properties of the lithospheric mantle above the Kerguelen plume (Indian Ocean). Geochem. Geophys. Geosyst. 9, Q04036.

- Brace, W. F., Kohlstedt, D. L., (1980). Limits on lithospheric stress imposed by laboratory experiments. J. Geophys. Res. 85(B11), 6248–6252.

- Brueckner, H., Carswell, D., Griffin, W., (2002). Paleozoic diamonds within a Precambrian peridotite lens in UHP gneisses of the Norwegian Caledonides. Earth Planet. Sci. Lett. 203, 805–816.

- Brueckner, H. K., (1998). Sinking intrusion model for the emplacement of garnet-bearing peridotites into continent collision orogens. Geology 26, 631–634.

- Bunge, H., 1982. Texture analysis in materials sciences, Buttleworth, London. Burov, E., Watts, A., (2006). The long–term strength of continental lithosphere : "jelly sandwich" or "crème brûlée" ?. Geol. Soc. Am. Bull. 16(1) , 4–10 .

- Bystricky, M., Kunze, K., Burlini, L., Burg, J.-P., (2000). High shear strain of olivine aggregates: Rheological and seismic consequences. Science 290, 1564–1567.

- Carswell, D. A., O'Brien, P. J., (1993). Thermobarometry and geotectonic significance of high-pressure granulites: Examples from the Moldanubian Zone of the Bohemian Massif in Lower Austria. J. Petrol. 34, 427–459.

- Carter, N. L., Ave'Lallemant, H. G., (1970). High temperature flow of dunite and peridotite. Geol. Soc. Am. Bull. 81, 2181–2202.

- Chemenda, A. I., Mattauer, M., Malavieille, J., Bokun, A. N., (1995). A mechanism for syn-collisional rock exhumation and associated normal faulting: Results from physical modelling. Earth Planet. Sci. Lett. 132, 225–232.
- Chopra, P. N., Paterson, M. S., (1984). The role of water in the deformation of dunite. J. Geophys. Res. 89(B9), 7861–7876.
- Cooke, R. A., (2000). High-pressure/temperature metamorphism in the St. Leonhard Granulite Massif, Austria: evidence from intermediate pyroxene-bearing granulites. Int. J. Earth Sci. 89, 631–651.
- Cooke, R. A., O'Brien, P. J., (2001). Resolving the relationship between high P–T rocks and gneisses in collisional terranes: an example from the Gföhl gneiss–granulite association in the Moldanubian Zone, Austria. Lithos 58, 33–54.
- Couvy, H., Frost, D. J., Heidelbach, F., Nyilas, K., Ungar, T., Mackwell, S., Cordier, P., (2004). Shear deformation experiments of forsterite at 11 GPa – 1400 °C in the multianvil apparatus. Eur. J. Mineral. 16, 877–889.
- Demouchy, S., Schneider, S. E., Mackwell, S. J., Zimmerman, M. E., Kohlstedt, D. L., (2009). Experimental deformation of olivine single crystals at lithospheric temperatures. Geophys. Res. Lett. 36, L04304.
- Dijkstra, A. H., Drury, M. R., Vissers, R. L. M., Newman, J., Van Roermund, H. L. M., (2004). Shear zones in the upper mantle: evidence from alpine– and ophiolite–type peridotite massifs. Geol. Soc., Lond., Spec. Publ. 224, 11–24.
- Dobretsov, N., Mísař, Z., Popov, E., (1984). The P–T conditions of equilibrium for some pyrope peridotite and country rocks in the Moldanubian area at Mohelno (Eastern Moravia, Czechoslovakia). Miner. Slov. 16, 87–95.
- Drury, M. R., Vissers, R. L. M., Wal, D., Hoogerduijn Strating, E. H., (1991). Shear localisation in upper mantle peridotites. Pure Appl. Geophys. 137, 439–460.
- Edel, J., Weber, K., (1995). Cadomian terranes, wrench faulting and thrusting in the central Europe Variscides: geophysical and geological evidence. Geol. Rundsch. 84, 412–432.
- Ellis, S., (1996). Forces driving continental collision: Reconciling indentation and mantle subduction tectonics. Geology 24, 699–702.
- Etheridge, M., Wilkie, J., (1979). Grainsize reduction, grain boundary sliding and the flow strength of mylonites. Tectonophysics 58, 159–178.

- Fiala, J., Matějovská, O., Vaňková, V., (1987). Moldanubian granulites and related rocks: petrology, geochemistry and radioactivity. Rozpr. Česk. Akad. Věd, Řada Mat. Přír. Věd 97, 1–102.
- Franke, W., (2000). The mid-European segment of the Variscides: tectonostratigraphic units, terrane boundaries and plate tectonic evolution, In: Franke, W., Haak, V., Oncken, O., D., T. (Eds.), Orogenic processes: Quantification and modelling in the Variscan Belt. Geological Society, London, Special Publications 179, 35–61.
- Franěk, J., Schulmann, K., Lexa, O., (2006). Kinematic and rheological model of exhumation of high pressure granulites in the Variscan orogenic root: example of the Blanský les granulite, Bohemian Massif, Czech Republic. Mineral. Petrol. 86, 253–276.
- Franěk, J., Schulmann, K., Lexa, O., Tomek, Č., Edel, J.-B., (2011). Model of syn-convergent extrusion of orogenic lower crust in the core of the Variscan belt: implications for exhumation of high-pressure rocks in large hot orogens. J. Metamorph. Geol. 29, 53–78.
- Frost, H., Ashby, M., (1982). Deformation mechanisms – recognition from natural tectonites, Pergamon Press, Oxford.
- Guillope, M., Poirier, J. P., (1979). Dynamic recrystallization during creep of single–crystalline halite: An experimental study. J. Geophys. Res. 84, 5557–5567.
- Guy, A., Edel, J.-B., Schulmann, K., Tomek, C., Lexa, O., (2011). A geophysical model of the Variscan orogenic root (Bohemian Massif): Implications for modern collisional orogens. Lithos 124, 144–157.
- Handy, M., (1989). Deformation regimes and the rheological evolution of fault zones in the lithosphere: the effects of pressure, temperature, grainsize and time. Tectonophysics 163, 119–152.
- Hasalová, P., Janoušek, V., Schulmann, K., Štípská, P., Erban, V., (2008b). From orthogneiss to migmatite: Geochemical assessment of the melt infiltration model in the Gföhl Unit (Moldanubian Zone, Bohemian Massif). Lithos 102, 508–537.
- Hasalová, P., Schulmann, K., Lexa, O., Štípská, P., Hrouda, F., Ulrich, S., Haloda, J., Týcová, P., (2008a). Origin of migmatites by deformation–enhanced melt infiltration of orthogneiss: a new model based on quantitative microstructural analysis. J. Metamorph. Geol. 26, 29–53.
- Hirth, G., Kohlstedt, D., (2003). Rheology of the upper mantle and the mantle wedge: A view from the experimentalists. Geophys. Monogr. 138, 83–105.
- Ildefonse, B., Billiau, S., Nicolas, A., (1995). A detailed study of mantle flow away from diapirs in the Oman ophiolite, In: Vissers, R., Nicolas, A. (Eds.), Mantle and lower crust exposed in oceanic ridges and in ophiolites. Kluwer, 163–177.

- Jackson, J., (2002). Strength of the continental lithosphere. GSA Today 12, Part 9, 4–9.
- Janoušek, V., Finger, F., Roberts, M., Frýda, J., Pin, C., Dolejš, D., (2004). Deciphering the petrogenesis of deeply buried granites: whole-rock geochemical constraints on the origin of largely undepleted felsic granulites from the Moldanubian Zone of the Bohemian Massif. Earth Env. Sci. T. R. So. 95, 141–159.
- Janoušek, V., Holub, F. V., (2007). The causal link between HP–HT metamorphism and ultrapotassic magmatism in collisional orogens: case study from the Moldanubian Zone of the Bohemian Massif. P. Geologist. Assoc. 118, 75–86.
- Jin, D., Karato, S.-I., Obata, M., (1998). Mechanisms of shear localization in the continental lithosphere: inference from the deformation microstructures of peridotites from the Ivrea zone, northwestern Italy. J. Struct. Geol. 20, 195–209.
- Johnson, E., Rossmann, G., (2003). The concentration and speciation of hydrogen in feldspars using FTIR and 1H MAS NMR spectroscopy. Am. Mineral. 88, 901–911.
- Jung, H., Karato, S.-I., (2001). Water-induced fabric transitions in olivine. Science 293, 1460–1463.
- Kamei, A., Obata, M., Michibayashi, K., Hirajima, T., Svojtka, M., (2010). Two contrasting fabric patterns of olivine observed in garnet and spinel peridotite from a mantle-derived ultramafic mass enclosed in felsic granulite, the Moldanubian Zone, Czech Republic. J. Petrol. 51, 101–123.
- Karato, S.-I., Toriumi, M., Fujii, T., (1980). Dynamic recrystallization of olivine single crystals during high–temperature creep. Geophys. Res. Lett. 7, 649–652.
- Kennedy, L. A., Russell, J. K., Kopylova, M. G., (2002). Mantle shear zones revisited: The connection between the cratons and mantle dynamics. Geology 30, 419–422.
- Klemme, S., O'Neill, H. S., (2000). The near–solidus transition from garnet lherzolite to spinel lherzolite. Contrib. Mineral. Petrol. 138, 237–248.
- Knipe, R., (1989). Deformation mechanisms – recognition from natural tectonites. J. Struct. Geol. 11, 127–146.
- Kratinová, Z., Závada, P., Hrouda, F., Schulmann, K., (2006). Non-scaled analogue modelling of AMS development during viscous flow: A simulation on diapir–like structures. Tectonophysics 418, 51–61.
- Lexa, O., Schulmann, K., Janoušek, V., Štípská, P., Guy, A., Racek, M., (2011). Heat sources and trigger mechanisms of exhumation of HP granulites in Variscan orogenic root. J. Metamorph. Geol. 29, 79–102.

- Liang, X., Zhou, S., Chen, Y. J., Jin, G., Xiao, L., Liu, P., Fu, Y., Tang, Y., Lou, X., Ning, J., (2008). Earthquake distribution in southern Tibet and its tectonic implications. J. Geophys. Res.-Sol. Earth 113, B12409.

- Machek, M., Ulrich, S., Janoušek, V., (2009). Strain coupling between upper mantle and lower crust: natural example from the Běstvina granulite body, Bohemian Massif. J. Metamorph. Geol. 27, 721–737.

- Mackwell, S. J., Kohlstedt, D. L., Paterson, M. S., (1985). The role of water in the deformation of olivine single crystals. J. Geophys. Res. 90(B13), 319–333.

- Mainprice, D., (2007). Seismic anisotropy of the deep Earth from a mineral and rock physics perspective, In: Schubert, G. (Eds.), Treatise on Geophysics vol. 2. Elsevier Ltd., 437–492.

- Mainprice, D., (1990). A FORTRAN program to calculate seismic anisotropy from the lattice preferred orientation of minerals. Comput. Geosci. 16, 385–393.

- Matějovská, O., (1967). Petrogenesis of the Moldanubian granulites near Náměšť nad Oslavou. Krystalinikum 5, 85–104.

- Matějovská, O., (1975). The Moldanubian gneiss series of south–western Moravia and its relation to granulites.. Věstn. Ústřed. Ústav. Geol. 50, 345–351.

- Means, W., (1990). Kinematics, stress, deformation and material behavior. J. Struct. Geol. 12, 953–971.

- Medaris, L. J., Wang, H., Mísař, Z., Jelínek, E., (1990). Thermobarometry, diffusion modelling and cooling rates of crustal garnet peridotites: Two examples from the Moldanubian zone of the Bohemian Massif. Lithos 25, 189–202.

- Medaris, L. J., Wang, H., Jelínek, E., Mihaljevič, M., Jakeš, P., (2005). Characteristics and origins of diverse Variscan peridotites in the Gföhl Nappe, Bohemian Massif, Czech Republic. Lithos 82, 1–23.

- Medaris, L., Ackerman, L., Jelínek, E., Toy, V., Siebel, W., Tikoff, B., (2009). The Sklené garnet peridotite: petrology, geochemistry, and structure of a mantle–derived boudin in Moldanubian granulite. J. Geosci. 54, 4, 301–323.

- Molnar, P., Chen, W.-P., (1983). Focal depths and fault plane solutions of earthquakes under the Tibetan plateau. J. Geophys. Res. 88, 1180–1196.

- Molnar, P., England, P., Martinod, J., (1993). Mantle dynamics, uplift of the Tibetan Plateau, and the Indian Monsoon. Rev. Geophys. 31, 357–396.

- Molnar, P., Lyon-Caen, H., (1988). Some simple physical aspects of the support, structure, and evolution of mountain belts.. Geol. Soc. Am. Spec. Pap. 218, 179–207.

- Monsalve, G., McGovern, P., Sheehan, A., (2009). Mantle fault zones beneath the Himalayan collision: Flexure of the continental lithosphere. Tectonophysics 477, 66–76.

- O'Neill, H. S. C., (1981). The transition between spinel lherzolite and garnet lherzolite, and its use as a Geobarometer. Contrib. Mineral. Petrol. 77, 185–194.

- Post, A., Tullis, J., (1999). A recrystallized grain size piezometer for experimentally deformed feldspar aggregates. Tectonophysics 303, 159 – 173.

- Precigout, J., Gueydan, F., Gapais, D., Garrido, C., Essaifi, A., (2007). Strain localisation in the sub-continental mantle – a ductile alternative to the brittle mantle. Tectonophysics 445, 318–336.

- Racek, M., Štípská, P., Pitra, P., Schulmann, K., Lexa, O., (2006). Metamorphic record of burial and exhumation of orogenic lower and middle crust: a new tectonothermal model for the Drosendorf window (Bohemian Massif, Austria). Mineral. Petrol. 86, 221–251.

- Racek, M., Štípská, P., Powell, R., (2008). Garnet–clinopyroxene intermediate granulites in the St. Leonhard massif of the Bohemian Massif: ultrahigh–temperature metamorphism at high pressure or not?. J. Metamorph. Geol. 26, 253–271.

- Ramberg, H., (1981). The role of gravity in orogenic belts. Geol. Soc., Lond., Spec. Publ. 9, 125–140.

- Ranalli, G., Murphy, D. C., (1987). Rheological stratification of the lithosphere. Tectonophysics 132, 281–295.

- Raterron, P., Amiguet, E., Chen, J., Li, L., Cordier, P., (2009). Experimental deformation of olivine single crystals at mantle pressures and temperatures. Phys. Earth Planet. In. 172, 74–83.

- Raterron, P., Wu, Y., Weidner, D. J., Chen, J., (2004). Low-temperature olivine rheology at high pressure. Phys. Earth Planet. In. 145, 149–159.

- Roux, V. L., Tommasi, A., Vauchez, A., (2008). Feedback between melt percolation and deformation in an exhumed lithosphere–asthenosphere boundary. Earth Planet. Sci. Lett. 274, 401–413.

- Rutter, E., Brodie, K., (1992). Rheology of the lower crust, In: Fountain, D., A. R., Kay, R. (Eds.), Continental Lower Crust. Elsevier, 201–267.

- Rybacki, E., Dresen, G., (2000). Dislocation and diffusion creep of synthetic anorthite aggregates. J. Geophys. Res. 105, 26017–26036.

- Sander, B., 1930. Gefügekunde der Gesteine, Springer, Vienna.

- Schmalholz, S. M., Podladchikov, Y., (1999). Buckling versus folding: Importance of viscoelasticity. Geophys. Res. Lett. 26, 2641–2644.

- Schmidt, N.-H., Olesen, N. O., (1989). Computer–aided determination of crystal–lattice orientation from electron channeling patterns in the SEM. Can. Mineral. 27, 15–22.

- Schmädicke, E., Evans, B. W., (1997). Garnet–bearing ultramafic rocks from the Erzgebirge, and their relation to other settings in the Bohemian Massif. Contrib. Mineral. Petrol. 127, 57–74.

- Schmädicke, E., Gose, J., Will, T. M., (2010). The P–T evolution of ultra high temperature garnet–bearing ultramafic rocks from the Saxonian Granulitgebirge Core Complex, Bohemian Massif. J. Metamorph. Geol. 28, 489–508.

- Schulmann, K., Konopásek, J., Janoušek, V., Lexa, O., Lardeaux, J.-M., Edel, J.-B., Štípská, P., Ulrich, S., (2009). An Andean type Palaeozoic convergence in the Bohemian Massif. C. R. Geosci. 341, 266–286.

- Schulmann, K., Kroner, A., Hegner, E., Wendt, I., Konopásek, J., Lexa, O., Štípská, P., (2005). Chronological constraints on the pre-orogenic history, burial and exhumation of deep–seated rocks along the eastern margin of the Variscan Orogen, Bohemian Massif, Czech Republic. Am. J. Sci. 305, 407–448.

- Schulmann, K., Martelat, J.-E., Ulrich, S., Lexa, O., Štípská, P., Becker, J. K., (2008). Evolution of microstructure and melt topology in partially molten granitic mylonite: Implications for rheology of felsic middle crust. J. Geophys. Res. 113, B10406.

- Schulmann, K., Schaltegger, U., Ježek, J., Thompson, A. B., Edel, J.-B., (2002). Rapid burial and exhumation during orogeny: Thickening and synconvergent exhumation of thermally weakened and thinned crust (Variscan orogen in Western Europe). Am. J. Sci. 302, 856–879.

- Skemer, P., Katayama, I., Jiang, Z., Karato, S.-I., (2005). The misorientation index: Development of a new method for calculating the strength of lattice–preferred orientation. Tectonophysics 411, 157–167.

- Soustelle, V., Tommasi, A., (2010). Seismic properties of the supra-subduction mantle: Constraints from peridotite xenoliths from the Avacha volcano, southern Kamchatka. Geophys. Res. Lett. 37, L13307.

- Soustelle, V., Tommasi, A., Bodinier, J. L., Garrido, C. J., Vauchez, A., (2009). Deformation and reactive melt transport in the mantle lithosphere above a large–scale partial melting domain: the Ronda Peridotite Massif, Southern Spain. J. Petrol. 50, 1235–1266.

- Soustelle, V., Tommasi, A., Demouchy, S., Ionov, D. A., (2010). Deformation and fluid-rock interaction in the supra-subduction mantle: Microstructures and water contents in peridotite xenoliths from the Avacha volcano, Kamchatka. J. Petrol. 51, 363–394.

- Šichtařová, I., (1981). Moldanubian amphibolites in the area SE of Náměšť nad Oslavou. Věstn. Ústřed. Ústav. Geol. 56, 203–214.
- Štípská, P., Powell, R., (2005). Does ternary feldspar constrain the metamorphic conditions of high-grade meta–igneous rocks? Evidence from orthopyroxene granulites, Bohemian Massif. J. Metamorph. Geol. 23, 627–647.
- Štípská, P., Schulmann, K., Kröner, A., (2004). Vertical extrusion and middle crustal spreading of omphacite granulite: a model of syn-convergent exhumation (Bohemian Massif, Czech Republic). J. Metamorph. Geol. 22, 179–198.
- Štípská, P., Schulmann, K., Powell, R., (2008). Contrasting metamorphic histories of lenses of high-pressure rocks and host migmatites with a flat orogenic fabric (Bohemian Massif, Czech Republic): a result of tectonic mixing within horizontal crustal flow?. J. Metamorph. Geol. 26, 623–646.
- Tajčmanová, L., Konopásek, J., Schulmann, K., (2006). Thermal evolution of the orogenic lower crust during exhumation within a thickened Moldanubian root of the Variscan belt of Central Europe. J. Metamorph. Geol. 24, 119.
- Thompson, A., Schulmann, K., Ježek, J., Tolar, V., (2001). Thermally softened continental extensional zones (arcs and rifts) as precursors to thickened orogenic belts. Tectonophysics 332, 115–141.
- Tikoff, B., Russo, R., Teyssier, C., Tommasi, A., (2004). Mantle–driven deformation of orogenic zones and clutch tectonics, In: Grocott, J., McCaffrey, K. J. W., Yaylor, G., Tikoff, B. (Eds.), Vertical coupling and decoupling in the lithosphere. Geological Society, London, Special Publications, 41–64.
- Tikoff, B., Teyssier, C., Waters, C., (2002). Clutch tectonics and the partial attachment of lithospheric layers. EGU S. Mueller Spec. Publ. Ser. 1, 57–73.
- Tollmann, A., (1982). Grossräumiger variszischer Deckenbau im Moldanubikum und neue Gedanken zum Variszikum Europas. Geotekton. Forsch. 64, 1–91.
- Tommasi, A., Mainprice, D., Canova, G., Chastel, Y., (2000). Viscoplastic self–consistent and equilibrium–based modeling of olivine lattice preferred orientations: Implications for the upper mantle seismic anisotropy. J. Geophys. Res. 105, 7893–7908.
- Tommasi, A., Tikoff, B., Vauchez, A., (1999). Upper mantle tectonics: three–dimensional deformation, olivine crystallographic fabrics and seismic properties. Earth Planet. Sci. Lett. 168, 173 – 186.
- Tommasi, A., Vauchez, A., Ionov, D. A., (2008). Deformation, static recrystallization, and reactive melt transport in shallow subcontinental mantle xenoliths (Tok Cenozoic volcanic field, SE Siberia). Earth Planet. Sci. Lett. 272, 65–77.

- Toy, V. G., Newman, J., Lamb, W., Tikoff, B., (2010). The role of pyroxenites in formation of shear instabilities in the mantle: Evidence from an ultramafic ultramylonite, Twin Sisters Massif, Washington. J. Petrol. 51, 55–80.

- Twiss, R. J., (1977). Theory and applicability of a recrystallized grain size paleopiezometer. Pure Appl. Geophys. 115, 227–244.

- Urban, M., (1992). Kinematics of the Variscan thrusting in the Eastern Moldanubicum (Bohemian Massif, Czechoslovakia): evidence from the Náměšť granulite massif. Tectonophysics 201, 371–391.

- Van der Wal, D., Chopra, P., Drury, M., Gerald, J. F., (1993). Relationships between dynamically recrystallized grain size and deformation conditions in experimentally deformed olivine rocks. Geophys. Res. Lett. 20, 1479–1482.

- Vauchez, A., Tommasi, A., Barruol, G., (1998). Rheological heterogeneity, mechanical anisotropy and deformation of the continental lithosphere. Tectonophysics 296, 61–86.

- Vissers, R. L. M., Drury, M. R., Hoogerduijn-Strating, E. H., Spiers, C. J., van der Wal, D., (1995). Mantle shear zones and their effect on lithosphere strength during continental breakup. Tectonophysics 249, 155–171.

- Vollmer, F. W., (1990). An application of eigenvalue methods to structural domain analysis. Geol. Soc. Am. Bull. 102, 786–791.

- Walter, M., Katsura, T., Kubo, A., Shinmei, T., Nishikawa, O., Ito, E., Lesher, C., Funakoshi, K., (2002). Spinel–garnet lherzolite transition in the system CaO–MgO–Al_2O_3–SiO_2 revisited: an in situ X-ray study. Geochim. Cosmochim. Acta 66, 2109–2121.

- Warren, J., Hirth, G., (2006). Grain size sensitive deformation mechanisms in naturally deformed peridotites. Earth Planet. Sci. Lett. 248, 438–450.

- Weijermars, R., (1993). Progressive deformation of single layers under constantly oriented boundary stresses. J. Struct. Geol. 15, 911–922.

Supplementary material

M-index and strength of lattice preferred orientation

Strength of a lattice preferred orientation can be expressed by different parameters. M-index was calculated for each olivine sample, also texture index (J-index) and fabric entropy parameters were calculated in Mtex (Bachmann et al., 2010). Texture index and fabric entropy parameters were calculated for both default kernel function and optimal kernel function for ODF estimation from given EBSD dataset. Both parameters show linear correlation with Mindex (Fig. A.1), which is in agreement with previous correlations of M- and J-indexes in Soustelle et al. (2010). Therefore, we assume the M-index as suitable representation of the fabric strength. Using of the optimal kernel function causes systematic vertical shift for both parameters.

Deformation mechanism maps (DMMs)

Deformation mechanism maps were introduced in rock deformation studies, following their development in material science in the seventies of the last century (Etheridge and Wilkie, 1979; Handy, 1989). However, extrapolation of experimental deformation mechanism map to natural conditions of deformation is not straightforward (e.g. Knipe, 1989; Means, 1990) and often out of reasonable scale and locally even contrary to microstructural observations. Nevertheless, several recent studies applied the DMM calculations to assess the rheological evolution of naturally peridotites (Warren and Hirth, 2006; Precigout et al., 2007). Therefore, an attempt is made to assess the rheological behavior of the Mohelno peridotite body and adjacent granulites for the P–T–D history discussed above. Olivine deformation mechanism maps (DMM) were constructed for expected mantle–crust transition temperature (900 °C) and for lower temperature limit for D3 folding (700 °C) together with anorthite DMM for 700 °C (Fig. A.2). Deformation mechanism maps show differential stress as a function of grain size for varied strain rates at constant temperature (Frost and Ashby, 1982). In our DMM the mantle rheology is represented by experiments by Hirth and Kohlstedt (2003) for dry olivine, whereas granulite is approximated by experimental data for synthetic anorthite with 0.07 % of water (Rybacki and Dresen, 2000). These plagioclase experiments were selected because of water content of natural feldspars, which ranges from 0.02 to 0.5 wt. % (Johnson and Rossmann, 2003).

Deformation mechanism maps (DMMs) are constructed to constrain the deformation conditions of the peridotite and granulite and show differential stress as a function of grain size for different strain

rates at constant temperature. Four different deformation mechanisms are actually proposed for olivine: dislocation creep (GSI), diffusion creep (GSS), GBS creep (using terminology of Hirth and Kohlstedt, 2003) and low-temperature plasticity (LTP) by Raterron et al. (2004). Two different deformation mechanisms are considered for anortite (Rybacki and Dresen, 2000): dislocation creep (GSI) and diffusion creep (GSS). These experimental data on synthetic plagioclase were selected because of water content of natural feldspars, which ranges from 0.02 to 0.5 wt. % (Johnson and Rossmann, 2003). The overall strain rate $\dot{\varepsilon}$ is then defined as the sum of the partial strain rates for each of the creeping mechanisms: $\dot{\varepsilon} = \dot{\varepsilon}_{\text{disl}} + \dot{\varepsilon}_{\text{diff}}$ for feldspar and for $\dot{\varepsilon} = \dot{\varepsilon}_{\text{disl}} + \dot{\varepsilon}_{\text{diff}} + \dot{\varepsilon}_{\text{GBS}} + \dot{\varepsilon}_{\text{LTP}}$ olivine, where $\dot{\varepsilon}_{\text{disl}}$ is the strain rate for dislocation creep, $\dot{\varepsilon}_{\text{diff}}$ for diffusion creep, $\dot{\varepsilon}_{\text{GBS}}$ for GBS creep and $\dot{\varepsilon}_{\text{LTP}}$ for low-temperature plasticity. Partial strain rates can be calculated according power-law equations for dislocation creep (GSI):

$$\dot{\varepsilon}_{disl} = A_{disl}\sigma^{n_{disl}} exp(\frac{-Q_{disl}}{RT}) \tag{0.0.1}$$

diffusion creep (GSS):

$$\dot{\varepsilon}_{diff} = A_{diff}\sigma^{n_{diff}} d^{-m_{diff}} exp(\frac{-Q_{diff}}{RT}) \tag{0.0.2}$$

GBS creep:

$$\dot{\varepsilon}_{GBS} = A_{GBS}\sigma^{n_{GBS}} d^{-m_{GBS}} exp(\frac{-Q_{GBS}}{RT}) \tag{0.0.3}$$

low-temperature plasticity:

$$\dot{\varepsilon}_{LTP} = A_{LTP} exp(-F_0 \frac{[1-(\sigma/\tau)^p]^q}{RT}) \tag{0.0.4}$$

where, A_{disl}, A_{diff}, A_{GBS}, n_{disl}, n_{diff}, n_{GBS}, m_{diff}, m_{GBS}, Q_{disl}, Q_{diff}, Q_{GBS}, R, T, σ and d, respectively are: according to each deformation mechanism, the pre-exponential constant, the stress exponent, the grain size exponent, the activation energy and, the gas constant 8.314 J.mol^{-1}K^{-1}, the temperature, the stress and the grain size. For LTP equation the additional parameters are: A_{LTP} a pre-exponential constant, F_0 the free energy for the dislocations to overcome friction and obstacles (sometimes refered as activation energy), τ the maximum glide resistance which quantifies the Peierls' stress, p and q two fitting parameters. Set of all values for olivine and anortite are listed in Table A.1. The deformation maps are divided into several fields: dislocation creep field (GSI), diffusion creep field (GSS) and specifically for olivine DMMs also GBS creep and low-temperature plasticity fields. Each field represents stress vs. grain size space for which one deformational mechanism is dominant e.g. for the dislocation creep field (GSI) $\dot{\varepsilon}_{\text{disl}} > (\dot{\varepsilon}_{\text{diff}} + \dot{\varepsilon}_{\text{GBS}} + \dot{\varepsilon}_{\text{LTP}})$ the bulk strain rate is dominated by

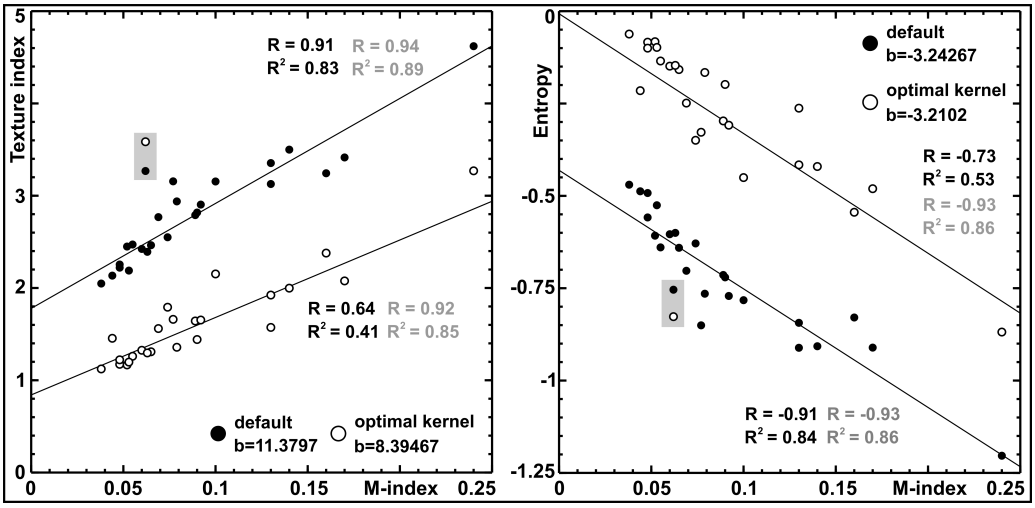

Figure A.1. Strength of olivine LPO in analysed samples illustrated by the M-index vs. texture index (J-index) (left) and M-index vs. entropy of the ODF (right) (see text for more detailed description). Correlation coefficients in black are for whole dataset, in grey from dataset with excluded value lying outside of trend (sample LN37, in grey rectangle). High value of correlation coefficient (R2) indicates mutual consistency of these two LPO strength parameters.

dislocation creep strain rate. Similarly in other DMM fields the other deformational mechanisms are dominant and control the bulk strain rate. Equilibrium between recrystallised grain size and stress is defined by different piezometric relations. For DMM of olivine the piezometers of Twiss (1977); Karato et al. (1980); Van der Wal et al. (1993) are used, for feldspar are shown HT piezometer of Twiss (1977) and LT piezometer of Post and Tullis (1999). All piezometers are listed in Table A.2.

Our calculations confirm that the DMM calculation approach is not robust enough to predict the rheological evolution of mantle rocks with the current database of natural microstructural observations and experimental data. However, the DMM approach should be cultivated in the future to avoid simplifying use of dislocation creep equations in lithosphere scale numerical modeling (Thompson et al., 2001; Burov and Watts, 2006).

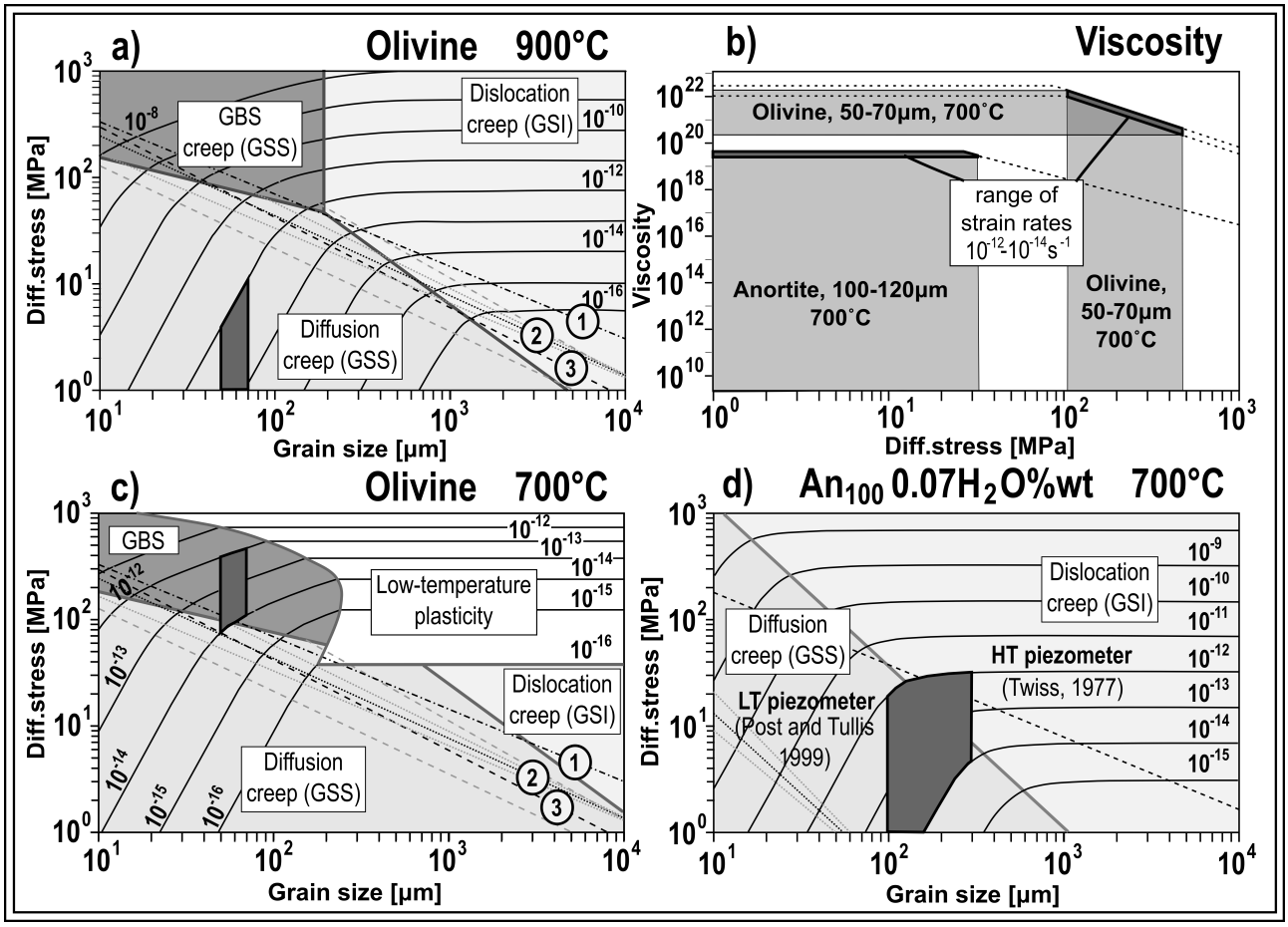

Figure A.2. a) Deformation mechanism map for olivine for measured grain size at constant temperature of 900 °C indicate diffusion creep as the main mechanism. b) Summarized graph of strength and viscosity for range of common natural strain rates (10^{-14}–10^{-12}). c,d) Deformation mechanism maps for olivine and plagioclase constructed at constant temperature of 700 °C shows difference in strength between both lithologies for range of natural strain rates. Measured grain sizes of olivine and feldspars indicate dislocation creep assisted by GBS and diffusional creep as the dominant operating deformation mechanisms, respectively. Olivine piezometers: 1) Twiss (1977), 2) Van der Wal et al. (1993), 3) Karato et al. (1980).

Table A.1

Olivine dry	***Hirth and Kohlstedt, 2003 ****Raterron et al, 2004**
$^{*}A_{disl}$	1,1.10^{5} MPa^{-n}.s^{-1}
$^{*}A_{diff}$	1,5.10^{9} MPa^{-n}.s^{-1}
$^{*}A_{GBS}$	6,5.10^{3} MPa^{-n}.s^{-1}
$^{*}n_{disl}$	3,5
$^{*}n_{diff}$	1
$^{*}n_{GBS}$	3,5
$^{*}m_{diff}$	3
$^{*}m_{GBS}$	2
$^{*}Q_{disl}$	530 ($\pm$ 4 kJ.mol^{-1})
$^{*}Q_{diff}$	375 ($\pm$ 50 kJ.mol^{-1})
$^{*}Q_{GBS}$	400 (kJ.mol^{-1})
$^{**}A_{ltp}$	2,6.10^{6} (+23 -2.3 s^{-1})
$^{**}F_0$	564 ($\pm$ 89 kJ.mol^{-1})
$^{**}\tau$	15,4 (+/- 1 GPa)
$^{**}p$	2/3
$^{**}q$	2
Anortite$_{100}$ 0.07 wt.% H_2O	**Rybacki and Dresden, 2000**
A_{disl}	$10^{2.6}$ MPa^{-n}.s^{-1}
A_{diff}	$10^{1.7}$ MPa^{-n}.s^{-1}
n_{disl}	3
n_{diff}	1
m_{diff}	3
Q_{disl}	356 ($\pm$ 9 kJ.mol^{-1})
Q_{diff}	170 ($\pm$ 6 kJ.mol^{-1})

Table A.1 Parameters for dislocation creep (GSI), diffusion creep (GSS) in olivine and anorthite and specifically for olivine also GBS creep and low-temperature plasticity creep.

Table A. 2 Equations and parameters for used piezometer relations for olivine and anorthite.

Mineral/Author	Relation	Parameters
Olivine		
Twiss (1977)	$\sigma(MPA) = BD^p$	B = *14.6*
		p = *-0.68*
		D = grain size in mm
Van der Wal (1993)	$\sigma(MPA) = (B/D)^{1/p}$	B = *1,5.10^4*
		p = *1.33*
		D = grain size in mm
Karato (1980)	$\sigma(MPA) = (B/D)^{1/p}$	B = *8,3.10^3*
		p = *1.18*
		D = grain size in mm
Feldspar		
Twiss (1977)	$\sigma(MPA) = BD^p$	B = *7.8*
		p = *-0.68*
		D = grain size in mm
Post and Tullis (1999)	$\sigma(MPA) = (B/D)^{1/p}$	B = *55*
		p = *0.66*
		D = grain size in mm

Origin of anisotropy of magnetic susceptibility in serpentinized peridotite

Vladimír KUSBACH[*,1,2], Karel Schulmann[2], Stanislav Ulrich[3], František Hrouda[1,4], Marta Chlupáčová[4], Fabienne Huber[5]

Affiliations

[1)] Institute of Petrology and Structural Geology, Charles University in Prague, Albertov 6, 12843 Praha 2, Czech Republic

[2)] Institut de Physique du Globe de Strasbourg, IPGS – UMR 7516, CNRS et Universite de Strasbourg (EOST), 1 Rue Blessig, 67084 Strasbourg, France

[3)] Geophysical Institute v.v.i., Academy of Sciences of the Czech Republic, Boční II/1401, 141 31, Praha 4, Czech Republic

[4)] AGICO Inc., Ječná 29a, Brno, Czech Republic

[5)] LhyGes EOST, Université de Strasbourg, 1 Rue Blessig, 67084 Strasbourg, France

(in preparation for Journal of Geophysical Research)

Abstract

The serpentinization of spinel to garnet Mohelno peridotite body is characterized by presence of the lizardite and iron oxides and alters 50% to 100% of the rock volume. Study of low temperature and high temperature variation of magnetic susceptibility indicates that the peridotite samples are subdivided into three main groups. Group I shows susceptibilities lower than 10^{-3} [SI] that corresponds to paramagnetic minerals only, while Group II and Group III show magnetic susceptibilities 10^{-3}-10^{-2} [SI] and higher than 10^{-2} [SI] characteristic for ferromagnetic minerals. The AMS reveals three main types of fabric: 1) Type I fabric characterized by clustered K_1 directions, girdle distribution of K_2 and K_3 directions, prolate shape of AMS ellipsoid, low degree of magnetic anisotropy and coincides with Group I, 2) the most common Type II fabric pattern marked by clustered K_1, K_2, K_3 directions, plane strain to oblate fabrics and generally high degree of susceptibility. 2) Type III fabric clustered K_3 directions, girdle distribution of K_1 and K_2 directions, mainly oblate shapes of AMS and intermediate to high degree of magnetic anisotropy. Magnetic foliation follows the fold shape of the peridotite in the Group I and II, while in the Group III there are foliations forming NW-SE trending great girdle as well as one strong subgroup of foliations dipping to the West at moderate angles. Magnetic lineation is gently plunging in the foliation without preferred orientation in the Group I, while in the Group II and III it is either gently plunging to the South or it concentrates around the peridotite fold axis moderately plunging to the West. The Group I samples reflect a fabric of peridotite. Advanced serpentinization and ferromagnetic fabric measured in the Group II and III can be explained as a result of two competing factors: 1) the penetration of H_2O-rich fluids along the grain boundaries in the fine-grained microstructure and crystallization of magnetite following grain boundary network mimetize the shape of olivine and pyroxene within mylonitic microstructure. 2) the deformation superimposed on almost random serpentine and magnetite matrix bearing well oriented olivine and pyroxene. In attempt to understand the evolution of the magnetic anisotropy a simple model of the magnetic fabric in the serpentinized peridotite has been constructed. Further, we discuss the influence of precursor peridotite microstructure on the magnetic fabric acquired during static serpentinization, and explained the deformational origin of the Group III magnetic fabric by large scale regional deformation recorded exclusively by ferromagnetic minerals in the Mohelno peridotite body.

Keywords

Anisotropy of magnetic susceptibility • AMS • peridotite • orogenic lower crust • serpentinization

Introduction

Studies of magnetic fabrics in mantle rocks are carried out mostly in ocean floor peridotites (Oufi et al., 2002; Hyndman and Peacock, 2003; Evans, 2010) and/or ophiolites (Borradaile and Lagroix, 2001; Borradaile and Lucas, 2003) attempting to determine various physical properties of the oceanic lithosphere. Studies of magnetic fabric in orogenic peridotites embedded in continental crust are less frequent (Ferré et al., 2005a; Hrouda et al., 2009a,b; Liu et al., 2010) although they may provide data about olivine lattice preferred orientation (Ferré et al., 2005b), primary magnetic fabric in continental lithospheric mantle (Hrouda et al., 2009b) and about serpentinization process during orogenesis (MacDonald and Ellwood, 1988; Richter and MacLeod, 1996; Jelenska and Werner, 1997; Borradaile and Lagroix, 2001; Borradaile and Lucas, 2003).

Serpentinization is a relatively low-temperature metamorphic process of hydration and/or fluid alteration of an ultramafic rock represented by a simple MgO-SiO_2-H_2O system (Hyndman and Peacock, 2003) which produces many different hydrous minerals, most importantly phyllosilicates of serpentine group (antigorite, lizardite, chrysotile), brucite and talc. The modal proportions of these minerals depend on ultramafic rock and fluid compositions, temperature and pressure (Manning, 1995; Hyndman and Peacock, 2003).

Stability of the different serpentine polymorphs was widely explored (Ulmer and Trommsdorff, 1995; Hacker et al., 2003; Hyndman and Peacock, 2003) with respect to temperature and pressure variations. For instance, the serpentine polymorph antigorite is stable at relatively high temperatures (300 °C to 620 °C) at pressure about 1 GPa in subduction zone settings. Rarely fibrous antigorite is reported for low grade metamorphic conditions and high-deformation setting at slow-spreading mid-oceanic ridge (Ribeiro Da Costa et al., 2008). For other two serpentine polymorphs – lizardite and chrysotile lower temperature conditions of around 200 °C were inferred (e.g. Evans, 1977). For temperatures lower than 500 °C in olivine-rich rocks (dunite, harzburgite, enriched harzburgite) serpentine occurs together with brucite (Hacker et al., 2003; Hyndman and Peacock, 2003) while talc can be present in mineral assemblage as product of high temperature (~700 °C) decomposition of pyroxene or as late brake-up product of antigorite (~200 °C; Hyndman and Peacock, 2003).

It is the serpentinization process along with mineralogical transformations mentioned above which radically change the magnetic properties of mantle rocks. The Fe partitioning into serpentine, brucite and magnetite, common magnetic minerals associated with olivine breakdown (rarely pure Fe) is the most important process that influences magnetic properties. Evans (2010) suggested that diffusion of Mg-Fe in olivine can minimize growth of magnetite during Mg-rich antigorite serpentinization at temperatures above 500 °C. On the other hand, low temperature Mg-rich lizardite serpentinization will inevitably produce magnetite. Therefore, it is important to recognize the P–T conditions of serpentinization in order to assess the magnetite origin in mantle rocks and its influence on magnetic properties.

The magnetic properties of serpentinised peridotite can be described in i) an ellipsoid of anisotropy of magnetic susceptibility (AMS) like degree of anisotropy, ii) shape of AMS ellipsoid and iii) orientation of principal magnetic susceptibility directions. The variations of these parameters in ultramafic body enclosed in continental crust provide information about temperature, fluid influx and deformation of mantle fragments and surrounding deep seated continental crust at late stages of orogenesis in general. In this work we studied anisotropy of magnetic susceptibility of one of largest peridotite body of European Variscan belt that underwent complex tectono-metamorphic history at high temperatures and high to moderate pressures (Chapter 2). An attempt is made to understand magnetic fabric from this highly serpentinized peridotite in order to characterize final stages of mantle – crust interactions during Carboniferous orogeny in the Bohemian Massif. We explore specific links between the olivine and orthopyroxene microfabric previously determined using electron back–scattered diffraction method and AMS ellipsoid. In addition, we discuss the role of serpentinization degree and increase of magnetite proportion on the bulk magnetic susceptibility, degree of anisotropy and orientation of magnetic fabrics. Finally, we provide a model of development of AMS fabric as a function of increasing serpentinization and decreasing bulk strength of peridotite during regional deformation.

Geological setting

The studied body of serpentinized Mohelno peridotite is enclosed within the Náměšť granulite massif (NGM) located in the Moldanubian Zone at the eastern margin of the Bohemian Massif (Fig. 1a). The Moldanubian Zone is the highest grade metamorphic unit of the Bohemian Massif interpreted as a deep part of the thickened orogenic root developed during Devonian to Carboniferous continen-

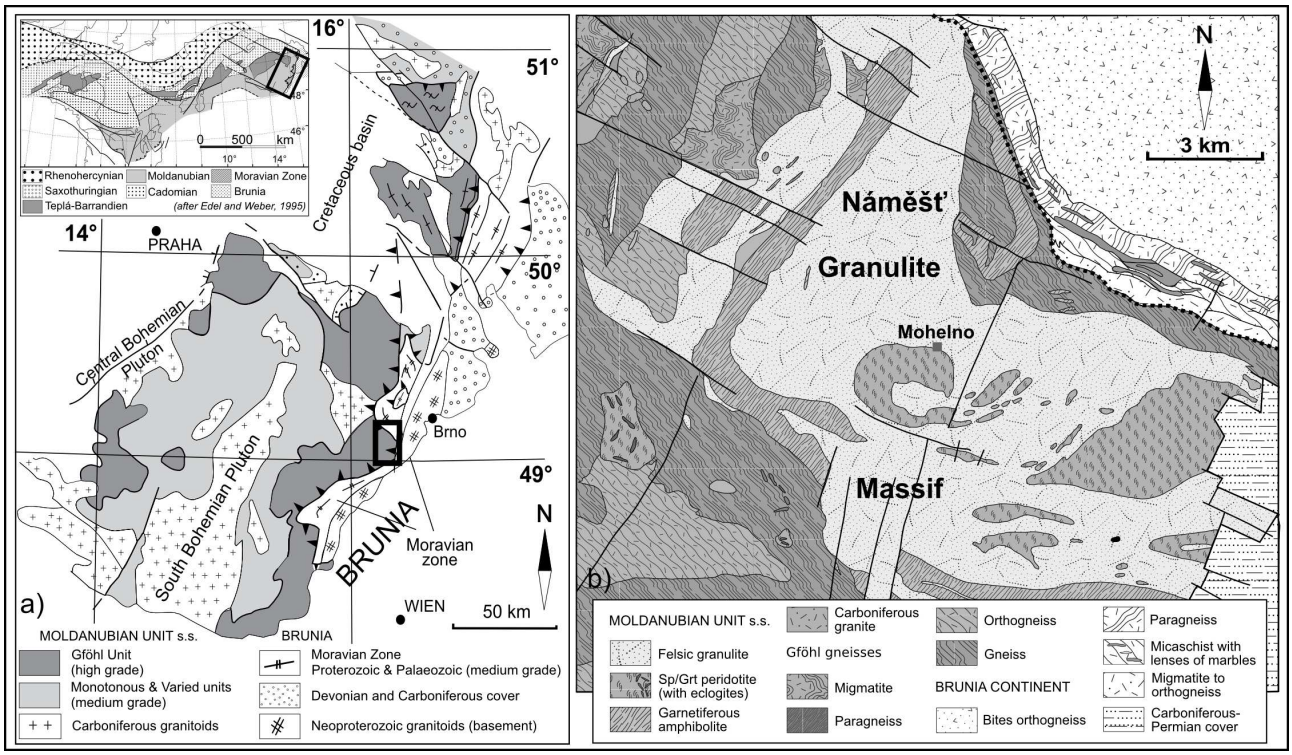

Figure 1. Regional and geological settings. (a) Sketch map of the eastern margin of the Bohemian Massif with high-grade Gföhl and medium-grade Monotonous and Varied units (after Franke, 2000). At top: inset with position of the Bohemian Massif in the framework of the European Variscides (after Edel and Weber, 1995). (b) Geological map of the surrounding area of the studied Mohelno peridotite (according 1:50000 map sheet of the Czech Geological Survey).

tal convergence (Schulmann et al., 2009). Based on structural position, lithologies and metamorphic conditions the Moldanubian Zone has been subdivided into the medium-grade sequence of metasedimentary and gneissic orogenic middle crust and high-grade orogenic lower crust represented by the Gföhl unit (Tollmann, 1982; O'Brien and Carswell, 1993). The orogenic lower crust was isothermally exhumed from bottom of orogenic root (peak metamorphic conditions of 800–1000 °C and 1.6–2 GPa; O'Brien and Carswell, 1993; Tajčmanová et al., 2006; Racek et al., 2008) to middle crustal levels (0.7–0.9 GPa at 800 °C; Štípská et al., 2004; Racek et al., 2006) by vertical extrusion mechanism. This event was followed by indentation of Brunia continental promontory (Schulmann et al., 2005) resulting in development of horizontal channel flow (Schulmann et al., 2008) associated with extensive melting at 0.4–0.7 GPa and 700–600 °C (Hasalová et al., 2008; Štípská et al., 2008).

Numerous peridotite fragments recorded the complex tectonic evolution of orogenic lower crust as suggested in Chapter 2 on the example of the Mohelno peridotite. This peridotite fragment forms large scale fold structure with thickness of ~1000 m of the northern limb decreasing to ~300 m of the southern one (Fig. 1b). According to previous studies (Medaris et al., 1990; Kamei et al., 2010; Chapter

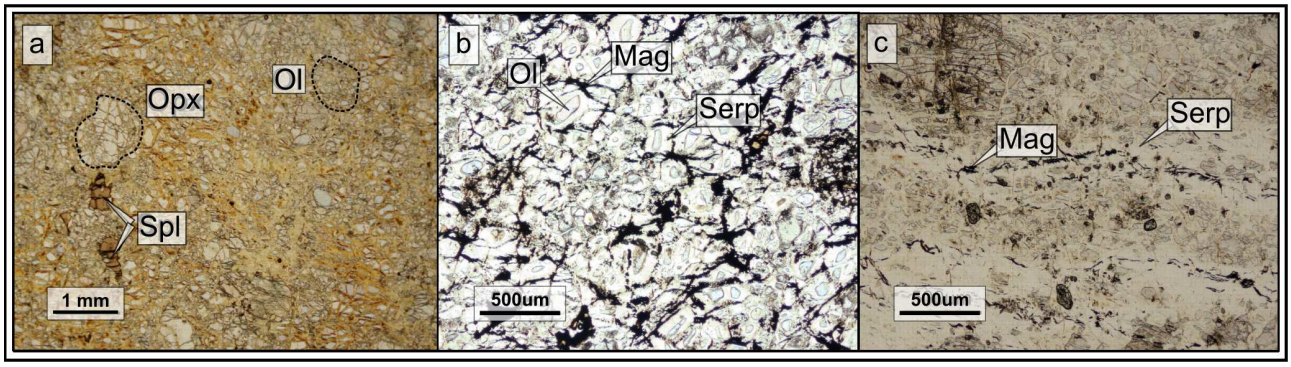

Figure 2. Typical serpentinization microstructures from the Mohelno peridotite body. (a) Mesh rim microstructure of massive serpentine devoid of opaque minerals with preserved coarse-grained harzburgite microstructure (*Ol – olivine, Opx – orthopyroxene, Spl - spinel*). (b) Mesh rim microstructure of massive serpentine with abundant opaque minerals around relics of olivine (*Mag – magnetite, Serp - serpentine*). (c) Microstructure with high modal volume of massive serpentine organized in sub-parallel serpentine layers concentrating batches and clusters of the opaque minerals.

2) the peridotite underwent complex tectonic and metamorphic intramantle history, emplacement into lower orogenic crust and exhumation within granulite complex to middle crustal levels. The Mohelno peridotite shows the geochemical signature typical for an asthenospheric origin and preserves four successive mineral assemblages (Medaris et al., 1990). First assemblage contains coarse-grained olivine, orthopyroxene, clinopyroxene and spinel. The original $spinel_1$ can be found also as inclusion in overgrowing pyrop garnet. That is further breakdown to clinopyroxene + spinel and amphibole + spinel (Stage IV) symplectites. Websterites to orthopyroxenites show porfyroclastic microstructure with original coarse-grained orthopyroxene porphyroclasts surrounded by finer grained polygonal orthopyroxene grains and interstitial fine-grained clinopyroxenes. Weakly serpentinized websterite layers are crosscut by polygonal network of fractures oriented normal to orthopyroxenite layers filled by serpentine. Using standard geothermobarometry on the mineral assemblage of garnet peridotites the maximal conditions of 2.3–2.8 GPa and temperature ~1200 °C (Medaris et al., 1990) or at 1.8-2.5 GPa at 1100-1250 °C (Kamei et al., 2010) were obtained while retrogression occurred at temperature ~850 °C and pressures 1 to 1.5 GPa (Kamei et al., 2010).

Four different deformation fabrics have been described within the Náměšť granulite massif enveloping the Mohelno peridotite body (Chapter 2). High-grade coarse-grained S1 granulite–facies fabric is refolded by isoclinal folds F2 leading to development of (ultra)mylonitic granulite–facies S2 fabric. The S2 foliation is generally following curved shape of the NGM and bears mineral lineation moderately plunging to the West. D3 event is related to large scale folding of peridotite sheet in mid-crustal conditions. The resulting S3 fabric is parallel to the S2 fabric in fold limbs, and it is characterized by

amphibolite–facies retrogression and partial melting. Finally, D4 deformation is reworking all earlier structures by subhorizontal shear zones of variable thickness, close to isoclinal folds and S4 migmatitic foliation which is pervasively developed in the East.

Structural record of the studied Mohelno peridotite comprise relics coarse-grained peridotite microstructure and milimetres to several centimetres thick layeres of websterites to orthopyroxenites reworked by pervasive deformation resulting in ubiquitous ultramylonitic fabric. The websterite bands are presently concordant or oblique with respect to the principal mylonitic fabric. The geometry of

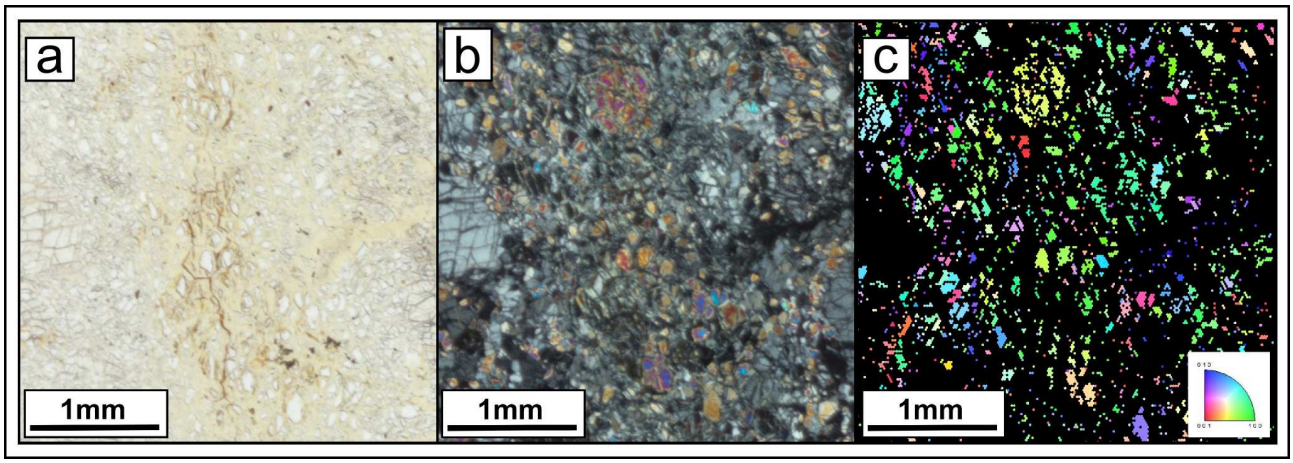

Figure 3. Microstructural record of the serpentinization static nature. (a) Microphotograph of the partly serpentinized peridotite microstructure in plane-polarized light. (b) Microphotograph of the same area in cross-polarized light, notice the similar colour of separated parts after individual olivine grain. (c) EBSD map of the olivine crystallographic axes orientation over the same area highlighting similar orientation of crystallographic axes for separated parts of one individual olivine grain *([100]-green, [010]-blue, [001]-red).*

the mylonitic fabric is defined by study of lattice preferred orientation (LPO) of olivine and pyroxene (Chapter 2). This mylonitic fabric is characterized by a steep foliation that follows the folded shape of the peridotite body. Two different types of olivine LPO pattern were distinguished and interpreted as fabric originated during emplacement into lower crust – axial(010) pattern and fabric developed during folding of peridotite in mid-crustal conditions – [100](0kl) pattern (Chapter 2).

Degree of serpentinization, microstructure and mineralogy

Degree of serpentinization of the main peridotite rock can be deduced from the mineral modal analysis using optical microscope. An obvious weakness of this approach is the size of the thin-sections used for mineral counting, which are not usually representative of the volume of sample used for the magnetic properties measurements (Oufi et al., 2002). The other approach is a density measurement of

Table 1. Density and degree of serpentinization

Sample	Density	S	S*
		(Miller and Christensen,1997)	(Oufi et al., 2002)
	[g/cm³]	D=3.300-0.785×S	D=3.326-0.777×S
1	2.372	1.182	1.228
2	2.451	1.081	1.126
3	2.583	0.913	0.956
4	2.607	0.882	0.925
5	2.644	0.836	0.878
6	2.656	0.820	0.862
7	2.671	0.802	0.843
8	2.683	0.786	0.828
9	2.711	0.750	0.792
10	2.691	0.775	0.817
11	2.708	0.754	0.795
12	2.718	0.741	0.782
13	2.800	0.637	0.677
14	2.842	0.583	0.622

*(for 80% Fo_{90} and 20% En_{90})

serpentinite samples to infer indirectly the degree of serpentinization (Christensen, 1978) based on the substantial difference between densities of unaltered peridotite forming minerals olivine (~3.337 g/m^3 for olivine Fo_{90}) and orthopyroxenes (~3.285 g/m^3 for enstatite) and the lower density of serpentine (~2.550 g/m^3). Volume increase associated with serpentinization is reported widely from serpentinized peridotites. Therefore, to achieve balanced reaction in sense of volume changes, significant amount of both MgO and SiO_2 (35 wt. % of original amount of SiO_2) has to be removed from the ultramafic system during leaching by fluids rich in MgO and SiO_2 (Toft, 1990; O'Hanley, 1992).

Density measurements performed in studied samples vary beetween 2.372-2.842 g/m^3 which was recalculated to yield degree of serpentinization (Miller and Christensen, 1997) in the range between 58% to 118%. (Tab. 1 Density and Degree of serpentinization). Degree of serpentinization estimated from the same density measurements using formula of Oufi et al. (2002) for hypothetical harzburgite with composition of 80% olivine (Fo_{90}) and 20% enstatite give similar range between 62% to 123%. Values of the degree of serpentinization higher than 100% are caused most likely by significant content of opal with considerably lower density (1.9-2.3 g/m^3).

Three main types of serpentinization microstructures were distinguished in studied samples (Fig. 2). The first type occurs occasionally in coarse-grained harzburgite (LN40) and shows a mesh of massive serpentine devoid of opaque minerals rimming remnants of olivines (Fig. 2a) and cross-cut by randomly intersecting fractures. The second type shows mesh of massive serpentine with abundant

opaque minerals around relics of olivine rim microstructure (Fig. 2b). Serpentine also often produces bastite (pseudomorphoses after orthopyroxene) reflecting the original pyroxene mineral cleavage. The third type of serpentine microstructure shows high modal volume of massive serpentine forming sub-parallel serpentine layers (Fig. 2c). Such serpentine rich layers are mostly devoid of relics of original minerals and are associated with irregular aggregates of opaque minerals. In contrast, layers with original mineral relics and lower amount of serpentine are coloured by iron oxide pigments. Despite

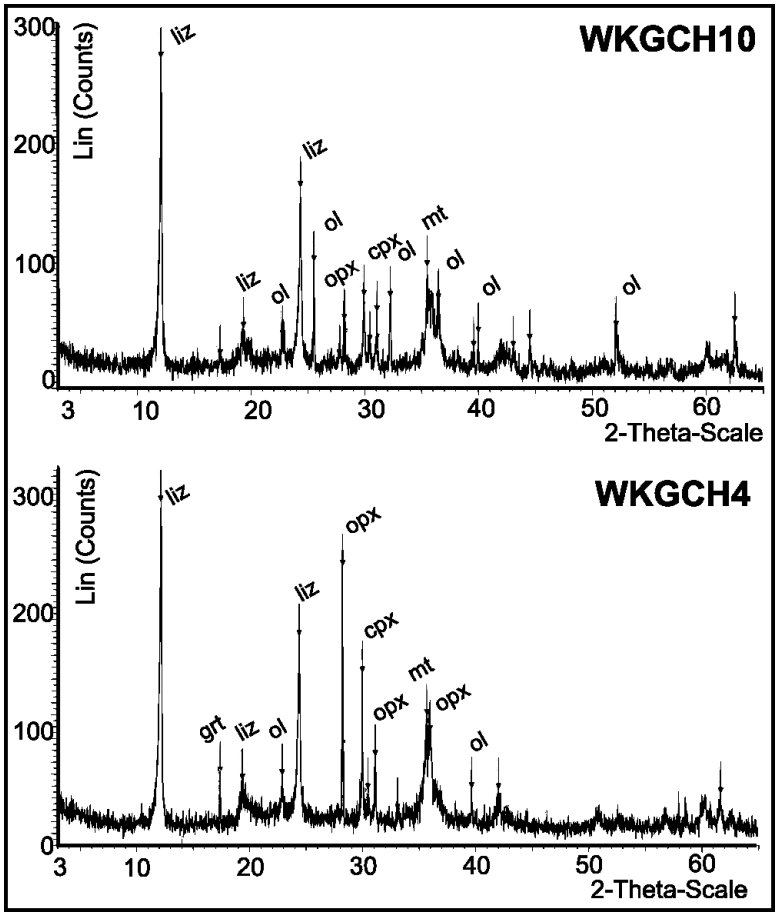

Figure 4. X-Ray Diffraction spectrum for spinel (WKGCH10) and garnet (WKGCH4) bearing serpentinized peridotite from the Mohelno peridotite body (*liz - lizardite, ol – olivine, opx – enstatite, cpx - acmite, mt – magnetite, grt – garnet*).

generally intense serpentinization, dismembered parts of single individual olivine grains exhibit original orientation as shown by EBSD mapping of lattice preferred orientation (Fig. 3). Serpentinization microstructures with fibrous serpentine variety characteristic for (high) deformation-enhanced origin (Wicks and Whittaker, 1977) were not observed in this study indicating low degree or absence of syn-serpentinisation massive deformation.

The X-ray diffraction (XRD) analyses were performed on samples of serpentinized spinel- and garnet-

bearing peridotites. The XRD spectrum of serpentinized peridotite was obtained with a RX Brüker D5000 diffractometer (LHyGeS EOST, University of Strasbourg) using Cu radiation and NaI scintillation detector in air. In both samples the presence of serpentine mineral, olivine, orthopyroxene, clinopyroxene and magnetite was confirmed. For both samples lizardite is the most common serpentine mineral. Also XRD spectrum confirmed presence of garnet in sample WKGCH4 (Fig. 4).

P-T conditions and tectonic setting of Mohelno peridotite serpentinization

The Mohelno peridotite body underwent multistage tectonic and deformational history (Chapter 2). It was shown that final tectonic history of Mohleno peridotite is associated with channel flow and progressive melt infiltration (with approximately 8 wt. % H_2O and 71 wt. % SiO_2) at conditions from 740 °C and 0.65 GPa to 660 °C and 0.35 GPa (Hasalová et al., 2008b). It is the pervasive melt flow, which keeps elevated temperatures in partialy molten mid-crustal channel and thus also in the embedded granulite massif, facilitating granulite retrogression in sub-horizontal S4 fabric (Chapter 2). Pressure-temperature conditions in the granulite surrounding studied peridotite body in the active mid-crustal channel are above the serpentinization isograde (antigorite isograde, O'Hanley and Wicks, 1995; Hyndman and Peacock, 2003) and at this stage the strong ultramafic peridotite did not undergo any serpentinization. Hasalová et al. (2008b) have shown that the last melt fraction in the mid-crustal migmatite is recorded at 660 °C and 0.35 GPa by the melt with approximately 8 wt. % H_2O and 71 wt. % SiO_2. Final cooling of the mid-crustal channel is responsible for crossing the solidus line of the granitic system and crystallization of the melt which caused instantaneous release of the large volume of fluid ($H_2O \pm$ aq. SiO_2). We suggest that at this stage the first antigorite was formed at temperature ~550 °C via reaction forsterite + talc + $H_2O \rightarrow$ antigorite and further at ~430 °C via reaction forsterite + $H_2O \rightarrow$ antigorite + brucite (Hyndman and Peacock, 2003). Hence, it is proposed that large quantity of hydrous fluid released from crystallizing melt within mid-crustal channel is responsible for the serpentinization of the studied peridotite body. Further decrease of the temperature to around 250 °C lead to olivine serpentinization via lizardite (and/or chrysotile) and/or recrystallization of antigorite to lizardite (O'Hanley and Wicks, 1995).

Magnetic properties of the serpentinite

Methodology

Oriented block samples were collected at 40 localities covering all outcrops of the serpentinized peridotite body. Oriented blocks were cut to oriented cubes (8-18 per locality) with a side of 20mm. The anisotropy of magnetic susceptibity (AMS) was measured with the KLY-3S Kappabridge in the AGICO Inc. (Brno, CZE) and KLY-4S Kappabridge (Jelínek and Pokorný, 1997) in the Institute of Geophysics in Prague. Data were statistically processed using the ANISOFT software (Jelínek and Kropáček, 1978; Hrouda and Hrušková, 1990; www.agico.com). The AMS data are characterised by parameters for the mean bulk susceptibility (K_m), degree of anisotropy (P) and shape (T) of the AMS ellipsoid and by orientation of the magnetic foliation and lineation. The K_m, P and T parameters are specify as $K_m=(K_1+K_2+K_3)/3$; $P=K_1/K_3$; $T=2ln(K_2/K_3)/ln(K_1/K_3)-1$, where $K_1 \geq K_2 \geq K_3$ are the principal susceptibilities (Nagata, 1961; Jelinek, 1981; Hrouda, 2010). The orientation of magnetic foliations and lineations are presented in equal area stereographic projection on lower hemisphere or as corresponding symbol for given locality on a map.

To assess the relative contributions of particular minerals to the rock susceptibility, the methods of the Maximum Theoretical Paramagnetic Susceptibility (MTPS) and the susceptibility variation with temperature were used. The first method calculates the MTPS from the Fe and Mn content determined from the whole-rock chemical analyses (Aydin et al., 2007; Hrouda, 2010). Dominant influence of the paramagnetic minerals on the rock susceptibility can be considered, when the measured rock susceptibility is equivalent to calculated MTPS. For rock susceptibilities higher than calculated MTPS, some Fe and/or Mn is presumably restrained in more susceptible ferromagnetic minerals. The second method uses characteristic features of the susceptibility vs. temperature curves. 20 coarsely powdered sample specimens were investigated in temperature intervals of -194 °C to 0 °C and 25 °C to 700 °C, using the CS-L and CS-3 Apparatuses respectively (Parma and Zapletal, 1991) with KLY-3S. Measured data were processed with SUFTE, SUFTEL and CUREVAL software (www.agico.com). The density measurements were conducted using microbalance and a pyctometer for measuring the sample volume.

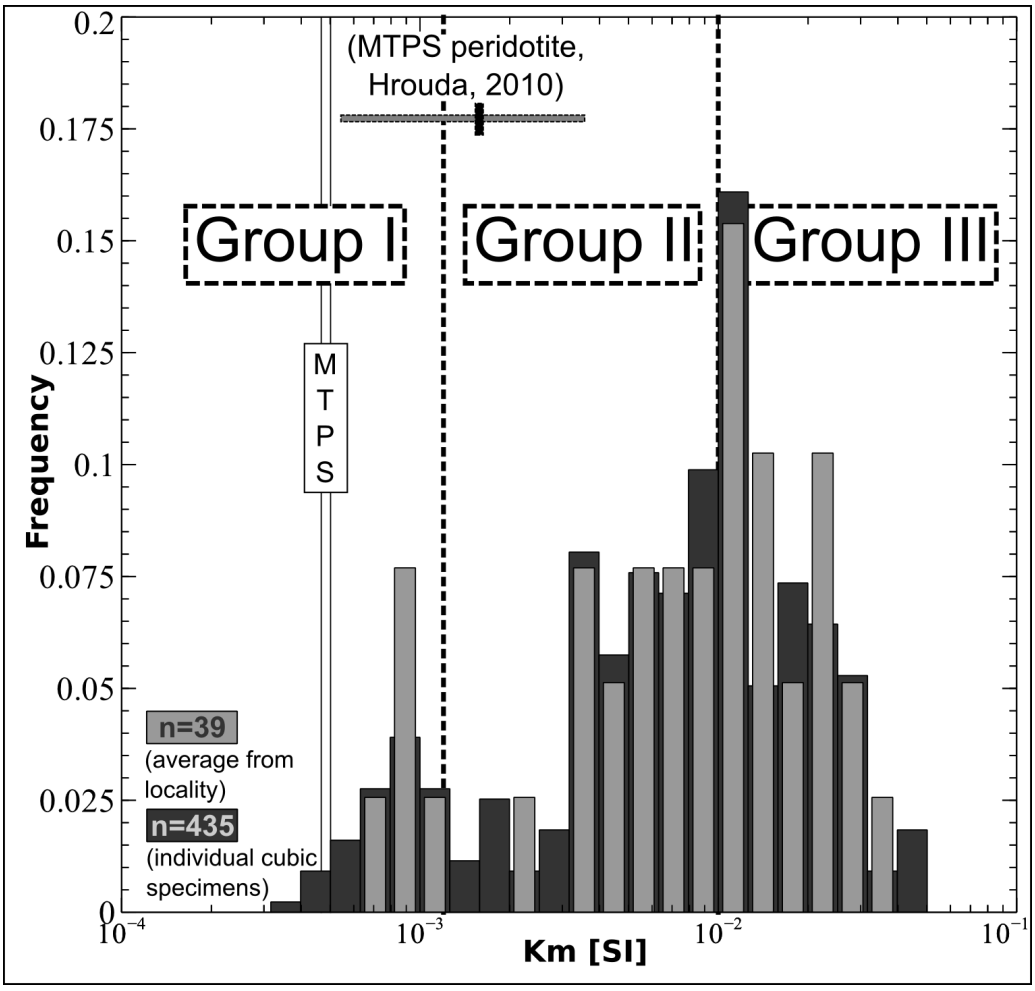

Figure 5. Histogram of bulk susceptibility values in the serpentinized peridotite with proposed separation into individual groups (Group I-III) based on mean bulk susceptibility. MTPS (*vertical line*) – Maximum Theoretical Paramagnetic Susceptibility, calculated from the actual whole-rock analyses (Chapter 2). MTPS (*horizontal line*) – distribution of various MTPS values for common peridotite composition (Hrouda, 2010).

1.2 Bulk magnetic susceptibility and mineralogy

The bulk susceptibility of the Mohelno serpentinite ranges from 7×10^{-4} to 4×10^{-2} [SI] (Fig. 5, Tab. 2). The specimens can be divided into three groups based on their mean bulk susceptibility. Group I shows susceptibilities lower than 2×10^{-3} [SI] and are further described as weakly magnetic specimens which correspond to weakly serpentinised microstructure type described above. The specimens with the bulk susceptibility between 2×10^{-3} and 1×10^{-2} [SI] were included in Group II and are referred as moderately magnetic specimens and correspond to second type of serpentinite microstructure. The Group III specimens with the bulk susceptibility higher than 1×10^{-2} [SI] are denoted as strongly magnetic specimens reflecting third type of serpentinite microstructure. The maximum theoretical paramagnetic susceptibility (MTPS) has been calculated from the contents of Fe and Mn in whole-

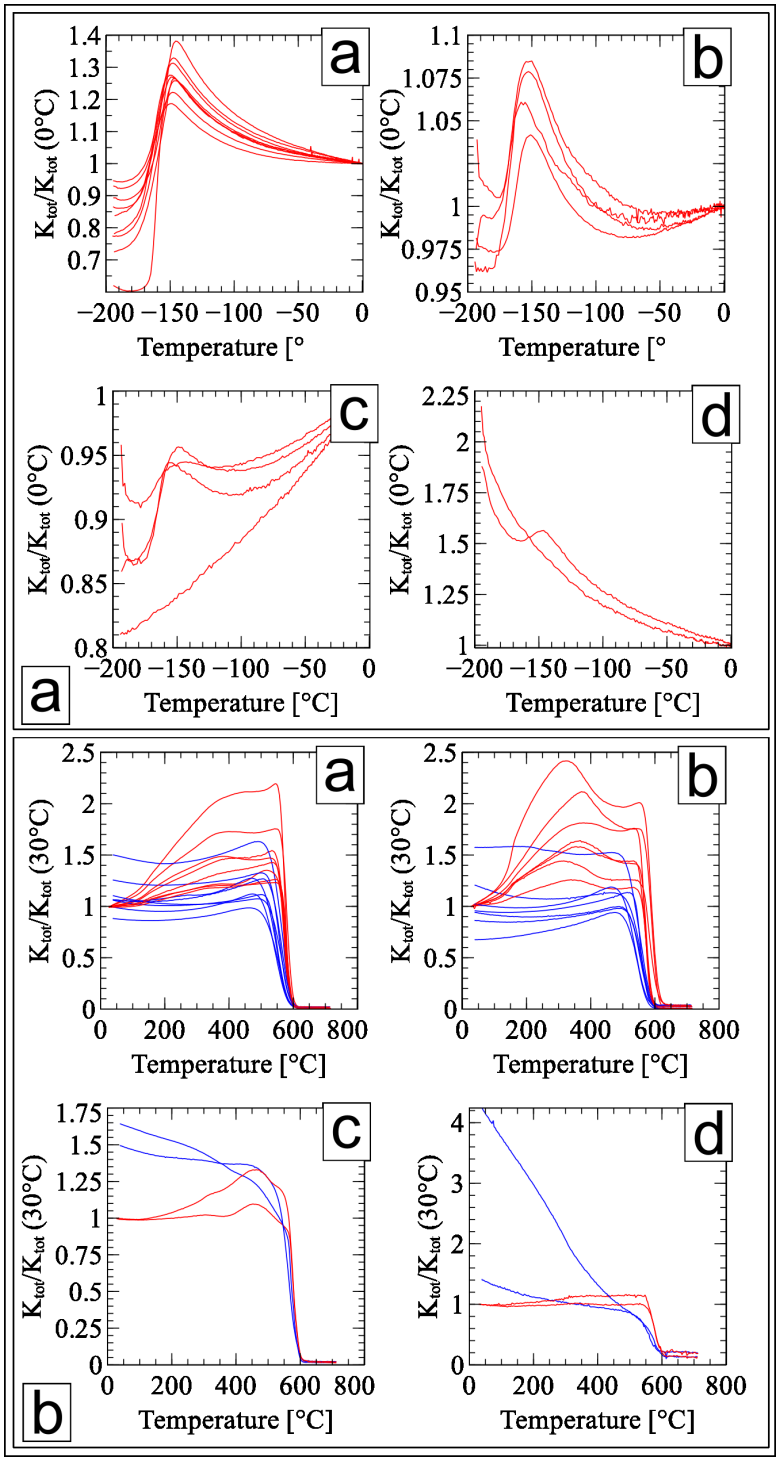

Figure 6. (a) The bulk susceptibility variations for temperatures between -194 °C to 0 °C normalised to bulk susceptibility at temperature 0 °C. (b) the bulk susceptibility variations in temperature interval 25 °C to 700 °C (*red* – heating curves, *blue* – cooling curves) are shown. Both subdatasets are divided in four categories according to the shape of the thermomagnetic curve to facilitate the data presentation, for detail division see the text.

rock analyses published by Medaris et al., (1990) according to Zapletal (1985) Eq.3 in Hrouda (2010) and results show values between 4.7×10^{-4} to 5×10^{-4} [SI] (Fig. 5).

Table 2. Magnetic Susceptibility and AMS dafa for the Mohelno peridotite

Group	Name	N	K_m	Normed principal susceptibilities			Anisotropy parameters				AMS principal directions					
			[1000×SI]	K_1	K_2	K_3	Pj	T	F	L	K_1		K_2		K_3	
								average			dec	inc	dec	inc	dec	inc
	WK90B	9	37.2	1.083	1.018	0.899	1.221	0.255	1.137	1.067	190	6	282	20	84	69
	WK90	9	31.5	1.069	1.008	0.923	1.166	0.128	1.095	1.062	203	20	314	45	97	38
	LN61	10	26.9	1.035	1.022	0.943	1.107	0.672	1.082	1.016	35	47	278	23	171	34
	WK141	12	24.6	1.027	1.022	0.951	1.092	0.740	1.073	1.011	272	2	180	48	4	42
	WK123	9	22.7	1.070	1.046	0.884	1.240	0.787	1.189	1.022	130	71	307	19	37	1
	LN56	11	21.9	1.067	1.027	0.906	1.188	0.517	1.133	1.040	271	48	9	7	105	41
	WK135	12	20.2	1.064	1.006	0.930	1.146	0.164	1.082	1.058	308	57	111	32	206	8
	LN95B	10	17.1	1.069	1.049	0.882	1.240	0.745	1.189	1.025	305	64	204	5	112	25
	WK142	10	16.1	1.070	1.006	0.924	1.161	0.161	1.091	1.063	196	7	94	59	290	30
High K_m	LN75	10	15.4	1.064	0.997	0.939	1.142	-0.046	1.064	1.073	255	46	58	43	156	9
	LN50	10	15.0	1.079	0.996	0.925	1.227	0.336	1.150	1.058	241	55	132	13	34	32
	LN31	11	13.2	1.044	1.017	0.939	1.119	0.482	1.083	1.028	81	21	343	20	214	60
	WK55	10	12.8	1.026	1.004	0.970	1.060	0.199	1.036	1.022	248	45	345	8	83	44
	WK108	17	12.5	1.046	1.000	0.954	1.097	0.027	1.049	1.046	344	71	75	0	165	19
	WK76	12	11.5	1.052	0.994	0.954	1.104	-0.160	1.042	1.059	334	41	210	32	97	32
	LN37	10	11.3	1.060	1.014	0.926	1.156	0.346	1.100	1.048	264	54	8	10	105	34
	WK132	10	10.6	1.076	0.978	0.946	1.154	-0.303	1.051	1.095	214	26	121	5	20	64
	LN160	10	10.3	1.102	1.062	0.837	1.356	0.739	1.276	1.037	259	47	24	28	131	30
	LN156	8	10.1	1.061	1.020	0.919	1.167	0.440	1.114	1.041	276	52	17	8	113	37

Table 2 (continue). Magnetic Susceptibility and AMS dafa for the Mohelno peridotite

Group	Name	N	K_m	Normed principal susceptibilities			Anisotropy parameters				AMS principal directions					
			[1000×SI]	K_1	K_2	K_3	Pj	T	F	L	K_1		K_2		K_3	
								average			dec	inc	dec	inc	dec	inc
	LN26	10	8.53	1.116	1.087	0.798	1.455	0.843	1.364	1.027	301	48	156	37	52	18
	WK75	11	8.40	1.046	0.991	0.963	1.089	-0.316	1.029	1.056	296	31	62	45	186	29
	LN10	12	8.33	1.079	1.051	0.870	1.273	0.742	1.212	1.029	267	25	43	56	167	21
	LN33A	10	7.37	1.076	1.028	0.896	1.213	0.506	1.150	1.046	170	7	286	75	78	14
	WK133	12	7.01	1.063	1.005	0.932	1.149	0.196	1.087	1.056	204	4	295	15	101	74
	WK134	14	6.37	1.063	1.020	0.918	1.164	0.429	1.111	1.043	183	48	315	31	61	26
	WK66	12	5.96	1.114	1.019	0.866	1.293	0.282	1.177	1.094	287	53	168	20	66	30
Medium K_m	WK175B	12	5.80	1.036	1.031	0.933	1.134	0.755	1.107	1.014	188	11	284	29	79	59
	WK175A	12	5.20	1.061	1.035	0.904	1.198	0.654	1.152	1.026	269	33	359	1	91	57
	WK105	18	4.36	1.069	0.990	0.942	1.142	-0.166	1.055	1.080	342	8	102	74	250	14
	WK77	9	4.06	1.073	1.049	0.878	1.248	0.756	1.195	1.025	266	5	357	14	157	76
	LN64	10	3.63	1.050	1.023	0.926	1.143	0.586	1.105	1.027	314	39	48	5	144	50
	WK129	10	3.49	1.086	1.026	0.888	1.233	0.434	1.157	1.058	304	62	193	11	98	26
	WK128	15	3.17	1.061	1.016	0.923	1.155	0.371	1.101	1.045	188	43	324	37	73	24
	WK60	12	2.16	1.030	1.012	0.958	1.079	0.501	1.057	1.018	312	15	208	41	57	45
	WK61	12	1.11	1.020	1.002	0.978	1.060	0.086	1.040	1.015	321	27	201	44	71	33
	LN40	8	0.86	1.030	1.002	0.969	1.065	0.092	1.035	1.028	5	20	247	53	107	30
Low K_m	WK169A	12	0.82	1.033	1.011	0.956	1.093	0.353	1.063	1.026	179	23	319	61	82	17
	WK63N	12	0.82	1.028	1.006	0.965	1.081	0.057	1.050	1.026	45	22	273	59	144	21
	WK170A	13	0.79	1.028	1.005	0.966	1.080	0.082	1.049	1.025	46	20	274	61	144	20

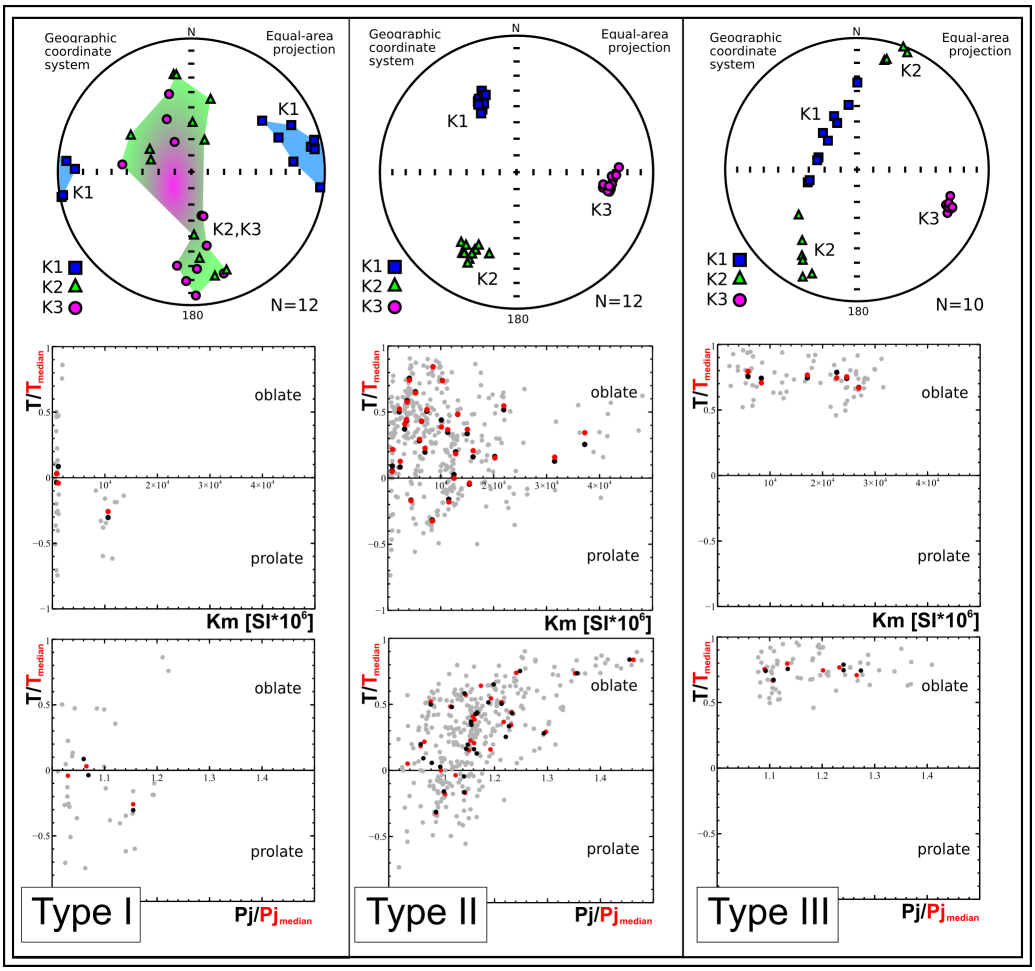

Figure 7. Three different AMS patterns from the Mohelno serpentinized peridotite according shape of magnetic ellipsoid, degree of anisotropy and orientation of susceptibility directions. For each pattern (in each column) from top to the bottom: (1) Orientation of principal susceptibility axes, equal-area projection on lower hemisphere. (2) *T vs.* K_m plot - relationship between shape parameter of the magnetic fabric and bulk susceptibility (shape parameter shows average and median value). (3) *T vs. Pj* plot - relationship between shape parameter of the magnetic fabric and degree of AMS (both shape parameter and degree of AMS show average and median value).

Analyses of thermomagnetic curves reveal that magnetite is probably present in all samples. In the Group III strongly magnetic specimens (Ln61, Ln75, Ln160) at low temperature curves indicate the well developed Verwey transition between -150 °C and -160 °C (Fig. 6a.a) and the heating curves show the distinct Curie temperature of magnetite (Fig. 6b.a). Clear Verwey transition is typical for coarse-grained pure magnetite, broadening and dissipation (Fig. 6a.b) is caused by grain size reduction and Fe substitution in magnetite (Kontny et al., 2004). Samples Ln50, Ln37, Ln61, Ln64, Ln95 from Fig. 6b.b show Curie temperatures (TC) in range of 583 °C to 608 °C (during heating sequence) and 572 °C and 597 °C (during cooling sequence). Slightly higher TC show influence of magnetite (in partly oxidated state) and/or maghemite (characteristic Curie temperature of maghemite is located in the

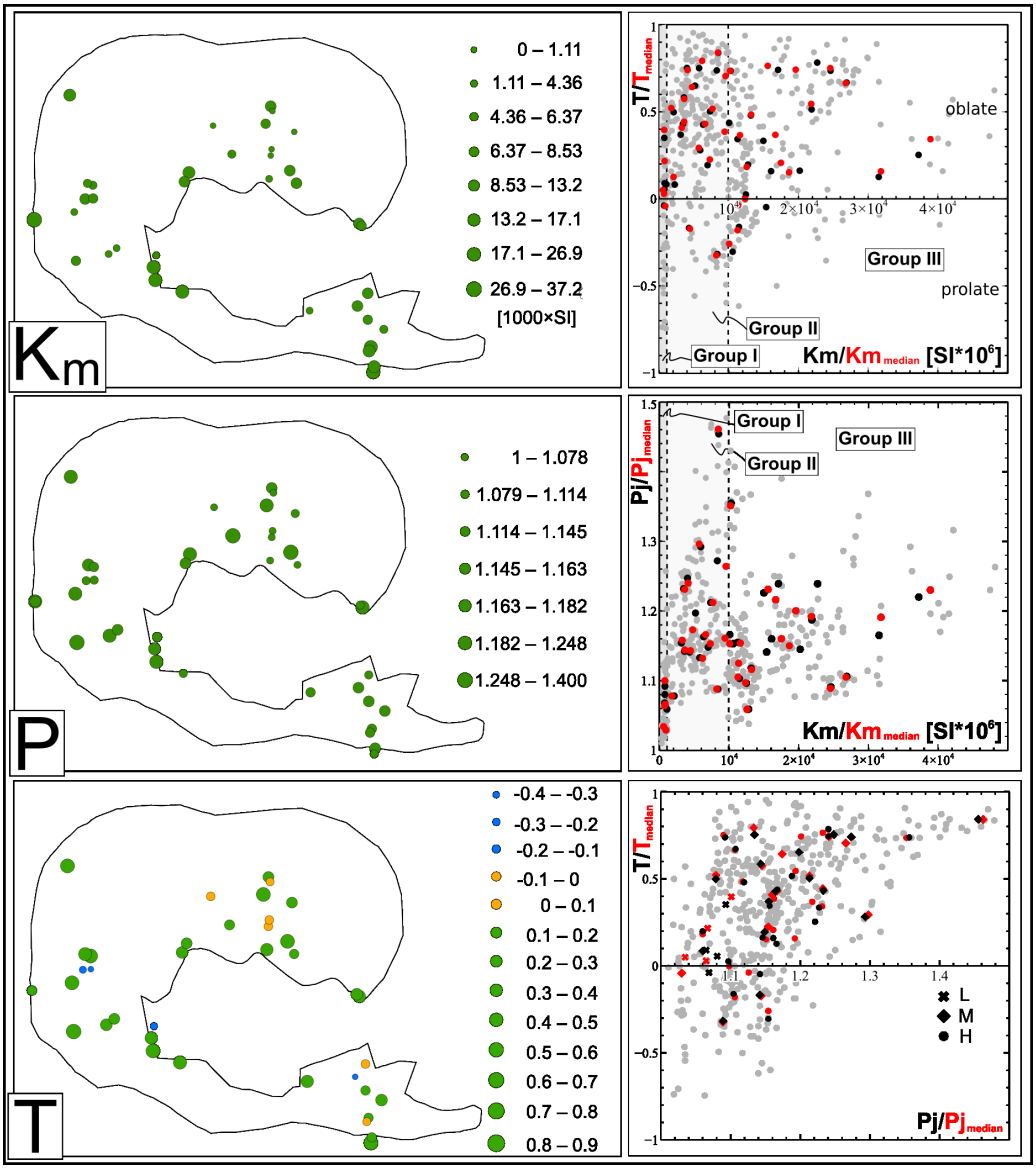

Figure 8. *Left column:* Spatial distribution of magnetic fabric (K_m bulk susceptibility, *Pj* degree of AMS, *T* shape parameter) within the Mohelno peridotite body. *Right column:* Complet magnetic fabric data from the Mohelno peridotite body. *T vs.* K_m plot - relationship between shape parameter of the magnetic fabric and bulk susceptibility (shape parameter shows average and median value). (3) *P vs.* K_m plot - relationship between degree of AMS and bulk susceptibility (degree of AMS shows average and median value). (4) *T vs. Pj* plot - relationship between shape parameter of the magnetic fabric and degree of AMS (both shape parameter and degree of AMS show average and median value).

interval 590 °C and 675 °C, Dunlop and Özdemir, 1997). In most samples (Ln50, Ln37, Ln61, Ln64, Ln95) also low-temperature (unstable) maghemite is determined by broader peak from around 300 °C to 450 °C. At temperatures above TC maghemite is disintegrated, oxidized magnetite is reduced and cooling curves show mostly only pure magnetite. Besides the magnetite and maghemite other ferromagnetic minerals appear in several samples. Distinct peaks at -150 °C to -140 °C could be caused by a none–specified member of the magnetite–chromite or magnetite–spinel solid solutions (Kontny

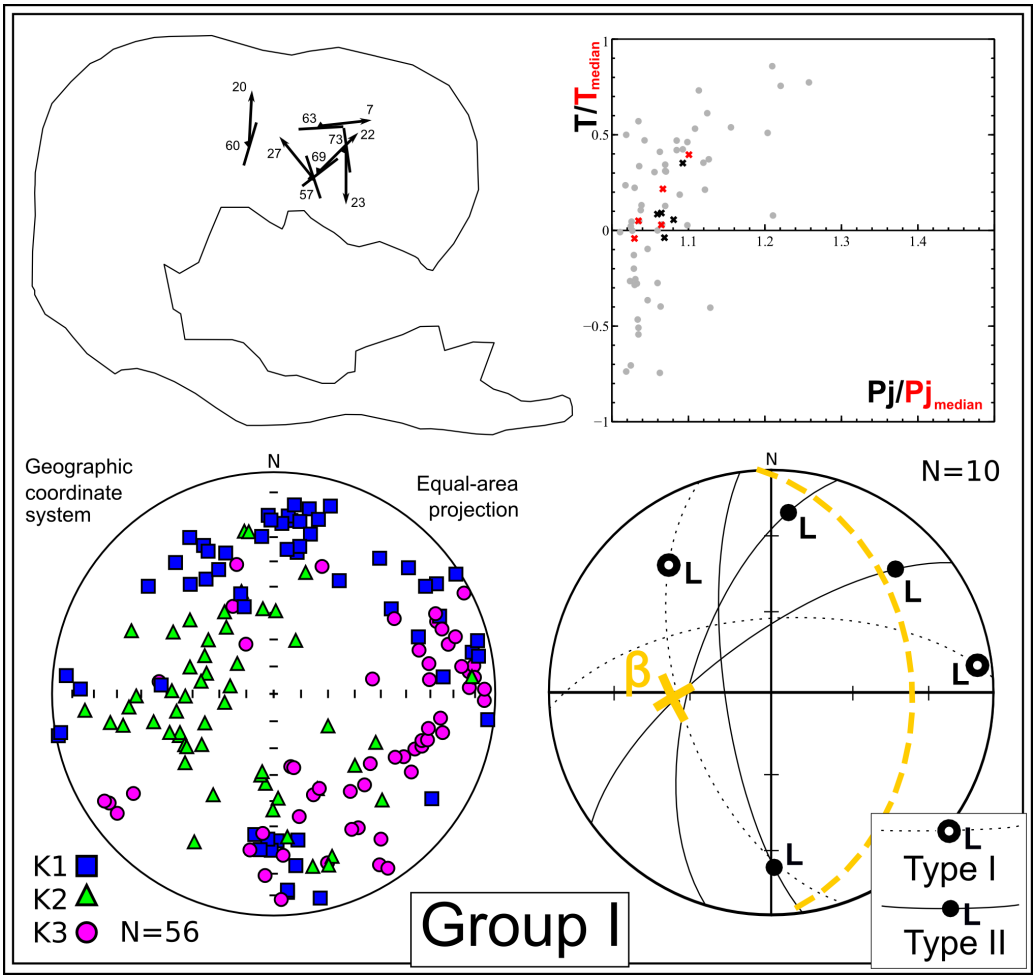

Figure 9. Overview of magnetic fabric data for Group I samples. *Top left*: Spatial distribution of magnetic foliation and lineation within the Mohelno peridotite body. *Top right*: *T vs. Pj* plot - relationship between shape parameter of the magnetic fabric and degree of AMS (both shape parameter and degree of AMS show average and median value). *Bottom left*: Orientation of principal susceptibility axes, equal-area projection on lower hemisphere. *Bottom right*: Orientation of magnetic foliation and lineation (L) with distinguished different AMS types with added orientation of megafold β-axis defined in Chapter 2, equal-area projection on lower hemisphere.

et al., 2004). Several peaks in sample Ln26 (Fig. 6b.c) at 450 °C to 500 °C show presence of similar spineloid only with higher content of the magnetite component. Only two samples from Group I with the lowest susceptibility (LN40) show influence of paramagnetic minerals below 0 °C interval (Fig. 6a.d). On the other hand, the heating curves for these samples showed influence of ferromagnetic magnetite as well and during cooling a susceptibility increases (Fig. 6b.d).

Whole-rock AMS magnetic fabric

The AMS patterns from the Mohelno serpentinite can be divided in three main types according to shape of magnetic ellipsoid, degree of anisotropy and the relative orientation of the principal axes

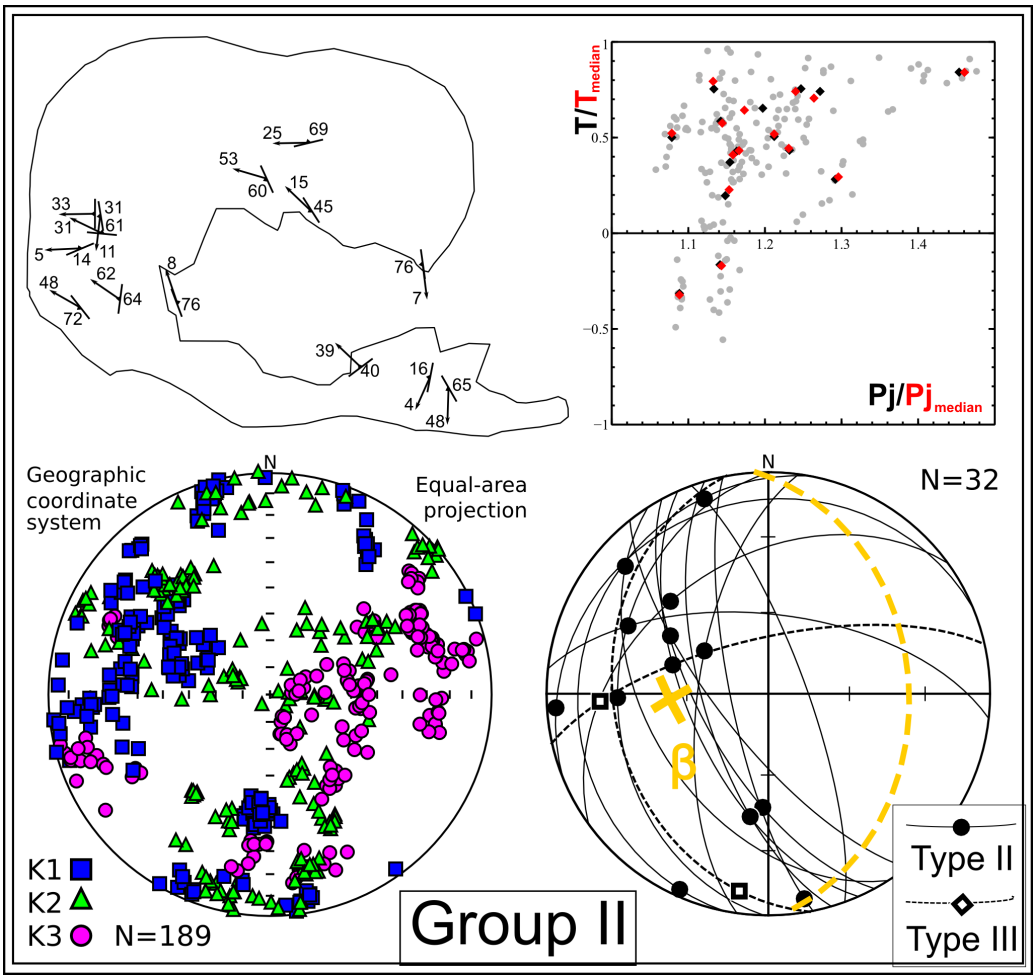

Figure 10. Overview of magnetic fabric data for Group II samples. *Top left:* Spatial distribution of magnetic foliation and lineation within the Mohelno peridotite body. *Top right: T vs. P* plot - relationship between shape parameter of the magnetic fabric and degree of AMS (both shape parameter and degree of AMS show average and median value). *Bottom left:* Orientation of principal susceptibility axes, equal-area projection on lower hemisphere. *Bottom right:* Orientation of magnetic foliation and lineation with distinguished different AMS types with added orientation of megafold β-axis defined in Chapter 2, equal-area projection on lower hemisphere.

of AMS ellipsoid (Fig. 7). The Type I fabric is characterized by clustered K_1 directions, girdle distribution of K_2 and K_3 directions, prolate to neutral shape of AMS ellipsoid and low degree of magnetic anisotropy . The most common Type II fabric pattern is marked by clustered K_1, K_2, K_3 directions, plane strain to oblate fabrics and generally high degree of susceptibility (for such AMS pattern both magnetic lineation and foliation are well constrained). The Type III fabric reveals clustered K_3 directions, girdle distribution of K_1 and K_2 directions, mainly oblate shapes of AMS and intermediate to high degree of magnetic anisotropy.

Spatial distribution of different parameters of AMS (K_{m}, T, P; Fig. 8) shows weak pattern of

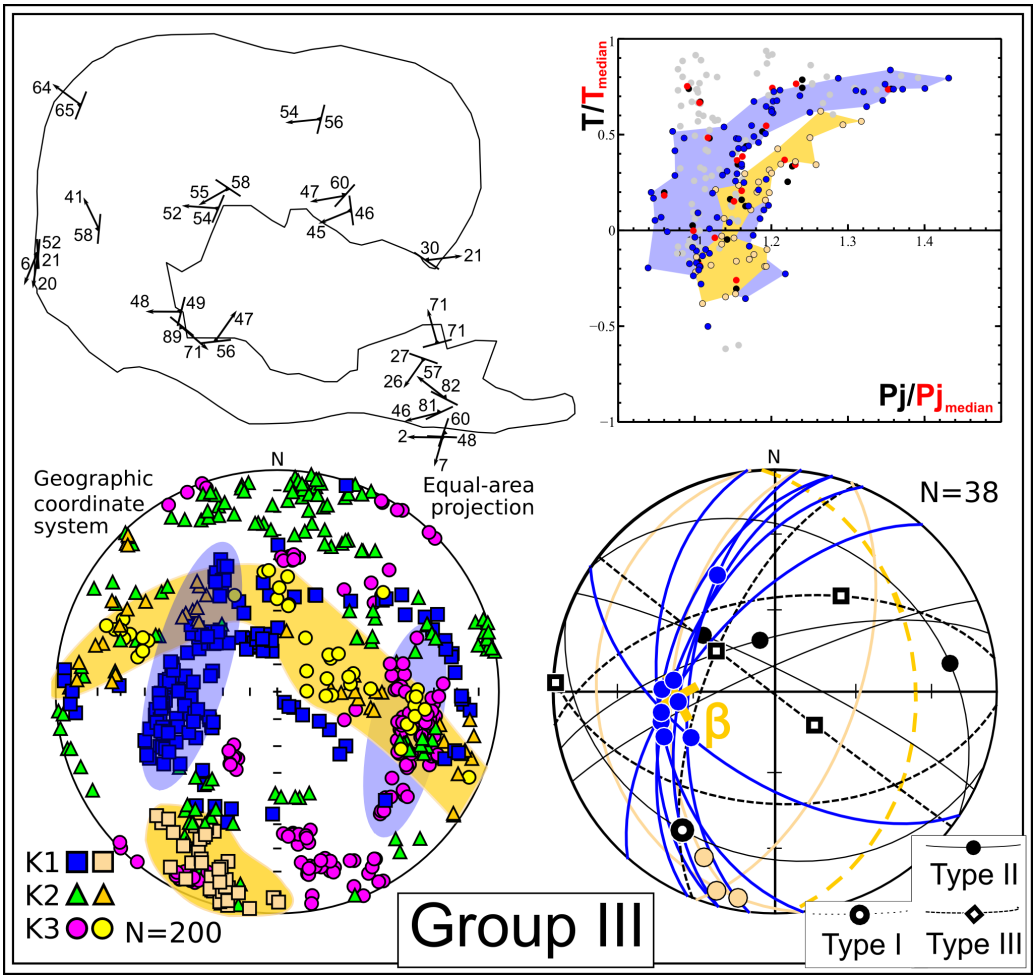

Figure 11. Overview of magnetic fabric data for Group III samples. *Top left:* Spatial distribution of magnetic foliation and lineation within the Mohelno peridotite body. *Top right: T vs. Pj* plot - relationship between shape parameter of the magnetic fabric and degree of AMS. Data for two different AMS fabrics within samples from Group III are highlighted by colour coding. Also shape parameter and degree of AMS show both average and median value. *Bottom left:* Orientation of principal susceptibility axes, equal-area projection on lower hemisphere. Two distinguished AMS fabrics are highlighted with different colour coding. *Bottom right:* Orientation of magnetic foliation and lineation with distinguished different AMS patterns with added orientation of megafold β-axis from Chapter 2, equal-area projection on lower hemisphere.

magnetic fabric. Nevertheless, the core of peridotite body is marked by lower degree of AMS and prolate shape of magnetic ellipsoid. High intensity of anisotropy of magnetic susceptibility and oblate shape of magnetic ellipsoid are frequent around the margin of the peridotite body.

Samples of low susceptibility Group I (Fig. 9) are located only in the core of the northern limb of the Mohelno peridotite body and belong to linear AMS fabrics Type I and II. These samples are characterized by low degree of AMS and neutral to oblate shape of AMS ellipsoid. K_1 directions are sub-horizontal and K_3 directions are distributed along a great circle, which pole coincides with the peridotite megafold hinge (β-axis of Sander, 1930). Samples from susceptibility Group II (Fig. 10) are

distributed along whole peridotite body belonging dominantly to Type II AMS fabric and rarely to oblate Type III AMS fabric pattern. Here, the degree of AMS is slightly higher compared to Group I and shape of AMS ellipsoid varies from slightly prolate to highly oblate. Patterns of K_1 directions and K_3 directions are scattered with maximal density of K_1 close to megafold axis. Mean susceptibility Group III samples (Fig. 11) are dispersed throughout the peridotite body represented dominantly by Type II and also by Type III AMS patterns. Samples show similar degree of AMS to Group II samples and shape of AMS ellipsoid ranges from slightly prolate to highly oblate. We recognize two main orientation of AMS ellipsoids: 1) SW trending K_1 directions and corresponding to NW–SE trending steep girdle of K_2, K_3 directions associated with mainly plane strain to prolate ellipsoids. 2) K_1 direction clustered close to megafold axis and the K_3 directions forming wide cluster plunging at medium angles to the East. Some Type III magnetic fabrics are also present but their magnetic lineations and foliations exhibit any obvious preferred orientation.

Model of serpentinization and magnetic susceptibility

Two step reaction model of serpentinisation

Variable values of the bulk susceptibility from the Mohelno serpentinite (Fig. 5), ranging from $7\text{x}10^{-4}$ to $4\text{x}10^{-2}$ [SI] and density measurements varying between 2.372–2.842 g/m^3 (Tab. 2) were compared to the other studies (Fig. 13) dealing with the relation between bulk magnetic susceptibility and grain density (Oufi et al., 2002; Bach et al., 2006). Such comparison together with microstructural and textural observations can be used to infer the sequence of serpentinization reactions in the studied serpentinite. For example the ODP 920 data from Oufi et al. (2002) shows concordance with single-step reaction model of olivine (Fo_{90}) and water to Mg-serpentinite, Mg-brucite, magnetite and hydrogen (Toft et al. 1990;), which is one of possible scenarios for the oceanic serpentinization (Evans, 2010). Our data, similarly to those of Bach et al. (2006), follow the trend of a two-step serpentinization sequence, which is another possible model for the harzburgite serpentinization. The first step is represented by an isochemical reaction of olivine (Mg#90) to serpentine (Mg#95) and Fe-rich brucite (Mg#75), which is not producing any magnetite (Type I microstructure). The second step is a reaction of Fe-rich brucite with aqueous silica to form serpentine and magnetite (Types II and III serpentinite microstructures). Breakdown of orthopyroxene to serpentine is a possible source of the aqueous silica in this scenario (Bach et al., 2006).

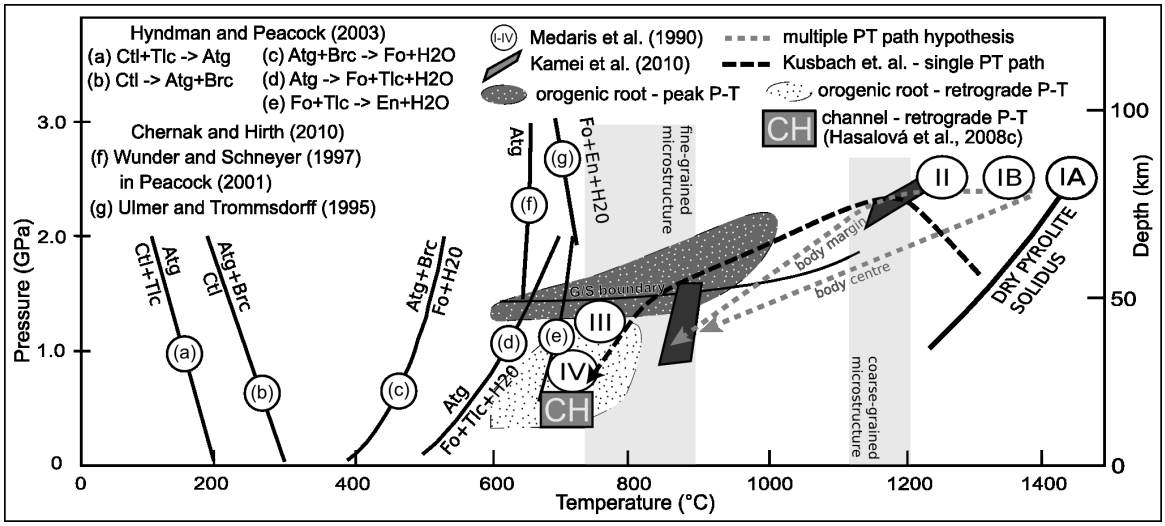

Figure 12. Pressure-temperature diagram showing complicated history of the Mohelno peridotite body (after Chapter 2). Condition in middle crust after Hasalová et al. (2008a). Antigorite isograde are from (a)-(e) Hyndman and Peacock, 2003, (f)-(g) Chernak and Hirth, 2010.

A lack or low production of magnetite during the early phase of serpentinization was also proposed by Evans (2010). Slow growth of antigorite at the expense of olivine at higher temperatures (as high as 500–600 °C) produces little to no magnetite due to slow Fe-Mg diffusion in olivine. This scenario has been discarded for the Mohelno peridotite body, because the reported olivine composition (Mg# 90, Kamei et al. 2010), similar to the olivine composition of the other peridotite bodies in the Bohemian Massif (Schmädicke et al., 2010) does not reach values of the Fe-enriched olivines Mg# 0.84-0.88 reported by Evans (2010).

Serpentinization sequence inferred from the relation between the bulk magnetic susceptibility and grain density is concordant with the proposed serpentinization along the P–T path of the peridotite body and microstructural observations. In the least serpentinized samples (Fig. 2a) locally preserved mesh rim microstructure of massive serpentine devoid of opaque minerals can be explained by high temperature (under 650 °C) isochemical reaction of olivine to antigorite and Fe-rich brucite producing no magnetite. Water necessary for the serpentinization of the peridotite might have been expelled from the melt draining through simultaneously retrogressed granulite. The second step of serpentinization is recorded in the mesh rim microstructure of massive serpentine with abundant opaque minerals surrounding relics of olivine (Fig. 2b) and bastites. This microstructure may originate via reaction of Fe-rich brucite with silica to serpentine and magnetite, which corresponds to the second step of the two-step sequence reported by other authors. The source of the aqueous silica could be

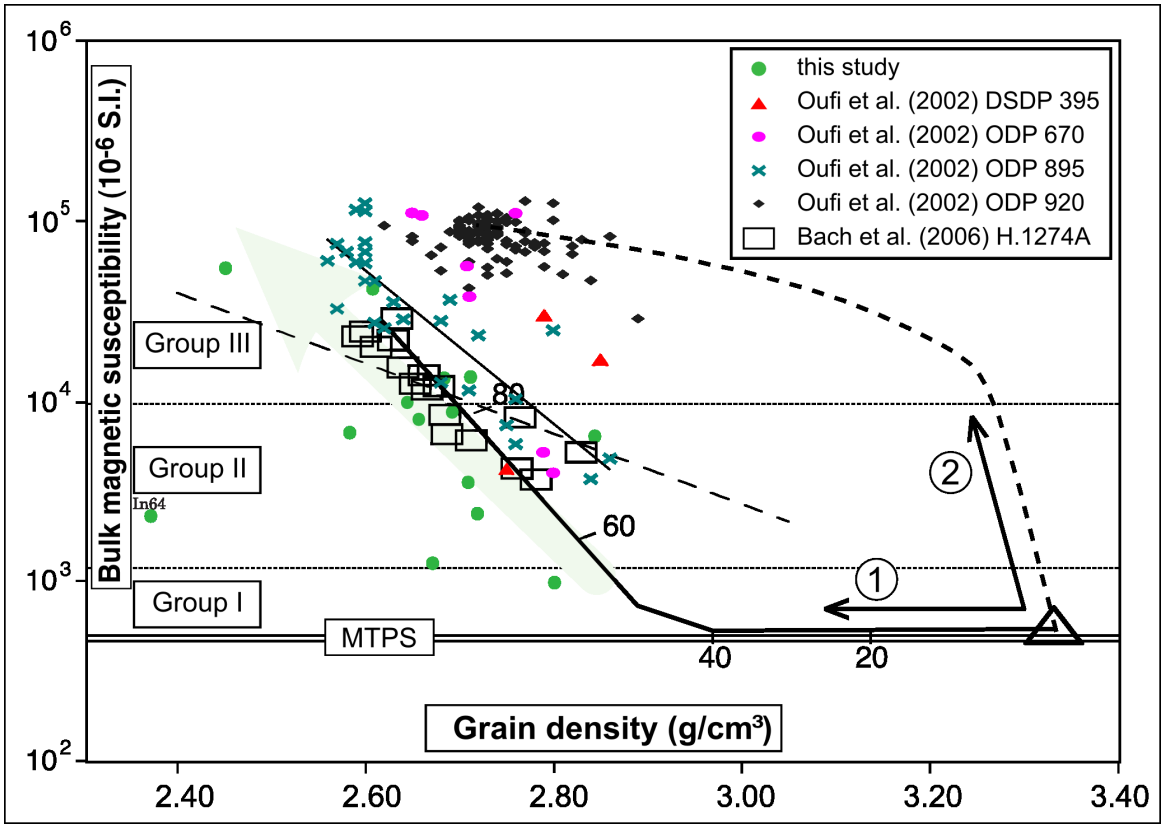

Figure 13. Relation between bulk magnetic susceptibility and grain density for Mohelno peridotite samples after Bach et al. (2006). Triangle represents a typical fresh peridotite, having similar bulk susceptibility as calculated MTPS for Mohelno peridotite. Line (1) represents two-step serpentinization model. Line (2) is calculated for a single-step serpentinization reaction. See Bach et al. (2006); Toft et al. (1990) for more detailed explanation.

internal and result from the breakdown of orthopyroxene to serpentine or external resulting from the fluid penetrating along retrograded and hydrated shear zones cross-cutting the surrounding granulite. Antigorite recrystallizes with decreasing temperature to form lizardite, which is presently the most abundant serpentine mineral according the XRD spectrum. In addition, further recrystallization of lizardite to chrysotile produces more magnetite, as lizardite can incorporate more iron in its structure than chrysotile (O'Hanley and Dyar, 1993; O'Hanley and Dyar, 1998). These changes during late serpentinization can be recorded in the third broadly represented microstructure with high modal volume of massive serpentine organized in sub-parallel serpentine layers (Fig. 2c) rich in batches and clusters of opaque minerals.

In conclusion, this progressive serpentinization sequence would result in presence of only paramagnetic minerals until the degree of serpentinization reaches ~50%. Exponential increase of the bulk magnetic susceptibility starts with decomposition of the Fe-rich brucite by aqueous silica forming ferromagnetic magnetite. Further growth of magnetite is possible also due to recrystallization between

different serpentine polymorphs.

Crystallographic relations in serpentinized peridotite

In order to understand the magnetic fabric of the Mohelno peridotite body, data dealing with correlation between crystallographic axes and axes of anisotropy of magnetic susceptibility ellipsoid were collected from the literature (Borradaile and Lagroix, 2001; Ferré et al., 2005; Boudier et al., 2009) for different ultramafic minerals (Fig. 14.a). Ferré et al. (2005) described the orientation and shape of the AMS ellipsoid within Fo_{98} olivine crystal. In his model, the principal susceptibilities K_1, K_2 and K_3 are respectively 1.205, 0.908 and 0.887 and are oriented as follows: K_1 is parallel to $[100]_{\mathrm{ol}}$ axis, K_2 to $[010]_{\mathrm{ol}}$ and K_3 to $[001]_{\mathrm{ol}}$. From site average tensor parameters the average bulk susceptibility $K_m = 1135 \pm 770$ [μSI] was calculated. Similarly, description of the AMS ellipsoid with respect to crystallographic orientation for orthopyroxene and serpentine (lizardite) was used according to Borradaile and Lagroix (2001). For orthopyroxene the principal susceptibilities K_1, K_2 and K_3 are respectively 1.445, 0.932 and 0.733 and are oriented as follows: K_1 is parallel to $[001]_{\mathrm{opx}}$ axis, and K_2 and K_3 are both parallel to $(\mathrm{hk0})_{\mathrm{opx}}$ plane. The serpentine AMS ellipsoid axes are more scattered, but the orientation pattern can be described as: K_3 is parallel to $[001]_{\mathrm{atg}}$ axis, K_1 is parallel to $(\mathrm{hk0})_{\mathrm{atg}}$ plane and K_2 is parallel to $(0\mathrm{kl})_{\mathrm{atg}}$ plane. The bulk susceptibility of the orthopyroxene and serpentine K_{m} are 4209 ± 945 [μSI] and 8734 ± 4849 [μSI], respectively. In all cases, the bulk susceptibility exceeds the one expected for the silicate lattice (< 1000 [μSI]), revealing the presence of iron oxide inclusions. Nevertheless, the silicate lattice retains some crystallographic control on the orientation of the principal susceptibilities (Borradaile and Lagroix, 2001).

Two different olivine LPO patterns in the Mohelno peridotite have been described: the [100](0kl) pattern and the axial[010] pattern (Chapter 2), and supported by the most common orthopyroxene LPO pattern [001](100) aligned with the orientation of the olivine LPO lineation (olivine crystal axis [100]) and foliation (olivine crystal plane (010)). Such observations can be used as the general framework for further consideration of the relationships between crystallographic patterns and AMS in the serpentinized peridotite. Unfortunately, the electron back-scattered diffraction (EBSD) measurement of the serpentine LPO is very complicated, because of serpentine strong tendency to amorphization during preparation and polishing (Van De Moortèle et al., 2010). Therefore, in order to consider crystallographic orientation of the serpentine, we adopted the topotactic relationships between olivine and antigorite of Boudier and Mainprice (2009), who reported a preferred orientation of the serpen-

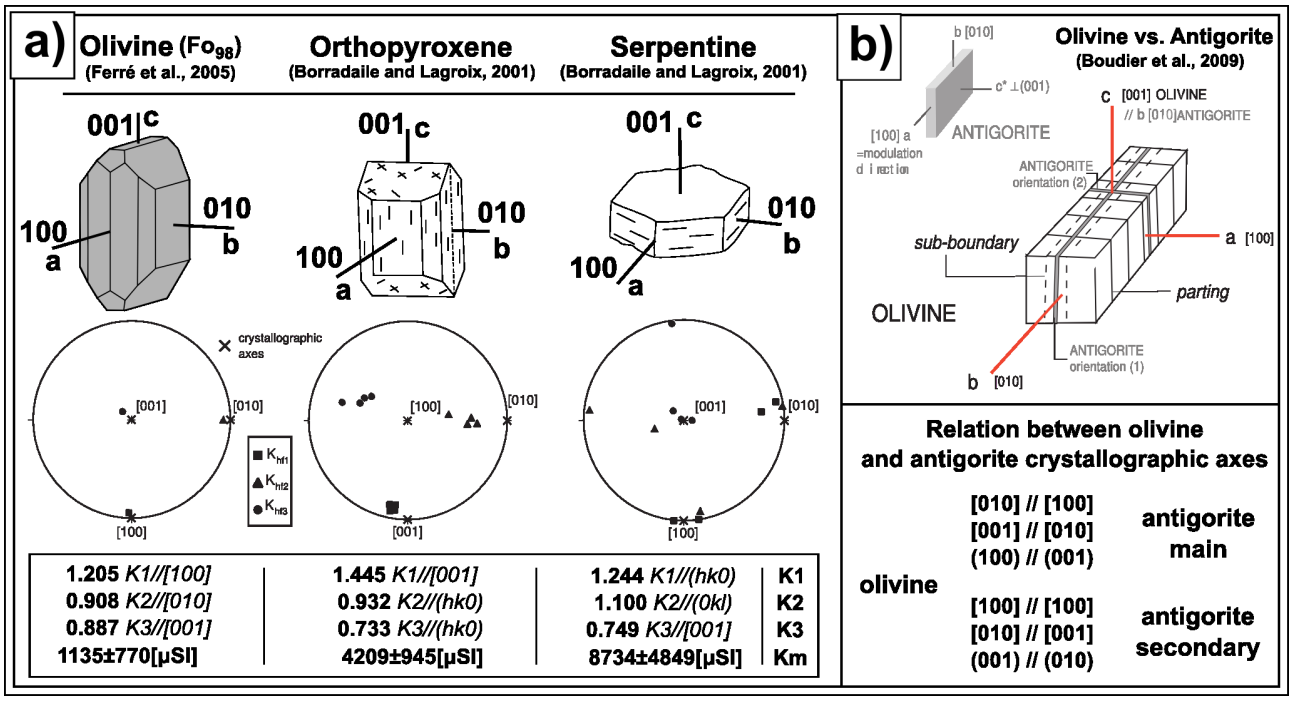

Figure 14. (a) Relation between crystallographic pole axes and anisotropy of magnetic susceptibility ellipsoid axes, together with values of K_1, K_2 and K_3 and bulk susceptibility for olivine (Ferré et al., 2005), orthopyroxene and serpentine (Borradaile and Lagroix, 2001) (b) Topotactic relationship between olivine and antigorite from rare antigorite schist (Boudier and Mainprice, 2009).

tine aggregate inherited from the olivine peridotite preferred orientation in serpentinized peridotite. These authors have shown that despite strong shear deformational history in the supra-subduction zone mantle wedge the topography of the olivine-serpentine interfaces is primarily controlled by fluid pathways along microcracks oriented in accordance with the orientation of olivine aggregate. Two different topotactic relationships between olivine and antigorite were described (Fig. 14b): $[100]_{atg}//[010]_{ol}$ and $[010]_{atg}//[001]_{ol}$ with plane in contact $(001)_{atg}//(100)_{ol}$ (further called serpentine main relationship) and $[100]_{atg}//[100]_{ol}$ and $[001]_{atg}//[010]_{ol}$ with plane in contact $(010)_{atg}//(001)_{ol}$ (further called serpentine secondary relationship).

All these data about the AMS of ultramafic minerals, LPO patterns of olivine and orthopyroxene in peridotite and topotactic relationships between olivine and serpentine, allow us to construct and explore a simple model of the magnetic fabric in the serpentinized peridotite. The main goal of this model is to emphasize some interesting features of the magnetic fabric caused only by topotactic relationships of the paramagnetic ultramafic minerals. Several simplifications and adjustments of the experimentally measured data were necessary. Firstly we assigned individual AMS ellipsoid axes to the only one best fitting crystallographic axis in the orthopyroxene and serpentine crystals. For the orthopyroxene we

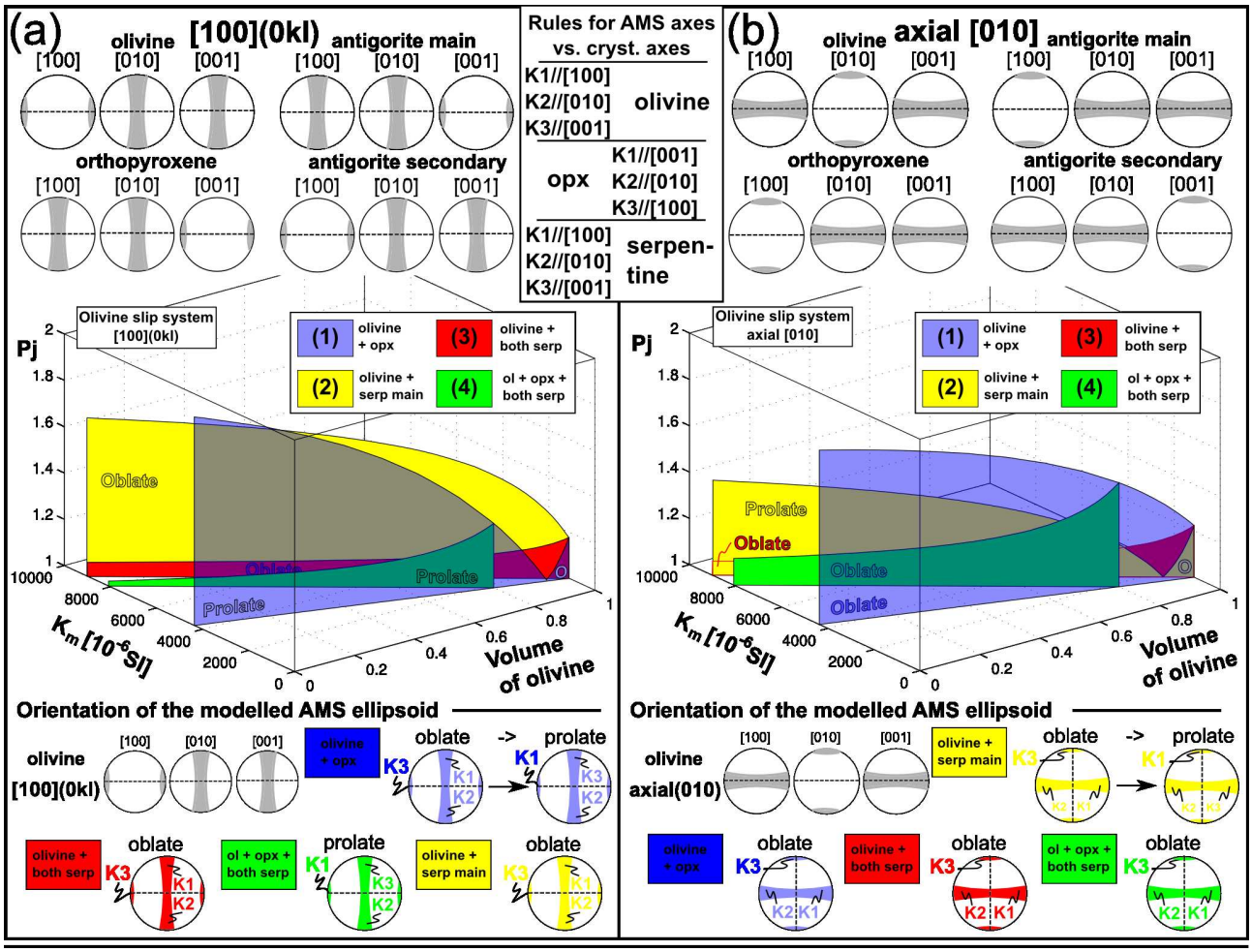

Figure 15. Simple model of the magnetic fabric in the serpentinized peridotite. (a) Model for peridotite with fabric governed by olivine [100](0kl) slip system. *Top* – topotactic relationships between crystallographic axes of the rock-forming minerals. *Middle* – diagram displaying modelled bulk susceptibility (K_{m}) vs. deegre of anisotropy (P_j) for various mineral and modal composition of serpentinized peridotite. Different mineral assemblages for the modelled rock are used (*blue* - olivine + orthopyroxene, *yellow* - olivine + serpentine growing in main topotactic orientation, *red* - olivine + serpentine growing in both topotactic orientations and *green* - olivine + orthopyroxene + serpentine growing in main topotactic orientation) varying also the modal composition of the assemblage. *Bottom* – the orientation of the modelled AMS ellipsoid with respect to the governing olivine slip system. (b) Model for peridotite with fabric dominated by olivine axial(010) slip system.

used K_1 parallel to $[001]_{\mathrm{opx}}$ axis, K_2 parallel to $[010]_{\mathrm{opx}}$ axis and K_3 parallel to $[100]_{\mathrm{opx}}$ axis (Lagroix and Borradaile, 2000). For the serpentine we assigned the less important K_1 and K_2 axes of the oblate AMS ellipsoid as follows: K_1 parallel to [100] axis and K_2 parallel to [010] axis, based on the frequency of the measured data (Borradaile and Lagroix, 2001).

Another simplification was replacement of the real sample LPO pattern with its ideal "single crystal" representation. In such representation the sample with the [100](0kl) LPO pattern has all [100] crystallographic axes clustered into single point, while [010] and [001] axes are uniformly distributed along girdle perpendicular to the [100]. Correlation between the olivine and orthopyroxene LPO

patterns allows to create similar representation also for the orthopyroxene. Finally, based on the topotactic relationships between olivine and antigorite, the same estimation can be done for both type of their topotactic contact (Fig. 15). Last adaptation in the model of the magnetic fabric is using olivine-antigorite topotactic relationship and paramagnetic properties of the lizardite because of lack of magnetic data for antigorite. As shown above, we propose that most of the serpentinization took place at HT condition and that antigorite was the primary serpentine mineral, which was during cooling statically pseudomorphosed by lizardite. This necessary adjustment represent the actual situation in the studied serpentinite.

The resulting AMS fabric is calculated by summing the AMS ellipsoids and K_m for individual phases (olivine, orthopyroxene, main serpentine and secondary serpentine) weighted by the volume proportion of the individual phase. Magnetic fabric parameters were explored for both olivine LPO patterns and for four different mineral compositions. Each explored composition then continuously varied in modal composition: (1) mineral composition of olivine and orthopyroxene goes from 100 % olivine + 0 % orthopyroxene to 0 % olivine + 100 % orthopyroxene; (2) similarly for olivine and serpentine in main topotactic orientation, the composition goes from 100 % olivine + 0 % main serpentine to 0 % olivine + 100 % main serpentine; (3) from 100 % olivine + 0 % main serpentine + 0 % secondary serpentine to 0 % olivine + 50 % main serpentine + 50 % secondary serpentine and (4) from 80 % olivine + 20 % orthopyroxene + 0 % main serpentine + 0 % secondary serpentine to 0 % olivine + 20 % orthopyroxene + 40 % main serpentine + 40 % secondary serpentine.

Modelled magnetic fabric demonstrate the influence of the olivine LPO pattern on the shape and degree of anisotropy of the AMS ellipsoid (Fig. 15). For example, the [100](0kl) LPO pattern, prolate AMS ellipsoid with composition 80% olivine, 20% orthopyroxene, no serpentine and $Pj = 1.27$ due to growth of serpentine in both orientations ends with the degree of anisotopy $Pj = 1.02$. On the other hand, for the axial[010] pattern and the same composition, the parcial "phase" AMS ellipsoids have different orientation leading to final oblate shape of the AMS ellipsoid and significantly higher degree of anisotropy values both at initial and final composition ($Pj_{inicial} = 1.44$ to $Pj_{final} = 1.11$).

The other implication of this approach is the orientation of bulk AMS ellipsoid (Fig. 15a). For given orientation of olivine crystallographic axes resulting from activity of [100](0kl) slip system following orientations of AMS ellipsoid are possible: 1) olivine + opx assemblage of ideal harzburgite yields oblate ellipsoid with K_3 parallel to [100] direction of olivine and K_1, K_2 form girdle in (100) for $>$ 95 % olivine (dunite) or prolate ellipsoid with K_1 parallel [100] and K_2, K_3 form girdle in (100) for $<$ 95 %

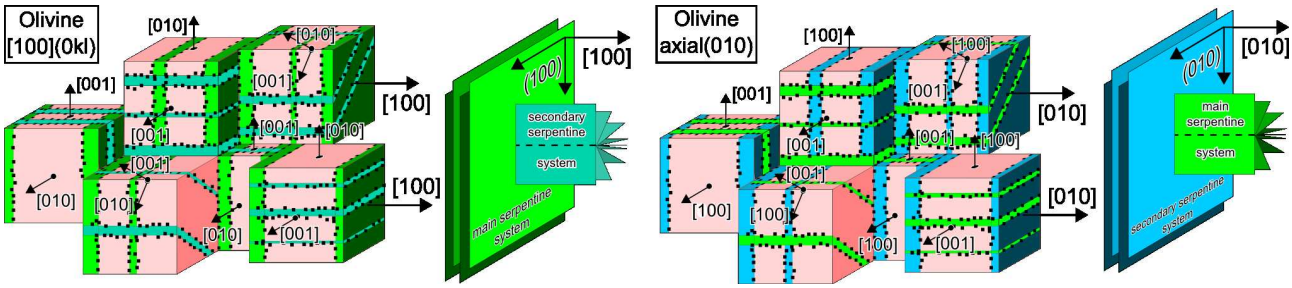

Figure 16. Idealized sketch of the peridotite/serpentinite microstructure illustrating topotactic relationships between olivine and serpentine leading to regular distribution of magnetite in the serpentinized peridotite. (a) for slip system [100](0kl), (b) for axial(010) slip system.

olivine (harzburgite). Olivine + antigorite parallel to two topotactic orientations and olivine+antigorite parallel to the main topotactic orientation yield the same orientation of oblate AMS ellipsoid as the former dunite model. The difference is only in degree of anisotropy, which is significantly higher for olivine +antigorite in main topotactic orientation compared to antigorite growing along two orthogonal olivine planes. Finally, assemblage olivine + opx + antigorite in two topotactic orientations produces prolate AMS ellipsoid with K_1 direction parallel to [100] olivine crystallographic direction and K_3, K_2 directions coinciding with (100) plane.

For orientation of olivine crystallographic axes resulting from axial [010] slip system the orientation of AMS ellipsoid is as follows: Olivine + opx assemblage exhibits oblate AMS ellipsoid with K_3 direction parallel to [010] direction of olivine and K_1, K_2 form girdle in (010) plane. The same orientations of oblate AMS ellipsoid show all modeled mineral assemblages which differ from each other in degree of anisotropy and bulk susceptibility. The only exception is the AMS ellipsoid for olivine + antigorite in main topotactic orientation which evolves from oblate to prolate with degree of serpentinisation.

The main implication of such a modeling is the possible distribution of AMS anisotropy generated by magnetite chains. The microstructural observations show that the magnetite is mainly growing either at the boundary of olivine and serpentine or between two serpentines as a result of retrograde reactions of antigorite to lizardite and magnetite. This implies that the newly grown magnetites are not distributed randomly but there is a significant influence of olivine and orthopyroxene crystallographic orientations which govern orientation of serpentine and magnetite minerals during static serpentinisation. Therefore, we suggest that the magnetite aggregates are following the AMS trends calculated for assemblages containing significant amount of serpentine (Fig. 16).

Origin of magnetic fabric in the Mohelno peridotite

The Mohelno peridotite reveals complex pattern of the magnetic fabric, expressed by various magnetic fabric patterns (Type I-III), by wide range of the bulk magnetic susceptibility and mean orientation of AMS orientation data. Dividing the AMS data into three groups (Group I-III) allowed to assign each group to individual step in the sequence of the serpentinization process. Important observation for the following interpretation is the static nature of the serpentinization lacking any structural or microstructural (Fig. 3) signs of the syn/post-serpentinization deformation.

The Group I represents probably the magnetic fabric from the earlier stage of the serpentinization process in the middle crustal conditions. Several data sources lead to this scenario, in particular: (1) the peridotite body is still plastically deformed in the mid-crustal conditions, therefore preservation of any mantle-related fabric is improbable; (2) the bulk magnetic susceptibility of the Group I is relatively close to the MTPS (calculated from chemical composition of serpentinite), showing lack or only minimal production of magnetite during serpentinization (Bach et al. 2006); (3) orientation of AMS mimetizing the olivine LPO foliation has intersection in β-axis of the peridotite fold (Fig. 9; Chapter 2); (4) presence of the Type I magnetic fabric pattern, which can be interpreted as growth of the serpentine ($\pm$ magnetite) along microcracks exploiting shape of olivine aggregate; (5) localization of Group I samples in the center of the wider northern limb of the peridotite fold, where the degree of serpentinization is supposed to remain low due to large distance from fluid source; (6) prevailing neutral shape of the AMS ellipsoid and low degree of anisotropy could result from the regular orientation of the overgrowing serpentine as ilustrated on the Fig. 16.

The Group II represents the transitional magnetic fabric between the Group I and III. Orientational magnetic foliation data are not showing girdle-like character of the Group I, neither magnetic foliation and lineation clustering typical for the Group III. The atypical Type III magnetic fabric pattern could be explained by serpentinite veins obliquely cross-cutting the serpentinite fabric partially following previous peridotite microstructure. Higher bulk susceptibility suggests presence of the magnetite, which can be produced by second step in the two-step serpentinization model (Bach et al., 2006) and grows around relics of olivine and equilibrating primary serpentine. In conclusion, the magnetic fabric is influenced both by the paramagnetic ultramafic minerals and newly grown magnetite (Fig. 16b).

The highest bulk susceptibility Group III, shows two principal orientations of AMS fabrics. The main magnetic mineral is ferromagnetic magnetite embedded in almost completely serpentinized peridotite.

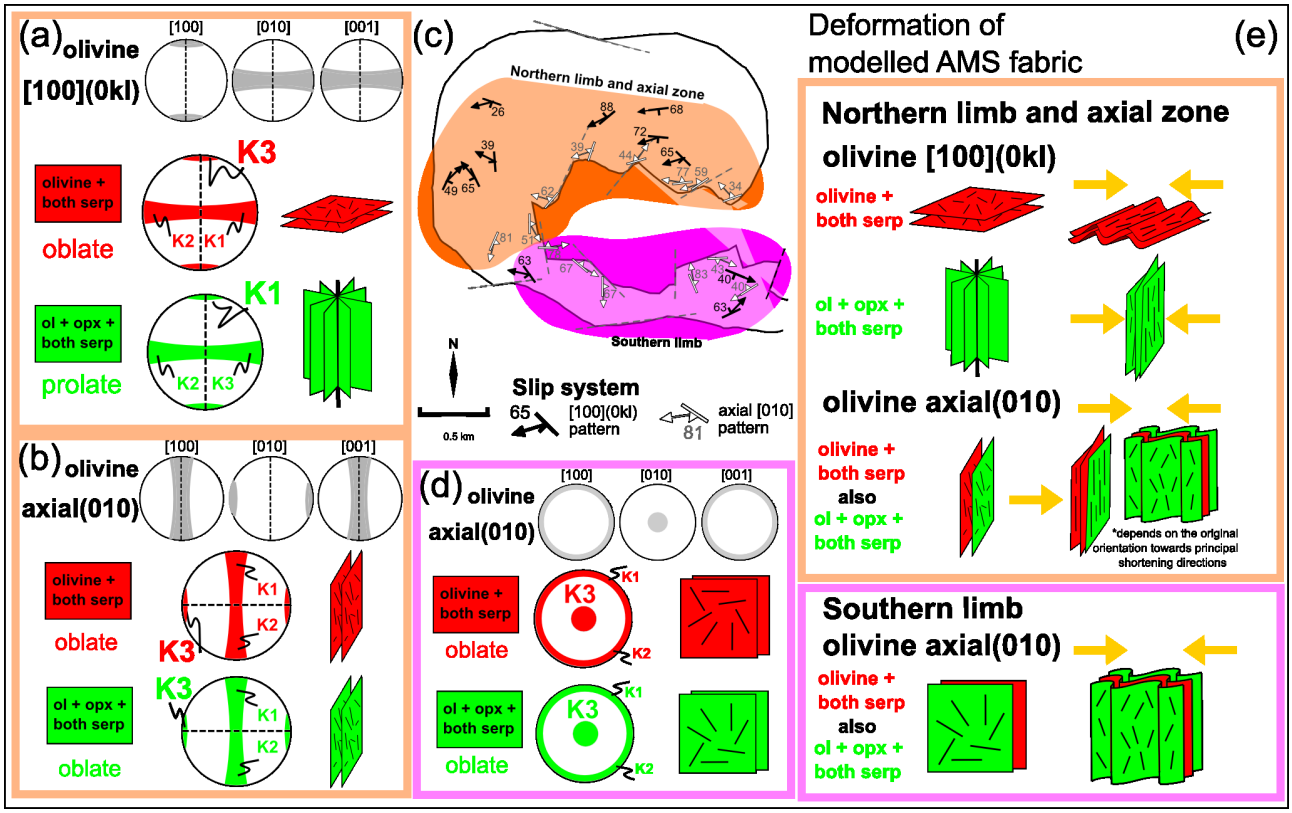

Figure 17. Sketch of different pre-deformational orientation of magnetic foliation and lineation constrained by primary peridotite fabric. Situation for different position within the peridotite fold and both main guiding olivine slip system is illustrated. (a) Ilustration of magnetic fabric induced by olivine [100](0kl) slip system in sample from northern (*orange*) part of the body with either olivine + antigorite in both topotactic orientations or olivine + orthopyroxene + antigorite in both topotactic orientations. (b) Ilustration of magnetic fabric induced by olivine axial(010) slip system in sample from northern (*orange*) part of the body with either olivine + antigorite in both topotactic orientations mineral assemblage or olivine + orthopyroxene + antigorite in both topotactic orientations assemblage. (c) Distribution of olivine LPO slip patterns within the peridotite fold divided into northern (*orange*) and southern (*violet*) part. (d) Ilustration of magnetic fabric induced by olivine axial(010) slip system in sample from southern (*violet*) part of the body with either olivine + antigorite in both topotactic orientations mineral assemblage or olivine + orthopyroxene + antigorite in both topotactic orientations assemblage. (e) Deformation of modelled magnetic fabric by E–W shortening both in the northern (*orange*) and southern (*violet*) part of the fold.

Atypical magnetic fabric pattern Type III is also present again in orientation oblique to the prevailing magnetic fabric orientations and can be explained by serpentinite veins obliquely cross-cutting the dominating magnetic fabric. Strong AMS fabrics of group III samples is incompatible with concept of static crystallization.

In order to explain this fabric pattern we show the distribution of modelled AMS fabrics for statically serpentinized peridotite following the regional distribution of olivine slip systems inside the peridotite fold (Chapter 2) (Fig. 17). This approach shows the AMS pattern for serpentinized peridotite prior to late deformation. In the axial zone and northern limb of the fold is dominant the [100](0kl) slip system, which implies the presence of oblate AMS ellipsoid and magnetic foliation perpendicular to

the fold hinge for olivine + serpentine assemblage or prolate AMS ellipsoid with K_1 direction parallel to the fold hinge for olivine + orthopyroxene + serpentine assemblage (Fig. 17a). In the southern limb of peridotite fold the olivine reveals predominantly presence of axial(010) slip system. In this domain the AMS fabric resulting from static serpentinisation reveals oblate ellipsoid with magnetic foliation parallel to olivine foliation and with the orientation of fold limb (Fig. 17d). It is evident that such a distribution of AMS fabrics is not compatible with orientation of Group III and II AMS fabrics, which correspond to dominant serpentine foliation measured in the field.

These fabrics can be explained by small deformation superimposed on the serpentinized peridotite with abundant magnetite surrounding well oriented relics of olivine and orthopyroxene. Indeed, Schulmann et al. (1991, 1994) shown, that the whole complex of the Gföhl unit is exposed to the large scale folding due to late E-W compression at low grade conditions. We therefore propose that this small strain increment causes weak deformation of the serpentinite body recorded by the Group III magnetic fabric and partial reorientation of Group II AMS fabric (Fig. 17). Accordingly, the assumed AMS fabric (case of olivine + serpentine oblate fabric) is affected by E–W shortening which induces folding of horizontal foliation defined by serpentine resulting in distribution of K_1 direction parallel to fold axis and K_3, K_2 directions forming E–W trending steep girdle (Fig. 11). The folding model is compatible with origin of prolate to plane strain ellipsoid (Fig. 11) as a result of shortening parallel to pre-existing oblate fabric (Schulmann and Ježek, 2011). Similarly, deformation of olivine + opx + serpentine assemblage results in development of AMS lineation parallel to peridotite fold hinge and magnetic foliation perpendicular to the principal shortening (Fig. 11 and 17). The dominant oblate fabric with increased degree of magnetic anisotropy is compatible with numerical modeling of shortening of prolate AMS fabric with long axis orthogonal to shortening direction (Schulmann and Ježek, 2011). It is the latter fabric, which is dominant in field and which is consistent with observed mineralogy. Finally, the shortening of magnetic fabrics from the southern fold limb results in development of girdle of steep AMS foliations with K_1 direction perpendicular to principal shortening (Fig. 17). In our model, the Group III samples represent an end–member related to deformation, while Group I reflects AMS pattern end–member resulting from mimetic overgrowths of olivine and orthpyroxene by serpentines along crystallographic grain boundaries. The Group II thus represents mixed stage bearing features of both end–member situations.

References

- Aydin, A., Ferré, E. C., Aslan, Z., (2007). The magnetic susceptibility of granitic rocks as a proxy for geochemical composition: example from the Saruhan granitoids, NE Turkey. Tectonophysics. 441, 85–95.

- Bach, W., Paulick, H., Garrido, C. J., Ildefonse, B., Meurer, W. P., Humphris, S. E., (2006). Unraveling the sequence of serpentinization reactions: petrography, mineral chemistry, and petrophysics of serpentinites from MAR 15°N (ODP Leg 209, Site 1274). Geophys. Res. Lett. 33, L1330.

- Borradaile, G. J., Lagroix, F., (2001). Magnetic fabrics reveal upper mantle flow fabrics in the Troodos Ophiolite Complex, Cyprus. J. Struct. Geol.Geology. 23, 1299–1317.

- Borradaile, G. J., Lucas, K., (2003). Tectonics of the Akamas and Mamonia ophiolites, Western Cyprus: magnetic petrofabrics and paleomagnetism. J. Struct. Geol. 25, 2053–2076.

- Boudier, F., B. A., Mainprice, D., (2009). Serpentine mineral replacements of natural olivine and their seismic implications: oceanic lizardite versus subduction–related antigorite. J. Petrol. 51, 495–512.

- Chernak, L. J., Hirth, G., (2010). Deformation of antigorite serpentinite at high temperature and pressure. Earth Planet. Sci. Lett. 296, 23–33.

- Christensen, N. I., (1978). Ophiolites, seismic velocities and oceanic crustal structure. Tectonophysics. 47, 131–157.

- Dunlop, D., Özdemir, Ö., 1997. Rock Magnetism. Fundamentals and frontiers, Cambridge University Press, Cambridge.

- Edel, J., Weber, K., (1995). Cadomian terranes, wrench faulting and thrusting in the central Europe Variscides: geophysical and geological evidence. Geol. Rundsch. 84, 412–432.

- Escartín, J., Hirth, G., Evans, B., (2001). Strength of slightly serpentinized peridotites: Implications for the tectonics of oceanic lithosphere. Geology 29, 1023–1026.

- Evans, B. W., (1977). Metamorphism of alpine peridotite and serpentinite. Annu. Rev. Earth Planet. Sci. 5, 397–447.

- Evans, B. W., (2010). Lizardite versus antigorite serpentinite: Magnetite, hydrogen, and life(?). Geology 38, 879–882.

- Ferré, E., Tikoff, B., Jackson, M., (2005a). The magnetic anisotropy of mantle peridotites: Example from the Twin Sisters dunite, Washington. Tectonophysics 398, 141.

- Ferré, E., Tikoff, B., Jackson, M., (2005b). Corrigendum to "The magnetic anisotropy of mantle peridotites: Example from the Twin Sisters dunite, Washington" [Tectonophysics 398 (2005) 141–166]. Tectonophysics 405, 233.

- Fiala, J., Matějovská, O., Vaňková, V., (1987). Moldanubian granulites: source material and petrogenetic considerations. Neu.Jb.Mineral., Abh. 157, 133–165.

- Franke, W., (2000). The mid-European segment of the Variscides: tectonostratigraphic units, terrane boundaries and plate tectonic evolution, In: Franke, W., Haak, V., Oncken, O., D., T. (Eds.), Orogenic Processes: Quantification and Modelling in the Variscan Belt. Geological Society, London, Special Publications 179, 35–61.

- Hacker, B. R., Abers, G. A., Peacock, S. M., (2003). Subduction factory 1. Theoretical mineralogy, densities, seismic wave speeds, and H_2O contents. J. Geophys. Res. 108, 2029.

- Handy, M. R., (1990). The solid–state flow of polymineralic rocks. J. Geophys. Res. 95, 8647–8661.

- Hasalová, P., Janoušek, V., Schulmann, K., Štípská, P., Erban, V., (2008b). From orthogneiss to migmatite: Geochemical assessment of the melt infiltration model in the Gföhl Unit (Moldanubian Zone, Bohemian Massif). Lithos 102, 508–537.

- Hasalová, P., Schulmann, K., Lexa, O., Štípská, P., Hrouda, F., Ulrich, S., Haloda, J., Týcová, P., (2008a). Origin of migmatites by deformation-enhanced melt infiltration of orthogneiss: a new model based on quantitative microstructural analysis. J. Metamorph. Geol. 26, 29–53.

- Hasalová, P., Štípská, P., Powell, R., Schulmann, K., Janoušek, V., Lexa, O., (2008c). Transforming mylonitic metagranite by open–system interactions during melt flow. J.Metamorph.Geol. 26, 55–80.

- Hrouda, F., (2010). Modelling relationship between bulk susceptibility and AMS in rocks consisting of two magnetic fractions represented by ferromagnetic and paramagnetic minerals – Implications for understanding magnetic fabrics in deformed rocks. J. Geo. Soc. India 75, 254–266.

- Hrouda, F., Faryad, S. W., Chlupáčová, M., Jeřábek, P., Kratinová, Z., (2009a). Determination of field–independent and field–dependent components of anisotropy of susceptibility through standard AMS measurement in variable low fields II: An example from the ultramafic body and host granulitic rocks at Bory in the Moldanubian Zone of Western Moravia, Czech Republic. Tectonophysics 466, 123.

- Hrouda, F., Faryad, S. W., Jeřábek, P., Chlupáčová, M., Vitouš, P., (2009b). Primary magnetic fabric in an ultramafic body (Moldanubian Zone, European Variscides) survives exhumation–related granulite–amphibolite facies metamorphism. Lithos 111, 95.

- Hrouda, F. Jelínek, V., Hrušková, L., (1990). A package of programs for statistical evaluation of magnetic anisotropy data using IBM–PC computers. EOS Trans. AGU.

- Hyndman, R. D., Peacock, S. M., (2003). Serpentinization of the forearc mantle. Earth Planet. Sci. Lett. 212, 417.

- Janoušek, V., Finger, F., Roberts, M., Frýda, J., Pin, C., Dolejš, D., (2004). Deciphering the petrogenesis of deeply buried granites: whole-rock geochemical constraints on the origin of largely undepleted felsic granulites from the Moldanubian Zone of the Bohemian Massif. Earth Env. Sci. T. R. So. Edinb. 95, 141–159.

- Janoušek, V., Holub, F. V., (2007). The causal link between HP–HT metamorphism and ultrapotassic magmatism in collisional orogens: case study from the Moldanubian Zone of the Bohemian Massif. P. Geologist. Assoc. 118, 75–86.

- Jelenska, M., Werner, T., (1997). Magnetic anisotropy parameters for the ultramafic and the gabbroic rocks from three boreholes from the Sudetes, Poland. Phys. Chem. Earth 22, 161–165.

- Jelínek, V., (1981). Characterization of the magnetic fabric of rocks. Tectonophysics 79, T63–T67.

- Jelínek, V., Pokorný, J., (1997). Some new concepts in technology of transformer bridges for measuring susceptibility anisotropy of rocks. Phys. Chem. Earth 22, 179–181.

- Jelínek, V., Kropáček, V., (1978). Statistical processing of anisotropy of magnetic susceptibility measured on groups of specimens. Stud. Geophys. Geod. 22, 50–62.

- Kamei, A., Obata, M., Michibayashi, K., Hirajima, T., Svojtka, M., (2010). Two contrasting fabric patterns of olivine observed in garnet and spinel peridotite from a mantle–derived ultramafic mass enclosed in felsic granulite, the Moldanubian Zone, Czech Republic. J. Petrol. 51, 101–123.

- Kontny, A., Woodl, A. B., Koch, M., (2004). Temperature–dependent magnetic susceptibility behaviour of spinelloid and spinel solid solutions in the systems Fe_2SiO_4–Fe_3O_4 and $(Fe,Mg)_2SiO_4$–Fe_3O_4. Phys. Chem. Miner. 31, 28–40.

- Lagroix, F., Borradaile, G. J., (2000). Magnetic fabric interpretation complicated by inclusions in mafic silicates. Tectonophysics 325, 207–225.

- Lexa, O., Schulmann, K., Janoušek, V., Štípská, P., Guy, A., Racek, M., (2011). Heat sources and trigger mechanisms of exhumation of HP granulites in Variscan orogenic root. J. Metamorph. Geol. 29, 79–102.

- Liu, Q., Zeng, Q., Zheng, J., Yang, T., Qiu, N., Liu, Z., Luo, Y., Jin, Z., (2010). Magnetic properties of serpentinized garnet peridotites from the CCSD main hole in the Sulu ultrahigh-pressure metamorphic belt, eastern China. J. Geophys. Res. 115, B06104.

- MacDonald, W. D., Ellwood, B. B., (1988). Magnetic fabric of peridotite with intersecting petrofabric surfaces, Tinaquillo, Venezuela. Phys. Earth Planet. In. 51, 301–312.

- Manning, C. E., (1995). Phase–equilibrium controls on SiO_2 metasomatism by aqueous fluid in subduction zones: reaction at constant pressure and temperature. Int. Geol. Rev. 37, 1074–1093.

- Matte, P., Maluski, H., Rajlich, P., Franke, W., (1990). Terrane boundaries in the Bohemian Massif: Result of large-scale Variscan shearing. Tectonophysics 177, 151–170.

- Matějovská, O., (1975). The Moldanubian gneiss series of south–western Moravia and its relation to granulites.. Věstn. Ústřed. Ústav. Geol. 50, 345–351.

- Matějovská, O., (1967). Petrogenesis of the Moldanubian granulites near Náměšť nad Oslavou. Krystalinikum 5, 85–104.

- Medaris, L. J., Wang, H., Mísař, Z., Jelínek, E., (1990). Thermobarometry, diffusion modelling and cooling rates of crustal garnet peridotites: Two examples from the Moldanubian zone of the Bohemian Massif. Lithos 25, 189–202.

- Miller, D. & Christensen, N. (1997). Seismic velocities of lower crustal and upper mantle rocks from the slow–spreading Mid–Atlantic ridge, South of the Kane transform zone (MARK), Proc. Oc. Dril. Prog., Sci. Res. 153.

- Nagata, T., 1961. Rock magnetism, Maruzen Company Ltd., Maruzen Tokyo.

- O'Brien, P., Carswell, D., (1993). Tectonometamorphic evolution of the Bohemian Massif: evidence from high pressure metamorphic rocks. Geol.Rundsch. 82, 531–555.

- O'Hanley, D. S., (1992). Solution to the volume problem in serpentinization. Geology 20, 705–708.

- O'Hanley, D. S., Dyar, M. D., (1993). The composition of lizardite 1T and the formation of magnetite in serpentinites. Am. Mineral. 78, 391–404.

- O'Hanley, D. S., Dyar, M. D., (1998). The composition of chrysotile and its relationship with lizardite. Can Mineral 36, 727–739.

- O'Hanley, D. S., Wicks, F. J., (1995). Conditions of formation of lizardite, chrysotile and antigorite, Cassiar, British Columbia. Can. Mineral. 33, 753–773.

- Oufi, O., Cannat, M., Horen, H., (2002). Magnetic properties of variably serpentinized abyssal peridotites. J. Geophys. Res. 107, 2095.

- Parma, J. & Zapletal, K. (1991). CS-1 apparatus for measuring the temperature dependence of low-field susceptibility of minerals and rocks (in co-operation with the KLY-2 Kappabridge).

- Racek, M., Štípská, P., Pitra, P., Schulmann, K., Lexa, O., (2006). Metamorphic record of burial and exhumation of orogenic lower and middle crust: a new tectonothermal model for the Drosendorf window (Bohemian Massif, Austria). Mineral. Petrol. 86, 221–251.

- Racek, M., Štípská, P., Powell, R., (2008). Garnet–clinopyroxene intermediate granulites in the St. Leonhard massif of the Bohemian Massif: ultrahigh-temperature metamorphism at high pressure or not?. J. Metamorph. Geol. 26, 253–271.

- Reinen, L. A., Weeks, J. D., Tullis, T. E., (1994). The frictional behavior of lizardite and antigorite serpentinites: Experiments, constitutive models, and implications for natural faults. Pure and Applied Geophysics 143, 317–358.

- Ribeiro Da Costa, I., Barriga, F. J., Viti, C., Mellini, M., Wicks, F. J., (2008). Antigorite in deformed serpentinites from the Mid-Atlantic Ridge. Eur. J. Mineral. 20, 563–572.

- Richter, C., K. P. & MacLeod, C. (1996). Magnetic fabrics and sources of magnetic susceptibility in lower crustal and upper mantle rocks from Hess Deep, Proc. ODP, Sci. Results, 147, 393–403.

- Sander, B., 1930. Gefügekunde der Gesteine, Springer, Vienna.

- Schmädicke, E., Gose, J., Will, T. M., (2010). The P–T evolution of ultra high temperature garnet–bearing ultramafic rocks from the Saxonian Granulitgebirge Core Complex, Bohemian Massif. J. Metamorph. Geol. 28, 489–508.

- Schulmann, K., Ježek, J., (2011). Some remarks on fabric overprints and constrictional AMS fabric in igneous rocks. Int. J. Earth Sci.

- Schulmann, K., Konopásek, J., Janoušek, V., Lexa, O., Lardeaux, J.-M., Edel, J.-B., Štípská, P., Ulrich, S., (2009). An Andean type Palaeozoic convergence in the Bohemian Massif. C. R. Geosci. 341, 266–286.

- Schulmann, K., Kroner, A., Hegner, E., Wendt, I., Konopásek, J., Lexa, O., Štípská, P., (2005). Chronological constraints on the pre-orogenic history, burial and exhumation of deep-seated rocks along the eastern margin of the Variscan Orogen, Bohemian Massif, Czech Republic. Am. J. Sci. 305, 407–448.

- Schulmann, K., Ledru, P., Autran, A., Melka, R., Lardeaux, J., Urban, M., Lobkowicz, M., (1991). Evolution of nappes in the eastern margin of the Bohemian Massif: a kinematic interpretation, Geol. Rundsch. 80, 73–92.

- Schulmann, K., Martelat, J.-E., Ulrich, S., Lexa, O., Štípská, P., Becker, J. K., (2008). Evolution of microstructure and melt topology in partially molten granitic mylonite: Implications for rheology of felsic middle crust. J. Geophys. Res. 113, B10406.

- Šichtařová, I., (1981). Moldanubian amphibolites in the area SE of Náměšť nad Oslavou. Věstn. Ústřed. Ústav. Geol. 56, 203–214.

- Štípská, P., Schulmann, K., Kröner, A., (2004). Vertical extrusion and middle crustal spreading of omphacite granulite: a model of syn-convergent exhumation (Bohemian Massif, Czech Republic). J. Metamorph. Geol. 22, 179–198.

- Štípská, P., Schulmann, K., Powell, R., (2008). Contrasting metamorphic histories of lenses of high–pressure rocks and host migmatites with a flat orogenic fabric (Bohemian Massif, Czech Republic): a result of tectonic mixing within horizontal crustal flow?. J. Metamorph. Geol. 26, 623–646.

- Tajčmanová, L., Konopásek, J., Schulmann, K., (2006). Thermal evolution of the orogenic lower crust during exhumation within a thickened Moldanubian root of the Variscan belt of Central Europe. J. Metamorph. Geol. 24, 119.

- Toft, P. B., Arkani-Hamed, J., Haggerty, S. E., (1990). The effects of serpentinization on density and magnetic susceptibility: a petrophysical model. Phys. Earth Planet. In. 65, 137–157.

- Tollmann, A., (1982). Grossräumiger variszischer Deckenbau im Moldanubikum und neue Gedanken zum Variszikum Europas. Geotekton. Forsch. 64, 1–91.

- Ulmer, P., Trommsdorff, V., (1995). Serpentine stability to mantle depths and subduction-related magmatism. Science 268, 858–861.

- Urban, M., (1992). Kinematics of the Variscan thrusting in the Eastern Moldanubicum (Bohemian Massif, Czechoslovakia): evidence from the Náměšť granulite massif. Tectonophysics 201, 371–391.

- Van De Moortèle, B., Bezacier, L., Trullenque, G., Reynard, B., (2010). Electron back–scattering diffraction (EBSD) measurements of antigorite lattice–preferred orientations (LPO). J. Microsc. 239, 245–248.

- Wicks, F. J., Whittaker, E. J. W., (1977). Serpentine textures and serpentinization. Can. Mineral. 15, 459–488.

General conclusions and orogenic scale tectonic implications

This work provides multidisciplinary geological research carried out on lower crust and upper mantle rock assemblage in the eastern margin of the Bohemian Massif, that forms one of the biggest exposure of these rocks in Variscan Europe. The research was focused on structure, petrology, geochemistry and geochronology of Mohelno peridotite massif enclosed in the Náměšť felsic granulite body, that is irregularly enveloped by an garnet-bearing amphibolite belt. Our and previous observations published elsewhere allow a subdivision of Variscan "orogenic root" in two distinct layers, which differ in age and origin (Lexa et al., 2011).

The deeper granulite – peridotite layer occurs in the lower crustal massifs all around the whole Bohemian Massif. The felsic Náměšť granulite body reveals remarkable geochemical and petrological stability recorded also in other granulites over the whole orogeny. However, the granulites from the eastern margin of the Bohemian Massif reveal the important presence of Devonian zircon U-Pb and Pb-Pb ages (~500–400 Ma). They are interpreted in the region of eastern margin of the Bohemian Massif as protolith ages (Schulmann et al., 2005; Tajčmanová et al., 2006). Importantly, the other granulite massifs, namely located in the western part of the Moldanubian Zone, are characterized by mid-Ordovician protolith ages (Janoušek et al., 2004, Janoušek and Holub, 2007). As proposed in the Chapter 1, the process of formation of continental crust may continue from Ordovician to Early Devonian, thereby producing both types of mafic and felsic magmas over the whole period of time. The Devonian protolith ages may imply that the Devonian part of "Saxothuringian crust" was underthrust underneath the autochthonous part of the Bohemian Massif before the rear Ordovician part, which occurs today in western part of the orogenic root domain. The Early Devonian origin of orogenic lower crust in the Náměšť Granulite is however significantly older than Late Devonian age of included mantle fragment, which is considered as asthenospheric in origin (Medaris et al., 2005).

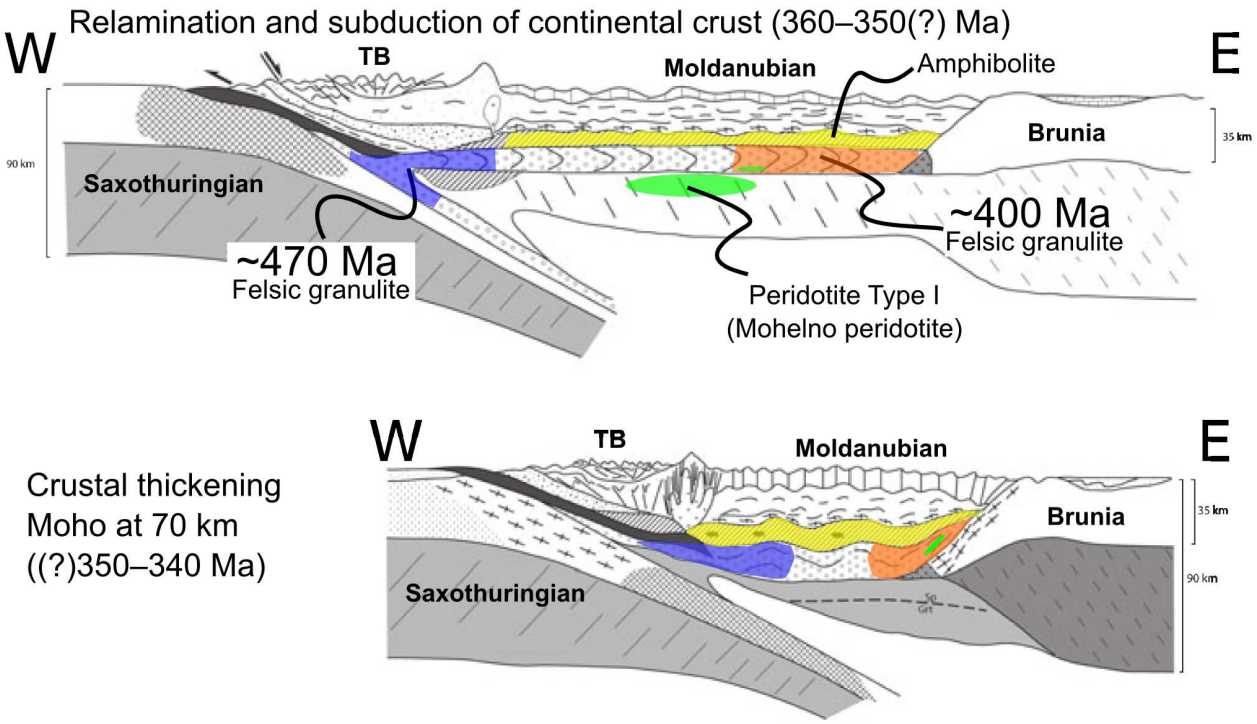

Figure 1. Section across Variscan orogen from Lexa et al. (2011), adopted to illustrate the idea of different timing of relamination and therefore peak metamorphism for granulites of the eastern margin of Bohemian Massif compared to their westerly counterparts.

Our work shows that the mantle was refertilized before being incorporated in the crust, which is a typical feature of asthenospheric mantle below slow spreading rifts (Dijkstra et al., 2001, 2003; Bodinier and Godard, 2007 and references therein). Therefore, it is very likely that the Late Devonian history recorded in the mantle fragment reflects only heterogeneous nature of subcontinental mantle lithosphere related to Devonian rifting (most likely in back arc position with respect to Saxothuringian subduction (Fig. 1) and is not genetically related to surrounding felsic granulites. The place of incorporation of mantle fragment to felsic granulite is impossible to determine, but its Devonian age coincides well with origin of Central Bohemian pluton – magmatic arc and ages of eclogites located in the Teplá suture (Schulmann et al., 2009). In conclusion, the Mohelno peridotite represents an autochthonous lithospheric mantle, that was sampled by granulite crust during relamination process.

The other information is coming from metamorphic U-Pb zircon ages from granulites, which are ranging between 353 to 340 Ma (Chapter 1). These ages were already reported by Schulmann et al. (2005) and Tajčmanová et al. (2010), which indicates a melting and associated crystallization of zircons from orogenic lower crust at the easternmost termination of the Bohemian Massif ten million years before similar event in the central part of the root. This can be interpreted as an event related to

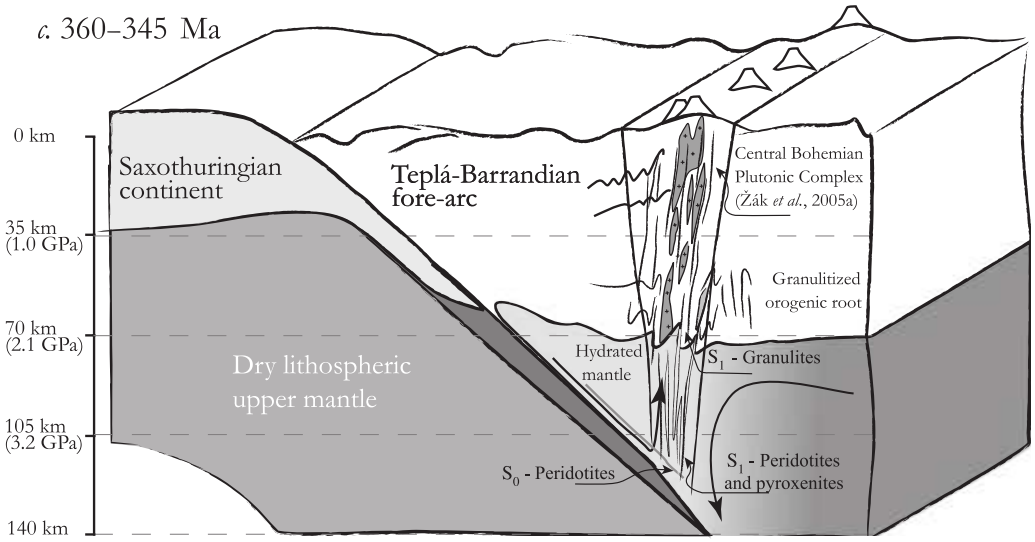

Figure 2. 3D geodynamic model of melt enhanced exhumation of Běstviná peridotite (from Machek et al., 2009).

peak of granulite–facies metamorphism which occurs earlier in the East than in the West. The reason of that can be deduced from the model of radioactive decay of highly radiogenic protoliths presented by Lexa et al. (2011). Using this approach, the subducted Devonian felsic crust is relaminated at the bottom of the root 15 My earlier than the Ordovician one in the rear part of the orogen, which was very likely not yet metamorphosed. At the time of arrival of Devonian part of lower crustal allochthon to the eastern margin of the root elapsed already 15 My of thermal relaxation, while the Ordovician part just arrived at the bottom of the root. This could be the reason, why the age of granulite–facies metamorphism (and melting) started 15 – 10 My years before the similar event in the rear part of the orogen. The previous comparative microstructural study of granulites and mantle rocks in the western part of the orogenic root showed, that the mantle fragments are heterogeneous in composition and peridotites themselves are partly coupled with surrounding granulite (Machek et al., 2009) (Fig. 2). These authors proposed, that vertical rheological heterogeneity (clinopyroxenite layering) in the mantle wedge due to melt percolation from the subduction zone is responsible for mechanical coupling between granulite and clinopyroxenite. This model suggests subvertical emplacement of upper mantle rocks into orogenic lower crust. The important ingredient of this model is an assumption, that this tectonic history is linked to the dynamics of ESE dipping Saxothuringian subduction zone during late Devonian and Early Carboniferous. However, the model proposed in this study (Chapter 2) differs from that of Machek et al. (2009), as the scale of the peridotite body as well as amount of mechanical reworking is quite different. The Mohelno peridotite body is almost completely recrystallized to fine

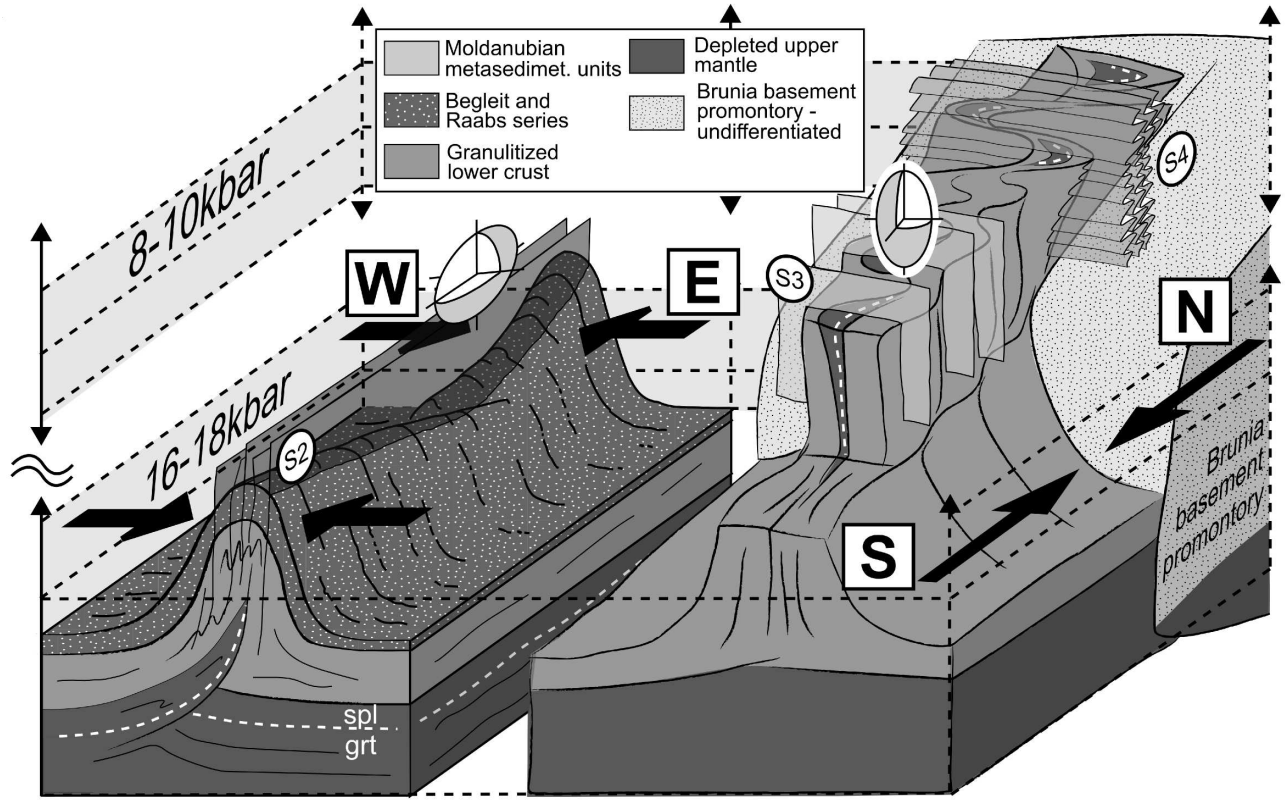

Figure 3. 3D tectono-metamorphic model of imbrications of mantle lithosphere and emplacement of peridotite sheet into folded lower crust during the shortening of the Variscan orogenic root. Example from the Náměšť Granulite Massif.

grained mylonite microstructure in proposed intra mantle shear zones, that facilitated emplacement of mantle sheets into lower crust of the root (Fig. 3). Similarly, Franěk et al. (2011) also suggest the importance of the Saxothuringian subduction dynamics on emplacement of peridotite sheets into south Bohemian granulites. All these studies imply, that the mantle fragments of different origin and composition have been emplaced into the orogenic lower crust all along the mantle wedge related to Saxothuringian subduction. All these studies agree in an exhumation phase resulting in vertical transfer of lower crustal and mantle material due to folding and vertical extrusion process. The lower crust and mantle arrived to the mid-crustal levels corresponding to pressure about 0.7–1 GPa.

The difference between final structure recorded in the mantle fragments in the western and the eastern part of the orogenic root is in N-S shortening induced by southward movements of Brunia promontory. Our study shows that mantle and surrounding lower crust were folded in depth 20 – 25 km during N-S shortening, that was almost orthogonal to Late Devonian – Early Carboniferous orogenic fabric.

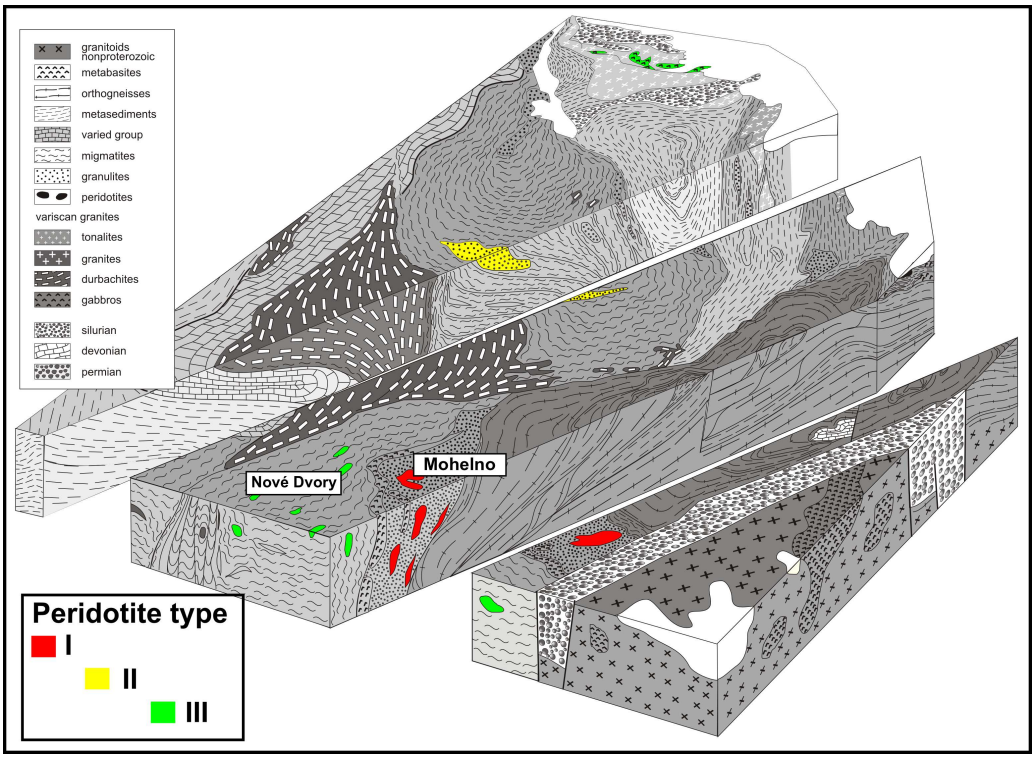

Figure 4. Block diagram with distribution of various garnet peridotite (peridotite types from Medaris et. al, 2005) along the eastern margin of Bohemian Massif (block diagram from Schulmann et al. 2005)

Excellent preservation of early fabrics and geographic position of studied granulites and peridotites indicate, that these rocks have been sampled in front of colliding Brunia promontory. Therefore, these areas provide a unique opportunity to study the crust – mantle interactions non-affected or weakly affected by middle crustal channel flow as discussed by Schulmann et al. (2008). Indeed, the positions and fabric of granulite – peridotite lower crustal sheets at the eastern margin of the Bohemian Massif show alternations with middle crust and potentially best examples of orogenic channel flow fabrics.

The heterogeneity of peridotite composition and variability P–T conditions in individual units of eastern margin of the Bohemian Massif imply a juxtaposition of palaeogeographically contrasting domains by the channel flow process. The best example is recent position of compositionally and geochemically different Mohelno and Nové Dvory peridotites (Fig. 4), that recently crop out 10 km from each other (e.g. Medaris et al., 1990). Mohelno peridotite is supposed to be exhumed due to intramantle shearing, vertical extrusion and thrusting at the beginning of Brunian indentation. In contrary, vertical movement of the UHP Nové Dvory (Nakamura et al., 2004) and similar types of peridotites (Type III according to Medaris et al., 2005) could be facilitated by heterogeneous vertical melt percolation in the mantle wedge responsible for lithological modification and subsequent strain

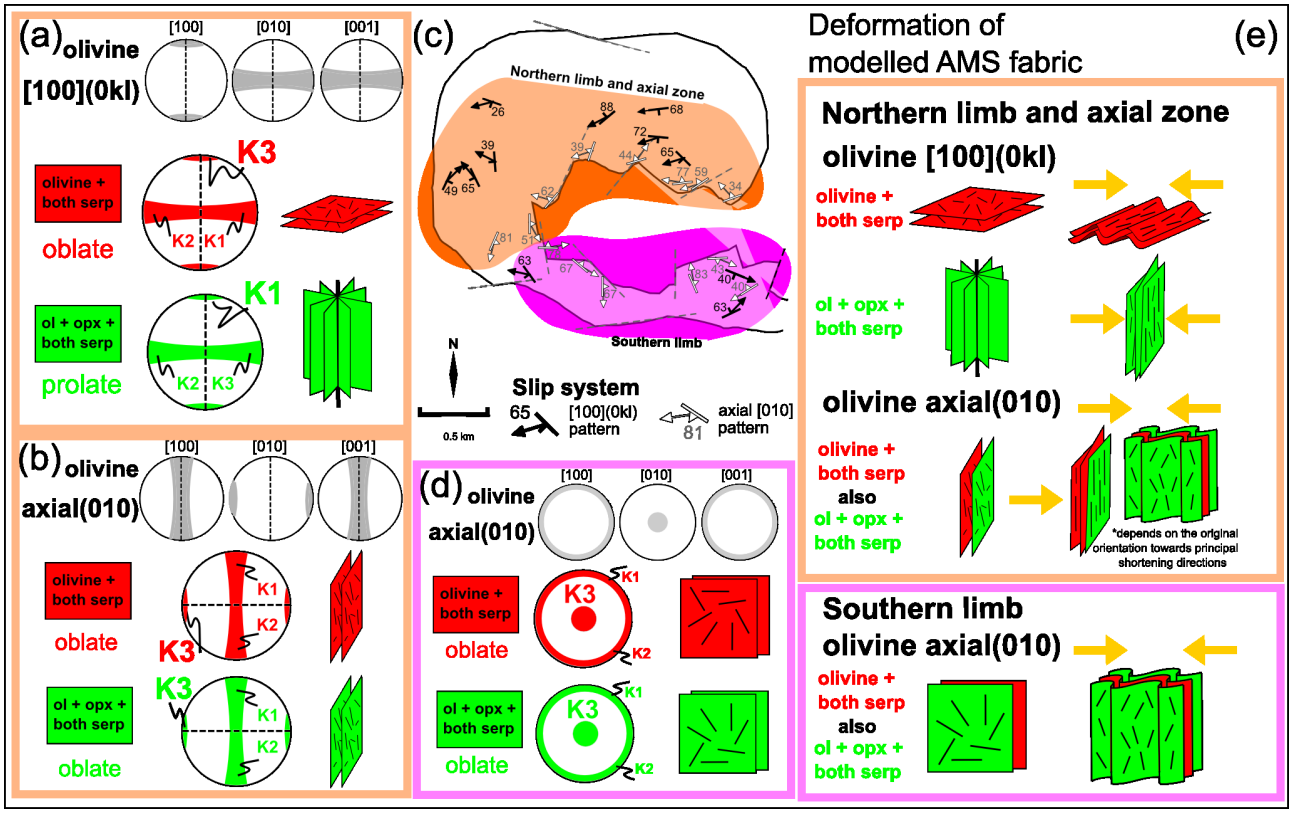

Figure 5. Sketch of our proposed model deducing the magnetic fabric from the primary crystallographic fabric, topotactic relationships between minerals and finally from orientation towards the main stress direction.

weakening in the pyroxene rich layers. Finally, it could be the lower crustal channel, that transported originally the UHP peridotite fragments throught orogenic root and later over continental promontory within channel flow hundreds of kilometers from the site of mantle-crust incorporation.

The late history of peridotite fragment was studied using study of anistropy of magnetic susceptibility coupled with analysis of serpentinisation process. The peridotite was serpentinized by two stage process, producing first antigorite and later lizardite + magnetite at the expense of olivine and orthopyroxene. The AMS study shown, that the serpentinisation was originally a static process related to release of fluids from crystallizing melts in the mid-crustal channel flow. However, the AMS fabrics indicate, that the serpentinite recorded a ductile strain, that is incompatible with static recrystallization hypothesis. The simple modelling of paramagnetic AMS fabric was used to conceptualy model possible fabric origin due to post-serpentinisation deformation.

We proposed a model of deformation of weak serpentine matrix including magnetite crystals (Fig. 5), that is compatible with late E–W shortening. Such an event is known at the eastern margin from previous studies of for instance Schulmann et al. (1991). Interestingly, the refertilized harzburgite

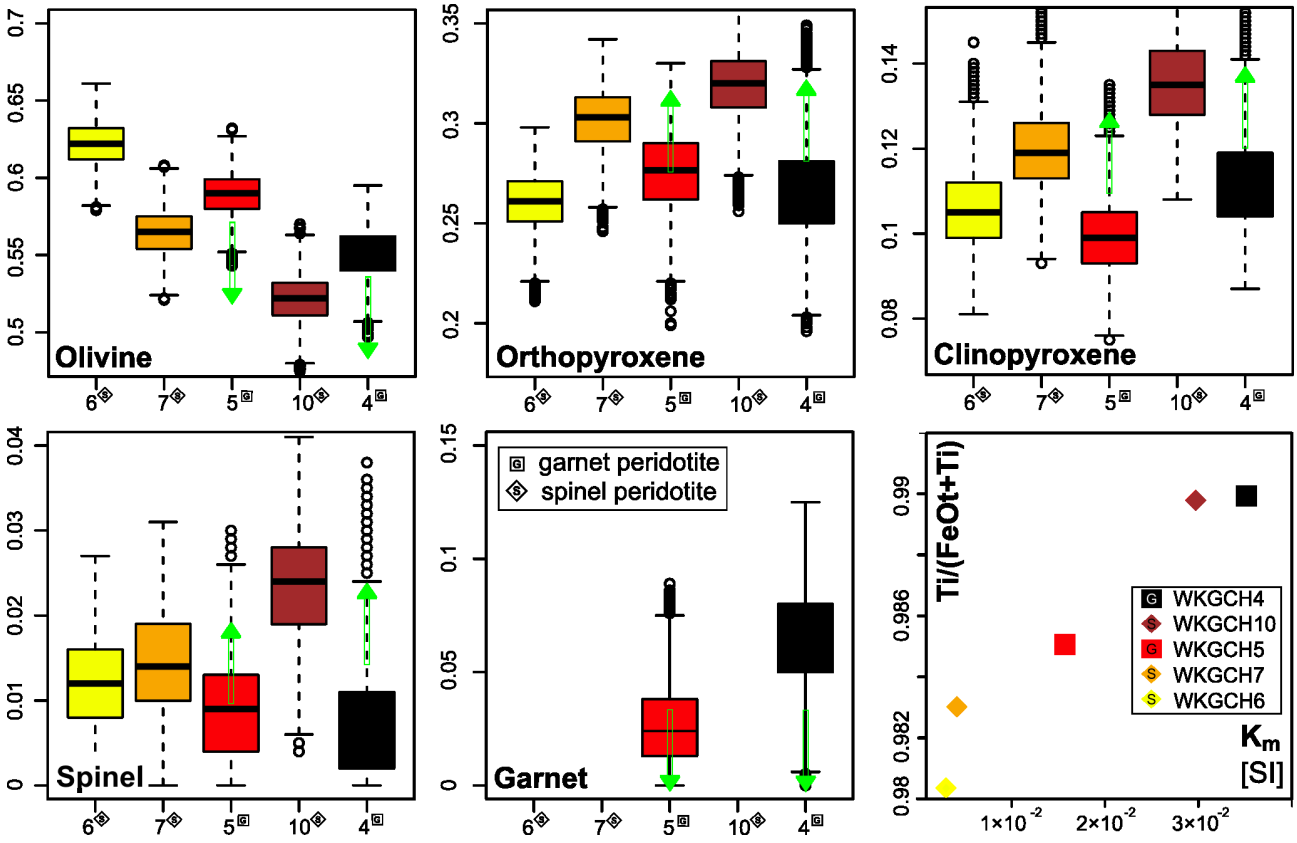

Figure 6. Modal compositions of the studied Mohelno peridotite reconstructed from published mineral analyses (Medaris et al., 2005; Kamei et al., 2010) and our whole-rock geochemical dataset. Trends in modal composition suggest refertilization of the Mohelno harzburgite.

shows higher degree of seprentinization, which is reflected by high bulk magnetic susceptibility. The AMS study thus contribute as an indirect method to evaluate the degree of fertilization of harzburgites in highly seprentinized rocks (Fig. 6).

References

- Bodinier, J.-L. & Godard, M. (2007). Orogenic, ophiolitic, and abyssal peridotites. In: Holland, H. D. & Turekian, K. K. (Ed.), Treatise on geochemistry, Pergamon.

- Dijkstra, A. H., Barth, M. G., Drury, M. R., Mason, P. R. D., Vissers, R. L. M., (2003). Diffuse porous melt flow and melt–rock reaction in the mantle lithosphere at a slow–spreading ridge: A structural petrology and LA-ICP-MS study of the Othris Peridotite Massif (Greece). Geochem. Geophys. Geosyst. 4, 8613.

- Dijkstra, A. H., Drury, M. R., Vissers, R. L. M., (2001). Structural petrology of plagioclase peridotites in the West Othris Mountains (Greece): melt impregnation in mantle lithosphere. J. Petrol. 42, 5–24.

- Janoušek, V., Finger, F., Roberts, M., Frýda, J., Pin, C., Dolejš, D., (2004). Deciphering the petrogenesis of deeply buried granites: whole-rock geochemical constraints on the origin of largely undepleted felsic granulites from the Moldanubian Zone of the Bohemian Massif. Earth Env. Sci. T. R. So. Edinb. 95, 141–159.

- Janoušek, V., Holub, F. V., (2007). The causal link between HP–HT metamorphism and ultrapotassic magmatism in collisional orogens: case study from the Moldanubian Zone of the Bohemian Massif. P. Geologist. Assoc. 118, 75–86.

- Lexa, O., Schulmann, K., Janoušek, V., Štípská, P., Guy, A., Racek, M., (2011). Heat sources and trigger mechanisms of exhumation of HP granulites in Variscan orogenic root. J. Metamorph. Geol. 29, 79–102.

- Medaris, L. J., Wang, H., Jelínek, E., Mihaljevič, M., Jakeš, P., (2005). Characteristics and origins of diverse Variscan peridotites in the Gföhl Nappe, Bohemian Massif, Czech Republic. Lithos 82, 1–23.

- Schulmann, K., Konopásek, J., Janoušek, V., Lexa, O., Lardeaux, J.-M., Edel, J.-B., Štípská, P., Ulrich, S., (2009). An Andean type Palaeozoic convergence in the Bohemian Massif. C. R. Geosci. 341, 266–286.

- Schulmann, K., Kroner, A., Hegner, E., Wendt, I., Konopásek, J., Lexa, O., Štípská, P., (2005). Chronological constraints on the pre-orogenic history, burial and exhumation of deep-seated rocks along the eastern margin of the Variscan Orogen, Bohemian Massif, Czech Republic. Am. J. Sci. 305, 407–448.

- Tajčmanová, L., Konopásek, J., Schulmann, K., (2006). Thermal evolution of the orogenic lower crust during exhumation within a thickened Moldanubian root of the Variscan belt of Central Europe. J. Metamorph. Geol. 24, 119.

- Tajčmanová, L., Soejono, I., Konopásek, J., Košler, J., Klotzli, U., (2010). Structural position of high-pressure felsic to intermediate granulites from NE Moldanubian domain (Bohemian Massif). J. Geol. Soc. Lond. 167, 329–345.

Résumé de la these en français

La compréhension de l'interaction entre la croûte continentale et le manteau pendant une orogenèse est un enjeu majeur pour comprendre les processus thermomécanique profonds au sein des orogènes et le comportement du manteau sous-continental pendant la collision. La chaîne varisque offre un site exceptionnel pour étudier les interactions tectoniques entre le manteau et la croûte inférieure grâce à la présence de corps de péridotites à spinelle et grenat au sein de massifs granulitiques à Ky–Kfs (Behr, 1961 – Saxony granulite massif; Gayk and Kleinschrodt, 2000 – Vosges Massif; Medaris et al., 1995 – Bohemian Massif). Dans le cœur de la chaîne varisque, la variété des relations entre les péridotites et les granulites/migmatites environnantes suggère un comportement thermique et mécanique complexe de la croûte inférieure orogénique et du manteau sous-jacent, ce qui pourrait refléter une histoire tectonique polyphasée.

De plus, les études de l'anisotropie sismique du manteau lithosphérique sous-continental par l'analyse de la biréfringence des ondes S et du déphasage temporel des ondes P révèlent des orientations et des intensités de fabriques contrastées. Elles mettent en valeur des fabriques différentes du manteau lithosphériques au sein des différentes unités de la chaîne varisque européenne (Babuška and Plomerová, 2006; Babuška et al., 2007, 2008). La subduction et la collision dévono-carbonifère pourrait être à l'origine de ces hétérogénéités comme le suggèrent Babuška et al. (2010). Selon cette étude, le manteau lithosphérique ferait partie intégrante de bloc individuels formant le massif de Bohème, rigides pendant l'événement collisionnel principal.

Le massif de Bohême est caractérisé par la présence de plusieurs centaines de corps de péridotites de taille, de composition et de degré de serpentinisation variés (Medaris et al., 2005). Ces massifs de péridotites du manteau sous-continental ont enregistrés différents trajets P–T. Plusieurs corps de péridotites (harzburgites à spinelle) ont pour origine le rifting pré-orogénique c'est-à-dire des conditions P–T et une géochimie semblable à celle du manteau asthénosphérique (Medaris et al., 2005). En revanche, d'autres corps (lherzolite à grenats) montrent des conditions P–T extrêmes de 1400 °C pour

40–50 kbar issues du coin mantellique échantillonné et exhumé dans la zone de subduction (Becker, 1996, 1997; Nakamura et al., 2004; Ackermann et al., 2009; Machek et al., 2009).

Même s'il existe de nombreuses études sur la compréhension de la pétrogenèse, des conditions métamorphiques (Medaris et al., 1995, 2006; Ackerman et al., 2009) associés à des études de pétrophysiques (fabriques) de ces roches (Kamei et al., 2010), il manque une étude détaillée pluridisciplinaire combinant les données de géochimie, de structurale, de pétrologie et de pétrophysique. Récemment, l'anisotropie de susceptibilité magnétique a été utilisée dans le but de comprendre la relation entre les fabriques internes des enclaves de péridotites et des granulites adjacentes (Hrouda et al., 2009). Il a été montré que les fabriques du manteau sont localement couplées avec celles de la croûte inférieure orogénique environnantes (Machek et al., 2009), suggérant soit une évolution rhéologique et tectonique commune entre le manteau lithosphérique et la croûte inférieure, soit un découplage complet avec des fabriques non similaires entre les deux lithologies (Hrouda et al., 2009).

L'étude de fragments de péridotites peut se faire par deux approches : 1) une étude régionale des fabriques des principaux corps péridotitiques par diffraction d'électrons rétrodiffusés dans les olivines et les pyroxènes, associée à une analyse de l'anisotropie de susceptibilité magnétique (ASM) afin de déterminer un modèle de fabriques dans le manteau sous-continental. 2) une étude pluridisciplinaire détaillée de quelques corps de péridotites et des roches encaissantes à l'aide des outils géochimiques, pétrologiques, structuraux/pétrophysiques et géochronologiques. La seconde approche permet de comprendre les processus liés à l'origine des roches mantelliques et crustales associées, leurs évolution P–T–t, les interactions mécaniques entre le manteau, la croûte inférieure et les unités supérieures. Dans ce travail, nous avons sélectionné la seconde approche, même si plusieurs autres corps mantelliques ont été aussi investigués. Nous avons sélectionné le corps serpentinisé d'harzburgite à spinelle et grenat de Mohelno et les granulites de Náměšt environnantes. Ces deux lithologies ont été étudiées de manière conjointe dans le but d'établir un modèle tectonique et pétrophysique pouvant être extrapolé à d'autres corps péridotitiques.

Ce manuscrit de thèse est formé de trois principaux chapitres qui utilisent différentes techniques et répondent aux différentes questions liés à l'origine des corps de péridotites et de leur comportement dans la croûte. Le premier chapitre est consacré à la géochimie et à la pétrogenèse des péridotites avec un modèle d'origine des roches encaissantes pré- et synorogénique. Le deuxième chapitre correspond à une étude combinée structurale et pétrophysique du massif de Mohelno dans le but d'expliquer le comportement mécanique des « nappes de charriage» de péridotites dans le cadre de l'évolution polyphasée

de la racine orogénique. Le troisième chapitre traite du développement de la serpentinisation et de l'anisotropie de susceptibilité magnétique dans les niveaux crustaux supérieurs pendant les derniers stades d'exhumation. Finalement, le dernier chapitre est un résumé des résultats obtenus jusqu'à présent combiné avec de nouvelles données pétrologiques et une perspective de modèle géotectonique à grande échelle de la branche orientale de la croûte inférieure orogénique du massif de Bohême.

Le premier chapitre est une étude géochimique, pétrologique et géochronologique d'un des plus gros massifs de croûte inférieur de la chaîne varisque européenne, le massif granulitique de Náměšt (NGM), situé à la bordure orientale du massif de Bohême. Ce chapitre présente de nouvelles données de géochimie sur roche totale, des données de pétrophysique ainsi que des datations in situ U-Pb de zircon par microsonde ionique (SHRIMP) des différentes fabriques dans les granulites. Les analyses géochimiques ont été réalisées dans trois lithologies majeures du NGM : les granulites acides à Ky-Kfs-Grt, les peridotites à spinelle et grenat et les amphibolites à grenat. Les principaux résultats de cette étude montrent que la signature géochimique des granulites du NGM est similaire à celles des autres granulites de la zone moldanubienne suggérant une pétrogénèse commune : une fusion partielle d'une croûte de composition granitique à la base d'une croûte continentale épaissie. La différence d'âge de protolith de lithologies à géochimie comparable pourrait indiquer que le processus de formation des précurseurs des granulites s'est déroulé à l'Ordovicien moyen et au Dévonien. En effet, les âges de protolith se concentrent au Dévonien inférieur dans le NGM, alors que les âges dans les granulites des autres massifs sont ordovicien moyen. De plus, l'âge de métamorphisme de 353 Ma dans le NGM est en moyenne 13 Ma plus vieux par rapport aux granulites plus occidentales. Les métabasites montrent des compositions d'E-MORB ou de basaltes intraplaques similaires aux autres occurrences datant du Cambrien tardif au début du Cambrien. Car leur chimie et leur position structurale est assez identique (Höck et al., 1997), il est très probable que les roches étudiés datent aussi du Paléozoïque inférieure et plus vraisemblablement du Cambrien tardif / début de l'Ordovicien. Les péridotites donnent des compositions d'harzburgites asthénosphériques refertilisées, probablement issues d'un environnement de dorsale lente. Même si les âges Nd-Sm peuvent être considérés comme des âges de refroidissement, il est plus probable qu'ils soient à relier à l'épisode de rifting (Beard et al., 1992; Becker, 1997) et donc que le processus de formation des péridotites étudiées soit du dévonien supérieur. Ce travail montre que les trois lithologies ne peuvent avoir pour origine le même environnement géodynamique. Les granulites sont issues d'une croûte continentale du Dévonien à l'Ordovicien moyen alors que les metabasites proviennent d'un rifting cambro-ordovicien, ce qui exclue

donc une origine commune. Sur la base de ces données et des évolutions P–T contrastées, il est proposé un model de « re-lamination » d'une croûte continentale allochtone sous une croûte continentale inférieure basique autochtone moldanubienne. Les âges métamorphiques précoces de la croûte inférieure allochtone comparés aux âges des massifs plus occidentaux sont interprétés comme une mise en place diachroniques et une échelle de temps différente de la maturation thermique des parties respectivement occidentales et orientales de la croûte relaminée. La géochimie du manteau reflète l'hétérogénéité de la composition du manteau sous-continentale échantillonné pendant le processus de re-lamination de la croûte. Ce mécanisme peut expliquer les variations significatives des conditions P–T du matériel mantellique au sein des différents massifs de granulites.

Le deuxième chapitre traite des intercalations de péridotites déformées dans des zones de cisaillement intra-mantelliques et replissées dans des conditions de la croûte inférieure à moyenne. Les modèles d'enveloppes rhéologique de la lithosphère sont discutés : 1) un manteau lithosphérique résistant et une croûte inférieure « fluide » pour un géotherme moyen et élevé, 2) un manteau lithosphérique peu résistant en raison d'études sismiques suggérant que le contraste de résistance entre le manteau et la croûte peut varier de plusieurs ordres de magnitude. Ces modèles sont basés sur des expériences et des données géophysiques alors que les données de terrains sont peu exploitées. La zone interne du massif de Bohême (chaîne varisque européenne) contient de larges complexes de granulites à Ky-Kfs avec des intercalations de péridotites à spinelle et grenat qui permettent de répondre à la question du contraste rhéologique entre le manteau et la croûte sur la base de données de terrain.

Le troisième chapitre est consacré à l'étude des fabriques magnétiques dans des corps de roches ultramafiques serpentinisées de la racine orogénique. L'étude permet de comprendre ces fabriques, leur lien avec les microstructures des olivines et des pyroxènes et l'évolution tectonique régionale. La température limite de serpentinisation en lien avec le développement des microstructures dans les péridotites de Mohelno indique que la serpentinisation se fait à l'état statique, après plissement.

En conclusion, les résultats sont corrélés aux études précédentes sur les autres écailles de péridotites au sein des granulites de la racine orogénique. Il est montré que l'incorporation de fragments de péridotites dans la croûte inférieure chaude et leur exhumation conjointe se déroule lors d'un cycle tectonique indépendant au sein d'un flux chenalisé à la marge orientale de l'orogène. Il est finalement suggéré que le manteau à la base de la croûte orogénique épaissie est déformable, probablement affecté par des zones de cisaillement hétérogènes et qu'il « ajuste » ses fabriques aux déformations situé dans le système orogénique situé juste au dessus. Il est très probable que de telles zones de cisaillements ne

soient pas détectables par les méthodes géophysiques.

References

- Ackerman, L., Jelínek, E., Medaris Jr., G., Ježek, J., Siebel, W., Strnad, L., (2009). Geochemistry of Fe-rich peridotites and associated pyroxenites from Horní Bory, Bohemian Massif: Insights into subduction-related melt-rock reactions. Chem. Geol. 259, 152–167.

- Babuška, V., Plomerová, J., (2006). European mantle lithosphere assembled from rigid microplates with inherited seismic anisotropy. Phys. Earth Planet. In. 158, 264–280.

- Babuška, V., Plomerová, J., Fischer, T., (2007). Intraplate seismicity in the western Bohemian Massif (central Europe): A possible correlation with a paleoplate junction. J. Geodyn. 44, 149–159.

- Babuška, V., Plomerová, J., Vecsey, L., (2008). Mantle fabric of western Bohemian Massif (central Europe) constrained by 3D seismic P and S anisotropy. Tectonophysics 462, 149–163.

- Babuška, V., Fiala, J., Plomerová, J., (2010). Bottom to top lithosphere structure and evolution of western Eger Rift (Central Europe). Int. J. Earth Sci. 99, 891–907.

- Becker, H., (1996). Geochemistry of garnet peridotite massifs from lower Austria and the composition of deep lithosphere beneath a Palaeozoic convergent plate margin. Chem. Geol. 134, 49–65.

- Becker, H., (1997). Petrological constraints on the cooling history of high-temperature garnet peridotite massifs in lower Austria. Contrib. Mineral. Petrol. 128, 272–286.

- Behr, H., (1961). Beitrage zur petrographischen und tektonischen Analyse des sachsischen Granulitgebirges. Frebierger Forschungshefte C 119, 5–118.

- Gayk, T., Kleinschrodt, R., (2000). Hot contacts of garnet peridotites in middle/upper crustal levels: new constraints on the nature of the late Variscan high–T/low–P event in the Moldanubian (Central Vosges/NE France). J. Metamorph. Geol. 18, 293–305.

- Hrouda, F., Faryad, S. W., Jeřábek, P., Chlupáčová, M., Vitouš, P., (2009). Primary magnetic fabric in an ultramafic body (Moldanubian Zone, European Variscides) survives exhumation-related granulite-amphibolite facies metamorphism. Lithos 111, 95.

- Höck, V., Montag, O., Leichmann, J., (1997). Ophiolite remnants at the eastern margin of the Bohemian Massif and their-bearing on the tectonic evolution. Mineral. Petrol. 60, 267–287.

- Kamei, A., Obata, M., Michibayashi, K., Hirajima, T., Svojtka, M., (2010). Two contrasting fabric patterns of olivine observed in garnet and spinel peridotite from a mantle-derived ultramafic mass enclosed in felsic granulite, the Moldanubian Zone, Czech Republic. J. Petrol. 51, 101–123.

- Machek, M., Ulrich, S., Janoušek, V., (2009). Strain coupling between upper mantle and lower crust: natural example from the Běstvina granulite body, Bohemian Massif. J. Metamorph. Geol. 27, 721–737.
- Medaris, L., Beard, B., Johnson, C., Valley, J., Spicuzza, M., Jelínek, E., Mísař, Z., (1995). Garnet pyroxenite and eclogite in the Bohemian Massif: geochemical evidence for Variscan recycling of subducted lithosphere. Geol. Rundsch. 84, 489–505.
- Medaris, L. J., Wang, H., Jelínek, E., Mihaljevič, M., Jakeš, P., (2005). Characteristics and origins of diverse Variscan peridotites in the Gföhl Nappe, Bohemian Massif, Czech Republic. Lithos 82, 1–23.
- Medaris, L. G., Ghent, E. D., Wang, H. F., Fournelle, J. H., Jelínek, E., (2006). The Spačice eclogite: constraints on the P–T–t history of the Gföhl granulite terrane, Moldanubian Zone, Bohemian Massif. Mineral. Petrol. 86, 203.
- Nakamura, D., Svojtka, M., Naemura, K., Hirajima, T., (2004). Very high-pressure (>4GPa) eclogite associated with the Moldanubian Zone garnet peridotite (Nové Dvory, Czech Republic). J. Metamorph. Geol. 22, 593–603.

Abstrakt

Deformační interakce mezi horninami na významném rozhraní kůra - litosférický plášť je jedním z hlavních procesů, jejichž pochopení umožní lépe popsat termomechanické procesy probíhající hluboko v rozsáhlých pohořích a především chování kontinentálního pláště během kolize kontinentálních desek. Tato disertační práce obsahuje tři hlavní kapitoly, představující výsledky různých geologických metod, využitých při zkoumání původu a deformačního chování peridotitových těles ve spodní kůře Variského orogenu.

Závěry v první kapitole na základě nových geochemických a geochronologických dat diskutují paleotektonickou pozici hlavních litologií v Náměšťském granulitovém masívu. Chemické složení felzických granulitů prokázalo jejich blízkou afinitu s ostatními granulity Moldanubické zóny. REE obsahy v amfibolitech lemujících Náměšťský granulitový masív ukazují na jejich původ v riftovém prostředí (E-MORB, WPT). Studie peridotitů ukázala, že peridotity jsou pravděpodobně refertilizované harzburgity a jejich původ pravděpodobně v prostředí pomalu se rozpínajících oceánských hřbetů. Precizní metodou SHRIMP U-Pb datování *in situ* zirkonů z Náměšťských granulitů, se podařil prokázat věk 353 Ma vrcholné metamorfózy hornin Variského orogenního kořenu exhumované na východním okraji Českého masívu.

Druhá kapitola prezentuje závěry ze strukturní studie Mohelenského peridotitu a okolních granulitů z Náměstského granulitového masívu. Jako jedinou efektivní metodou pro studium vnitřní stavby peridotitu se kvůli rozsáhlé serpentinizaci ukázalo měření přednostní mřížkové orientace (EBSD). V serpentinizovaném peridotitu byly zjištěny dva odlišné olivínové skluzné systémy, jejichž distribuce společně s detailním strukturním mapováním v okolním Náměšťském granulitovém masívu umožnily vysvětlit reologické chování peridotitového tělesa v prostředí kořene orogenu. V této kapiole jsme se pokusili vytvořit geotektonický model, který popisuje historii peridotitového tělesa v rámci mnoha fází tektonické historie orogenního kořenu.

Ve třetí kapitole představujeme výsledky z analýzy serpentinizačních procesů v Mohelenském peri-

dotitu a jejich vlivu na magnetickou stavbu peridotitu, především na anizotropii magnetické susceptibility (AMS). Tři rozdílné stavby odlišitelné v magnetických měřeních z Mohelenského peridotitu reprezentují postupný proces serpentinizace a nárůst významu deformační složky magnetické stavby nad složkou primární (způsobenou přednostní orientací krystalů a zákonitým růstem produktů serpentinizace). Vytvořený model vzniku magnetické stavby založený na přednostní orientaci hlavních horninotvorných krystalů popisuje dobře chování pozorované v serpentinizovaném peridotitu.

Všechny tyto poznatky potvrdily a umožnily rozvinout dříve představený model původu Moldanubických granulitů (Janoušek et al., 2004; Lexa et al., 2011).